Turning a growth cone into a synapse: Molecular and cellular mechanisms underlying the wiring of neurons

Dissertation

zur

Erlangung des Doktorgrades (Dr. rer. nat.)

der

Mathematisch-Naturwissenschaftlichen Fakultät

der

Rheinischen Friedrich-Wilhelms-Universität Bonn

vorgelegt von

Thorben Pietralla

aus Mönchengladbach

Bonn, November 2025

Angefertigt mit Genehmigung der Mathematisch-Naturwissenschaftlichen Fakultät der Rheinischen Friedrich-Wilhelms-Universität Bonn

Gutachter/Betreuer: Prof. Dr. Frank Bradke
Gutachter: Prof. Dr. Walter Witke

Tag der Promotion: 06.02.2026
Erscheinungsjahr: 2026

Table of contents

TABLE OF CONTENTS **1**

TABLE OF FIGURES **3**

ABBREVIATIONS **5**

SUMMARY **8**

INTRODUCTION **10**

DEVELOPMENT OF THE NERVOUS SYSTEM 11

CYTOSKELETAL ORGANISATION IN NEURONS 17

The neuronal actin cytoskeleton *17*

Microtubules and their role in growth *25*

NEURITE FORMATION 30

THE NEURONAL GROWTH CONE 31

NEURONAL POLARISATION AND THE SPECIFICATION OF AN AXON 32

MECHANISMS OF AXON GROWTH AND ELONGATION – LESSONS FROM CELL MIGRATION 36

SYNAPTIC CONNECTIONS AND TRANSMISSION OF INFORMATION 41

REGENERATION FAILURE OF CNS NEURONS AND THE CONTRIBUTION OF DEVELOPMENTAL AND MATURATION PROCESSES 43

OBJECTIVES - HOW DO NEURONS GROW AND LOSE THEIR INTRINSIC GROWTH POTENTIAL? 47

RESULTS **49**

GROWTH BEHAVIOUR OF HIPPOCAMPAL NEURONS IN CULTURE 49

'Mixed culture' system to track whole cell morphology *49*

Changes in growth speed of neurites in the course of development *51*

ACTIN FILAMENTS BECOME STABILISED IN THE GROWTH CONE OF DEVELOPING NEURONS OVER TIME 53

CHANGE IN DEPENDENCE ON ACTIN POLYMERISATION FOR NEURITE GROWTH IN THE COURSE OF DEVELOPMENT 59

ACTIN DEPOLYMERISATION CAUSES MICROTUBULE BUNDLING DEFECTS IN YOUNG NEURONS 64

STABILISATION OF MICROTUBULES FAILS TO RESCUE THE GROWTH DEFECT 70

OVEREXPRESSION OF MICROTUBULE BUNDLING PROTEINS PARTIALLY RESCUES THE GROWTH DEFECT 76

NEURONS OVEREXPRESSING THE ACTIN-REGULATOR COFILIN BEHAVE SIMILARLY TO THE CYTO D/LAT A-TREATED NEURONS 82

MYOSIN-II ACTIVITY REGULATES GROWTH IN YOUNG NEURONS BUT NOT IN POLARISED NEURONS 87

AN ANTAGONISM OF THE ARP2/3 COMPLEX AND MYOSIN-II ALLOWS THE FORMATION OF A POLARISED MORPHOLOGY 89

ARP3 IS MAYBE REQUIRED FOR AXON ELONGATION 96

NEURONS BECOME ELECTRICALLY ACTIVE WHEN GROWTH RATES ARE REDUCED 98

CHRONIC DEPOLARISATION INHIBITS GROWTH IN POLARISED NEURONS 101

DISCUSSION **105**

Growth reduction of maturing hippocampal neurons is not caused by reduced actin turnover rates 105
Actin polymerisation is required for fast axon elongation in early developmental phases 110
Microtubule bundling and their contribution for neurite elongation 111
Myosin-II activity restricts growth and maintains polarity 117
The Arp2/3 complex is involved in axon elongation 119
Cofilin activity during development 120
The role of electrical activity in axon growth 123
Outlook - How to elicit regeneration after spinal cord injury? 127

MATERIALS AND METHODS 129

Materials 129
Chemicals 129
Drugs 131
Equipment 131
Consumables 132
Media, buffers, and solution 133
Antibodies 135
Methods 136
Animals 136
Primary hippocampal and cortical neuron culture 136
Neuron transfection and infection 138
DNA constructs and generation of expression vectors 139
Immunocytochemistry 139
G/F-actin assay 140
Western blot 141
Microscopy 142
Patch clamp electrophysiological recordings 143
Use of generative artificial intelligence 144
Analysis and quantification 145
Quantification of the length of the longest neurite and second longest neurite 145
Image analysis 145
Quantification of neuronal polarisation 146
Quantification of immunoblots 147
Tracking and quantification of EB3 comets 147
Statistical analysis and preparation of graphs 147

REFERENCES 148

ACKNOWLEDGEMENTS 184

Table of figures

Figure 1: Graphical summary of investigation by which changes of the actin cytoskeleton influence growth of developing hippocampal neurons over time in culture. 9
Figure 2: Scheme of neurogenesis and formation of axon-dendrite polarity in the developing embryonic cortex 13
Figure 3: Extracellular signals lead to organisation and changes in intracellular mechanisms 16
Figure 4: Establishment of neuronal polarity in culture 16
Figure 5: Actin filament assembly and disassembly 18
Figure 6: Actin-binding and regulating proteins 19
Figure 7: Microtubule assembly and dynamics 27
Figure 8: The neuronal growth cone 32
Figure 9: Preparation scheme for mixed neuron cultures 50
Figure 10: Growth behaviour of hippocampal neurons in culture over time 52
Figure 11: Actin cytoskeleton in developing neurons 55
Figure 12: Change in actin stability in growth cones of developing hippocampal neurons 58
Figure 13: Stabilisation of actin filaments with Jasplakinolide only affects young neurons 60
Figure 14: Actin depolymerisation differentially affects neurite length at different stages of development 62
Figure 15: Actin depolymerisation with Latrunculin A differentially affects neurite length at different stages 63
Figure 16: Actin destabilisation causes microtubule bundling defects. 66
Figure 17: Actin and tubulin properties in growth cones of Cyto D treated neurons at different developmental stages 67
Figure 18: Microtubules are more bundled over time in developing neurons 68
Figure 19: Cyto D-treated neurons have higher growth speed of EB3-comets and also show microtubule debundling 69
Figure 20: Inhibition of Myosin-II rescues actin depolymerisation based growth reduction 71
Figure 21: Blebbistatin prevents debundling of microtubules 72
Figure 22: Increased Tubulin intensity in Taxol treated neurons 74
Figure 23: Actin depolymerisation reduces growth-promoting effect of Blebbistatin and Taxol 75
Figure 24: Actin depolymerisation mediated growth defect is not rescued with Taxol 76
Figure 25: Overexpression of MAP2c prevents microtubule debundling upon Cyto D treatment 78

Figure 26: MAP2c overexpression partially rescues growth defect 79
Figure 27: Overexpression of mTau prevents microtubule debundling..... 80
Figure 28: mTau overexpression partially rescues the actin depolymerisation based growth defect 81
Figure 29: Cofilin phosphorylation state in cultured neurons over time 83
Figure 30: Overexpression of hCofilin-1 via plasmid and virus in hippocampal neurons 85
Figure 31: Cofilin overexpression differentially affects neurite growth at different stages of development 86
Figure 32: Blebbistatin enhances neurite growth in young neurons until DIV 2 88
Figure 33: Antagonism of Arp2/3 complex and Myosin II in young neurons 90
Figure 34: Arp3 inhibition causes retraction in young but not in mature neurons 91
Figure 35: Arp3 and Arp2 are expressed throughout development in cultured cortical neurons 93
Figure 36: Arp3 is necessary for axon elongation..... 94
Figure 37: Blebbistatin rescues length of minor neurites but not length of the longest neurite after CK-666 treatment 95
Figure 38: Arp3 protein level is reduced in cultured neurons after Cre expression 97
Figure 39: Arp3 loss reduces the length of the longest neurite..... 98
Figure 40: Neurons become electrically active during maturation and are depolarised upon KCl treatment 100
Figure 41: KCl treatment does not affect young neurons but middle stage neurons.... 103
Figure 42: KCl induced growth reduction is reversible 104

Abbreviations

2D	Two-dimensional
3D	Three-dimensional
AAV	Adeno-associated virus
ABP	Actin-binding protein
Ac	*Aequorea coerulescens*
ADF	Actin depolymerising factor
ADF-H	Actin depolymerising factor homology domain
ADP	Adenosine diphosphate
AIS	Axon initial segment
AnkG	Ankyrin G
AP	Action potential
Arp	Actin-related protein
ArpC	Actin-related protein 2/3 complex subunit
ATP	Adenosine triphosphate
Blebb	Blebbistatin
BSA	Bovine Serum Albumin
BMP	Bone morphogenetic protein
CAMSAP	Calmodulin-regulated spectrin-associated protein
Cacna2d2	Calcium voltage-gated channel auxiliary subunit alpha 2 delta 2
CAG	CMV enhancer-chicken beta-actin promoter
Cav	Voltage-gated calcium channel
C-domain	Central domain
Cdc42	Cell division cycle 42
ChR	Channelrhodopsin
CLASP	CLIP-associating protein
CLIP	Cytoplasmic linker protein
CMV	Cytomegalovirus
CNS	Central nervous system
CP	Cortical plate
Cre	Cre recombinase protein
CSPG	Chondroitin sulfate proteoglycan
Cyto D	Cytochalasin D
DIV	Day *in vitro*
DMSO	Dimethyl sulfoxide
Dpr	Defective proboscis extension response

DREADD	Designer receptor exclusively activated by designer drugs
DRG	Dorsal root ganglion
E	Embryonic day
EB	End-binding protein
EDTA	Ethylenediaminetetraacetic acid
EGTA	Ethylene glycol-bis(2-aminoethyleter)-N,N,N',N'-tetraacetic acid
Ena	Enabled
F-actin	Filamentous actin
FBS	Fetal Bovine Serum
G-actin	Globular actin
GAPDH	Glyceraldehyde-3-phosphate dehydrogenase
GC	Genome copies
GDP	Guanosine diphosphate
GFP	Green fluorescent protein
GTP	Guanosine triphosphate
HBSS	Hank's balanced salt solution
HRP	Horse radish peroxidase
HS	Horse serum
IZ	Intermediate zone
Jasp	Jasplakinolide
kDa	Kilodalton
Lat A	Latrunculin A
LIMK	LIM domain kinases
MACF1	Microtubule actin cross-linking factor 1
MAP	Microtubule-associated protein
MEM	Minimal essential media
Mena	Mammalian enabled
MLC	Myosin light chain
MPS	Membrane periodic skeleton
MTOC	Microtubule organising centre
Munc13	Mammalian uncoordinated-13
MZ	Marginal zone
NEC	Neuroepithelial cell
p-	phosphorylated
PBS	Phosphate-buffered saline
P-domain	Peripheral domain

PFA	Paraformaldehyde
Pi	Phosphate, inorganic
PIC	Protease inhibitor cocktail
PLL	Poly-L-lysine
PNS	Peripheral nervous system
Rab	Ras-related in brain
Rac1	Ras-related C3 botulinum toxin substrate 1
Ras	Rat sarcoma
RFP	Red fluorescent protein
RGC	Radial glia cell
Rho	Ras homolog family member
RIM	Rab3-interacting molecule
ROCK	Rho-associated protein kinase
ROI	Region of interest
SCG	Superior cervical ganglion
SD	Standard deviation
SDS	Sodium dodecyl sulfate
SEM	Standard error of the mean
sEPSC	Spontaneous excitatory postsynaptic current
SSH	Slingshot protein phosphatase
SVZ	Subventricular zone
TBS	Tris-buffered saline
TCP	Tubulin carboxypeptidase
T-domain	Transition domain/zone
+Tip	Plus-end binding proteins
Trim46	Tripartite motif-containing protein 46
TTL	Tubulin tyrosine ligase
TTX	Tetrodotoxin
Tuj	β-III-tubulin
Vasp	Vasodilator-stimulated phosphoprotein
VZ	Ventricular zone
WASP	Wiskott-Aldrich syndrome protein
WAVE	WASP-family verprolin homologous protein
WT	Wild-type
γ-TuRC	γ-tubulin ring complex

Summary

The development and wiring of the nervous system are highly organised and regulated processes depending on a precise timing to connect the right paths. To connect with designated targets, neurons form an axon which extends until it reaches its synaptic partners. For this, neurons possess an enormous growth capacity and grow rapidly during development. The cytoskeleton, actin filaments, microtubules and intermediate filaments, are the conductor of these developmental processes. However, during neuronal maturation the growth capacity is lost and neurons fail to regenerate. This is attributed to a growth inhibiting environment but also to a low intrinsic growth propulsion of mature neurons. In young neurons, a dense actin network in minor neurite tips restricts the outgrowth of the axon. Increasing actin dynamics allows axonal outgrowth.

Here, I investigated in cultured hippocampal neurons whether increased stabilisation of actin filaments and attenuated actin dynamics contribute to the decline of growth capacity and reduce growth and regeneration of mature neurons. By manipulating different aspects of actin dynamics, pharmacologically and genetically, I showed that young neurons depend on precisely regulated actin dynamics to drive axon growth, while mature neurons are less dependent on actin to drive growth (Figure 1). I propose that neurons switch their mode of growth in the course of development from a more actin-dependent to a rather actin-independent way of growth. The outgrowth of the axon is controlled by contractile actomyosin that limits neurite extension. The axon escapes this growth restriction, while the other neurites remain growth-restricted, to maintain a polarised morphology.

I found that reduced actin dynamics in mature neurons seem not to be the reason for reduced growth capacity of mature neurons. Instead, the onset of the transmission of electrical signals correlates with the decline in growth rates, supporting the hypothesis that growth and transmission activity are mutually exclusive. Chronic depolarisation negatively affected the growth of polarised neurons. Thus, the underlying mechanisms by which physiological electrical activity negatively affects the ability of CNS neurons to grow need to be addressed in the future.

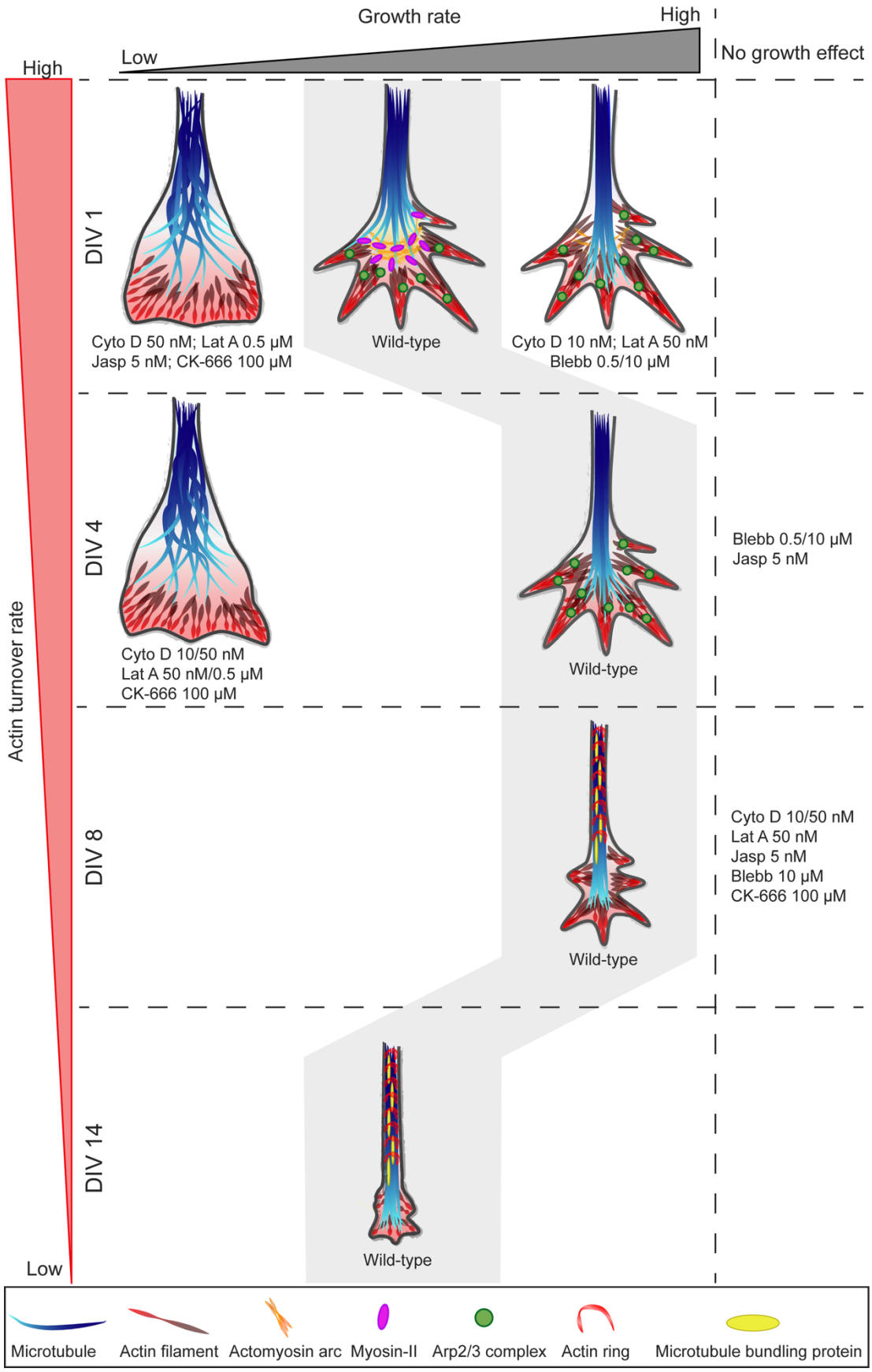

Figure 1: Graphical summary of investigation by which changes of the actin cytoskeleton influence growth of developing hippocampal neurons over time in culture.

Introduction

The nervous system is not an artificial neural network but the real source of our intelligence. It is a system composed of simple components, yet highly complex in its organisation and incredible in its abilities.

Receptors sense changes in the environment, be it temperature, light or touch. These sensations are converted into electrical impulses and sent to the processing centre, the brain. Within the brain, the multitude of incoming sensations is integrated and processed, generating a percept. The brain then sends commands in form of electrical impulses to effectors, including muscles and organs, to elicit a response. Protective reflexes do not even require the brain but are triggered via much shorter paths in the spinal cord, which enables even faster reaction times.

From receptors, incoming information is sent via sensory neurons to the central nervous system (CNS), composed of the brain and the spinal cord, while commands are sent to the executing units via motor neurons. The peripheral nervous system (PNS) connects the CNS to the limbs and organs and contains the axons of sensory and motor neurons.

The directed flow of information, from sensory neurons to the CNS and back via motor neurons, is possible through the polarised architecture of neurons, which they acquire during development. Upon polarisation, they form a signal receiving compartment: the dendrites, and a signal forwarding compartment: the axon. Signals are transmitted from one neuron to another through electrical and chemical synapses. Through this wiring, the entire body is connected to the brain. For this, the signal-transmitting axons span very long distances in our body, in some cases up to one meter in humans (Burdett and Freeman, 2014).

To form these circuits, neurons possess an enormous growth capacity during development, enabling the axon to cover huge distances within the developing organism by growing to the designated targets. However, in adults, injured neurons of the CNS fail to regrow and cannot regenerate (Ramon y Cajal, 1928). Thus, disruption of the connections between sensory receptors and motor effectors is typically associated with a loss of function. Lost functions are rarely recovered and usually remain impaired for the rest of the affected individual's life. Finding ways to regenerate the injured nervous system is, therefore, an important goal.

One approach to promote regeneration in the adult is to recapitulate developmental mechanisms (Hilton and Bradke, 2017). However, this approach requires understanding of the molecular and cellular mechanisms of how neurons grow during development and why these cells decrease growth rates and stop to grow.

The fact that neurons grow with such competence during development, indicates that there is an underlying switch in growth potential towards the end of development, between circuit formation and adulthood. Indeed, for both cultured neurons and neurons developing *in*

vivo, there is a developmental decline in growth capacity and onset of regeneration failure (Hilton and Bradke, 2017; Koseki et al., 2017; Lane et al., 2007). What constitutes this shift to very low growth potential is not yet clear. The identification, and subsequent suppression, of mechanisms which reduce growth potential, therefore, represents an approach to regenerate injured neurons. Switching off or reversing these growth-inhibiting processes potentially enable regeneration in adults.

The conductor of these developmental processes, described above, is the cytoskeleton. Actin filaments and microtubules enable the cell to migrate, to change morphology and to grow processes like the axon and dendrites. For this, these structures are dynamic in order to be able to react flexibly to changes in the environment. However, we still do not fully understand how the cytoskeleton orchestrates growth of neuronal processes. Further, it is unclear whether changes of the cytoskeleton, for example an increased stabilisation of actin filaments, is a reason why maturing CNS neurons reduce their growth propulsion and if this represents the switch of growth potential in maturing neurons. Therefore, I focus on the actin cytoskeleton and will investigate how actin dynamics contribute to neuronal growth, how it changes over time in cultured CNS neurons and whether these changes contribute to a decline of intrinsic growth capacity in maturing neurons.

In the following, I will review the current knowledge of how neurons develop and grow, the role of the cytoskeleton in these processes and what developmental and cellular mechanisms are required for the proper function of neurons but are already known to contribute to regeneration failure.

Development of the nervous system

The nervous system is composed of billions of neurons. The human brain, as the control centre of the body, contains 86 billion neurons alone (Azevedo et al., 2009). The development of the nervous system is a highly orchestrated process involving the specification of neural progenitors, their differentiation into neurons and glia, and the establishment of intricate neural circuits.

Most of the neurons are generated during gestation. The development of the nervous system begins around the third week of gestation, marked by the formation and thickening of the neural plate (Thau et al., 2025). The CNS is then formed by the inward folding of the neural plate, forming the neural tube. The neural tube further develops into the brain and spinal cord. Neurons are generated from progenitor cells (Figure 2A) (Paridaen and Huttner, 2014). The wall of the neural tube is constituted of a single layer of neuroepithelial cells (NEC). With ongoing development, these NECs change their identity and turn into radial glia cells (RGC) (Figure 2A), the main source generating neurons and glia cells in the cerebral cortex (Paridaen and Huttner, 2014). RGCs span the whole cortex and are attached with their endfeet at the apical/ventricular site as well as at the basal/pial surface

of the developing cortex. These neuronal progenitor cells (NECs as well as RGCs) undergo symmetric cell division and self-renew and thereby maintain and increase the pool of progenitors. When RGCs start to divide asymmetrically, the progenitors maintain their population by creating a daughter RGC but also generate a new cell type (Figure 2A). These first comprise neurons, and later, glia cells (Paridaen and Huttner, 2014). For further increase of the number of cells in the brain, progenitor cells divide under self-consumption, and generate two new neurons or glial cells (Figure 2A). The initiation of asymmetric cell division of progenitor cells is the onset of neurogenesis, leading to the formation of the billions of neurons required to construct the brain.

In late neurogenesis, when all neurons have been generated, RGCs switch from a neurogenesis mode to the creation of glia cells, astrocytes and oligodendrocytes (Paridaen and Huttner, 2014). In contrast, microglia, the immune cells of the brain, derive from erythromyeloid progenitor cells in the yolk sac, which migrate from there into the developing brain (Ginhoux and Prinz, 2015). Far from initial descriptions as “glue” holding neurons together, glia fulfil important functions. They influence neuronal migration and polarisation, as well as regulate synapse formation and pruning (Allen and Lyons, 2018). In addition, they are involved in brain homeostasis, provide the metabolic support critical for neuron function and represent the CNS’ immune system (Zuchero and Barres, 2015).

Similar to the cortex, neurons in the hippocampus are generated from progenitor cells and pyramidal projection neurons use radial glia cells as a scaffold to radially migrate to their final position (Khalaf-Nazzal and Francis, 2013). Interneurons tangentially migrate into the hippocampus. However, neuronal types of different lineage and sites of origin reside in the hippocampus but are often comparable with the equivalent cell types in the neocortex (Khalaf-Nazzal and Francis, 2013).

In general, the hippocampus consists of the *dentate gyrus* region and the *cornu ammonis* (CA) region, which is differentiated into CA1, CA2 and CA3 fields that are laminated with pyramidal cells in a characteristic strata of an inside-out layering (Khalaf-Nazzal and Francis, 2013). The pyramidal neurons in CA1-CA3 are generated by a relatively large area of neuroepithelium. In the different fields, neurogenesis peaks at different days between E14 and E16, but continues until early postnatal stages (Khalaf-Nazzal and Francis, 2013). When these pyramidal neurons leave the ventricular zone (VZ), they exhibit a multipolar morphology and migrate towards the hippocampal plate to form the different layers. However, these cells pause extensively in the intermediate zone (IZ) (Khalaf-Nazzal and Francis, 2013). It is hypothesised, that the long pausing of migrating neurons in the IZ coordinates the formation of the hippocampus between different cell types, including interneurons and *dentate gyrus* cells. The majority of neurons (roughly 85-90%) of CA1 are pyramidal neurons while interneurons represent only 10-15% of the

total neuronal population (Chauhan et al., 2021; Pelkey et al., 2017). Further, dentate granule cells are more numerous than pyramidal neurons in the adult hippocampus but are generated postnatally (Benson et al., 1994). Thus, the preparation of embryonic hippocampal cultures yields a relatively simple cell population, the majority of which are pyramidal excitatory neurons.

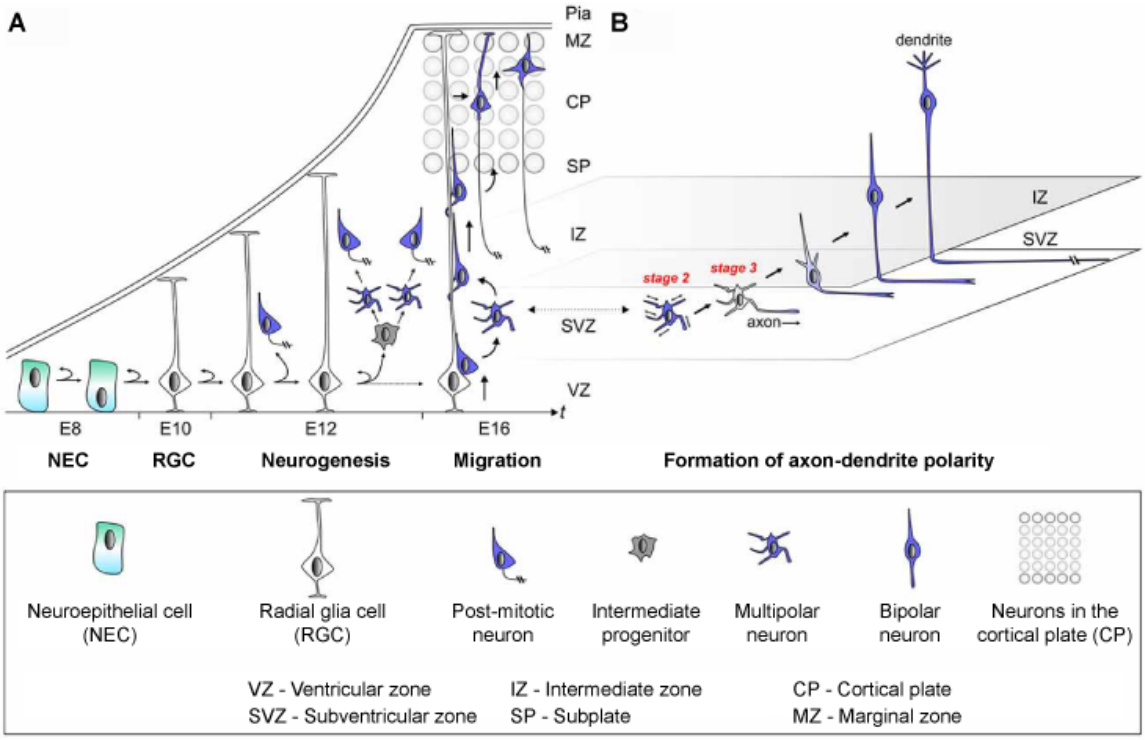

Figure 2: Scheme of neurogenesis and formation of axon-dendrite polarity in the developing embryonic cortex

(A) Principal types of neural progenitor cells, neuroepithelial and radial glia cells (NEC and RGC) and the progeny they produce for neurogenesis in the course of cortical development. After being generated by asymmetric or self-consuming symmetric division in the ventricular zone (VZ) and subventricular zone (SVZ), neurons migrate along RGCs towards the cortical plate (CP). Neurons are also generated by intermediate progenitors (IP) in the SVZ. (B) During migration in the developing cortex, neurons establish their polarity by forming a leading and a trailing process. Initially neurons exhibit a multipolar morphology (stage 2) in the SVZ. Subsequently they specify the axon and transit to stage 3. While the axon remains in the intermediate zone (IZ) as the trailing process, the cell body and leading process migrate upwards to the CP. In the CP, the leading edge develops into dendrites. Subplate (SP), marginal zone (MZ). Modified from (Hansen et al., 2017)

After neurons are generated from progenitor cells, they migrate along the RGC scaffold to their final destination and position of residence within the brain (Buchsbaum and Cappello, 2019). To connect to other regions within the brain and even regions beyond the brain, neurons undergo the process of polarisation. This pivotal step in neuronal development is the acquisition of structurally and functionally distinct axonal and dendritic compartments. It is fundamental for directional signalling and synaptic connectivity and often takes place during the period of neuronal migration (Figure 2B) (Hansen et al., 2017). Typically, neurons form several dendrites and a single axon. Dendrites receive information from other neurons or receptors, for example, photoreceptors. Incoming signals are processed in the cell body, and a corresponding signal in the form of an action potential (AP) is

transmitted via the axon to the target regions. Axons are the cables that bridge the distance between the position of the neuron's cell body and the target region. At the target regions, axonal terminals form connections with downstream neurons, upstream neurons for feedback loops, or muscle cells and convey information via electrical or chemical synapses. Thus, important information to dictate voluntary movement is transmitted from the brain via descending axonal tracts. For example, pyramidal neurons of the primary motor cortex send corticospinal axons that can reach up to 1 m to interneurons and lower motor neurons in the spinal cord (Quintá, 2021). The spinal cord then forwards the information via secondary motor neurons to muscles, causing their activation and subsequent movement of the individuum.

The formation of these network connections is divided into three steps (Lewis et al., 2013). First, the axon is specified from multiple neurites during neuronal polarisation. Second, the specified axon elongates and is guided to its specific target regions, and third, once the axon reaches the region of destination, it branches and forms presynaptic connections. It is debated whether the formation of neurites is an additional step that occurs independently before axon formation, or is already part of axon formation.

Initially, newborn neurons are symmetric and have a multipolar morphology in the subventricular zone. These neurons have multiple extending and retracting processes (Figure 2B) (Hansen et al., 2017). At one point, the symmetry breaks and extrinsic factors as well as intrinsic pathways determine the future axon and dendritic compartment. The neuron adopts a bipolar morphology and starts to locomote along the RGC scaffold. While the trailing process remains in the intermediate zone, the neuron translocates its cell body towards the cortical plate with the leading process finding the way. The leading process will eventually form the dendrites while the trailing process extends to its target regions.

A multitude of extrinsic as well as intrinsic cues and factors are involved in this precisely organised process, which is still not fully understood (Hansen et al., 2017; Schelski and Bradke, 2017) (Figure 3). In the developing tissue, cell-cell interactions as well as secreted factors like Reelin, brain derived neurotrophic factor, semaphorins, transforming growth factor β, and others influence polarisation and migration of newborn neurons *in vivo*. However, the fact that neurons polarise even without these extracellular factors shows that the neuron's intrinsic pathways are sufficient to break symmetry (Dotti et al., 1988). External cues might only act as a triggering system for a coordinated activation of the intrinsic polarisation program at the right time and place in the developing tissue (Hansen et al., 2017). Though in cultured neurons, specification of the axon is a random process, and every neurite has the potential to become the axon (Dotti and Banker, 1987; Goslin and Banker, 1989). In contrast, for example, cortical neurons in the mouse brain form an axon at the site of the cell that faces the apical surface (Lewis et al., 2013), suggesting

that external cues instruct the site of axon specification while intrinsic mechanisms carry out the formation of the axon.

Over the past decades, it has become evident that the cytoskeleton of neurons is a main effector instructing various developmental processes like neuronal polarisation, axon elongation, as well as formation and modulation of synaptic connections (Kevenaar and Hoogenraad, 2015; Neukirchen and Bradke, 2011). Various extracellular cues and signals activating surface receptors in addition to adhesion molecules lead to the cytoskeleton as the primary executor of changes in cell morphology and migration (Figure 3). To reduce the complexity of *in vivo* process and to study cell intrinsic pathways involved in neuronal polarisation and development, cell culture approaches have been established to analyse neuronal polarity in a simplified environment (Dotti et al., 1988). Cultured neurons have provided invaluable insights into the temporal and spatial dynamics of cytoskeletal rearrangement during neuronal development. These models recapitulate key stages of *in vivo* development, including neurite outgrowth, axon-dendrite specification and synaptogenesis.
The formation of neuronal polarity *in vitro* is divided into five stages, from a spherical cell to a mature neuron equipped with the necessary machinery to transmit information (Figure 4) (Dotti et al., 1988). After plating of dissociated hippocampal neurons, they attach to the surface and form spherical cells with dynamic lamellipodia (stage 1). Shortly later, a few hours after plating, several short cellular extensions occur (stage 2), called neurites, with an average length of about 10 µm (Figure 4). These minor neurites are highly dynamic and constantly extend and retract. Within the first one or two days in culture, the establishment of polarity is induced when one of these neurites eventually starts to elongate rapidly while the other minor processes remain short (stage 3). In stage 4, the axon continues to extend and the minor processes will become dendrites, after a week of culture. Dendrites also increase their length but grow more slowly than axons (Dotti et al., 1988). Finally, axonal terminals form presynaptic sites and contact dendritic spines of other neurons (stage 5). The number of stages is not linearly reflected by the number of days in culture. Stage 2 neurons are already observed a few hours after plating, while further maturation takes several days to weeks (Dotti et al., 1988).

Cytoskeletal dynamics are key for the development of the nervous system, including neurite formation, polarity and maintenance of connectivity (Menon and Gupton, 2016; Neukirchen and Bradke, 2011). The neuronal cytoskeleton is composed of microtubules, actin filaments and neurofilaments. The cytoskeletal polymers are dynamic structures that enable cells to acquire a certain shape and structure. The interaction among the various cytoskeletal filaments and a multitude of other proteins, along with cellular membranes,

allows to change cellular shape and is crucial for migration and morphogenesis during development (Hohmann and Dehghani, 2019).

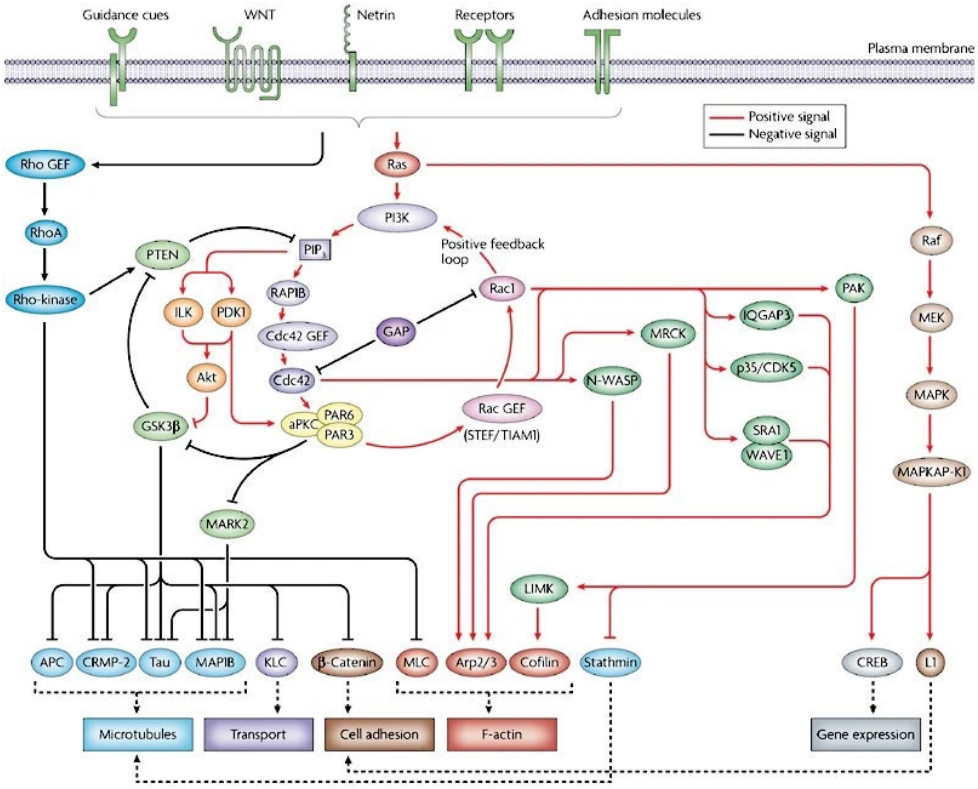

Figure 3: Extracellular signals lead to organisation and changes in intracellular mechanisms

In response to the activation of cell surface receptors by extracellular ligands or adhesion molecules, intracellular signalling pathways are triggered that lead to changes in cellular components and activities. Many of these signalling pathways converge on the cytoskeleton components, microtubules and actin filaments, resulting in structural changes or effects in dynamicity. From (Arimura and Kaibuchi, 2007)

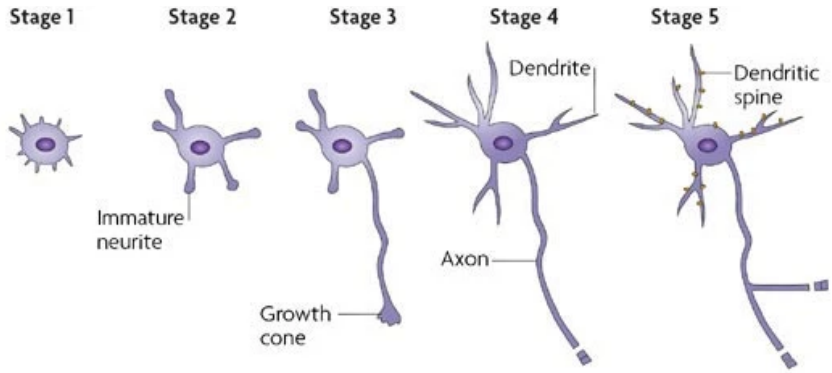

Figure 4: Establishment of neuronal polarity in culture

Schematic representation of neuronal polarisation in culture. Polarisation of hippocampal neurons is divided into five stages. After plating, neurons adhere to the surface and form a round sphere with lamellipodia and filopodia forming (stage 1). These protrusions develop into several minor neurites (stage 2). One of these neurites is selected to become the axon and starts to grow out rapidly (stage 3). After a few days, the remaining neurites develop into dendrites (stage 4). In the course of maturation synaptic connections are established (stage 5). Modified from (Arimura and Kaibuchi, 2007)

Cytoskeletal organisation in neurons

The cytoskeleton is essential for all cellular processes involving the shape of cells, organisation of the growth cone and many other processes like cell migration. It provides structure, stability, motility and due to its ability to change dynamics, it provides the tools to enable the cell to react to external stimuli and changes in the environment. Extra- along with intracellular signals regulate the polymerisation and depolymerisation of these polymers, changing cytoskeletal organisation. Together these polymers interact to orchestrate multiple cellular processes: dynamic changes enable intracellular transport of cargo, cell division, migration, polarisation and multiple other cellular events.

The neuronal actin cytoskeleton

Many cellular processes like growth cone protrusion and cell migration are driven by the neuronal actin cytoskeleton. The actin cytoskeleton is composed of globular (G-) actin monomers, which are assembled and polymerised to filamentous actin (F-actin) (Figure 5). Actin filaments are bi-helical polymers of two strands of actin monomers with a diameter of 6 – 9 nm.

These polymers have a polar structure with a plus end, and a minus end (Schneider et al., 2023). These terms are used interchangeably with barbed end and pointed end respectively. The polarity of the polymer is determined by the orientation of the monomers within the filament and by the bound adenine nucleotides (Flynn, 2013). Actin monomers are bound to either adenosine triphosphate (ATP) or adenosine diphosphate (ADP).

Monomeric actin subunits spontaneously assemble into elongated polymers once a critical concentration is reached, which is lower for ATP-G-actin compared to ADP-G-actin (Schneider et al., 2023). F-actin can grow from both ends unless the concentration of actin monomers is below the concentration needed for polymer assembly. Near steady-state conditions, actin polymerisation occurs at the barbed-ends and actin depolymerisation at the pointed-ends, resulting in actin treadmilling (Figure 5). Actin treadmilling is the ”flow” of actin-units from the barbed end to the pointed end through the filament.

When ATP-bound G-actin is added to the barbed end of the filament (Figure 5), the ATP is quickly hydrolysed into ADP-Pi within the filament, based on the ATPase activity of the polymer (Lappalainen et al., 2022). When the Pi is released, ADP-bound actin remains in the older portion of the filament. At the pointed end, the hydrolysed actin is released as ADP-actin. The ADP-actin monomer is recycled and converted to ATP-actin and can be incorporated at the barbed end again (Figure 5). This “aging” of actin subunits within the filament is critical for the regulation of actin filaments by actin-binding proteins (ABP). The barbed end with a short part of fresh ATP-bound subunits is followed by a middle region characterised by ADP-Pi-actin, and an old segment of ADP-actin (Lappalainen et al.,

2022). Many ABPs have a preferential binding activity for one of the nucleotide states, resulting in the sorting of ABPs along the filament, thereby influencing actin organisation and turnover (Carlier et al., 1993; Carlier et al., 1997; Pak et al., 2008; Vinson et al., 1998). The growth rate of actin filaments is determined by the addition of monomers to the barbed end and thereby by the availability of ATP and regenerated ATP-actin monomers (Lappalainen et al., 2022; Pollard, 2016). Further, the depolymerisation speed at the pointed end influences treadmilling speed and filament length.

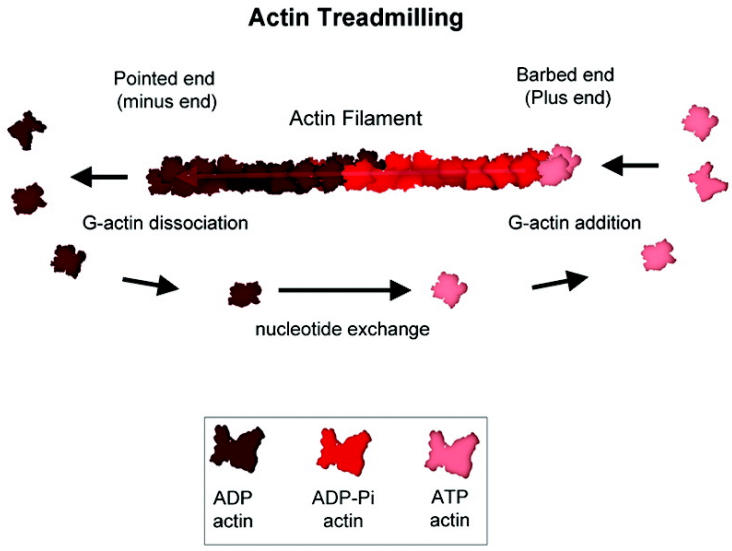

Figure 5: Actin filament assembly and disassembly

ATP-bound monomeric globular actin (G-actin) assembles into polar bi-helical filaments (F-actin) with a plus-end (barbed end) and a minus-end (pointed end). The polarity of the filaments is determined by the orientation of the monomers and the non-covalent binding of adenine nucleotides. In the filament, ATP is hydrolysed into ADP-Pi, which releases the Pi, resulting in ADP-actin subunits. At the pointed end, ADP-actin is depolymerised from the filament and ADP is exchanged by ATP. In the ATP-bound state, the monomer can be re-added to the barbed end of the filament. This cycle of actin monomers through the filament is known as treadmilling. From (Flynn, 2013)

The assembly and disassembly of actin filaments is dynamic and heavily controlled by actin regulators. Many of such factors have been identified, which influence various aspects of the actin cytoskeleton (Figure 6). These actin-regulating proteins help to organise the actin cytoskeleton in the cell. ABPs influence the nucleation and disassembly rate of actin filaments, induce the nucleation from existing filaments, arrange filaments to certain structures like bundles or meshes, or move and use filaments based on motor activity. Further, existing filaments can be capped, severed and stabilised by ABPs.

Actin filaments are generated at or near the cell membrane from a pool of unassembled G-actin monomers from actin nucleation factors. Here, the barbed end of the filament faces the membrane and actin polymerises, pushing against the cell membrane. Three classes of actin nucleation factors are known, including formins, the actin-related protein (Arp) 2/3 complex, and tandem-monomer-binding nucleators (Pollard, 2016) (Figure 6).

Formins mediate actin nucleation at the membrane and remain associated with the barbed end of filaments, supporting the polymerisation. Members of the formin family, like diaphanous-related formins or disheveled-associated activator of morphogenesis, generate new actin filaments but also regulate the continued polymerisation of existing filaments. This is due to their ability to stay associated with growing barbed ends. In addition, they work cooperatively with profilin-actin complexes to increase monomer addition (Schutt et al., 2022; Zweifel and Courtemanche, 2020). Thus, formins function as hinged dimers binding two actin monomers, leading to the formation of linearly aligned actin filaments (Chesarone et al., 2010). Formin-mediated actin nucleation leads to the generation of bundled F-actin in filopodia (Mellor, 2010).

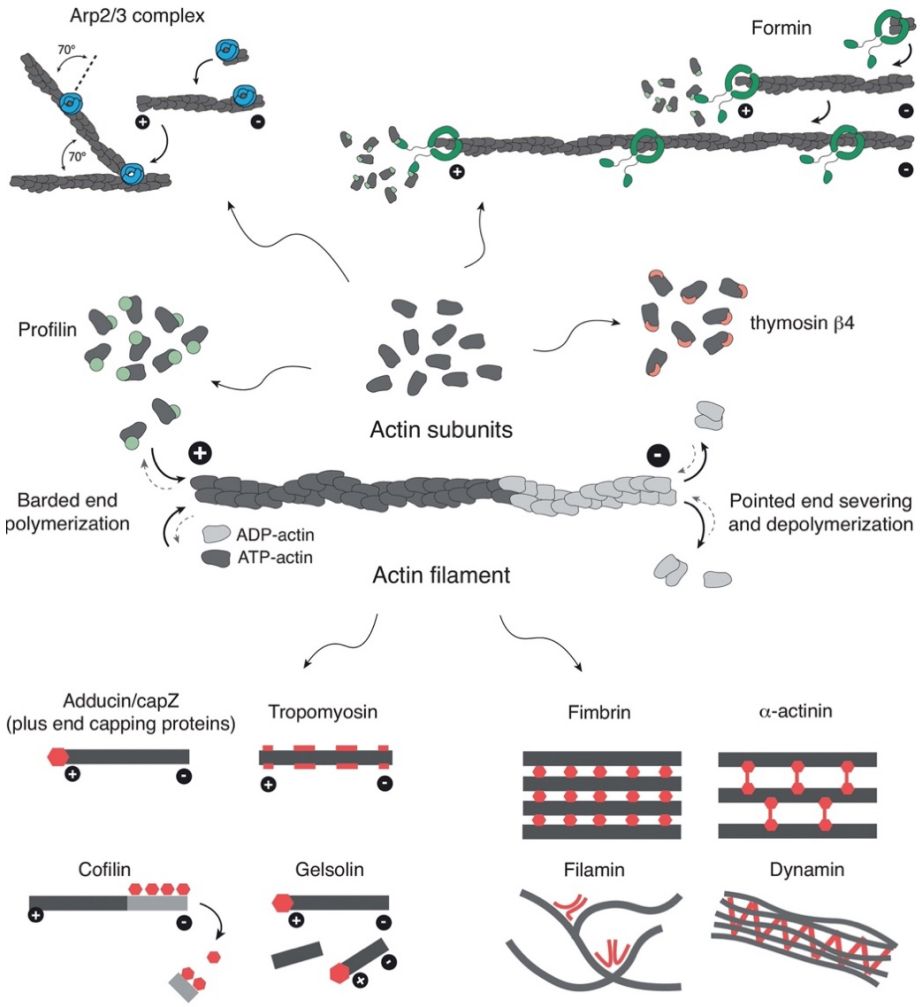

Figure 6: Actin-binding and regulating proteins

Actin-binding proteins (ABP) regulate the dynamics and organisation of actin filaments. ABPs like Arp2/3 complex or formins assemble new filaments from monomers. Profilin and β-thymosin bind to actin monomers and thereby control the availability of monomers for actin assembly. Actin filaments are severed and depolymerised by ADF/cofilin and gelsolin. Filaments of actin are bundled and organised by proteins like fimbrin, filamin, dynamin and others. In addition, various isoforms of tropomyosin regulate the accessibility of actin filaments for other regulating proteins or recruit them to existing actin polymers. From (Leite et al., 2021)

In contrast, the actin nucleator Arp2/3 complex generates branched actin networks for lamellipodia formation. Arp2/3 requires an existing mother filament to generate a new

filament. The complex binds to the parent filament and creates a new actin branch in a 70° angle, forming a mesh-like actin network (Figure 6) (Lappalainen et al., 2022). It preferably binds to newly synthesised ATP- and ADP-Pi actin filaments (Flynn, 2013; Ichetovkin et al., 2002; Jensen et al., 2012). The Arp2/3 complex comprises seven subunits (Stradal et al., 2025). The two actin-related proteins Arp2 and Arp3, which are actin-like subunits, act as a seed for the emerging filament. The other five subunits, ArpC1 to ArpC5, form the structural core of the complex, mediate the binding to the side of the mother filament, and are involved in binding of nucleation-promoting factors (Balcer et al., 2010). The Arp2/3 complex is activated by nucleation-promoting factors like Wiskott-Aldrich syndrome protein (WASP) and WASP-family verprolin homologous proteins (WAVE), which funnel actin monomers to the complex (Stradal et al., 2025). In turn, WASP and WAVE are activated by the small Ras homolog family member (Rho-) GTPases cell division cycle 42 (Cdc42) and Rat sarcoma-related C3 botulinum toxin substrate 1 (Rac1).

Additional factors increase the polymerisation rate of existing filaments. Proteins of the Enabled (Ena)/Mammalian enabled (Mena)/Vasodilator-stimulated phosphoprotein (Vasp) family are potent factors for the polymerisation of filaments in neurons (Gertler et al., 1996; Lanier et al., 1999; Lebrand et al., 2004). For this purpose, they bind the barbed end of a filament and facilitate the transfer of a G-actin monomer bound to profilin to the filament's plus-end and also protect the barbed-end from capping proteins. Profilin is involved in maintenance of the G-actin monomer pool (Figure 6). The protein acts as a nucleation and polymerisation inhibitor as it sequesters G-actin, but turns into an elongator based on the cooperative function with formins and members of the Ena/Mena/Vasp family, accelerating monomer addition (Ferron et al., 2007; Leite et al., 2021; Witke, 2004). In addition, profilin promotes actin polymerisation by exchanging ADP for ATP on actin monomers and funnels them back to the plus-end, enabling "fresh" monomer addition to the barbed-end.

Actin turnover is also regulated by generation of a surplus amount of free G-actin available for F-actin polymerisation, for example at the leading edge, regulated by profilin and β-thymosin (Flynn, 2013; Lee et al., 2013). In developing neurons, the critical concentration for F-actin polymerisation is easily achieved, since up to 80% of total actin is in its monomeric form and specifically enriched at the leading edge (Flynn et al., 2012). As not to randomly assemble actin filaments within the cell, the availability of G-actin for spontaneous nucleation is limited and suppressed by profilin and β-thymosin sequestering actin monomers, thereby regulating controlled actin polymerisation (Pollard, 2016).

Further, polymerisation of actin filaments and filament length is also regulated by plus-end capping proteins like adducin and the actin filament capping protein Z or the pointed-end capping protein tropomodulin (Leite et al., 2021). By binding to one of the ends of the

filament, such capping proteins control subunit dissociation and polymerisation, thus regulating elongation and stability of F-actin (Schneider et al., 2023). Further, capping proteins compete with other ABPs for binding of barbed- and pointed-ends and thereby additionally controlling accessibility of actin filaments for these ABPs, influencing actin dynamics (Schneider et al., 2023). On the other hand, ABPs like profilin or Ena protect barbed-ends from capping proteins to maintain F-actin polymerisation.

At the pointed end, increased actin depolymerisation and severing of filaments regulate turnover rates and actin function. One of the main actin depolymerising factors is the actin depolymerising factor (ADF)/cofilin family. This protein family consists of ADF, cofilin-1 and cofilin-2. There are two related protein families and their members contain actin depolymerising factor homology (ADF-H) domains. These include twinfilins, which contain two ADF-H domains. Twinfilins exhibit a species-specific function in depolymerising actin filament ends, while in yeast, these proteins depolymerise barbed- as well as pointed ends, in mice, only accelerated barbed end depolymerisation of twinfilin isoforms is observed (Hilton et al., 2018). The third family, which members have an ADF-H domain, is the actin-binding protein 1/drebrin family. However, in drebrin the ADF-H domain loses its actin-binding ability and actin depolymerisation activity (Grintsevich et al., 2010; Poukkula et al., 2011). Instead, drebrin interacts with and bundles actin filaments via two adjacent domains, a coiled coil and a helical domain in the N-terminal half (Worth et al., 2013).

ADF/cofilin proteins are ubiquitously expressed in eukaryotic cells (Gurniak et al., 2005; Maciver and Hussey, 2002), highlighting their importance for actin regulation. The activity of these proteins is essential for development, as the loss of cofilin-1 is embryonic lethal (Gurniak et al., 2005). Cofilin-2 was considered a muscle-specific form of cofilin, but is also found postnatally in the brain and contributes to the activity of the cofilin family in adult neurons (Bläsius, 2016; Tedeschi et al., 2019). ADF/cofilin preferentially binds to the “older” ADP-bound proportion of actin filaments and thereby localises towards the pointed-end (Figure 6) (Carlier et al., 1997; Pak et al., 2008). The proteins sever existing filaments and increase the loss of monomers at the pointed-end, therefore, the ADF/cofilin family proteins have filament-severing and depolymerisation activity. By depolymerisation and severing of actin filaments, they keep the pool of actin monomers, available to be added to the barbed end again, increased (Flynn et al., 2012). Thereby, ADF/cofilin accelerates the rate of actin treadmilling. The turnover of actin driven by severing and depolymerisation of actin filaments by ADF/cofilin is essential for neurite formation (Flynn et al., 2012) and increases neurite outgrowth when overexpressed (Meberg and Bamburg, 2000).

The activity of cofilin is precisely regulated via phosphorylation (Mizuno, 2013). ADF/cofilin is inactivated by phosphorylation at the serine residue at position 3 (S3). This

phosphorylation is mediated by LIM domain kinases (LIMK1/2) and testicular protein kinase 1 and 2. The inactivation of ADF/cofilin is reversed based on dephosphorylation by phosphatases of the slingshot family (SSH1, 2 and 3) (Mizuno, 2013). When ADF/cofilin is phosphorylated at S3 (p-cofilin), the actin binding, severing and depolymerisation activity is inhibited. In turn, various factors regulate the activity of the kinases and phosphatases. For example, the Rho A signalling pathway leads to the activation of LIMK via Rho-associated protein kinase (ROCK) (Ohashi et al., 2000). Activated Rho A binds to and activates ROCK. Then ROCK phosphorylates and activates LIMK, which in turn phosphorylates and inactivates cofilin, increasing actin filament stability and formation. LIMK and SSH are also regulated via calcium-signalling affecting calcineurin, which activates SSH, or calcium/calmodulin-dependent protein kinase II or VI, which lead to the activation of LIMK (Mizuno, 2013).

The actin motor protein myosin-II contributes to the mechanical breakage of actin filaments (Haviv et al., 2008). Myosin-II is a molecular motor that drives the formation and is enriched in actin arcs. Actin arcs are composed of actin-myosin-II structures of antiparallel contracted actin filaments mainly found in the transition zone of growth cones and behind the leading edge of migrating cells (Burnette et al., 2011; Medeiros et al., 2006). These structures are also referred to as the actomyosin cytoskeleton (Costa and Sousa, 2020). In the growth cone of neurons, actin arcs lie parallel to the leading edge. Here, myosin-II activity drives compression of actin arcs and impedes the protrusion of microtubules from the central domain into the periphery of growth cones along filopodia (Dupraz et al., 2019). The family of the actin motor myosin consist of 13 different classes in humans (Costa and Sousa, 2020). Non-muscle myosin-II is present in every cell type and plays important roles in neurons, where it is involved in polarity, motility, growth and regeneration. There are three isoforms of myosin-II, non-muscle myosin-IIA, -IIB and -IIC (Costa and Sousa, 2020). They consist of six subunits, two regulatory light chains (MLC), two essential light chains and two heavy chains. The heavy chains contain the head domain, as well as the motor domain and the actin binding site. The bipolar filaments of myosin-II bind anti-parallel actin filaments, and under hydrolysis of ATP, the myosin heads move towards the barbed-end, leading to contraction of actomyosin (Costa and Sousa, 2020). Activity of myosin-II is regulated in a phosphorylation-dependent manner by the regulatory MLC (Kollins et al., 2009). When MLC is phosphorylated at serine residue 19 (S19), myosin-II is able to move along actin filaments and exert motile forces. In the growth cone of neurons, myosin-IIA is located within the central domain of the growth cone and along the axon, whereas myosin-IIB is found in the transition zone and peripheral area of the growth cone. Activity of myosin-II has been implicated in various processes required during neuronal development, like regulation of actin retrograde flow, growth cone engorgement and axon

elongation and guidance (Costa and Sousa, 2020). The function of myosin-II in these processes will be discussed later.

Aside from the aforementioned regulators of the actin cytoskeleton, many other proteins are involved in actin function. Actin filaments are arranged in bundles via proteins like fimbrin, α-actinin and dynamin (Figure 6). Crosslinking of actin filaments occurs via filamin. Another notable regulator of actin filaments is the family of tropomyosins. Tropomyosins bind along existing actin filaments. Here, they form coiled-coil parallel dimers and head-to-tail polymers along the length of actin filaments (Gunning et al., 2015) (Figure 6). Mammals have more than 40 isoforms of tropomyosin. The evidence for tropomyosins as master regulators of actin filaments is based on the observation that spatially distinct actin filaments are bound to different tropomyosins (Gunning et al., 2015). Further, it was suggested that formins specify which tropomyosin is added to a growing filament. Tropomyosins regulate the interaction of actin filaments with other ABPs, depending on the tropomyosin isoform (Gunning et al., 2015). For example, tropomyosin regulates the accessibility of actin filaments for ADF/cofilin and recruit these proteins for increased actin turnover. In contrast, other tropomyosins prevent recruitment of ADF to filaments and thereby stabilise them. In various studies, tropomyosins have been implicated in mechanisms relevant for neuronal development, organisation and function (Abouelezz et al., 2020; Schevzov et al., 2005; Suchowerska et al., 2017).

Based on the regulation and organisation of actin filaments through ABPs, the actin cytoskeleton forms various superstructures. Specific repertoires of ABPs are engaged in a spatio-temporal way to form and regulate distinct actin structures that drive the organisation and development of the cell (Flynn, 2013). This involves an active assembly of actin filaments, their organisation, actin retrograde flow and the disassembly of the actin structures at the right time and place.

Bundling of long unipolar actin filaments leads to the formation of finger-like protrusions called filopodia. Classically, these structures have been considered as sensors for the extracellular environment and detection of guidance cues for pathfinding (Wit and Hiesinger, 2023). Filopodia are highly dynamic structures and are generated by actin nucleators like formins, which generate bundled F-actin (Flynn, 2013). In addition, actin filament bundling proteins like fascin, facilitate the formation of filopodia via bundling of actin filaments, but also independent of its bundling activity (Zanet et al., 2012). While filopodia contain bundled linear actin filaments, in lamellipodia, which are sheet-like protrusions, the actin cytoskeleton is organised like a mesh consisting of branched actin filaments (Innocenti, 2018). Generation of a branched actin network requires activity of the Arp2/3 complex. Whether filopodia or lamellipodia are formed depends on the presence

and activity of ABPs at a certain location (Flynn, 2013). At such distinct sites, ABPs compete for actin monomers for nucleation of filopodia and lamellipodia.

Another actin structure within neurons are actin patches, which are discrete, dynamic mesh-like structures composed of accumulated actin filaments (Arnold and Gallo, 2014). These arrangements of F-actin, with sizes ranging from two to three µm in diameter, are found in various parts of the neuron *in vitro* and *in vivo*, along the axon shaft, in the axon initial segment, in dendrites and also in the cell body. These patches are not protrusive structures but can give rise to filopodia (Arnold and Gallo, 2014).

The latest actin structure to be identified in neurons is the membrane periodic skeleton (MPS), which is a sub-membranous cytoskeleton, composed of periodic actin- and spectrin-rings spaced 190 nm apart (Xu et al., 2013). This periodic cytoskeleton organisation starts to develop in proximal parts of the axon in stage 3 neurons from day *in vitro* 2 (DIV 2) and continues to be established towards distal regions of the axon in maturing neurons (Zhong et al., 2014). The ABP adducin, which caps short actin filaments, associates with actin rings along the axon in neurons from DIV 6-7 on (Zhong et al., 2014). The formation of this periodic skeleton is thought to provide mechanical support for the axon, protecting it against mechanical stress. In addition, the periodic organisation of anchored ion channels influences the propagation of APs along the axon (Costa and Sousa, 2021).

To study the various functions of the actin cytoskeleton in neuronal development, scientists have used different natural toxins and small molecules that influence and manipulate actin dynamics. Among these are Cytochalasins, which are fungal metabolites that inhibit actin polymerisation by capping the barbed-end of actin filaments and thereby prevent the addition of new actin monomers (Figure 12A) (Cooper, 1987). When addition of actin monomers at the barbed-end is blocked, ongoing depolymerisation of filaments at the pointed-end leads to a disassembly and reduction of F-actin. Another group of natural actin depolymerising drugs are Latrunculins. These toxins form a 1:1 molar complex with G-actin, thereby preventing actin polymerisation due to the reduction of monomeric actin that can be added to the barbed end (Coué et al., 1987). A second class of actin drugs includes actin filament stabilisers. One commonly used drug to interfere with actin disassembly is Jasplakinolide (Jasp) (Cramer, 1999). Jasp stabilises actin filaments and prevent their disassembly. Additionally, it increases actin polymers in purified actin as well as in cells (Cramer, 1999). For the investigation of the function of myosin-II, the small molecule Blebbistatin (Blebb) has been extensively used. Blebb locks myosin-II in an actin-detached state by binding to the ATPase intermediate with ADP and Pi bound at the active site, slowing Pi release (Kovacs et al., 2004). Thus, the use of actin-manipulating

drugs has helped to decipher the function of the actin cytoskeleton in various processes of neuronal development.

Microtubules and their role in growth

The second main polymer necessary for proper cellular function are microtubules. These polymers are composed of α- and β-tubulin heterodimers which form protofilaments (Figure 7). Each microtubule is assembled of 13 of these protofilaments, forming a hollow tube with a diameter of 25 nm.

Various isoforms of α- and β-tubulin are expressed in the brain (Redeker, 2010). Only one isoform, β-III-tubulin (Tuj-1), exhibits an almost exclusive neuronal expression pattern (Katsetos et al., 2003). However, β-III-tubulin is also expressed as part of the mitotic spindle in other cell types, among others in human skin fibroblast, human keratinocytes and in a subpopulation of cells of peripheral sheath tumours (Jouhilahti et al., 2008).

The third tubulin isoform, γ-tubulin, serves as a template for the nucleation of microtubules (Vinopal and Bradke, 2025). It is associated with microtubule organising centres (MTOC) that serve as stabilisation and initiation points for the generation of microtubules. For nucleation of microtubules, γ-tubulin forms the γ-tubulin ring complex (γ-TuRC) (Vinopal and Bradke, 2025). Various mechanisms have been identified for microtubule nucleation with the γ-TuRC complex as a basis and proteins like cyclin-dependent kinase 5 regulatory subunit-associated protein 2, Augmin or AT-hook transcription factor (AKNA) as stimulators of γ-TuRC activity. Several different organelles serve as an MTOC. The most prominent MTOC is the centrosome. However, a recent study revealed that centrosomal microtubule nucleation is dispensable for polarisation in projection neuron. Instead, finely tuned centrosomal microtubule nucleation activity is required for the migration of neurons during cortical development (Vinopal et al., 2023). In the course of development, the activity of the centrosome as an MTOC is downregulated, and acentrosomal processes dominate (Stiess et al., 2010; Vinopal and Bradke, 2025; Vinopal et al., 2023). In contrast to the centrosome, nucleation of microtubules from the Golgi apparatus is not involved in the migration process of neurons, but contributes to axon growth.

Further, organelles like Ras-related in brain (Rab) 5- and Rab11-positive endosomes enable microtubule nucleation in *Drosophila* and *Caenorhabditis elegans* (Vinopal and Bradke, 2025). These findings indicate that, based on their nucleation source, different networks of microtubules in neurons exist, which contribute to different cellular processes. Further research needs to identify the exact mechanisms by which nucleation strategy contributes to which process in the cell, and at what time point one mechanism is preferred over the other.

Similar to actin filaments, microtubules are polar structures. They have a plus-end with β-tubulin exposed and a minus-end with α-tubulin exposed. *In vitro*, both ends dynamically

polymerise and depolymerise, though the plus-end is the fast-growing end and the only end that grows in cells (Jiang and Akhmanova, 2011). The minus end slowly grows *in vitro*, but within cells it is usually stabilised or it is the site of disassembly. Therefore, plus-end and minus-end differ in their structural and biochemical properties, causing differences in their kinetics and the plus-end is much more dynamic. However, the minus-end of microtubules is usually capped by γ-TuRC, Calmodulin-regulated spectrin-associated proteins (CAMSAP) or other capping proteins, which stabilise the end and therefore prevent dynamic changes as observed at the plus-end (Vinopal and Bradke, 2025). From the MTOC, microtubules polymerise towards the plus-end. Microtubules undergo phases of polymerisation and growth, growth pausing or rapid disassembly, termed as "catastrophe" (Figure 7) (Lawrence and Zanic, 2019). Catastrophe starts from the plus-end and leads to the complete loss and disassembly of the microtubule. These catastrophic events are stopped and rescued by regaining a stabilising cap or, for example, by cytoplasmic linker protein (CLIP)-associating proteins (CLASPs) before microtubules are disassembled completely (Lawrence and Zanic, 2019). In rescued microtubules, CLASP proteins re-initiate the polymerisation and assembly of microtubules, causing their regrowth. These dynamics allow microtubules to rapidly reorganise upon signalling from extra- as well as intracellular pathways, enabling the cell to react to changes.

The stability of microtubules is regulated via the status of the β-tubulin-bound guanosine nucleotide and posttranslational modifications-dependent recruitment of effector proteins (Chen et al., 2021; Roostalu et al., 2020). When incorporated in polymerising microtubules, β-tubulin is bound to guanosine triphosphate (GTP) (Figure 7). Once the GTP-bound β-tubulin is part of the polymerising microtubule, the GTP is hydrolysed to guanosine diphosphate (GDP) (Zhou et al., 2023). The newly GTP-bound β-tubulin forms a cap on the growing plus-end and provides stability allowing the microtubule to grow (Roostalu et al., 2020). When the cap of GTP-bound β-tubulin is lost, the end becomes highly unstable leading to rapid disassembly and catastrophe. Microtubule-associated proteins (MAPs), like CLASPs prevent complete catastrophe by stabilising microtubules. Similar to actin filaments, the status of bound guanosine nucleotides on the tubulin is important for localisation of MAPs to the microtubule (Yon et al., 2025; Zanic et al., 2009). For example, the plus-end tracking protein end-binding protein 1 (EB1) preferentially binds to GTP-tubulin. This preferential binding is utilised as an experimental tool: polymerisation of microtubules is visualised using plus-end-binding proteins like EB1 or EB3. Live imaging of EB3, coupled to a fluorophore, is used for tracking of "comet-like" structures that represent polymerising microtubules (Stepanova et al., 2003). Typically, the polymerisation or growth speed, the lifetime and the growth length of comets are analysed in addition to the number of observed comets.

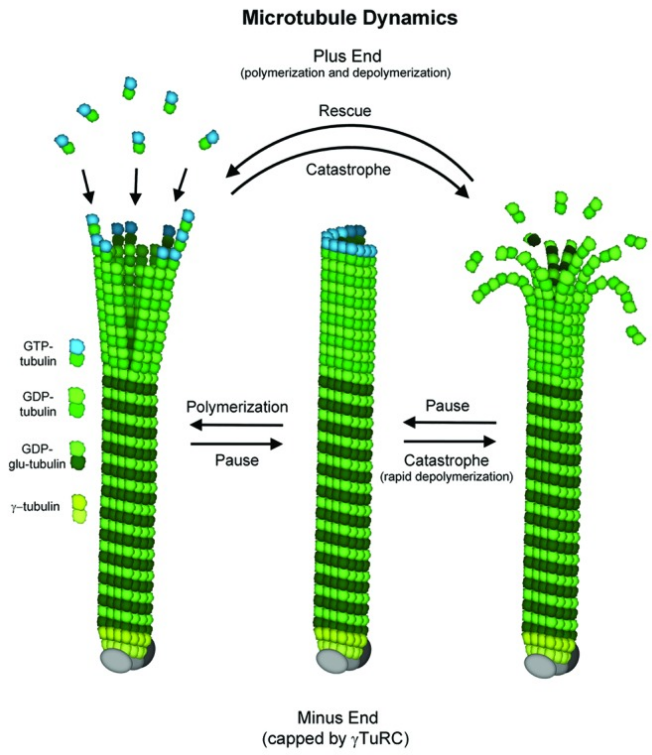

Figure 7: Microtubule assembly and dynamics

Microtubules are polar polymers with a plus-end and a minus-end. These polymers are composed of the assembly of 13 protofilaments, which are formed by α- and β-tubulin heterodimers. The minus end is capped by γ-tubulin ring complex (γ-TuRC) or CAMSAPs preventing the disassembly at the minus-end but also serving as nucleating centres. Polymers assemble and grow towards the plus-end. At the tip, a GTP-bound tubulin cap stabilises the plus-end and prevents disassembly. When the stabilising cap is lost by hydrolysation of GTP to GDP the polymers quickly depolymerise, known as catastrophe. The complete disassembly of microtubules is prevented by stabilising microtubule-associated proteins (MAPs) resulting in the rescue. When these assembly and disassembly processes are stopped, microtubules undergo growth pausing. From (Flynn, 2013)

The dynamic properties and stability of microtubules are regulated via posttranslational modifications. Microtubules are modified by tyrosination and detyrosination, acetylation, phosphorylation, glutamylation and glycylation (Viar and Pigino, 2024). Tyrosination has been identified as a marker for dynamic unstable microtubules. Detyrosination is considered a marker for more stable and less dynamic microtubules (Moutin et al., 2021). Tyrosinated microtubules quickly depolymerise in presence of the microtubule depolymerising drug Nocodazole, while detyrosinated polymers are less sensitive and remain polymerised. α-tubulin undergoes cycles of detyrosination and tyrosination mediated by a tubulin carboxypeptidase (TCP), removing the carboxy-terminal tyrosine and a tubulin tyrosine ligase (TTL), which adds tyrosine back to α-tubulin. TTL preferentially acts on soluble tubulin, which indicates that young, freshly polymerised microtubules are initially tyrosinated before they are detyrosinated and become less dynamic and more stable. In neurons, detyrosinated tubulin are found in axon shafts, while the more labile tyrosinated microtubules are enriched in the growth cone (Moutin et al., 2021). Complete loss of the tyrosination enzyme TTL is embryonically lethal, underlining

the importance of the posttranslational modification-mediated regulation of microtubules during development (Erck et al., 2005; Moutin et al., 2021).

Another posttranslational modification that is considered a marker for stable microtubules is acetylation. Acetylation of lysine 40 in the α-tubulin chain, which is located within the microtubule lumen, is catalysed by a tubulin acetyltransferase preferentially acting on microtubules (Moutin et al., 2021). Acetylated tubulin is enriched in axons compared to dendrites and represents long-lived stable microtubules (Gomis-Ruth et al., 2008; Witte et al., 2008). Blocking acetylation of α-tubulin results in axon over-branching and excessive growth measured as total axon length (Moutin et al., 2021; Wei et al., 2018), however, acetylation alone is not sufficient to induce axon formation (Witte et al., 2008). While acetylation seems to directly promote microtubule stability by altering the conformation of the flexible loop containing lysine 40 (Eshun-Wilson et al., 2019), tyrosination and detyrosination do not change microtubule dynamics but affect microtubule stability through selective recruitment of effectors like mitotic centromere-associated kinesin (Chen et al., 2021; Peris et al., 2009).

In addition to regulating microtubule dynamics via the state of bound nucleotides or posttranslational modifications, MAPs are key regulators of microtubule dynamics and organisation. Similar to the actin cytoskeleton, a long list of regulators influence microtubule polymerisation and stability, bundling or severing or the transport of cargo. Classically, proteins are considered as MAP when they influence the stability and bundling of microtubules. Here, I refer to MAPs as all proteins that are able to bind to microtubules, influencing and regulating any function of these, including microtubule-binding proteins. MAPs are classified into five groups: (i) motile MAPs, which are motor proteins like kinesin and dynein, moving on microtubules generating forces and move microtubules or cargo, (ii) microtubule depolymerising and severing MAPs, (iii) microtubule nucleators, (iv) microtubule end-binding proteins associated with either the plus- or minus-end, and (v) structural MAPs, a group of proteins that bind and stabilise microtubules (Bodakuntla et al., 2019).

The main structural MAPs in neurons are MAP1A/MAP1B and MAP2/Tau (Melkova et al., 2019; Noiges et al., 2002). All these proteins stabilise microtubules and prevent catastrophe events, enable bundling of microtubules, and regulate the binding of other proteins to the polymer. The high expression level of specific MAPs in neurons indicates how important they are for neuronal morphogenesis by their ability to tightly bundle and organise linear microtubule arrays, for example in neurites and in the long axon (Dehmelt and Halpain, 2004; Halpain and Dehmelt, 2006). This is also highlighted by their functional redundancy (Takei et al., 2000; Teng et al., 2001), underlying the importance of microtubule bundling and stabilisation for neuronal development. MAPs have different

expression patterns. MAP2 localises to dendrites and stabilises microtubules, while Tau stabilises microtubules in the axon (Binder et al., 1986). Though the low molecular weight isoform of MAP2, MAP2c, also localises to the axon (Meichsner et al., 1993). This distinct expression pattern allowed the use of these proteins as markers for the different compartments in many studies. Suppression of MAP2 expression affects early phases of neuronal development and prevents the progression of neurons from stage 1 to stage 2 (Caceres et al., 1992). Here, specifically, the formation of bundled microtubules by MAP2c is important (Dehmelt et al., 2003). In the axon, Tau is involved in bundling of microtubules in the axon shaft up to the growth cone (Biswas and Kalil, 2018). Blocking Tau expression reduces axon extension (Biswas and Kalil, 2018; Caceres et al., 1991).
Microtubule EB proteins, especially plus-end binding proteins (+Tips) modify microtubule assembly and disassembly by controlling rates of growth, catastrophe and rescue. The members of the +Tips family, EB1 and EB3, accumulate at the plus-end of growing microtubules (Sayas and Avila, 2014). As mentioned above, they are used as markers for microtubule dynamics. Both proteins are involved in neurite outgrowth (Sayas and Avila, 2014).

As discussed above, the distinct cytoskeleton structures do not act alone but with mutual interaction. Therefore, it is not surprising that some cytoskeleton-regulating proteins bind to both polymers directly or at least to regulatory proteins of the other polymer. For example, the microtubule actin cross-linking factor 1 (MACF1) binds actin as well as microtubules, thereby organising the interplay of the cytoskeleton components and their proper organisation (Moffat et al., 2017). Another example is Tau, which binds to actin filaments and facilitates the growth of actin filaments along microtubules but also co-aligns microtubules with actin filaments to guide them (Biswas and Kalil, 2018; Elie et al., 2015). Many other proteins are involved in the crosstalk of actin and microtubules.

The third key player of the cytoskeleton in neurons are neurofilaments, which are specialised intermediate filaments of the nervous system (van Asperen et al., 2024). Neurofilaments are involved in the radial expansion of axonal calibre and maintenance of the diameter, providing mechano-resistance. These polymers will not be discussed here further, as they seem to be not as important as actin filaments and microtubules for axon formation and elongation. However, neurofilaments are more and more linked to neurodegenerative diseases and the revelation of their function within neurons has just started (van Asperen et al., 2024).

In summary, both cytoskeletal structures, actin filaments as well as microtubules, are highly regulated and organised structures. This is the basis for their ability to rapidly

assemble or disassemble, providing the possibility of fast structural changes. Thus, rapid dynamic alterations in the organisation of all the aforementioned polymers are essential for formation of a complex nervous system. In the next section, I will outline how these dynamics together contribute to the generation of the nervous system.

Neurite formation

The first step in wiring of the nervous system is the formation of a neurite. The initiation and extension of neurites, neuritogenesis, already requires cytoskeletal dynamics. Here, I see neurite formation as an additional, separate and necessary step prior to polarisation, since these neurites will become axons and dendrites. It requires a malleable actin cytoskeleton at the outer cell periphery and bundling of microtubule arrays (Dehmelt et al., 2003; Flynn et al., 2012).

Neurites emerge by two mechanisms or modes for neurite formation involving the coordination of actin and microtubules. In stage 1 neurons, a circumferential lamellipodium collapses in certain regions while it extends in others. This establishes nascent growth cones that will become the newly formed neurite in which microtubules follow the lead of the advancing leading edge (Flynn, 2013). Then, microtubules bundle to form and stabilise the neurite shaft, supported by MAPs like MAP2c, Tau and MAP1B. Contractile forces, which are generated by myosin-II activity, compress actin arcs in the growth cone neck, promoting the bundling of microtubules (Burnette et al., 2008).

The second mechanism involves a single filopodia that gives rise to a neurite. Filopodia protrude, become stable, engorge with cytoplasm as well as microtubules, and form a growth cone (Flynn, 2013).

Stabilisation of the actin network inhibits neurite formation, while increased actin destabilisation accelerates the formation of neurites (Flynn et al., 2012). A main regulator of actin dynamics in this early stage is the ADF/cofilin family. The combined ablation of ADF as well as cofilin-1 leads to a complete immobilisation of actin dynamics, stopping retrograde flow, arresting neuronal development in stage 1 (Flynn et al., 2012). Thus, actin severing and depolymerisation at the minus end keeps the actin cytoskeleton dynamic and malleable and thereby enables neurite outgrowth. Actin retrograde flow is distinct from the aforementioned treadmilling. Treadmilling is the flow of actin monomer-units through the filament by polymerisation and depolymerisation. Retrograde flow, on the other hand, is the centripetal movement of the entire actin network. This retrograde flow is driven by actin polymerisation at the leading edge and by myosin-II activity pulling on actin filaments, moving them backwards. Retrograde flow is also organised by the severing activity of ADF/cofilin (Flynn et al., 2012; Tedeschi et al., 2019). However, dynamic actin alone is not sufficient but necessary to induce neurites, radial oriented actin filaments like those in filopodia, are required as well. Though, radial oriented actin filaments are also not

sufficient to induce neuritogenesis in absence of actin turnover. Thus, formation of neurites requires the correct organisation of actin filaments and maintenance of actin dynamics (Flynn, 2013). The formation of neurites is supported by microtubules, which form into parallel bundles and protrude out of the neuronal sphere. Destabilisation of microtubules inhibits neuritogenesis (Flynn et al., 2012).

Once neurites are formed, these structures are highly dynamic and grow, extend and retract. The end of developing neurites is tipped by a growth cone. The growth cone is a central player in neurite growth and axon guidance as it is the neuron's sensing organ (Lowery and Van Vactor, 2009).

The neuronal growth cone

The growth cone is a highly specialised, dynamic and fan-like structure with a highly coordinated organisation of the cytoskeleton. The growth cone is divided into three regions (Figure 8). In the central (C-) domain, the least dynamic part of the growth cone, bundled stable microtubules enter from the neurite shaft and splay out in the growth cone. The outer peripheral (P-) domain of the growth cone is dominated by actin structures and is highly dynamic. This P-domain exhibits filopodia as well as lamellipodia. Both actin structures are highly dynamic, they form, extend and retract within a short period of time, allowing the neuron to sense and react to the environment (Dent et al., 2011). Single unstable, dynamic microtubules protrude from the C-domain into and explore the peripheral area (Figure 8), required for growth cone turning and steering (Challacombe et al., 1997; Suter et al., 2004). At the interface between the microtubule-rich C- and actin-dominated P-domain is the transition (T-) zone. In the T-zone, contractile actin networks are compressed and impede the protrusion of microtubules from the C- in to the P-domain (Dupraz et al., 2019). These contractile actin networks, also known as actin arcs, are transversely oriented bundles of actin filaments generated by myosin-II. The actin motor myosin-II moves along anti-parallel actin filaments and thereby drives the formation of these contractile structures (Dent et al., 2011).

The growth cone undergoes a constant change in its structure while neurites extend and retract. Further, most studies investigating the mechanisms underlying neurite growth, focusing on the growth cone, have used cultured neurons in a two-dimensional (2D) environment on a stiff glass surface. A recent study showed that in a three-dimensional (3D) collagen matrix gel, which better recapitulates the *in vivo* environment, the morphology of the growth cone is different from the classical known growth cone organisation (Santos et al., 2020). In 3D cultures, the 2D-observed spread and fan-like structure is not maintained, and growth cones appear "spiky". However, microtubules protrude further into the P-domain because restricting actin structures are not present growth cones of neurons grown in 3D (Santos et al., 2020). In a 3D collagen environment,

neurites extend faster. As the environment in CNS tissue is even more complex than in a 3D gel, how neuronal growth cones are organised *in vivo* and enable robust extension of neurites and axons will be investigated in the future (Alfadil and Bradke, 2023). It will be informative to explore whether in a complex tissue, growth cones form the well-known structure of 2D conditions or rather a spiky morphology observed in 3D gels.

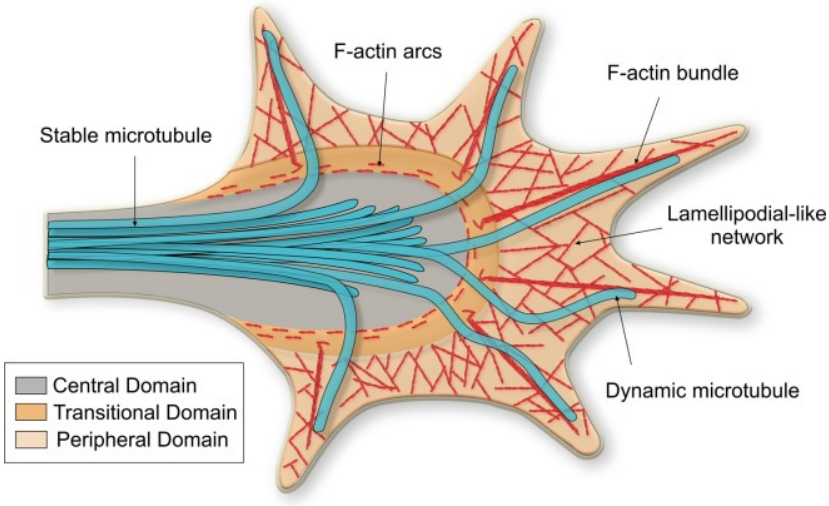

Figure 8: The neuronal growth cone

Classically, the growth cone is divided into three compartments. In the central domain, stable microtubules enter from the axon shaft and start to splay out. The peripheral domain is dominated by the actin cytoskeleton, forming filopodia and lamellipodia. A few dynamic microtubules extend from the C- into the P-domain. The barrier between these two compartments is the T-zone which is characterised by actin arcs that hinder microtubules from entering the P-domain. When microtubules enter the P-domain, they are guided along filopodia to the outer area. In the P-domain, actin filaments are oriented with the barbed-end facing the membrane, and the pointed-end is directed toward the central domain. From (Cammarata et al., 2016)

Neuronal polarisation and the specification of an axon

Neurons in culture form several neurites, each of these neurites has the potential to become the axon or to develop into dendrites (Dotti and Banker, 1987). While the future axon grows rapidly, dendrites are restrained from growing. The processes that are involved in the specification of the axon have been studied extensively. Many individual factors that influence polarisation have been identified, both *in vitro* and *in vivo*.

A main factor driving the polarisation are signalling pathways and feedback loops that tightly control actin and microtubule dynamics (Schelski and Bradke, 2017). While feedback loops can trigger the accumulation of polarity effectors in one single neurite, promoting its growth and subsequent specification as the axon, other feedback loops inhibit the growth of neurites by globally depleting polarity effectors (Schelski and Bradke, 2017).

Polarisation is not only the growth promotion of a single selected neurite but also actively restraining other neurites from growth. Lin and colleagues revealed an antagonism of

myosin-II and the Arp2/3 complex keeping neurites in an oscillatory state until one neurite escapes and becomes the axon (Lin et al. manuscript in preparation).

Initially, the organisation and orientation of cellular organelles including the Golgi complex, centrosome and mitochondria was correlated with the formation of an axon (Bradke and Dotti, 1997; de Anda et al., 2005; Lewis et al., 2013). More recent studies reveal that the centrosome is downregulated during development and centrosomal activity is dispensable for axon extension (Stiess et al., 2010). Neurons are able to extend an axon even when the centrosome is ablated. Further, centrosome-mediated microtubule nucleation is not required for axon formation in cortical projection neurons (Vinopal et al., 2023). However, precise activity of the centrosome mediates radial migration of projection neurons during the development of the cortex. An imbalance in microtubule polymerisation activity of the centrosome impairs the migration of neurons, though without affecting their polarity (Vinopal et al., 2023).

In contrast, manipulation of Golgi-mediated microtubule nucleation is not involved in regulating of neuronal migration in the cortex but is needed for extension of the axon. Downregulation of the number of microtubules formed at the Golgi does not influence the polarity of neurons, but microtubules originating from the Golgi seem to fuel axon extension (Vinopal et al., 2023). How Golgi-mediated microtubule nucleation contributes to axon extension is not yet clear. In *Drosophila* neurons, the *cis*-to-*trans* orientation of specific Golgi stacks contributes to a polarised orientation of microtubules specifically in the axon (Yagoubat and Conduit, 2025). Whether a similar mechanism is in place in murine neurons needs to be investigated. In *Drosophila* da sensory neurons, the Golgi consists of several small Golgi stacks throughout the whole cell (Yagoubat and Conduit, 2025; Yano et al., 2005), while in murine neurons the Golgi is rather organised as a connected network. Nonetheless, Golgi outposts are found in dendrites and satellite Golgi in dendrites as well as in axons (Kemal et al., 2022). How exactly the Golgi and its acentrosomal microtubule nucleation contributes to axon extension in mammalian neurons needs to be addressed in further research.

For enhanced elongation rates, as observed in the axon upon polarisation, membrane material is required to expand the cellular membrane. Therefore, it is not surprising, that increased membrane trafficking into the future axon is necessary for its rapid elongation (Bradke and Dotti, 1997). Here, the transport of membrane material as well the exocytosis and insertion in the membrane of growing neurites are important for proper axon formation (Dupraz et al., 2009; Wang et al., 2011). The plasmalemma precursor vesicles associated with the GTPase Rab10 are transported into the axon. The knockdown as well as the knockout of Rab10 and its upstream activator lethal giant larvae 1 affects polarisation and neurite length *in vitro* and *in vivo* (Wang et al., 2011). Newly synthesised membrane protein and material is preferentially added at axonal growth cones in rat hippocampal

neurons (Craig et al., 1995). Thus, when vesicles reach the extending neurite tip, they are inserted into the membrane for membrane expansion. One mechanism that is involved in insertion of these plasmalemmal precursor vesicles, is the translocation and activation of the exocyst complex by the small GTPase TC10 (Dupraz et al., 2009).

Beside the molecular polarisation, where the accumulation of the polarity effector Rap1b in a single neurite, prior to morphological polarisation, is observed (Schelski and Bradke, 2017; Schwamborn and Puschel, 2004), the actin cytoskeleton exhibits different dynamics prior to morphological polarisation (Bradke and Dotti, 1999). Actin filaments in the growth cone of the neurite that will become the axon, are more dynamic and susceptible to degradation upon treatment with Cytochalasin D (Cyto D).

Further, activity of cofilin is required for axon formation (Garvalov et al., 2007). The knockdown of cofilin via small-interfering RNA (siRNA) inhibits axon formation. Further, the knockout of Cdc42 increases the amount of p-cofilin, and inhibits axon formation (Garvalov et al., 2007). Both revealing the importance for actin depolymerisation based dynamics for axon formation. In line with a requirement for dynamic, instable actin filaments for axon formation, treatment with the actin stabilising drug Jasp either prevents axon formation (Flynn et al., 2012) or when already formed, causes axon retraction based on actomyosin contractility in embryonic chick DRGs (Gallo et al., 2002).

In addition to the important role of actin depolymerisation in axon specification, the formation of a branched actin network by the Arp2/3 complex is required for axon formation and growth (Tahirovic et al., 2010). When Rac1, an activator of the Arp2/3 complex via the WAVE regulatory complex, is knocked out in mice, neurons fail to form an axon. In contrast to earlier findings which proposed Arp2/3 to be a negative regulator of growth cone translocation (Strasser et al., 2004), Lin and colleagues revealed that Arp2/3 complex activity is required for axon formation (Lin et al. manuscript in preparation). Neurons missing the subunit Arp3 form neurites but are unable to extend these neurites to allow axon outgrowth. Cultured neurons of an Arp3 knockout mouse show dramatic changes in growth cone morphology, failing to form the fan-like structure lacking lamellipodia (Lin et al. manuscript in preparation). This phenotype is supposed to arise from an antagonism of Arp2/3 complex with myosin-II.

Previous studies already provided evidence for a role of myosin-II in controlling extension and growth of axons (Costa and Sousa, 2020; Dupraz et al., 2019; Kollins et al., 2009; Wylie and Chantler, 2003). In stage 2, prior to specification of the axon, neurites undergo growth oscillations with cycles of extension and retraction (Lin et al. manuscript in preparation). Arp2/3 mediated formation of branched actin network relaxes the myosin-II mediated tension and allows extension of the neurite. When myosin-II dominates, it leads to contraction of the actin network and subsequently to retraction of the whole neurite (Lin et al. manuscript in preparation). Inhibition of myosin-II with Blebb allows neurites to

extend and form an axon, even when Arp3 is knocked out (Lin et al. manuscript in preparation). This local-excitation-global-inhibition system established by Arp2/3 complex and myosin-II antagonism keeps neurites in an oscillatory growth and retraction state, controlling polarisation (Lin et al., manuscript in preparation).

In contrast to a less stable actin cytoskeleton being favourable for axon formation, more stable microtubules are linked to the specification of axons. Already before polarisation, one neurite in morphologically unpolarised neurons exhibits different distribution of microtubule posttranslational modifications (Witte et al., 2008). Likewise, the axon exhibits posttranslational modifications of microtubules, which are associated with more stable microtubules. In stage 3 neurons, acetylated microtubules are found in the axon, while they are not abundant in minor neurites. In line with this, minor neurites of polarised neurons exhibit greater retraction than the axon when treated with the microtubule destabilising drug Nocodazole (Witte et al., 2008). Mild stabilisation of microtubules with low doses of Taxol overcomes the growth restriction of minor neurites and turn them into an axon, similar to local application of Cyto D (Bradke and Dotti, 1999; Witte et al., 2008). In the most distal part of the axon, the growth cone, neurons maintain a pool of tyrosinated and highly dynamic microtubules (Moutin et al., 2021). However, neurons that lack TTL contain no tyrosinated tubulin and exhibit accelerated neurite growth and premature axonal differentiation. Further, these cells have similar levels of detyrosinated microtubules in axons and dendrites and an increased proportion of neurons with two or more axons, which shows that enrichment of stable detyrosinated microtubules is controlling axon formation (Moutin et al., 2021). In line, neurons that overexpress the TCP vasohibin-2 show an increased proportion of cells with two axons.

For a long time, the microtubule array in the neurite and axon shaft was thought to be stationary. Recently, a retrograde movement of the whole microtubule array within neurites was reported (Burute et al., 2022; Schelski and Bradke, 2022). This newly identified form of microtubule dynamics seems to play a role in axon elongation. Shortly after morphological polarisation, the speed of microtubule retrograde flow decreases in the axon while it is maintained in minor neurites (Schelski and Bradke, 2022). Artificially slowing down retrograde flow speed, by anchoring microtubules to the plasma membrane, leads to the formation of multiple axons (Burute et al., 2022). A slowdown of the retrograde movement of the microtubule array is therefore sufficient to instruct polarisation. Whether the reduction of retrograde microtubule movement is also necessary for axon specification remains an open question. Likewise, the pathways and the exact mechanisms of how retrograde flow is organised and regulated are still unidentified. These mechanisms and pathways include microtubule motor protein dynein and the actin cytoskeleton (Burute et al., 2022; Schelski and Bradke, 2022).

The axonal compartment exhibits a particular organisation of microtubules. Most of the microtubules in axons are oriented with the plus-end out towards the growth cone (van Beuningen and Hoogenraad, 2016). In contrast, dendrites have a mixed polarity with 50% plus-ends out. Before polarisation, the majority of microtubules (80%) are oriented with their plus-ends away from the soma, and a minority of microtubules exhibit an opposite orientation (van Beuningen and Hoogenraad, 2016). The establishment of this particular orientation of plus-end out microtubules in axons is established directly after polarisation (Yau et al., 2016). Since the uniform orientation of microtubules occurs shortly after polarisation, the necessity of this organisation for defining and selecting a particular neurite to become the axon is still to be clarified. However, the uniform arrangement of microtubules is necessary for polarised transport and maintenance of axonal identity (van Beuningen and Hoogenraad, 2016; van Beuningen et al., 2015). The MAP tripartite motif-containing protein 46 (TRIM46) has been identified to bundle parallel microtubules with their plus-end out in the specified axon (van Beuningen et al., 2015). Loss of TRIM46 reduces the number of polarised cells and results in a dendrite-like microtubule orientation in all neurites. Here, TRIM46 already accumulates in one of the neurites at the transition from stage 2 to 3 (van Beuningen et al., 2015). A recent in vivo study shows that TRIM46 is required for microtubule fasciculation but not for axon specification or establishment of the axon initial segment (AIS) (Melton et al., 2024). In contrast, maintenance of the AIS mediated by Ankyrin G (AnkG) is required to preserve axonal identity (Hedstrom et al., 2008). When AnkG is lost, the AIS is dismantled and axons acquire the molecular pattern of dendrites and form spines. The AIS marks the barrier between the somatodendritic and the axonal compartment, functions as gatekeeper for axonal identity and is the site for generation of APs before these propagated along the axon (Leterrier, 2018).

Taken together, axon specification and formation require tightly regulated dynamics of the cytoskeleton: a dynamic actin network and stable, uniformly oriented microtubules, but also the maintenance of its identity.

Mechanisms of axon growth and elongation – lessons from cell migration

Once the axon has formed and is specified, it extends until it reaches its target region. The advancement of growth cones and thus the growth and extension of neurites and axons occurs through the repetitive progression of three steps: protrusion, engorgement and consolidation (Lowery and Van Vactor, 2009).

For protrusion, the edges of the peripheral growth cone extend its membrane. This is driven by filamentous actin polymerisation (Dent et al., 2011). During engorgement, dynamic microtubules from the C-domain advance into the former T-zone where the

compressing actin arcs are disassembled. Vesicles and organelles are transported along microtubules and fill the space that was previously an actin-dominated area. Ultimately, for consolidation, the proximal part of the growth cone resumes a cylindrical shape by compressing and bundling microtubules, forming a new segment of the neurite or axonal shaft. Microtubules are again compressed by actin arcs in the new C-domain. By repeating these three steps, the growth cone moves forward, resulting in neurite elongation. However, neurite growth is not a steady and continuous process, as growth cones also undergo cycles of pausing and retraction (Dent et al., 2011; Dupraz et al., 2019). As discussed above, retraction is part of the oscillatory growth behaviour of minor neurites in unpolarised neurons (Dotti et al., 1988; Lin et al. manuscript in preparation). Though, retraction occurs in axons as well. Here, it is observed as competitive growth of different axonal branches, while the outgrowth of one axonal process is invariably accompanied by the simultaneous retraction of another process, belonging to the same axon (Hutchins and Kalil, 2008). Further, mis-targeted axons retract alternatively to atrophy or neuronal death, for example, such a retraction is seen in the withdrawal of all but one axon from each muscle fibre (Gan and Lichtman, 1998). Such retraction events involve the reconfiguration of the cytoskeleton (He et al., 2002), and are necessary for the establishment of the correct connectivity. However, to elicit regeneration and re-growth of injured axons it is necessary to understand the mechanisms of axonal growth. What are the mechanisms that involve the cytoskeleton to drive neurite extension and axon elongation?

Axonal growth can be seen as migration without movement of the cell body and nucleus. Therefore, it is not surprising that axon growth and elongation through the complex environment of cellular tissue shares significant parallels with cell migration (Short et al., 2016). In the past decades, mainly two different modes of axon elongation were discussed, “pushing” and “pulling”.

The two main strategies of how a single cell migrates are amoeboid or mesenchymal based cell migration (Lintz et al., 2017). In amoeboid migration, the cell rapidly moves adhesion-independent by blebbing, the formation of hemispherical protrusions by detachment of the plasma membrane from the underlying actin cortex (Garcia-Arcos et al., 2024), while mesenchymal migration is characterised by an adhesion-dependent mechanisms, stress fibre formation, polarisation and formation of a leading and a trailing edge (Pankova et al., 2010). Migrating cells are not bound to one of these modes of migration but can transition from one mode to the other (Behrooz and Shojaei, 2024; Chen et al., 2023). In this way, migrating cells adapt to different environments. These modes of migration have been used to describe the movement of the growth cone, and thus, axon elongation (Alfadil and Bradke, 2023). Pfenninger described axon elongation as a

"leukocyte on a leash", the growth cone that migrates like a cell coupled to the cell body by the axon (Pfenninger, 1986).

One of the earliest models to explain axon growth and elongation was the clutch hypothesis. In this model, the retrograde actin flow is coupled via adhesions to the substrate the cell is growing on. Engagement of the clutch results in an internal reduction of retrograde flow, and ongoing actin polymerisation generates tractions forces which move the growth cone forward by "pulling" on the substrate (Lowery and Van Vactor, 2009; Mitchison and Kirschner, 1988). A "pulling", mesenchymal adhesion-dependent mode of migration is observed in fibroblasts (Santos et al., 2020). Fibroblasts engage with the extracellular matrix via adhesions and apply forces to individual collagen fibres, thereby pull themselves forward. For "pulling" along a substrate and generation of the retrograde flow, the activity of myosin-II and actomyosin contraction is required. The requirement for actomyosin in axon growth is dependent on the substrate (Ketschek et al., 2007). When embryonic day 7 (E7) chicken dorsal root ganglia neurons are grown on laminin, which allows the formation of adhesions via integrin, myosin-II inhibition decreases rates of axon extension. In contrast, growing these explants on poly-lysine, a low-adhesive environment, myosin-II inhibition promotes growth (Ketschek et al., 2007). This indicates that in a low-adhesive environment, myosin-II activity cannot be used to generate growth-promoting forces but is instead growth-inhibiting. This growth inhibition of myosin-II on a low-adhesive substrate is linked to the prevention of microtubules from entering the P-domain of growth cones by actin arcs. In CNS neurons, inhibition of myosin-II results in increased elongation rates, but only in the presence of actomyosin arcs (Dupraz et al., 2019; Santos et al., 2020).

Early research already showed that neurons also grow in an adhesion-independent way in a liquid medium (Letourneau, 1975). In line with this observation, CNS neurons, in particular hippocampal neurons, extend their neurites in an adhesion-independent manner in a 3D environment (Santos et al., 2020). As mentioned above, under such 3D conditions, the growth cone does not exhibit actin arcs as observed in 2D culture conditions, and microtubules advance unhindered into the leading edge of the growth cone. Based on such findings, the growth of axons is described as ameboid-like, independent of adhesions and based on cell-internal pushing forces. In this model, polymerising microtubules provide the force required to "push" the extending growth cone forward (Franze, 2020).

From this perspective, the dense actin network in the growth cone periphery is considered as a steric hindrance and limiting factor, preventing microtubules protrusion further from the C-domain to the leading edge (Coles and Bradke, 2015). In line with this, depolymerisation of actin filaments in *Aplysia californica* bag-neurons results in a quick occupation of the previous actin-dominated space by microtubules in the growth cone (Forscher and Smith, 1988). Also, neurons treated with Cyto D grow undisturbed in 2D,

which indicates that actin polymerisation and turnover is not required for growth but rather limiting it (Santos et al., 2020). In a 3D environment, the same treatment does not affect neurite length, suggesting that the effect is based on the disassembly of actin arcs, which are not present in growth cones in a 3D collagen gel.

When actin dynamics are high, microtubules penetrate the leading edge and promote growth. In line with this, destabilisation of the actin cytoskeleton promotes growth as well as regeneration (Bradke and Dotti, 1999; Tedeschi et al., 2019), similar to myosin-II inhibition (Dupraz et al., 2019). Whether actin arcs formed by myosin-II activity are relevant for developmental axon growth *in vivo* remains to be shown. Nonetheless, direct inhibition of myosin-II at the site of injury promotes regeneration (Heo et al., 2025). Further, a neuron-specific knockout of the myosin-II upstream regulator Rho A enhances regeneration after injury in the spinal cord, by limiting myosin-II activity in response to the inhibitory extracellular environment (Stern et al., 2021). Maintaining Rho A activity in glial cells is important to prevent astrogliosis, which is suppressed by Rho A-mediated activation of Yes-activated protein signalling. Both studies clearly show that myosin-II is relevant in a regeneration context, indicating that it is involved in limiting growth capacity in adults, but the role during developmental growth *in vivo* remains to be studied.

The protrusion of microtubules into the peripheral domain is not only blocked by actin arcs, but also the retrograde flow of actin itself restricts microtubules from entering the P-domain and leads to direct removal of microtubules from the P-domain (Coles and Bradke, 2015; Zhou et al., 2002). The actin cytoskeleton is indispensable for growth cone steering and guidance of the growing axon (Kalil and Dent, 2005). However, filopodial and lamellipodial activity are not necessary for growth, and neurites extend without a growth cone (Marsh and Letourneau, 1984), favouring the model that microtubules provide the necessary machinery for axon elongation. Conversely, early studies reported that neurons treated with Cyto B form “rounded-up” growth cones and cease elongation (Yamada et al., 1971). Further, considering the forces generated by polymerising microtubules, Miller and Suter conclude that these forces are too small to “push” the growth cone forward and to be the driver of axon elongation, unless microtubules would stall against a barrier, which they do not (Miller and Suter, 2018).

Aside from the assembly and polymerisation of microtubules, single polymers are slid or polymers are moved in bulk (Athamneh et al., 2017). Microtubule sliding is the movement of microtubules relative to other microtubules, driven by motor proteins like kinesin-1 (Guha et al., 2021), and is distinct from microtubule retrograde flow of the whole microtubule array (Schelski and Bradke, 2022). Sliding of microtubules contributes to neurite formation, but the role in elongation is unclear. Recently, it was suggested that microtubule sliding contributes to the arrangement of a mixed polarity of microtubules in dendrites of developing neurons (Iwanski et al., 2025). In axons with a parallel orientation

of microtubules, sliding is less abundant, and microtubule sliding leads to axon extension rates of a few µm per hour, but often, axons exhibit much faster growth rates (Miller and Suter, 2018).

In contrast to the minor contribution of microtubule sliding, not being capable of accounting for observed axon elongation rates, bulk transport of microtubules can account for the major forward movement needed for growth cone advance (Athamneh et al., 2017). This bulk forward movement of microtubules is in opposite to the reported retrograde flow of the whole microtubule array (Schelski and Bradke, 2022). However, the retrograde flow of microtubules slows down in the axon and thereby may enable bulk forward movement. Nevertheless, microtubule patches in the axon shaft did not exhibit anterograde movement (Schelski and Bradke, 2022).

The bulk movement of microtubules occurs at the same rate of neurite elongation and both processes highly correlate (Athamneh et al., 2017). It might be possible that bulk forward movement of microtubules is only a process to keep track with the advancing growth cone, filling up the free space behind the P-domain of protruding growth cones. For bulk microtubule advance, the assembly of microtubules is necessary (Athamneh et al., 2017). Causal data for the involvement of microtubule bulk movement in axon elongation have not been presented as of yet. Also, microtubule assembly and forward translocation occur in growth cones with minimal net advance. This results in increasing growth cone size, as the growth cone is filled up with cytoskeletal and organelle mass transported along with microtubules (Miller and Suter, 2018). The occurrence of bulk forward movement during very slow elongation makes it questionable whether bulk transport is the driver of elongation. Nevertheless, movement of the whole microtubule array seems to be involved in axon elongation as the retrograde flow of the whole microtubule array slows down shortly after polarisation and thereby enables and contributes to fast axon growth (Burute et al., 2022; Schelski and Bradke, 2022).

Also, “pushing” forces based on polymerisation of actin filaments at the leading edge seem to be too small to solely drive axon elongation (Miller and Suter, 2018). Reversat and colleagues propose that the principal mechanism of cell migration is the coupling of retrograde actin flow to traction forces, adhesion-dependent but also adhesion-independent, and that this is a basic mechanism for cell migration (Reversat et al., 2020). Adhesion-dependent and -independent migrations are variants of the same principle and potentially operate interchangeably.

Contractile forces are also generated in the axon (Miller and Suter, 2018). These contractile forces involve activity of myosin-IIA in the axon, which oppose contractile forces generated by myosin-IIB in the growth cone. When the contractile forces in the axon are low compared to the growth cone, rapid elongation ensues. In the model of Miller and Suter, axon elongation is based in internal forces driven by actin assembly, its retrograde

flow mediated by myosin-II, and forces in the axonal shaft. Axon elongation depends on the balance between the force in the axon and the force generated in the growth cone. Most of the studies that were considered for this model focused on sensory neurons, so this model still considers coupling of actin to the substrate, which is not necessary in CNS neurons (Santos et al., 2020). Whether CNS neurons and sensory neurons share the same mechanisms of axon elongation awaits future clarification. Overall, axon elongation is not only controlled by a single force-generating process, but rather a balance of multiple force-generating processes that together orchestrate elongation.

Much evidence has been presented in the past decades for any of these models describing axon elongation. Still, the relative contributions of the different mechanisms to neurite growth are controversial. Thus, further research is needed to elucidate the exact mechanism and whether this is cell type and environment dependent. Additionally, it might be possible that growing axons switch their mode of growth, like migrating cells.

Synaptic connections and transmission of information

When neurons elongated to the designated target regions, they form contacts with their postsynaptic partners. Contact between the pre- and postsynaptic partners is established by terminal arborisation of axons. Terminal arbors are fine and branched structures at the end of an axon that form synaptic connections with other neurons or cells (Kalil and Dent, 2014). While terminal arbors of motor neurons form presynaptic connections to muscle cells, so-called neuromuscular junctions (Rodriguez Cruz et al., 2020), in the brain, almost all synapses formed by axons are *en passant* synaptic connections (Sudhof, 2021). These synaptic connections do not form at axon terminals, but like pearls on a string, along the axon shaft. Axons form thousands of these connections.

All of these presynaptic specialisations transmit information via the same release machinery. This release machinery is formed by soluble N-ethylmaleimide-sensitive factor attachment protein receptors that mediate membrane fusion, synaptotagmins and their complexin cofactors that enable Ca^{2+}-triggering (Sudhof, 2021). Further, Rab3-interacting molecules (RIM), RIM binding proteins and mammalian uncoordinated-13 (Munc13) proteins that build the active zone scaffold, tether synaptic vesicles and are involved in recruitment of Ca^{2+}-channels to neurotransmitter release sites (Sudhof, 2021).

The active zone is the site where vesicles loaded with neurotransmitters fuse with the axonal membrane to release their content to the synaptic cleft, resulting in the activation of receptors at the postsynaptic site, transmitting information. For this transmission of information, a pool of vesicles is located close to the active zone on the presynaptic site. When an AP travels along the axon shaft, voltage-gated Ca^{2+}-channels are activated and allow influx of Ca^{2+}-ions to the presynaptic site, triggering the release of neurotransmitter-containing vesicles.

An AP is a rapid, transient electrical impulse generated by a rapid change in voltage across the cell membrane. This impulse is based on the influx of sodium ions through voltage-gated channels into the neuron, increasing the resting potential of around -60 mV relative to the outside, causing a depolarisation of the cell. Subsequently, a rush out of potassium ions repolarises the cell and return it to its negative resting potential. In this way, neurons transmit information in form of electrical impulses through the body.

As neurons form connections, the cytoskeleton undergoes further remodelling to support synaptogenesis and also synaptic plasticity. F-actin is required for the assembly of presynaptic sites during the early stages of synaptogenesis (Chia et al., 2013; Zhang and Benson, 2001). When actin polymerisation is inhibited by Latrunculin A (Lat A) in early stages of synapse formation at DIV 5, synaptophysin clusters are lost and all F-actin is depolymerised by 8 h of treatment (Zhang and Benson, 2001). In older neurons, at DIV 12, depolymerisation of filamentous actin does not lead to a reduction in synaptic connections, as synaptophysin clusters remain intact and Lat A treatment requires at least 16 h to depolymerise all actin. These results show that F-actin is crucial for the initial formation and building of the synapse, but not for structural integrity afterwards and that actin filaments become more stable over time. Long-term treatment over 24 h with Lat A revealed a pool of exceedingly stable F-actin in DIV 20 neurons, which is not depolymerised by Lat A within the treatment time (Zhang and Benson, 2001). This stabilisation of F-actin is enhanced by treatments with KCl, suggesting that depolarisation influences actin stability.

Actin filaments are involved in many steps during synapse assembly and function (Chia et al., 2013). The filaments function as a scaffold for presynaptic proteins and organise their clustering. This stabilises these components in early pre-synapses, alongside other scaffolding and adhesion molecules. In mature synapses, actin is involved in the organisation and translocation of synaptic vesicles from the reserve to the readily releasable pool. Additionally, actin regulates their endocytosis (Doussau and Augustine, 2000; Nelson et al., 2013; Rust and Maritzen, 2015). Further, remodelling of actin structures is essential for pre- and postsynaptic plasticity. In general, synaptic plasticity requires remodelling of the actin cytoskeleton, and these processes are needed for forming and strengthening synaptic connections, which are essential for learning and memory (Cingolani and Goda, 2008; Jedrzejewska-Szmek and Blackwell, 2019).

The contribution of microtubules to presynaptic assembly and function is more elusive because of a dearth of studies on how microtubules may function at these specific sites (Dent, 2020). As microtubules are the main long-distance transport tracks for the delivery of cargo in neurons, microtubule dynamics and kinesin-based transport play a role in the delivery of synaptic vesicle precursors to *en passant* synapses (Dent, 2020). Tubulin

directly interacts with the presynaptic proteins synapsin I, synaptotagmin I and α-synuclein, which suggests a functional connection between vesicle clustering and neurotransmitter release (Parato and Bartolini, 2021). In line with this, microtubules are associated with mitochondria and synaptic vesicles close to the active zone.
Further, polymerisation of microtubules is often initiated or terminated at synapses. Microtubules are non-centrosomally nucleated at the site of *en passant* synapses, serving as tracks for bidirectional movement of synaptic vesicles between synaptic boutons (Dent, 2020; Qu et al., 2019). Nucleation of microtubules is activity-dependent and inhibition of microtubule nucleation impaired high-frequency evoked neurotransmitter release. Motor-proteins like kinesin family member 1A are involved in the unloading of cargo at synapses because of their decreased affinity for GTP-loaded tubulin at the growing plus-end of microtubules, which is supported by the observation of increased polymerisation going on at presynaptic sites (Dent, 2020). How microtubules contribute to the assembly and function of presynaptic sites, especially along the axon shaft, besides their role in transport and delivery of synaptic material, remains to be studied.

Regeneration failure of CNS neurons and the contribution of developmental and maturation processes

During development, neurons exhibit enormous growth potential, enabling them to extend across vast distances within the developing organism. In all of these processes, cytoskeleton dynamics are essential, and must even be suppressed in minor neurites to establish morphological and functional polarity. What changes within the neuron cause this growth potential to be lost?

Neurons in the adult CNS fail to regenerate after an injury. This phenomenon was already described by Ramon y Cajal (Ramon y Cajal, 1928). Initially, it was assumed that the low regenerative capacity of adult neurons is based solely on a growth-inhibitory environment created after an injury. This inhibitory environment includes myelin, chondroitin sulfate proteoglycans (CSPGs), the formation of a glial scar and further factors limiting axon growth after an injury (Quraishe et al., 2018). Therefore, many approaches have targeted the inhibitory environment to induce axon regeneration, for example, by degrading CSPGs or blocking the Nogo receptor (Cooke et al., 2022). The inhibitory environment and the scar that injured axons are exposed to are one of the main contributors to regeneration failure, and are reviewed elsewhere (Bradbury and Burnside, 2019).
Over the past decades, it became evident that a very low intrinsic growth and regeneration capacity contributes to a failing re-growth of injured neurons (He and Jin, 2016). Failed neuronal regeneration is relevant to both neurodegenerative diseases and traumatic injury

to the brain or spinal cord. Spinal cord injury represents a particularly striking example, where depending on severity and site of lesion, injury leads to loss of descending control of multiple organ systems. These can comprise both autonomic functions, and somatic functions such as voluntary movement, bladder control and sexual function. These effects are permanent and are thought to affect 27 million people worldwide (James et al., 2019), highlighting the importance of developing regenerative treatments.

After an injury to the CNS axons, these cell processes retract from the injury site. Though a few axons can be observed that sprout for a limited distance, the majority of CNS axons fail to regenerate (Bradke et al., 2012). Instead of reforming a growth cone which would promote regeneration, injured axons form a swelling at their ends, filled with disorganised microtubules and accumulated vesicles and organelles (Bradke et al., 2012; Ertürk et al., 2007). These retraction bulbs are still found in patients 42 years after spinal cord injury (Ruschel et al., 2015). For robust regeneration, such a retraction bulb needs to transform into a growth cone (Bradke et al., 2012). The transformation of retraction bulbs is supported by treatments with the microtubule-stabilising drug Taxol, which leads to reorganisation of microtubules in retraction bulbs, while the destabilisation with Nocodazole enhances bulb formation (Ertürk et al., 2007). The stabilisation of microtubules is sufficient to induce regeneration and to enhance recovery of behaviour after spinal cord injury (Griffin et al., 2023; Hellal et al., 2011; Ruschel et al., 2015). This effect is due to a reduction in retraction bulbs, but also a reduction of the fibrotic scar, making the environment more permissive for regeneration.

Not only disorganised microtubules but also missing actin dynamics play a role in regeneration failure. One experimental method to study axon regeneration uses the “conditioning lesion”. This is a phenomenon in which a pre-lesion of the peripheral branch of a sensory axon, induces a regenerative response following subsequent lesion to its central branch in the spinal cord (Richardson and Issa, 1984; Smith and Skene, 1997).

As discussed before, a dynamic actin cytoskeleton is required for neurite formation, axon specification and also for axon elongation. In line with this, growth competence of these dorsal root ganglion (DRG) neurons is associated with enhanced actin dynamics via cofilin activation (Tedeschi et al., 2019). Cofilin activity, especially its severing of actin filaments, is important for regeneration, as neurons with a knockout of cofilin fail to regenerate (Tedeschi et al., 2019). All the three members of the ADF/cofilin family, ADF, cofilin-1 and cofilin-2, compensate for each other. Increasing cofilin activity by overexpression is sufficient to promote regeneration.

Further, the actin regulator myosin-II plays a role in the regeneration of neurons. Direct inhibition of myosin-II as well as neuron-specific knockout of the myosin-II activator Rho A enhances regeneration after an injury (Heo et al., 2025; Stern et al., 2021). Already during development, myosin-II is a negative regulator of neurite growth (Amano et al., 1998;

Dupraz et al., 2019; Kollins et al., 2009; Wylie and Chantler, 2003). These results show that not only for development, but also for regeneration after an injury, the axon depends on properly organised and specifically dynamic cytoskeleton components. If neurons know how to organise and regulate their cytoskeleton to grow an axon why do they fail to do so in adulthood?

Neurons lose their ability to regenerate their axons during maturation in embryonic and postnatal development (Hilton et al., 2024). Over the years, more and more evidence emerged, suggesting that the developmental dynamic growth of axons and their function as transmitters of information are mutually exclusive. As the CNS cannot renew itself like the skin or liver, neurons have to function throughout the whole lifespan of the organism. In some cases, this requires neurons and the whole nervous system to function for more than 110 years, in the case of humans (Shikimoto et al., 2022). To do so, neurons mature and transform from a situation where they grow and assemble the components needed for their function, to a fixed state for effective transmission of information (Hilton et al., 2024). This switch from a motile, electrically inactive structure to a stable and electrically active structure is currently seen to be one of the major reasons why adult CNS axons lose their intrinsic regeneration potential. On the other hand, these changes and the switch go hand in hand with the maturation of the neuron, which is necessary to enable neurons to fulfil their designated function as transmitters of information. Though, it seems that neurons, at least DRG neurons, do not lose their growth competence during maturation but rather suppress it.

When DRG neurons reacquire growth competence they do not globally upregulate growth-promoting factors, but rather downregulate components that prevent growth and regeneration in mature neurons (Hilton et al., 2022). Whether such a mechanism, in which growth competence is suppressed rather than downregulated, can be transferred to CNS neurons remains to be investigated. However, it is not only the suppression of growth competence that leads to regeneration failure, since also growth promoting factors become downregulated, for example, the growth-associated protein 43 (Karimi-Abdolrezaee et al., 2002). Further, a proteomic screen of different growth states of DRG neurons revealed Glypican-1 as an upregulated factor promoting axon growth *in vitro*, when those neurons re-acquired growth competence (Fährmann, 2025). Thus, the reduction in growth competence comprises the suppression of growth, but also the downregulation of growth promoting factors. The upregulation of growth promoting factors like Glypican-1, is sufficient to overcome suppressing mechanisms and an inhibitory environment and enhances axon growth.

Processes that are part of neuronal maturation, which are involved in limiting regeneration of adult neurons, are changes in gene expression, intracellular transport, signalling, and

the cytoskeleton (as mentioned above) (Hilton et al., 2024). In the past few years, it has become more evident that a further component that is established during maturation contributes to regeneration failure, which is synapse formation and the onset of neurotransmission. Already 15 years ago, it was reported that conditioning of DRG neurons causes a silencing of neurons accompanied by improved growth (Enes et al., 2010). Stimulating neuronal activity inhibits axon growth in adult DRG neurons, which is mediated by voltage-gated calcium channel (Ca_V) 1.2 channels. Downregulation of this channel by genetic ablation enhances peripheral nerve regeneration (Enes et al., 2010). Expanding the evidence that activity suppresses growth, the calcium voltage-gated channel auxiliary subunit alpha2delta2 (Cacna2d2) suppresses axon growth (Tedeschi et al., 2016). This calcium channel triggers Ca^{2+} influx in response to AP firing, and indeed, the growth-suppressing effect is based on calcium influx through Ca_V2 channels. Pharmacological blocking of these calcium channels with Pregabalin promotes regeneration after spinal cord injury (Tedeschi et al., 2016).

Besides electrical activity and the activity-mediated Ca^{2+} influx influencing axon growth, a recent study reveals that components of the vesicle release machinery of synapses also limit regeneration capacity in sensory neurons (Hilton et al., 2022). The scaffolding proteins RIM1 and RIM2, as well as Munc13, which are involved in tethering and docking vesicles at the active zone, are downregulated when DRG neurons acquire growth competence. In line, deletion of all RIM or Munc13 isoforms promotes axon growth *in vitro* (Hilton et al., 2022). Deletion of all three Munc13 isoforms is sufficient to promote regeneration after a complete dorsal column spinal cord injury. The exact mechanism by which the priming and tethering of vesicles to the active zone of synapses inhibits growth is unclear. Whether such proteins as Cacna2d2, RIM and Munc13 also limit CNS neuron regeneration is an open question, since most of these discoveries are based on DRG neurons as a model system. Since DRG neurons are not part of the CNS, a direct transfer of these findings to CNS neurons is not possible. For example, in hippocampal neurons, the loss of Munc13 reduces neurite outgrowth in early neurite outgrowth, but is compensated at the time of synaptogenesis (Broeke et al., 2010). Therefore, more research in CNS neurons is needed to study whether the described mechanisms, found to suppress growth in DRG neurons, can be applied to CNS neurons as well. Nevertheless, CNS neurons like cortical neurons exhibit a decline in regenerative ability when they transition from an axon elongation to a synapse formation state (Hilton et al., 2024; Koseki et al., 2017). Based on these findings, the picture that neuronal growth and transmission of information exclude each other is strengthened. The exact mechanisms by how neuronal activity and transmission of information prevent growth remain to be studied, potentially, they affect the cytoskeleton, which is a main driver of growth.

Objectives - how do neurons grow and lose their intrinsic growth potential?

Millions of people worldwide suffer from the consequences of a spinal cord injury (James et al., 2019), and millions more suffer from other diseases that lead to the degeneration of the nervous system and require regenerative therapies (Ashraf et al., 2023; Ralph et al., 2024). To date, there is no effective treatment option to enable regeneration after injuries or degeneration. In the case of spinal cord injuries, the most effective therapy is currently rehabilitation, but its success becomes limited the more severe the injury to the spinal cord gets (Dietz and Fouad, 2014). To elicit regeneration after an injury, we need to understand the factors that limit growth. This includes the growth-inhibiting environment but also the reduction of intrinsic growth capacity in the course of neuronal development and maturation.

As part of the intrinsic growth potential, the understanding of the mechanisms by which neurons grow or stop growing is important for the development of an effective treatment and “cure” for spinal cord injuries. Although there have been countless studies investigating growth, our understanding of growth mechanisms is still incomplete. This is also due to the large number of different model systems and different culture conditions, which also reflect the complexity of the conditions in the developing organism. Our understanding of growth-suppressing mechanisms, which are developmentally required for the maturation and function of neurons, is slowly beginning to grow, but is still fragmentary. Therefore, it is also important to investigate what developmental and maturation-dependent processes suppress growth in mature CNS neurons.

We know that a dynamic and malleable actin cytoskeleton is necessary in development to form neurites and to enable their growth. On the other hand, an increase in actin filament stability in the course of development was reported. Further, reactivating actin dynamics was sufficient to elicit regeneration, indicating that maturing neurons downregulate their actin turnover, limiting their regenerative capacity. In this work, I will investigate in cultured hippocampal neurons when an increased stabilisation of actin filaments occurs and whether this contributes to a decline in axonal growth. Further, I will investigate potential regulators that are involved in stabilising actin filaments.

In addition, many studies have focused on early stages for analysis of neurite and axon growth mechanisms, but we do not know whether growth mechanisms differ during development and whether these, like cell migration, can and may also change depending on the environment. To investigate whether growth mechanisms can change in the course of development, I will analyse whether cytoskeletal dynamics and their contribution to axon growth change at later time points in cultured neurons. Elucidating the mechanisms that limit regeneration will potentially provide us with additional targets to develop regenerative

therapies for patients suffering from degenerated and injured neurons. Only if we understand the growth mechanisms of neurons and the regeneration-limiting processes can we orchestrate a regeneration response.

Results

This study aimed to investigate how neurons grow and wire the nervous system, as well as the mechanisms that contribute to the decline of growth capacity in maturing neurons. Therefore, I used pharmacological and genetic techniques to influence potential regulators of neuronal growth in cell culture, to decode what drives – or hinders – axon growth, as described in the following results section.

Growth behaviour of hippocampal neurons in culture

The establishment of the nervous system in the developing organism is a highly complex process. It involves a multitude of cell intrinsic and extrinsic factors that, as a whole, lead to an immaculate formation of the neuronal network. Studying these processes in the living and developing organism is the gold standard. However, our ability to manipulate, image and analyse neurons *in vivo* is quite limited given how complex living tissues are. Therefore, cell culture approaches have been established to simplify complex biological processes, allowing easy manipulation and analysis of, for example, neurons (Banker and Cowman, 1977; Harrison, 1907).

To investigate mechanisms that contribute to the growth of neurons and processes that lead to the reduction of growth capacity, I analysed the growth behaviour of hippocampal neurons in culture over time. Whilst reports of growth and development of neurons in culture exist, functional and morphological properties of cells are heavily influenced by variations in cell density, culture media composition and inclusion of a glia feeding layer (Biffi et al., 2013; Jones et al., 2012; Yang et al., 2017; Young et al., 2000). Moreover, requirement of a specific level of cell density for culture survival makes tracking individual cell morphology difficult, especially in more mature neurons with a complex dendritic tree architecture and a highly branched axonal compartment.

'Mixed culture' system to track whole cell morphology

To identify and analyse individual cell morphologies, I used the approach of a 'mixed culture' system described by Gomis-Rüth and colleagues (Gomis-Ruth et al., 2014). Briefly, a preparation of wild-type (WT) neurons is mixed with a low percentage of fluorescently labelled neurons and cultured together. As described in the previous protocol, two timed-pregnant animals are needed for the preparation of a 'mixed culture'. Since the mating success of animals varies, the dependence on two timed-pregnant animals pregnant at the same time makes this protocol complicated. In the case that one of the required animals is not pregnant, the setup of a 'mixed culture' is not possible. To circumvent this issue, I modified the protocol by mating a WT animal with a heterozygous carrier of the green fluorescent protein (GFP) mouse line (Figure 9A). This mouse line

expresses GFP under the ubiquitous 'CAG' promoter, which is composed of the cytomegalovirus (CMV) enhancer and a fragment of the chicken β-actin promoter and is called "Actin-GFP" here (Okabe et al., 1997). Mating a heterozygous carrier of the GFP line with a WT animal yields a 50% chance for a GFP-positive (GFP^+) embryo. Thus, one litter typically provides both WT as well as GFP expressing cells. When embryos are isolated for hippocampal neuron preparation at E17.5, the genotype of the embryos was easily determined by placing the bodies on a blue-light table (Figure 9A). After identification of the genotype, WT and GFP^+ hippocampi were separately prepared for neuron culture.

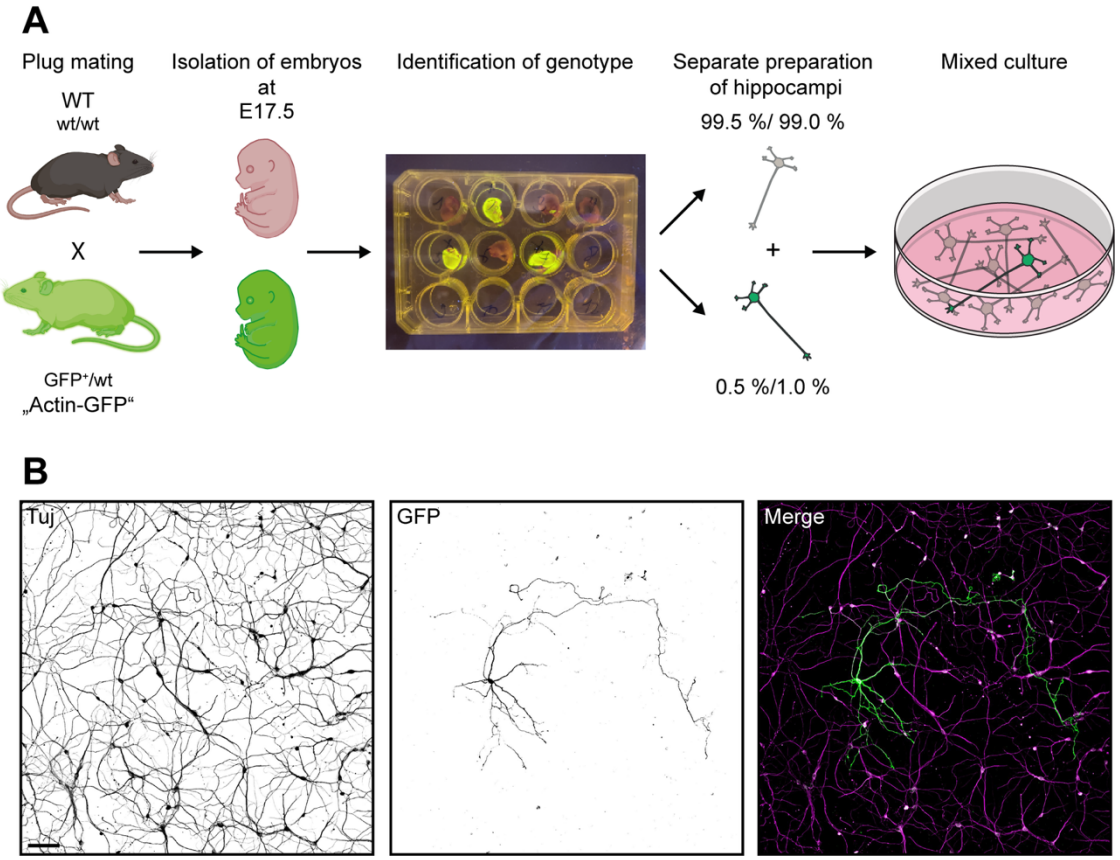

Figure 9: Preparation scheme for mixed neuron cultures

(A) Scheme for preparation of a 'mixed culture'. Wild-type (WT) animals are timed-mated with a heterozygous (GFP+/wt) counterpart of a GFP-mouse line. At embryonic day 17.5 (E17.5), embryos are isolated from the mother and kept separately. Embryo bodies are placed on a blue-light table to quickly identify their genotype. WT and GFP+ hippocampi are separately prepared and the cell concentration is determined. Based on the desired proportion, WT and GFP+ cells are mixed and cultured together. (B) Representative images of day in vitro (DIV) 7 neurons stained for β-III-tubulin (Tuj) and GFP. Images were created from stitched tiles. Scale bar 100 µm.

Depending on how long the neurons will be kept in culture, different ratios of WT and GFP^+ neurons were plated. For experiments where 'mixed cultures' were analysed within two to three days, a higher percentage of GFP^+ neurons was used (1%). When neurons were cultured for long time in culture, for example, for 28 days, a lower proportion of GFP^+ (0.5%) cells is recommended. This reduces the likelihood that GFP^+ neurons will coalesce,

which prevents tracking individual cell morphology. Reducing the number of pregnant animals needed for this method increases its reliability and aligns with the 3R principles - reduce, refine and replace the use of animals in research.

Having individual neurons fluorescently labelled enables tracking their morphology especially in later developmental stages when neurons have acquired a complex and extended morphology (Figure 9B). Using a GFP-expressing mouse line for this culture approach is more precise than a plasmid-based transfection, since it allows to accurately titrate the number of GFP^+ cells mixed in to WT neurons. A transfection-based approach, like nucleofection, can stress the sensitive neurons and transfection rates vary making it less reproducible to always have the correct number of GFP-expressing cells. Moreover, in a stable GFP-mouse line, the expression level is more consistent and expressed over the whole time of the culture, especially important for later time points.

Changes in growth speed of neurites in the course of development

To analyse the growth properties of hippocampal neurons throughout their development in culture, mixed cultures containing 0.5% GFP^+ cells were fixed at different time points between one and 28 days *in vitro* (DIV) (Figure 10A). Quantification of the length of the longest neurite showed a logistic growth curve (Figure 10B) with neurons reaching an average length of 3354 µm ± 453 µm (mean ± standard deviation (SD)) after 28 DIV. While young neurons (DIV 1 – 2) initially slowly increased their neurite length (Figure 10C), corresponding to the time they needed to polarise (Figure 10D), growth rates increased up to 251 µm/d ± 43 µm/d and 248 µm/d ± 51 µm/d (mean ± standard error of the mean (SEM)) at DIV 7 and DIV 10 respectively, when neurons elongate their axons. Subsequently, growth rates of the length of the longest neurite continuously decreased again to 34 µm/d ± 14 µm/d at DIV 28. Here, the total neurite length of individual neurons at the different time points was not quantified, but could be an informative value to assess whether hippocampal neurons switch from a growth in length mode to a branching growth mode when they mature and make synaptic connections, similar to DRG neurons (Tedeschi et al., 2016).

As expected, the growth kinetics of the minor neurites differed from those of the longest neurite (Figure 10). To analyse these kinetics, the length of the second longest neurite was quantified, corresponding to minor neurites at earlier stages and dendrites at later stages of neuronal development. The growth curve of the second longest neurite shows a logistic form similar to the length of the longest neurite (Figure 10B and F). Dendrites reached only one-tenth of the length of the longest neurite with an average length of 307 µm ± 8 µm (mean ± SD). This is due to the growth restriction in minor neurites that enable the polarised morphology of hippocampal neurons (Dotti et al., 1988). The growth limitation of minor neurites was reflected in their reduced growth rates. The highest growth

rates of minor neurites were found at DIV 1 with 41 µm/d ± 2 µm/d (mean ± SD) when neurons form neurites (Dotti et al., 1988) (Figure 10D and G). Subsequently, growth rates were reduced while polarised neurons fuelled elongation of the longest neurite (Figure 10C, D and G). Similar to the longest neurite, the growth rate of dendrites was further reduced after two weeks in culture (Figure 10G).

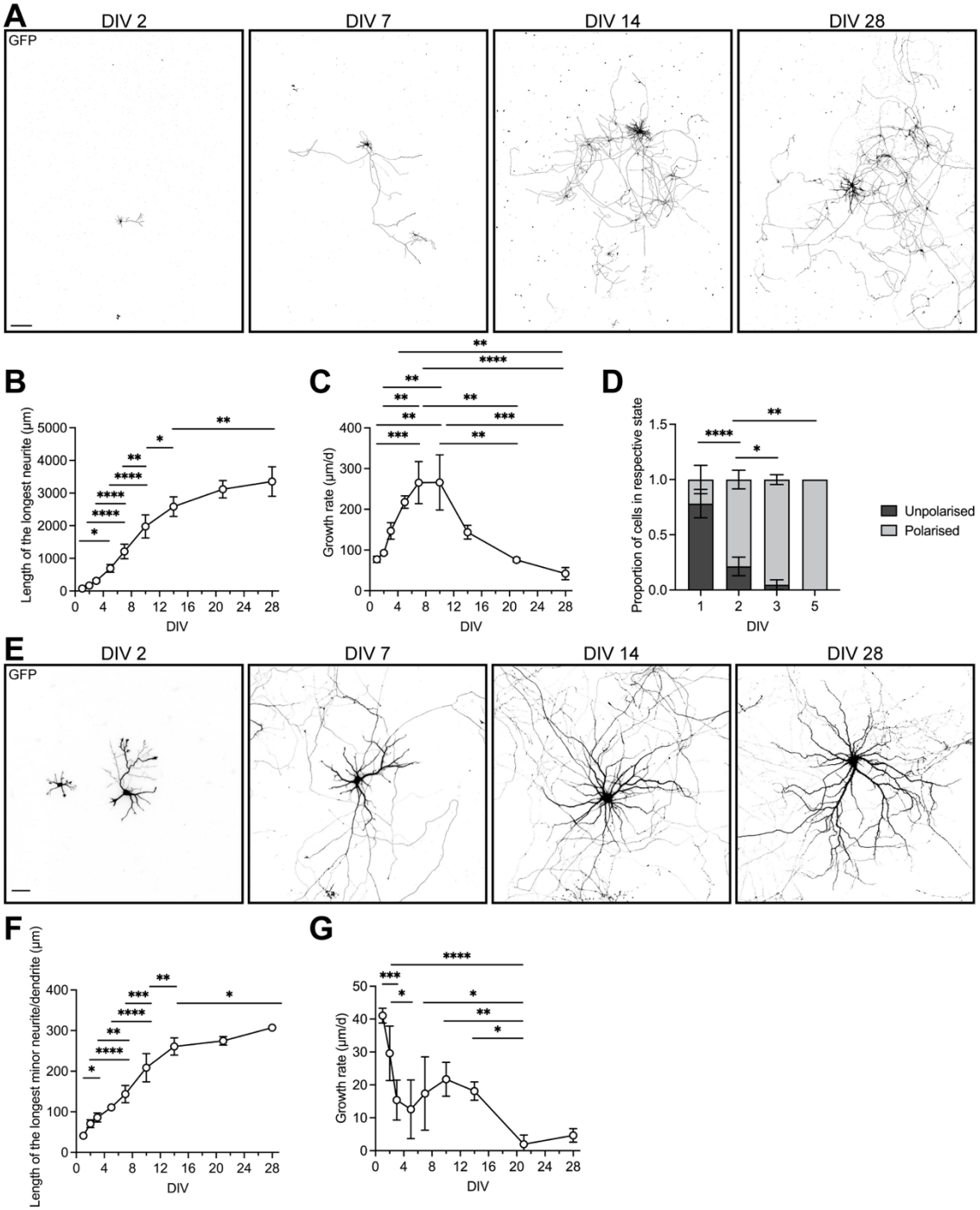

Figure 10: Growth behaviour of hippocampal neurons in culture over time

(A) Representative images of hippocampal neurons fixed at the indicated days *in vitro* (DIV). Neurons were stained for GFP. Images were generated from stitched tiles. Scale bar 250 µm. (B) The length of the longest neurite per neuron was quantified at the different DIVs. Values are plotted as mean ± standard deviation (SD) from n = 5 experiments, with N = 694 (DIV 1), 651 (DIV 2), 717 (DIV 3), 280 (DIV 5), 380 (DIV 7), 197 (DIV 10), 96 (DIV 14), 111 (DIV 21) and 100 (DIV 28) individual neurons traced in total. **** p<0.0001, **p<0.01, *p<0.05, not significant not indicated by one-way ANOVA with Tukey's multiple comparisons post-test. Each

mean was compared with every other mean. Not all significantly different comparisons are shown. (C) Growth rate in µm/d quantified as the slope of the data in (B) plotted as the mean ± standard error of the mean (SEM) from n = 5 experiments. ****p<0.0001, ***p<0.001, **p<0.01, not significant not indicated by one-way ANOVA with Tukey's multiple comparisons post-test. Each mean was compared with every other mean. (D) Quantification of the proportion of unpolarised and polarised neurons at the indicated time points, depicted as a percentage of neurons in the respective state. Neurons were considered polarised when the longest neurite was longer than 100 µm. Plotted is the mean ± SD from n = 5 experiments, with similar N like in (B). ****p<0.0001, **p<0.01, *p<0.05, not significant not indicated with two-way ANOVA for simple effects within each column with Tukey's multiple comparisons post-test. (E) Representative images of hippocampal neurons fixed at the indicated DIV, focusing on the dendritic compartment. Samples were stained for GFP. Images were generated from stitched tiles. Sale bar 50 µm. (F) Quantification of the length of the longest minor neurite/dendrite. For the quantification, the length of the second longest neurite was measured. Values are plotted as mean ± SD from n = 4 experiments, with N = 252 (DIV 1), 271 (DIV 2), 282 (DIV 3), 168 (DIV 5), 253 (DIV 7), 223 (DIV 10), 200 (DIV 14), 213 (DIV 21) and 191 (DIV 28) individual neurons traced in total. ****p<0.0001, ***p<0.001, **p<0.01, *p<0.05, not significant not indicated by one-way ANOVA with Tukey's multiple comparisons post-test. Each mean was compared with every other mean. Not all significantly different comparisons are shown. (G) Growth rate of minor neurites/dendrites in µm/d was quantified as the slope of changes in length of minor neurites/dendrites in (F). Mean ± SD is plotted from n = 4 experiments. ****p<0.0001, ***p<0.001, **p<0.01, *p<0.05, not significant not indicated by one-way ANOVA with Tukey's multiple comparisons post-test. Each mean was compared with every other mean. Not all significantly different comparisons are shown.

Overall, the observed growth behaviour is in line with our current knowledge of hippocampal neuron development in culture (Dotti et al., 1988). Initially, neurons exhibit a reduced growth rate when they form neurites and have not yet polarised. Upon polarisation, a rapid growth phase leads to the establishment of the well-known morphology of a neuron with a single long axon and several short dendrites. The observed mitigation of growth (Figure 10C and G) marks the time when neurons transition to a more stable and mature state and integrate into functional neural networks. This transition from a rapid growth to a more stable and mature state with reduced growth offers a unique opportunity to study mechanisms contributing to the decline in neuronal growth capacity. This time may mark the onset of growth reduction and inhibiting processes, which potentially persist for the lifespan of a neuron and thus also prevent regeneration (Hilton et al., 2024). Since neurons downregulate their growth rates also in such a simplified 2D-culture environment, it suggests that it is a cell-intrinsic process. What are those processes and mechanisms that are set into action to maintain stable neuronal networks but prevent the regeneration of injured neurons?

Actin filaments become stabilised in the growth cone of developing neurons over time

The neuronal cytoskeleton has been identified as a key driver of neurite formation and growth during development (Bradke and Dotti, 1999; Flynn et al., 2012; Mitchison and Kirschner, 1988; Witte et al., 2008). On the other side, pathological or missing cytoskeleton dynamics contribute to regeneration failure after neurons have been injured (Ertürk et al., 2007; Tedeschi et al., 2019). Focusing on the actin cytoskeleton, it became evident over the years that a dynamic actin cytoskeleton is favourable for neurite growth as well as

axon regeneration (Bradke and Dotti, 1999; Tedeschi et al., 2019). In line, stabilisation of actin filaments with Jasp leads to retraction and reduced growth due to reduced actin turnover (Gallo et al., 2002). It was reported that actin filaments become increasingly stable in maturing neurons (Allison et al., 1998; Zhang and Benson, 2001). Further, it is known that specific actin filaments are stabilised in the membrane-periodic skeleton (Zhong et al., 2014), in presynaptic sites (Zhang and Benson, 2001) and dendritic spines (Koskinen et al., 2014), contributing to the maintenance of these structures. Since neurite growth is associated with a dynamic actin cytoskeleton, this raises the question of whether stabilised actin filaments contribute to the decline in growth capacity in maturing neurons. Others have observed more stable actin filaments at around the same time when neurons started to downregulate their growth rates (Figure 10C, Zhang and Benson 2001).

To examine a potential role of stabilised actin filaments in the downregulation and decline in growth capacity, I analysed the actin cytoskeleton of cultured hippocampal neurons at different timepoints. Specifically, I decided to analyse actin filaments at DIV 2, DIV 7 and DIV 14, respectively. At these time points, neurons have polarised and initiated axon elongation (DIV 2), exhibited the highest growth rate during axon elongation (DIV 7) and have started to downregulate growth rates (DIV 14) (Figure 10).

First, I looked at the general distribution of actin filaments by high-resolution imaging of fixed hippocampal neurons stained with Phalloidin and Tuj (Figure 11A). As prior reported (Fine and Bray, 1971; Yamada et al., 1971), I found actin filaments highly enriched in axonal as well as dendritic tips, throughout development (Figure 11A). In later stages, at DIV 14, actin filaments became also enriched along axonal and dendritic shafts corresponding to pre- and postsynaptic terminals (Hotulainen and Hoogenraad, 2010; Rust and Maritzen, 2015). When I looked at overall changes during development on a whole cell level there was no difference in the mean F-actin intensity (Figure 11B, C and D). Since locally, in distinct compartments of the cell, the actin cytoskeleton can be regulated differently, I analysed actin filament intensities specifically in axonal growth cones. Whilst no difference was detected between F-actin intensity in DIV 2 and 7 growth cones, axonal growth cones of DIV 14 neurons showed approximately 50% reduced intensity values compared to earlier timepoints (Figure 11E and F). Such a developmental reduction in F-actin intensity was also described for chicken sensory neurons when developmental stage E7 was compared to E14 (Jones et al., 2006).

Not only was actin filament intensity reduced, but also the overall size of growth cones decreased over time (Figure 11G). This is again similar to growth cones of developing chicken sensory neurons *in vitro* (Jones et al., 2006).

As a second approach to evaluate changes in global actin cytoskeleton in developing neurons, I performed a G-/F-actin ratio assay at the different developmental time points (Figure 11H and I). Although there was a small increase in F-actin levels in DIV 7 and 14

neurons, no difference in the ratio of G- to F-actin was observed (Figure 11H and I). This observation is in line with an unchanged F-actin intensity on a whole cell level observed in fixed neurons (Figure 11C). Overall, besides a reduced F-actin intensity in growth cones of DIV 14 neurons, no change in the general properties of actin filaments was observed in developing neurons. Actin filament polymerisation at the leading edge contributes to growth cone advance (Lowery and Van Vactor, 2009). Whether sole reduction of actin filaments in growth cones of DIV 14 is already sufficient to lead to a decline in growth capacity needs to be discussed.

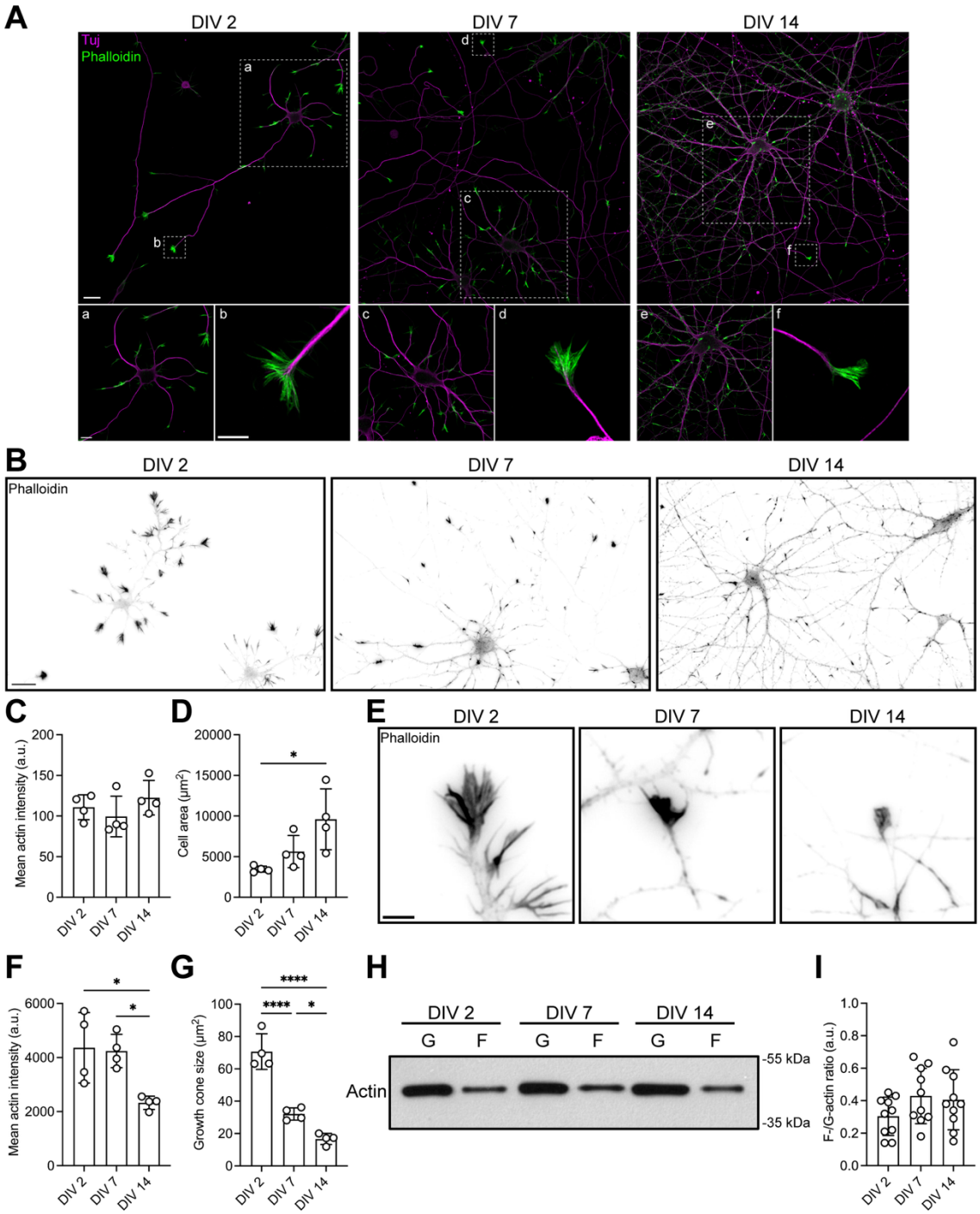

Figure 11: Actin cytoskeleton in developing neurons

(A) High resolution images of hippocampal neurons from the indicated DIV stained for Tuj and F-actin. Scale bars are 20 µm for the overview images, 10 µm for the cell body, and 5 µm for the growth cone images. (B) Representative images of hippocampal neurons from the indicated time points *in vitro*. Neurons were stained with Phalloidin. Scale bar 25 µm. (C) Quantification of the mean actin intensity for regions of interest (ROIs) as in (B). Values are plotted as mean ± SD from n = 4 experiments, with N = 319 (DIV 2), 307 (DIV 7) and 306 (DIV 14) ROIs measured in total. Each mean was compared with every other mean. ****p<0.0001, ***p<0.001, **p<0.01, *p<0.05, not significant not indicated by Kruskal-Wallis test with Dunn's multiple comparisons post-test. (D) Quantification of cell area in ROIs, as in (B). Area was based on α-tubulin staining (not shown). Values are plotted as mean ± SD from n = 4 experiments and the same N as in (C). *p<0.05, not significant not indicated by one-way ANOVA with Tukey's multiple comparisons post-test. Every mean was compared to every other mean. (E) Representative images of growth cones of hippocampal neurons from the indicated time points *in vitro*. Samples were stained with Phalloidin. Scale bar 5 µm. (F) Quantification of mean actin filament intensities in growth cones. The area for quantification was manually drawn around the growth cones based on Phalloidin staining. Values are plotted as mean ± SD from n = 4 experiments, with N = 322 (DIV 2), 307 (DIV 7) and 308 (DIV 14) individual growth cones measured in total. *p<0.05, not significant not indicated by one-way ANOVA with Tukey's multiple comparisons post-test. Each mean was compared to every other mean. (G) Quantification of growth cone area. Growth cone area was quantified by manually drawing the area of the growth cone based on Phalloidin staining. Values are plotted as mean ± SD from n = 4 experiments, with the same N as in (F). ****p<0.0001, *p<0.05 by one-way ANOVA with Tukey's multiple comparisons post-test. Every mean was compared to every other mean. (H) Representative western blot for G-/F-actin assay performed at the indicated time points. Blots were propped for pan-actin. Protein size is indicated in kilodalton (kDa). (I) Quantification for (H) of the relative F-/G-actin intensity. Values are plotted as mean ± SD from n = 5 experiments, with two replicas each (N = 10). ****p<0.0001, ***p<0.001, **p<0.01, *p<0.05, not significant not indicated by Kruskal-Wallis test with Dunn's multiple comparisons post-test.

Next, to assess whether a stabilisation of actin filaments contributes to a reduction in neuronal growth capacity, I analysed actin filament stability and turnover rate at the three different time points I described above. To investigate actin filament stability, I used the actin-manipulating drug Cyto D, which has been used in many previous studies to analyse actin functions in neuronal development (Allison et al., 1998; Bradke and Dotti, 1999; Forscher and Smith, 1988; Letourneau et al., 1987). Cytochalasins bind to the barbed end of actin filaments and thereby prevent the addition of new actin monomers and inhibit polymerisation (Figure 12A) (Cooper, 1987). At the same time, depolymerisation at the pointed end is still possible, and actin filaments are degraded over time. Depending on the current turnover rate and stability, the depolymerisation of actin filaments occurs at different rates.

To assess actin filament stability and turnover rates, I treated cultured neurons at the different time points for 10 minutes with 1 µM Cyto D or dimethyl sulfoxide (DMSO) as a control. After 10 minutes, neurons were immediately fixed and stained for F-actin with Phalloidin (Figure 12B). Quantification of F-actin intensity on a whole cell level showed no decrease upon Cyto D treatment at any of the time points (Figure 12B, C and D). When I looked at the growth cone specifically, Cyto D treatment led to a two-third reduction in actin filament intensity at DIV 2 (Figure 12E and F). Also, at DIV 7, the treatment with Cyto D decreased F-actin intensities. The effect at DIV 7 was not as strong as it was at DIV 2. At DIV 7, more actin filaments remained within the growth cone after 10 minutes of treatment (Figure 12E and F). In contrast, at DIV 14, the 10-minute treatment did not change F-actin intensities. This reduced decrease in actin filaments can be caused by either reduced depolymerisation at the pointed end or increased stabilisation of existing filaments.

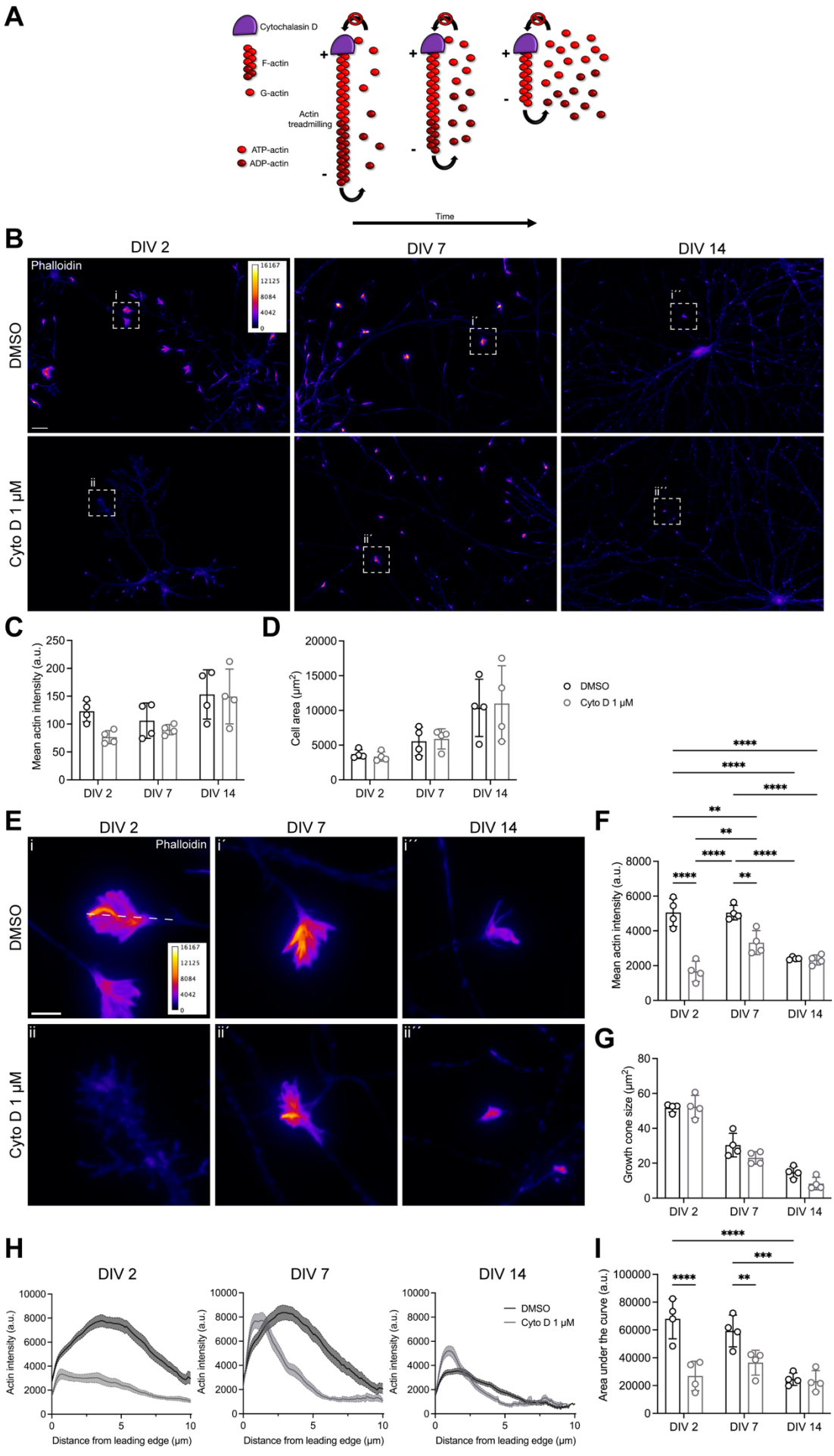
A
Cytochalasin D
F-actin
G-actin
Actin treadmilling
ATP-actin
ADP-actin
Time
B
DIV 2
DIV 7
DIV 14
Phalloidin
DMSO
Cyto D 1 µM
C
Mean actin intensity (a.u.)
D
Cell area (µm²)
DMSO
Cyto D 1 µM
E
F
Mean actin intensity (a.u.)
G
Growth cone size (µm²)
H
Actin intensity (a.u.)
Distance from leading edge (µm)
I
Area under the curve (a.u.)

Figure 12: Change in actin stability in growth cones of developing hippocampal neurons

(A) Scheme for the mechanism of action for the actin depolymerising drug Cytochalasin D (Cyto D). Cyto D binds to the barbed end (plus end) of filamentous actin and prevents the addition of new actin monomers to existing filaments. At the pointed end, depolymerisation is not disturbed, and actin filaments are degraded over time depending on depolymerisation rate and stability of the filaments. (B) Representative images of ROIs after treatment with either DMSO or 1 µM Cyto D for 10 minutes at the indicated time points. Neurons were stained with Phalloidin to visualise F-actin. Scale bar 20 µm. Insets are shown in (E). (C) Quantification for the mean F-actin intensity after treatment with DMSO or 1 µM Cyto D as shown in (B). Values are plotted as mean ± SD from n = 4 experiments, with N = 337 (DMSO, DIV 2), 334 (Cyto D, DIV 2), 321 (DMSO, DIV 7), 316 (Cyto D, DIV 7), 314 (DMSO, DIV 14) and 307 (Cyto D, DIV 14) ROIs quantified in total. ****p<0.0001, ***p<0.001, **p<0.01, *p<0.05, not significant not indicated by two-way ANOVA with Sidak's multiple comparison post-test. Every mean was compared to the mean within the same group (DMSO vs Cyto D). (D) Quantification for cell area in ROIs, as in (B). Cell area was quantified based on α-tubulin staining (not shown). Values are plotted as mean ± SD from n = 4 experiments, with N as in (C). ****p<0.0001, ***p<0.001, **p<0.01, *p<0.05, not significant not indicated by two-way ANOVA with Sidak's multiple comparison post-test. Every mean was compared to the mean within the same group (DMSO vs Cyto D). (E) Insets of representative growth cones of hippocampal neurons after treatment with DMSO or Cyto D as indicated from (B). Dashed line indicates the line scan from (H) and (I). Scale bar 5 µm. (F) Quantification of mean actin intensity in growth cones after treatment with DMSO or Cyto D as shown in (E). The area for quantification was manually drawn around the growth cones based on Phalloidin staining. Values are plotted as mean ± SD from n = 4 experiments, with N = 200 (DMSO DIV 2, Cyto D DIV 2, DMSO DIV 7, Cyto D DIV 7, DMSO DIV 14) and 199 (Cyto D DIV 14) individual growth cones quantified in total. ****p<0.0001, **p<0.01, not significant not indicated by two-way ANOVA with Tukey's multiple comparison post-test. Every mean was compared to every other mean. (G) Quantification for growth cone area of growth cones quantified in (F) based on Phalloidin staining. Values are plotted as mean ± SD from n = 4 experiments, with N like in (F). ****p<0.0001, ***p<0.001, **p<0.01, *p<0.05, not significant not indicated by two-way ANOVA with Sidak's multiple comparison post-test. Every mean was compared to the mean within the same group (DMSO vs. Cyto D). (H) Quantification of a line scan along the longitudinal axis of the growth cone from the leading edge to the neurite shaft, as indicated by the dashed line in (E). Values are plotted as mean ± SEM along the longitudinal axis of the growth cone in µm from n = 4 experiments, with N = 40 growth cones analysed in total. (I) Quantification for the area under the curve of a line scan, as in (H). The area under the curve was quantified for every individual experiment, with N = 10 growth cones quantified for each experiment and condition. Values are plotted as mean ± SD from n = 4 experiments. ****p<0.0001, ***p<0.001, **p<0.01, not significant not indicated by two-way ANOVA with Tukey's multiple comparison post-test. Every mean was compared to the mean within the same row and column (DMSO vs. Cyto D and DMSO DIV 2 vs. DIV 7 vs. DIV 14/ Cyto D DIV 2 vs. DIV 7 vs. DIV 14).

Similar to the previous experiment (Figure 11), control growth cones of DIV 2 and DIV 7 neurons had 50% higher F-actin intensity than DIV 14 growth cones (Figure 12F). The treatment with 1 µM Cyto D did not cause changes in growth cone area, indicating that there was no collapse of the growth cone at any of the time points (Figure 12G).

To examine where the actin filaments are lost within the growth cone, I performed a line scan from the leading edge towards the neurite shaft (dashed line) (Figure 12E). Analysis revealed that at DIV 2, actin filaments are depolymerised equally throughout the growth cone (Figure 12E and H). At DIV 7, the remaining actin filaments upon Cyto D treatment were present at the leading edge and peripheral domain, then show marked reduction towards the neurite shaft. F-actin intensity was equally distributed at DIV 14. Quantification of the area under the curve as a measure of F-actin amounts confirmed the previous quantification for the whole growth cone area (Figure 12F, H and I). These results clearly show that higher F-actin intensities were caused by reduced depolymerisation at the pointed end in the transition and central zone of the growth cone. The majority of longer filaments are oriented predominantly with their barbed end towards the leading edge (Lewis and Bridgman, 1992).

This actin stability assay showed that actin filament turnover or stability is already changed in DIV 7 neurons and even further at DIV 14. Thus, a reduction in turnover rates or increased actin filament stability was already observed when neurons exhibited the fastest growth rates at DIV 7 to DIV 10 (Figure 10C and Figure 12F). This would indicate that fast turnover of actin filaments is not *per se* required for fast axonal growth.

Change in dependence on actin polymerisation for neurite growth in the course of development

It seems that neurons at a later stage of development grow their axon undisturbed in the presence of more stable actin filaments or reduced actin turnover. To further verify this, I examined how neurons behave in response to more stable actin filaments. Therefore, I treated cultured neurons with the actin filament stabilising drug Jasp. To investigate the effect of actin stabilisation on neurite growth at different developmental stages, I designed the following treatment scheme: for the first group (early), the treatment was started 6 h after plating, and neurons were analysed at DIV 2 (Figure 13A). This enables investigation of the effect in early development when neurons form neurites and polarise. The second group (middle) was treated with Jasp after three days in culture and analysed at DIV 5 and DIV 7, respectively. At this time, neurons have polarised, and the young axon initiates its elongation. For the third group, cells were allowed to grow undisturbed in culture for seven days before the treatment was applied (late), allowing for investigation of later developmental stages (Figure 13A).

As expected, and in line with previous results (Flynn et al., 2012; Gallo et al., 2002), treatment of young neurons with 5 nM Jasp led to a reduction in neurite growth (Figure 13A, B and C). When I applied the same treatment to DIV 3 neurons that already had an axon, no growth reduction was observed (Figure 13D and E). Similarly, DIV 7 neurons showed no difference in the length of the longest neurite when treated for two days with 5 nM Jasp (Figure 13F and G). Once neurons were polarised, actin stabilisation did not affect axon growth.

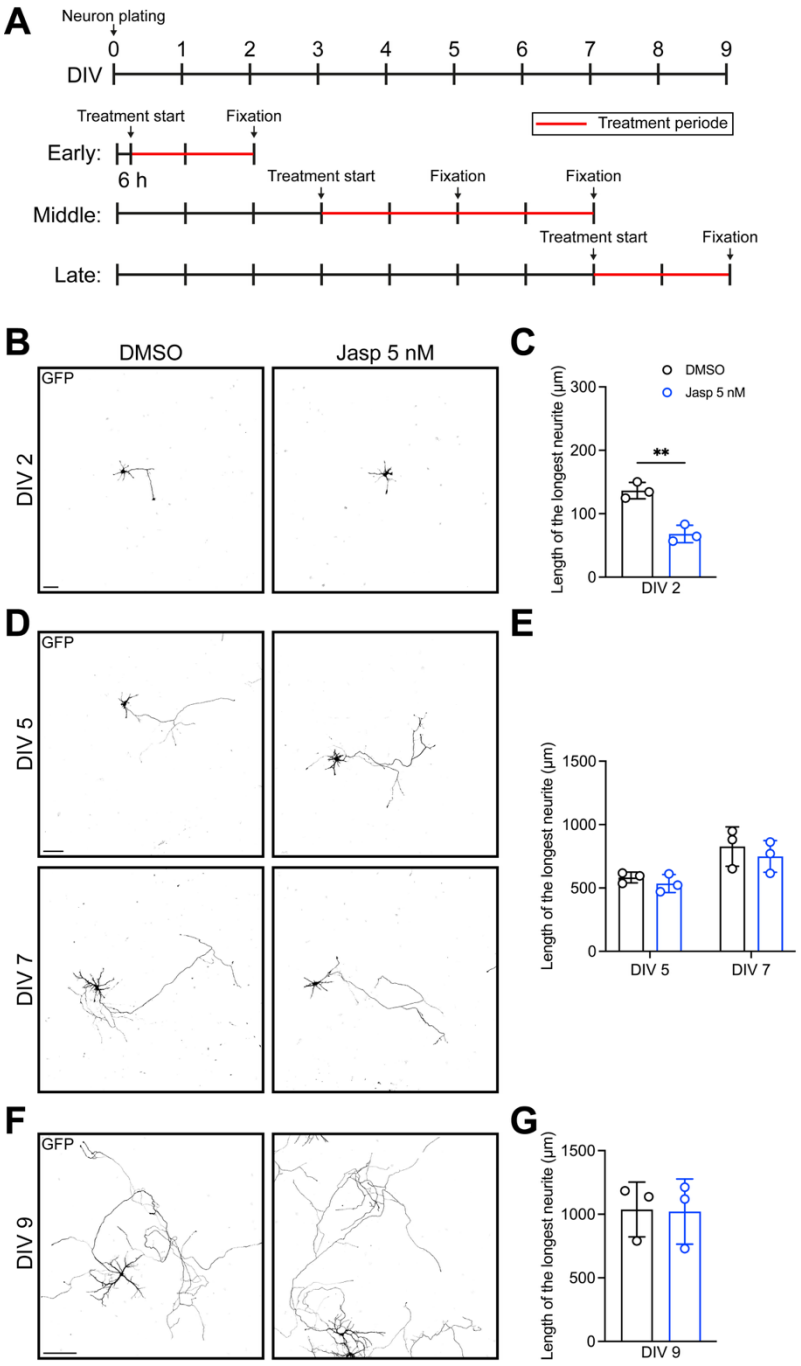

Figure 13: Stabilisation of actin filaments with Jasplakinolide only affects young neurons

(A) Treatment scheme for experiments to analyse the effect of cytoskeleton manipulating drugs on neuronal development at different time points. For analysis on effects in early stages neurons are treated 6 h after plating, and the effect was quantified on DIV 2. For analysis of effects on the middle stages, neurons are cultured undisturbed for three days. At DIV 3 the treatment is applied, and neurons are analysed after another two or four days in culture. For investigating effects on late development, neurons were cultured for seven days before the treatment was applied. Two days after treatment started, the cells were analysed. (B) Representative images of hippocampal neurons at DIV 2 after treatment with DMSO or 5 nM Jasplakinolide (Jasp). Samples were stained for GFP. Images were generated from stitched tiles. Scale bar 50 µm. (C) Quantification for the length of the longest neurite of neurons treated with either DMSO or 5 nM Jasp. Values are plotted as mean ± SD from n = 3 experiments, with N = 443 (DMSO) and 236 (Jasp 5 nM) individual neurons traced in total. **p<0.01 by unpaired two-tailed Student's t-test. (D) Representative images of hippocampal neurons at the indicated time points treated with either DMSO or 5 nM Jasp. Neurons were stained for GFP. Images were generated from stitched tiles. Scale bar 100 µm. (E) Quantification for the length of the longest neurite at the indicated time points for neurons with the indicated treatment. Values are plotted as mean ± SD from n = 3 experiments, with N = 556 (DMSO, DIV 5), 444 (Jasp 5 nM, DIV 5), 492 (DMSO, DIV 7), and 433 (Jasp 5 nM, DIV 7) individual neurons quantified. ****p<0.0001, ***p<0.001, **p<0.01, *p<0.05,

not significant not indicated by two-way ANOVA with Sidak's multiple comparison post-test. Every mean was compared to the other mean within the same group (DMSO vs. Jasp 5 nM). (F) Representative images of hippocampal neurons at DIV 9 treated for two days with DMSO or Jasp as indicated. Samples were stained for GFP. Images were created from stitched tiles. Scale bar 200 µm. (G) Quantification for the length of the longest neurite of neurons treated with DMSO or Jasp. Values are plotted as mean ± SD from n = 3 experiments, with N = 307 (DMSO) and 289 (Jasp) individual neurons traced in total. ****p<0.0001, ***p<0.001, **p<0.01, *p<0.05, not significant not indicated by unpaired two-tailed Student's t-test.

To investigate the function of more stable actin filaments at later stages of development, I depolymerised actin filaments at the different stages of development (Figure 13A). I decided to use low doses of actin polymerisation inhibitors as I reasoned that high doses may mask a potential differential effect on growth. When young neurons were treated with 10 nM and 50 nM Cyto D, respectively, I found that only the treatment with 10 nM led to enhanced neurite growth (Figure 14A and B). Inhibiting actin polymerisation with the higher dose of Cyto D caused shorter neurites. Treatment of DIV 3 neurons with the same concentrations caused a reduction in the length of the longest neurite for both conditions (Figure 14C and D). At DIV 7, the length of the longest neurite was not affected in any of the treatment groups (Figure 14E and F).

To validate the results observed for the effect of Cyto D treatment on neurite length, I performed the same experiments with Lat A. Lat A is also an actin depolymerising drug but works through a different mechanism of action, sequestering actin monomers (Coué et al., 1987). Here, I also used a lower (50 nM) and a higher (0.5 µM) concentration. Similar to the experiments with Cyto D, only the low concentration of Lat A enhanced neurite length in young neurons, while the higher concentration caused a reduction of the length of the longest neurite (Figure 15A and B). In the middle stage, both concentrations caused a decrease in the length of the longest neurite while the higher concentration seemed to have a slightly stronger growth reducing effect (Figure 15C and D). Treatment of late neurons showed no effect of 50 nM Lat A on the length of the longest neurite, similar to Cyto D treatments (Figure 14F and Figure 15E and F). Both actin filament manipulating drugs, with different mechanisms of action, revealed a similar phenotypic outcome (Figure 14 and Figure 15).

These experiments demonstrated a developmental change in the dependence on actin polymerisation and filaments of hippocampal neurons. In young neurons, a dynamic actin cytoskeleton is needed for neurite extension, but once an axon has formed, neuron growth is not inhibited by more stable actin filaments. This indicates that more stable actin filaments, *per se*, are unlikely to cause the developmental decline in neuron growth capacity. Further, it seems that the dependency on actin polymerisation and turnover for neurite growth changes once neurons have formed an axon. These observations raise two questions: what is the function of stabilised actin filaments and reduced actin turnover at the later stages of development, and how is the stabilisation and reduction in turnover regulated?

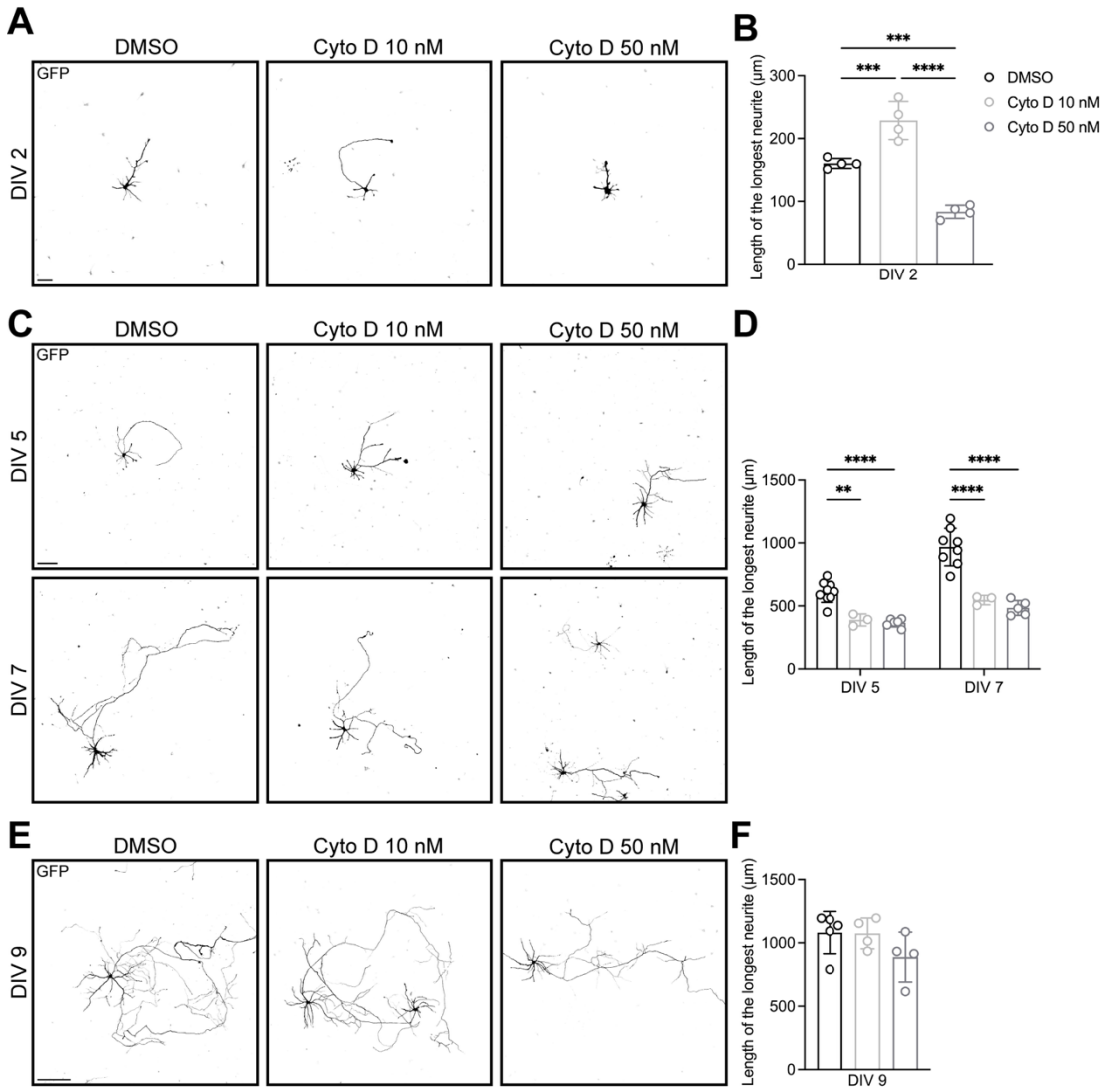

Figure 14: Actin depolymerisation differentially affects neurite length at different stages of development

(A) Representative images of DIV 2 neurons with the indicated treatment as indicated in Figure 13A. Samples were stained for GFP. Images were generated from stitched tile scans. Scale bar 50 µm. (B) Quantification of the length of the longest neurite for neurons in (A). Values are plotted as mean ± SD from n = 4 experiments, with N = 683 (DMSO), 582 (Cyto D 10 nM) and 464 (Cyto D 50 nM) neurons analysed in total. ****p<0.0001, ***p<0.001 by one-way ANOVA with Tukey's multiple comparison post-test. Each mean was compared to every other mean. (C) Representative images of hippocampal neurons at the indicated time points treated with either DMSO, 10 nM Cyto D or 50 nM Cyto D as indicated in Figure 13A. Neurons were stained for GFP. Images were created from stitched tiles. Scale bar 100 µm. (D) Quantification for the length of the longest neurite at the indicated time points for neurons with the indicated treatment. Values are plotted as mean ± SD from n ≧ 3 experiments, with N = 1461 (DMSO, DIV 5), 342 (Cyto D 10 nM, DIV 5), 1032 (Cyto D 50 nM, DIV 5), 1312 (DMSO, DIV 7), 365 (Cyto D 10 nM, DIV 7) and 925 (Cyto D 50 nM, DIV 7) individual neurons quantified in total. ****p<0.0001, **p<0.01, not significant not indicated by two-way ANOVA with Tukey's multiple comparison post-test. Every mean was compared to the other mean within the same group (DMSO vs. Cyto D 10 nM vs. Cyto D 50 nM). (E) Representative images of hippocampal neurons at DIV 9 treated for two days with DMSO, Cyto D 10 nM or Cyto D 50 nM as indicated. Samples were stained for GFP. Images were generated from stitched tiles. Scale bar 200 µm. (F) Quantification for the length of the longest neurite of neurons treated with DMSO or Cyto D. Values are plotted as mean ± SD from n ≧ 4 experiments, with N = 493 (DMSO), 388 (Cyto D 10 nM) and 408 (Cyto D 50 nM) individual neurons traced in total. ****p<0.0001, ***p<0.001, **p<0.01, *p<0.05, not significant not indicated by one-way ANOVA with Tukey's multiple comparison post-test. Each mean was compared with every other mean.

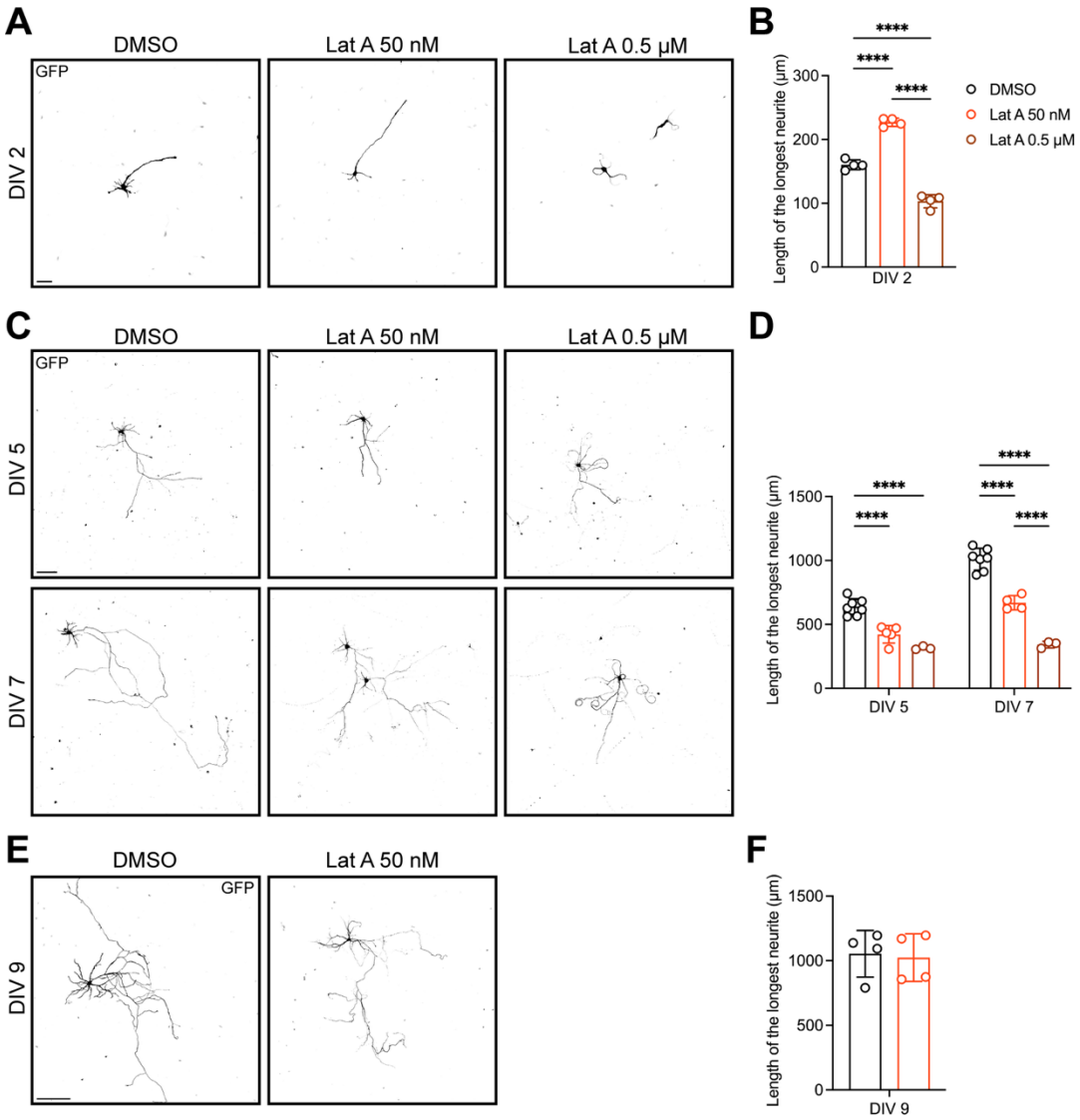

Figure 15: Actin depolymerisation with Latrunculin A differentially affects neurite length at different stages

(A) Representative images of neurons at DIV 2 with the indicated treatments and treatment time as indicated in Figure 13A. Samples were stained for GFP. Images were generated from stitched tile scans. Scale bar 50 µm. (B) Quantification of the length of the longest neurite for neurons in (A). Values are plotted as mean ± SD from n = 4 experiments, with N = 683 (DMSO), 614 (Lat A 50 nM) and 480 (Lat A 0.5 µM) neurons analysed in total. ****p<0.0001, by one-way ANOVA with Tukey's multiple comparison post-test. Each mean was compared to every other mean. (C) Representative images of hippocampal neurons at the indicated time points treated with either DMSO, 50 nM Lat A or 0.5 µM Lat A as indicated with the stated timeline as in Figure 13A. Neurons were stained for GFP. Images were created from stitched tiles. Scale bar 100 µm. (D) Quantification for the length of the longest neurite at the indicated time points for neurons with the indicated treatment. Values are plotted as mean ± SD from n ≧ 3 experiments, with N = 1247 (DMSO, DIV 5), 972 (Lat A 50 nM, DIV 5), 109 (Lat A 0.5 µM, DIV 5), 1005 (DMSO, DIV 7), 790 (Lat A 50 nM, DIV 7) and 68 (Lat A 0.5 µM, DIV 7) individual neurons quantified in total. ****p<0.0001, not significant not indicated by two-way ANOVA with Tukey's multiple comparison post-test. Every mean was compared to the other means within the same group (DMSO vs. Lat A 50 nM vs. Lat A 0.5 µM). (E) Representative images of hippocampal neurons at DIV 9 treated for two days with DMSO, Lat A 50 nM or Lat A 0.5 µM as indicated. Samples were stained for GFP. Images were generated from stitched tiles. Scale bar 200 µm. (F) Quantification for the length of the longest neurite of neurons treated with DMSO or Lat A as indicated. Values are plotted as mean ± SD from n = 4 experiments, with N = 374 (DMSO) and 311 (Lat A 50 nM) individual neurons traced in total. ****p<0.0001, ***p<0.001, **p<0.01, *p<0.05, not significant not indicated by unpaired two-tailed student's t-test.

Actin depolymerisation causes microtubule bundling defects in young neurons

Since similar treatments affect neurite growth differently at different developmental stages, I wanted to investigate the underlying effect. The tip of the neurite is the place where growth occurs. To better understand how actin depolymerising treatments differently affect neurite growth, I analysed the effect on the growth cones of treated neurons using high resolution imaging.

For this, cultured neurons were treated at 6 h, DIV 3 and DIV 7 with either 10 or 50 nM Cyto D or DMSO as a control for 18 h, respectively. After 18 h of treatment, neurons were fixed under conditions ideal for preservation of the cytoskeleton. In control conditions, the typical arrangement of actin filaments and microtubules in growth cones was observed (Figure 16A). From the neurite shaft, a bundle of microtubules enters the fan-like and actin-rich growth cone and starts to spread while single microtubules extend to the peripheral regions (Vitriol and Zheng, 2012). Growth cones of DIV 1 neurons treated with 10 nM Cyto D showed no changes in the growth cone organisation of actin filaments and microtubules. In contrast, growth cones of neurons treated with 50 nM Cyto D lose the growth cone neck, the clear separation of growth cone and axon shaft, which is accompanied by increased spread of microtubules reminiscent of a brushwood broom (Figure 16A). In the peripheral region, the actin cytoskeleton seemed to be undisturbed but did not exhibit the linear parallel arrangement of actin filament bundles compared to control growth cones. Further, the strict transition from neurite shaft to the growth cone area was lost, losing the clear separation between these two compartments (Figure 16A).

To quantify the spread of microtubules along the longitudinal axis of the growth cone, I used an ImageJ (Schindelin et al., 2012) plugin developed to analyse diameters of blood vessels, called VasoMetrics (McDowell et al., 2021). Quantification of microtubule spread along the longitudinal axis confirmed the impression of increased spreading of microtubules in growth cones treated with 50 nM Cyto D (Figure 16A, B and C). Microtubules were more spread within the growth cone, but also started to unbundle further away from the leading edge compared to the control (Figure 16B). In contrast, when treated with 10 nM Cyto D, microtubule spread quantification revealed an increase in microtubule bundling. When I looked at growth cones of DIV 4 neurons, both concentrations of Cyto D caused increased spreading and debundling of microtubules (Figure 16A, D and E). The extent of microtubule debundling seemed to be concentration dependent at this stage. Similar to DIV 1, treatment with 50 nM Cyto D led to the loss of a clear separation of the neurite shaft and growth cone area. No effect on microtubule debundling upon Cyto D treatment was observed in DIV 8 neurons, though the organisation of the actin cytoskeleton seemed to be disturbed (Figure 16A, F and G).

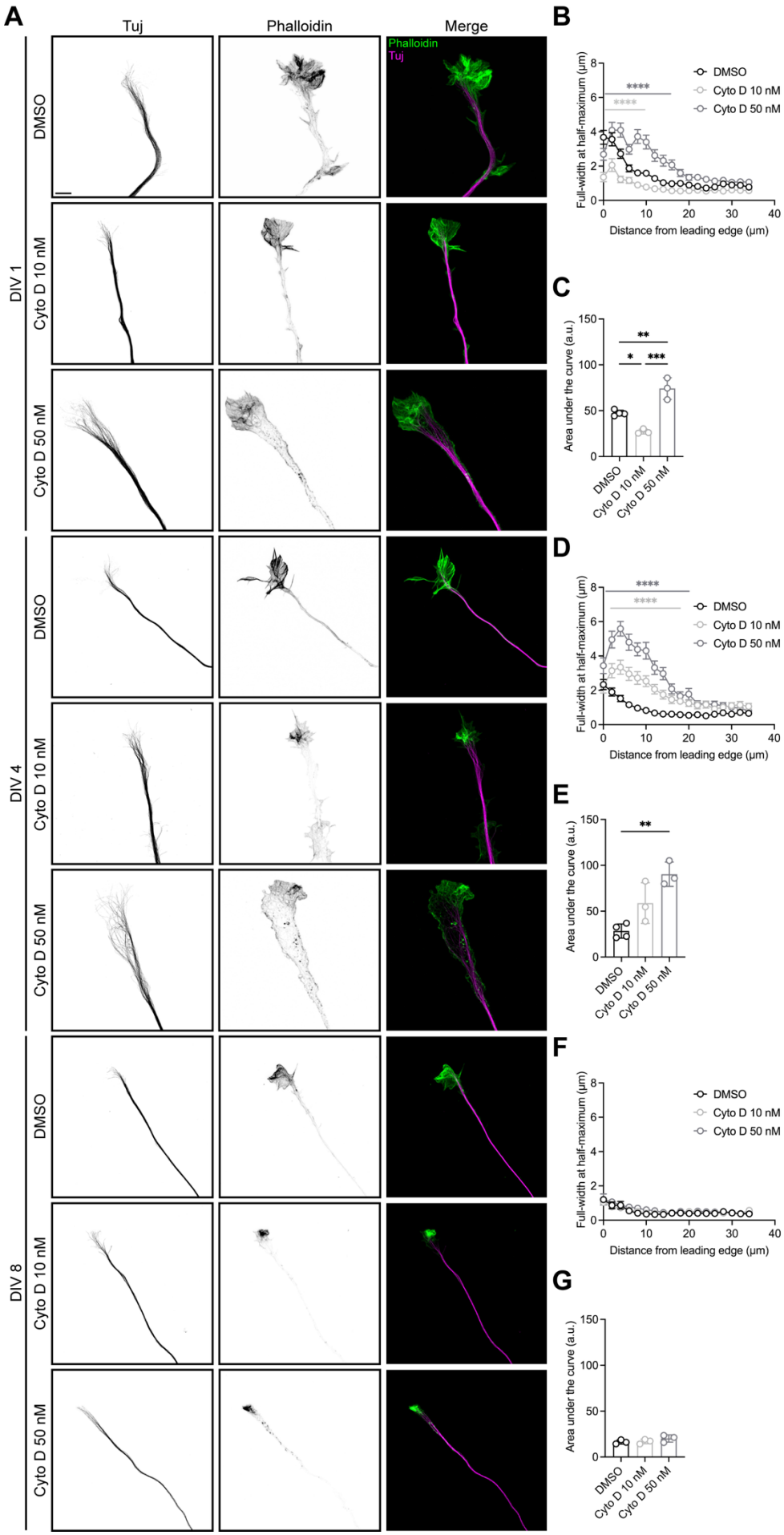
A
Tuj
Phalloidin
Merge
Phalloidin
Tuj
DIV 1
DIV 4
DIV 8
DMSO
Cyto D 10 nM
Cyto D 50 nM
B
Full-width at half-maximum (µm)
Distance from leading edge (µm)
DMSO
Cyto D 10 nM
Cyto D 50 nM
****
****
C
Area under the curve (a.u.)
**
*
***
D
Full-width at half-maximum (µm)
Distance from leading edge (µm)
****
****
E
Area under the curve (a.u.)
**
F
Full-width at half-maximum (µm)
Distance from leading edge (µm)
G
Area under the curve (a.u.)

Figure 16: Actin destabilisation causes microtubule bundling defects.

(A) Representative images of high-resolution scans of growth cones at the indicated DIVs after 18 h with the indicated treatments stained for F-actin with Phalloidin and Tuj. Scale bar 5 µm. (B) Quantification for microtubule bundling of DIV 1 growth cones. Microtubule bundling is quantified in 2 µm steps as the full-width at half-maximum intensity (of Tuj) along the longitudinal axis of the growth cone from the leading edge to the neurite shaft. Values are plotted as mean ± SEM from n = 3 experiments, with N = 35 (DMSO), 26 (Cyto D 10 nM), and 30 (Cyto D 50 nM) individual growth cones analysed in total. ****p<0.0001, not significant not indicated by two-way ANOVA with Dunnett's multiple comparison post-test. Simple effects within rows were compared with the control group (DMSO) only. Simplified depiction of significant differences. (C) Quantification of the area under the curve, as in (B), for every independent experiment representing the overall extent of microtubule debundling. Values are plotted as mean ± SD for n = 3 experiments. ***p<0.001, **p<0.01, *p<0.05 by one-way ANOVA with Tukey's multiple comparison post-test. Each mean was compared with every other mean. (D) Quantification for microtubule bundling of DIV 4 growth cones. Microtubule bundling is quantified in 2 µm steps as the full-width at half-maximum intensity (of Tuj) along the longitudinal axis of the growth cone from the leading edge to the neurite shaft. Values are plotted as mean ± SEM from n = 3 experiments, with N = 43 (DMSO), 31 (Cyto D 10 nM), and 33 (Cyto D 50 nM) individual growth cones analysed in total. ****p<0.0001, not significant not indicated by two-way ANOVA with Dunnett's multiple comparison post-test. Simple effects within rows were compared to the control group (DMSO) only. Simplified depiction of significant differences. (E) Quantification of the area under the curve, as in (D), for every independent experiment representing the overall extent of microtubule debundling. Values are plotted as mean ± SD for n = 3 experiments. **p<0.01, not significant not indicated by one-way ANOVA with Tukey's multiple comparison post-test. Each mean was compared with every other mean. (F) Quantification for microtubule bundling of DIV 8 growth cones. Microtubule bundling is quantified in 2 µm steps as the full-width at half-maximum intensity (of Tuj) along the longitudinal axis of the growth cone from the leading edge to the neurite shaft. Values are plotted as mean ± SEM from n = 3 experiments, with N = 29 (DMSO, Cyto D 10 nM and Cyto D 50 nM) individual growth cones for each condition analysed in total. Not significant not indicated by two-way ANOVA with Dunnett's multiple comparison post-test. Simple effects within rows were compared to the control group (DMSO) only. Simplified depiction of significant differences. (G) Quantification of the area under the curve, as in (F), for every independent experiment representing the overall extent of microtubule debundling. Values are plotted as mean ± SD for n = 3 experiments. Not significant not indicated by one-way ANOVA with Tukey's multiple comparison post-test. Each mean was compared with every other mean.

To quantify changes in the actin cytoskeleton and the protrusion depths of microtubules towards the leading edge upon Cyto D treatment, I performed line scans from the leading edge towards the neurite shaft (Figure 17A). Due to high variations in actin intensity across the independent experiments, I did not detect changes in overall actin intensity between control and Cyto D-treated growth cones at any of the time points (Figure 17C). Looking at the distribution of actin filaments in the growth cones, I observed that 50 nM Cyto D did not change actin filament intensity in the peripheral growth cone area but led to an earlier decrease of actin filament intensity in the transition- and central domains of the growth cones compared to control (Figure 17B). Treatment with 10 nM Cyto D even increased the abundance of F-actin in the area closest to the leading edge, and then showed a mark and faster decrease towards the T- and C-domains compared to the control.

Since the actin cytoskeleton restricts microtubules from entering the peripheral growth cone area (Dupraz et al., 2019; Lowery and Van Vactor, 2009; Santos et al., 2020), I also looked at changes in tubulin abundance after Cyto D treatment close to the leading edge (Figure 17D). Growth cones of DIV 1 neurons treated with 10 nM Cyto D showed higher tubulin intensity closer to the leading edge compared to control. Treatment with 50 nM Cyto D did not change tubulin intensity at this stage but was reduced in growth cones of DIV 4 neurons. In DIV 8 neurons, no change in tubulin intensity in comparison to the control was observed (Figure 17D).

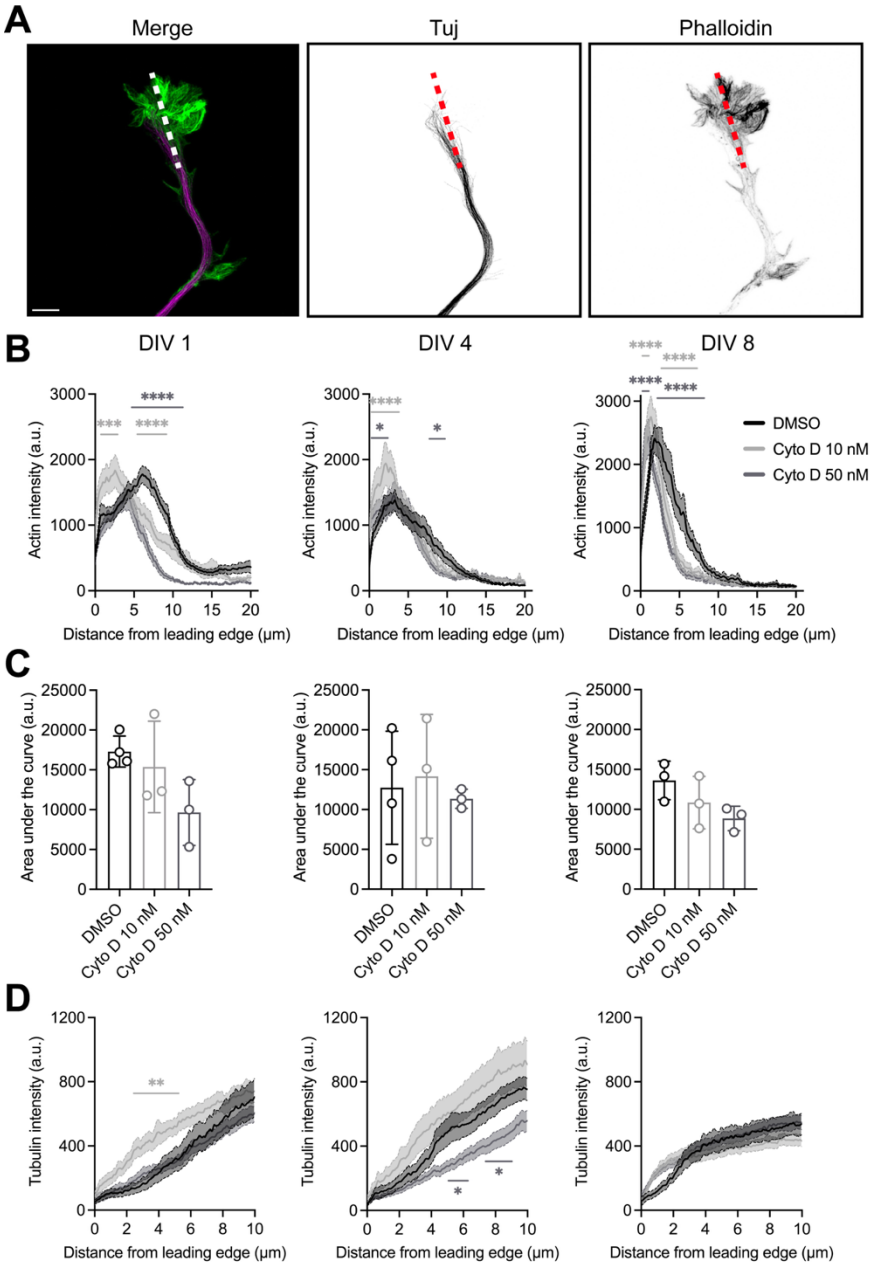

Figure 17: Actin and tubulin properties in growth cones of Cyto D treated neurons at different developmental stages

(A) Representative image of a growth cone (same growth cone as in Figure 8A, DIV 1, DMSO). The dashed line indicates how the intensity pattern along the longitudinal axis of the growth cone from the leading edge to the neurite shaft was measured. A line width of 100 pixels was used for all measurements. The leading edge was defined based on Phalloidin staining. Scale bar 5 µm. (B) Actin intensity along the longitudinal axis of the growth cone from the leading edge towards the neurite shaft was quantified for growth cones at DIV 1, DIV 4 and DIV 8 as indicated. Values are plotted as mean ± SEM from n = 3 experiments, with the same N as in Figure 16. ****p<0.0001, ***p<0.001, *p<0.05, not significant not indicated by two-way ANOVA with Tukey's multiple comparison post-test. Simple effects within rows were compared with every group. Simplified depiction of significant differences between control (DMSO) and treatment groups (Cyto D). (C) Quantification for the area under the curve as a measure of overall actin intensity from (B). Values are plotted as mean ± SD from n = 3 independent experiments, with the same N as in (B). Not significant not indicated by one-way ANOVA with Tukey's multiple comparison post-test. Each mean was compared with every other mean. (D) Tubulin intensity along the longitudinal axis of growth cones at the indicated time points from the leading edge towards the neurite shaft. Values are plotted as mean ± SEM from n = 3 independent experiments, with the same N as in (B). **p<0.01, *p<0.05, not significant not indicated by two-way ANOVA with Dunnett's multiple comparison post-test. Simple effects within rows were compared to the control group (DMSO) only. Simplified depiction of significant differences.

Additionally, I observed that over time, microtubules became more and more bundled in control growth cones (Figure 18A, B and C).

To evaluate the effect of Cyto D treatment in living cells, I treated DIV 3 neurons with 50 nM Cyto D or DMSO 18 h before imaging. For visualisation of microtubule dynamics, neurons were transfected with the plus-end marker EB3 (Figure 19A). Analysis of EB3 comet dynamics was done with the u-track software of the Danuser lab (Jaqaman et al., 2008). While the overall number of detected EB3 comets in growth cones remained unchanged, comets in Cyto D-treated cells showed an increase in growth speed (Figure 19A and B). Since the lifetimes of these comets were unchanged between the two groups, the growth length of EB3 in Cyto D-treated cells was higher due to increased speed. Maximum intensity projection was used to visualise microtubule tracks for quantification of microtubule bundling (Figure 19A, C and D). Similar to fixed neurons, microtubule tracks in Cyto D-treated live growth cones appeared unbundled and disorganised.

Overall, the observed effect on microtubule bundling upon Cyto D treatment can explain the previously observed differences in neurite growth at different developmental stages (Figure 14 and Figure 16). When microtubules are bundled together, growth rates increase, while scattered and unbundled microtubules lead to decreased growth rates.

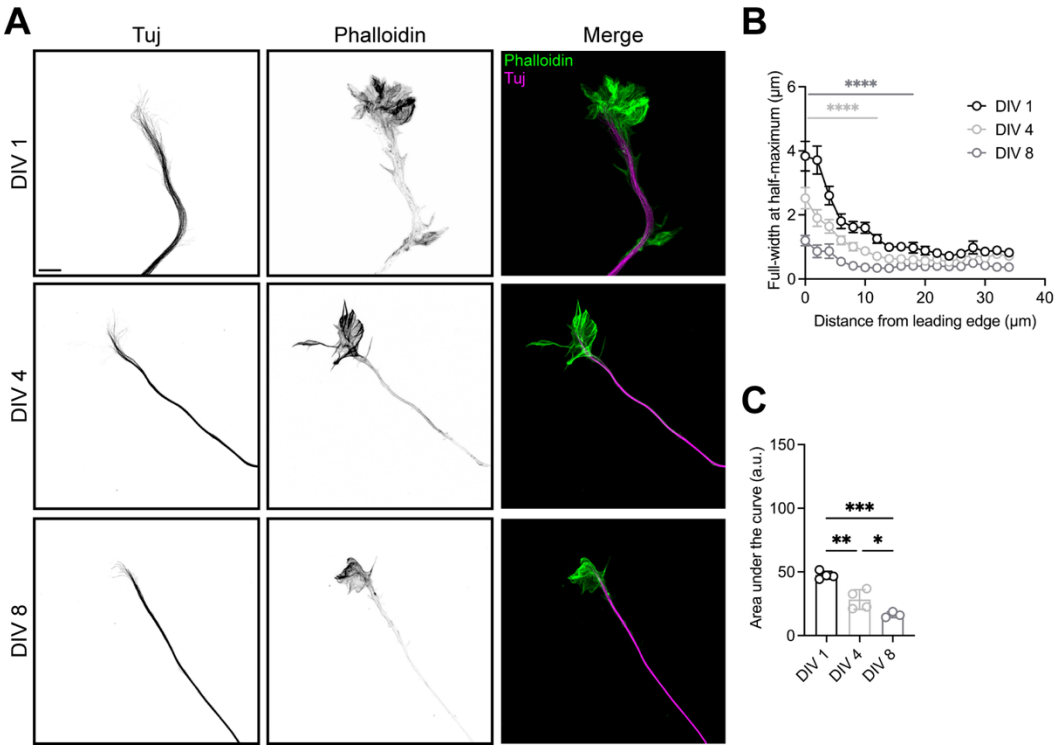

Figure 18: Microtubules are more bundled over time in developing neurons

(A) Representative images of growth cones from the indicated time points stained with Phalloidin for F-actin and Tuj. Same images as DMSO controls in Figure 16A. Scale bar 5 µm. (B) Quantification for microtubule debundling. The full-width at half-maximum intensity of Tuj was used as a readout for the spreading of microtubules from the leading edge along the longitudinal axis of the growth cone to the neurite shaft. Same data as DMSO groups of different time points in Figure 16. Values are plotted as mean ± SEM from n ≧ 3 independent experiments, with N = 28 (DIV 1), 35 (DIV 4) and 29 (DIV 8) growth cones quantified in total. ****p<0.0001, not significant not indicated by two-way ANOVA with Dunnett's multiple comparison post-test. Simple effects within rows were compared to DIV 1 only. Simplified depiction of significant differences. (C)

Quantification for the area under the curve as a measure of the extent of microtubule debundling in (B). Values are plotted as mean ± from n ≧ 3 independent experiments with the same N as in (B). ***p<0.001, **p<0.01, *p<0.05 by one-way ANOVA with Tukey's multiple comparison post-test. Each mean was compared with every other mean.

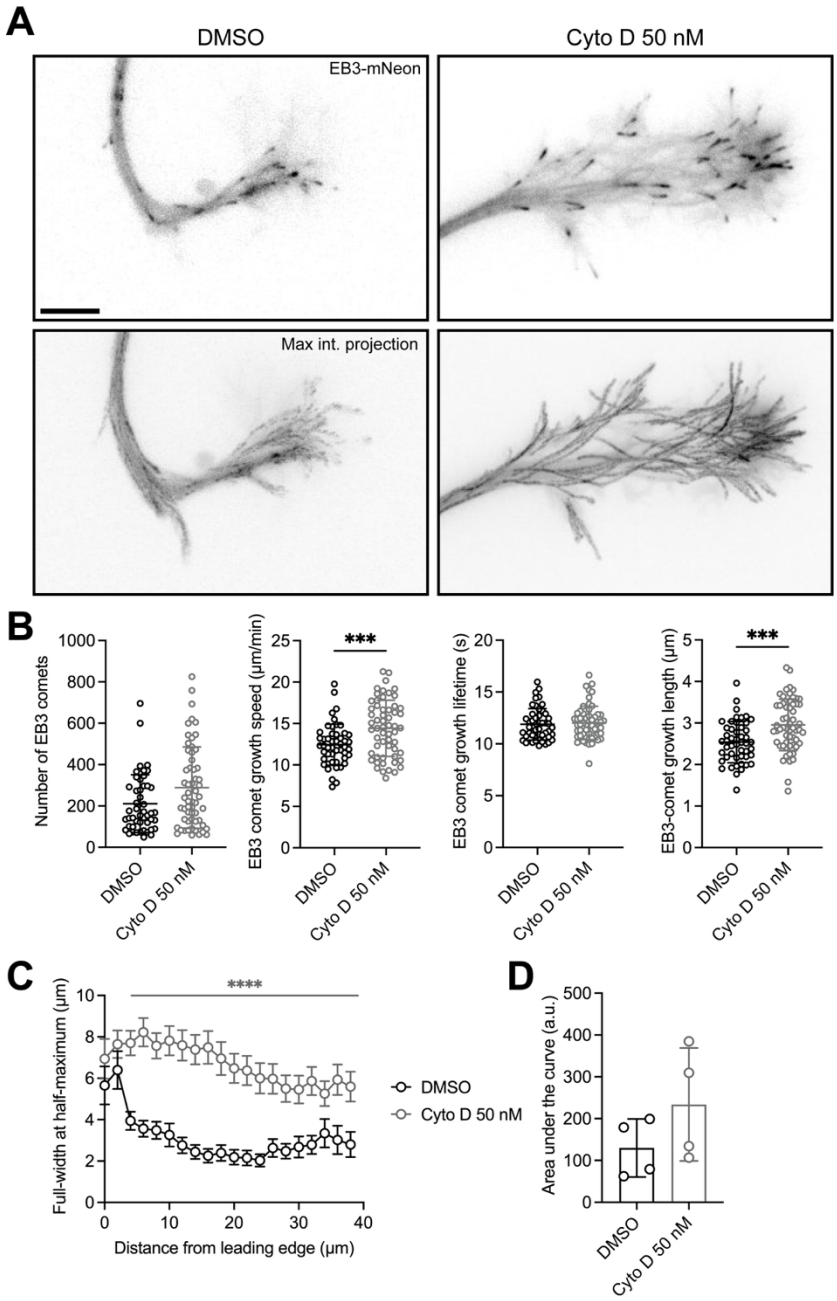

Figure 19: Cyto D-treated neurons have higher growth speed of EB3-comets and also show microtubule debundling

(A) Representative growth cones of neurons at DIV 4 imaged for microtubule dynamics with microtubule plus-end binding protein EB3 expression. The upper part is a single frame of a two-minute imaging with an image taken every two seconds. 18 h before imaging, neurons were treated with either DMSO or 50 nM Cyto D. The lower part shows the maximum intensity projection of the full two-minute video collapsed to a single frame showing EB3 tracks. Scale bar 5 µm. (B) Quantification of microtubule plus-end binding protein EB3 dynamics with the u-track software of the Danuser lab (Jaqaman et al., 2008). Shown are the number of detected EB3 comets, EB3 comet growth speed (µm/min), EB3 comet growth life time (s) and EB3 comet growth length (µm) for DMSO as well as Cyto D (50 nM) treated neurons. Values are plotted es means ± SD from n = 3 independent experiments, with N = 49 (DMSO) and 58 (Cyto D) analysed growth cones in total. ***p<0.001, not significant not indicated by Mann-Whitney test for the number of EB3 comets and EB3 comet lifetime, and unpaired two-tailed student's t-test for EB3 comet growth speed and EB3 comet growth length. (C) Quantification for the extent of microtubule debundling upon Cyto D treatment. Maximum intensity projections of EB comet tracks like in (A) were quantified for the full-width at half-maximum intensity of EB3 comet tracks

from the leading edge to the neurite shaft. Values are plotted as mean ± SEM from n = 4 experiments, with N = 54 (DMSO) and 63 (Cyto D) maximum intensity projections analysed in total. ****p<0.0001, not significant not indicated by two-way ANOVA with Sidak's multiple comparison post-test. Simplified depiction of significant differences. (D) Quantification of the area under the curve as a measure for the extent of microtubule debundling based on EB3 comet tracks in (A). Values are plotted as mean ± SD from n = 4 independent experiments with the same N as in (C). Not significant not indicated by unpaired two-tailed Student's t-test.

Stabilisation of microtubules fails to rescue the growth defect

Microtubules provide the force to push the growing neurite tip forward (Franze, 2020). When microtubules are bundled together, the pushing force of each individual microtubule, up to 3-5 pN, can linearly add up (Franze, 2020; Laan et al., 2008). In this way, increased bundling may provide a higher pushing force, allowing neurites to grow faster. This is reflected by my results, which show increased neurite length when neurites exhibit more bundled microtubules and reduced length when microtubules are dispersed (Figure 14 and Figure 16). When microtubules are unbundled upon Cyto D treatment, the pushing force of each microtubule is spread over a larger area, reducing neurite growth. Stabilisation of microtubules is sufficient to enhance neurite growth (Witte et al., 2008). Is stabilisation of microtubules also sufficient to rescue the actin depolymerisation mediated growth defect?

Furthermore, myosin-II activity supports the bundling of growing microtubules in the growth cone neck by lateral movement of actin arcs in *Aplysia* bag cell neurons (Burnette et al., 2008). Inhibition of myosin-II with Blebb causes unbundling of microtubules. On the other hand, myosin-II activity inhibits microtubule penetration in the peripheral growth cone domain by the formation of actin arcs, reducing neurite growth (Dupraz et al., 2019).

To examine whether stabilisation of microtubules is sufficient to rescue reduced growth and to analyse a potential contribution of myosin-II in bundling of microtubules, I combined the treatment of Cyto D with either Taxol or Blebb. Neurons were treated 6 h after plating with 50 nM Cyto D or with a combination of Cyto D with either 1 nM Taxol or 0.5 µM Blebb. Every 24 h, a sample was fixed and the length of the longest neurite quantified. After 72 h in culture, stabilisation of microtubules with 1 nM Taxol was not sufficient to compensate for the Cyto D-mediated growth defect (Figure 20A and B). In contrast, inhibition of myosin-II with Blebb restored neurite growth, and neurite length was similar to control.

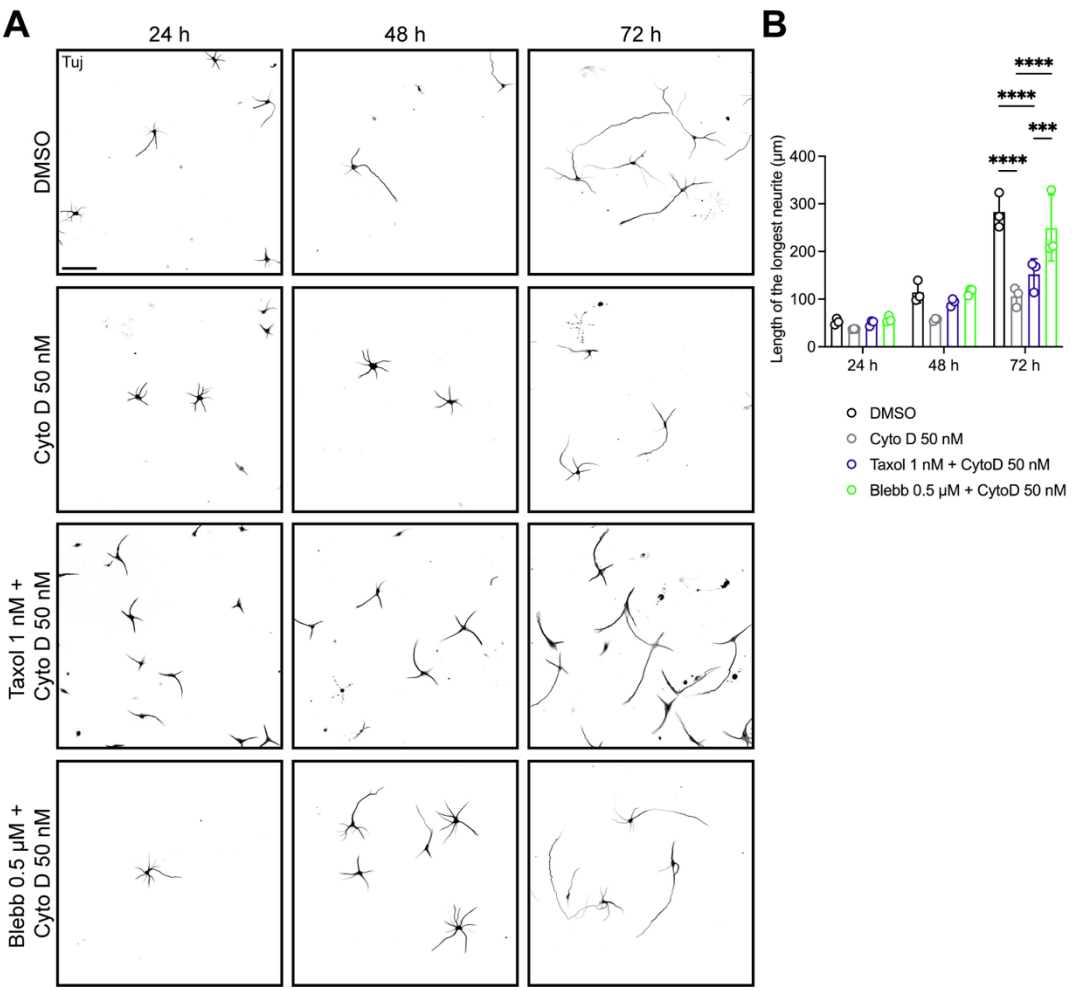

Figure 20: Inhibition of Myosin-II rescues actin depolymerisation based growth reduction

(A) Representative images of hippocampal neurons at the indicated time points with the shown treatments. Treatments were applied 6 h after plating, and cells were fixed every 24 h after plating for 72 h in total. Neurons were stained for Tuj. Images were generated from stitched tiles. Scale bar 100 µm. (B) Quantification for the length of the longest neurite. Values are plotted as mean ± SD from n = 3 independent experiments, with N = 695 (DMSO), 661 (Cyto D 50 nM), 589 (Taxol 1 nM + Cyto D 50 nM), 695 (Blebb 0.5 µM + Cyto D 50 nM) for 24 h, 719 (DMSO), 551 (Cyto D 50 nM), 735 (Taxol 1 nM + Cyto D 50 nM), 600 (Blebb 0.5 µM + Cyto D 50 nM) for 48 h, and 590 (DMSO), 617 (Cyto D 50 nM), 666 (Taxol 1 nM + Cyto D 50 nM), 557 (Blebb 0.5 µM + Cyto D 50 nM) for 72 h individual neurons analysed in total. ****p<0.0001, ***p<0.001, not significant not indicated by two-way ANOVA with Tukey's multiple comparison post-test. Simple effects within rows were analysed and each mean was compared to every other mean in the same group (DMSO vs. Cyto D 50 nM vs. Taxol 1 nM + Cyto D 50 nM vs. Blebb 0.5 µM + Cyto D 50 nM).

To understand how Blebb treatment rescued neurite growth while Taxol failed, I analysed growth cones of the different treatment groups with high resolution imaging (Figure 21A). Similar to previous experiments, treatment with Cyto D resulted in a splitting up of microtubule bundles along the neurite shaft and loss of the typical growth cone architecture (Figure 21A, B and C). Also, growth cones treated with a combination of Cyto D and Taxol exhibited this morphology of a missing growth cone architecture and massively dispersed microtubules. In contrast to the previous report where myosin-II inhibition increased microtubule unbundling in *Aplysia* bag cell neurons (Burnette et al., 2008), here I found the opposite effect. When treated with Blebb in addition to Cyto D,

microtubules remained bundled, similar to control conditions and the neurite was tipped with an actin-rich structure (Figure 21A, B and C).

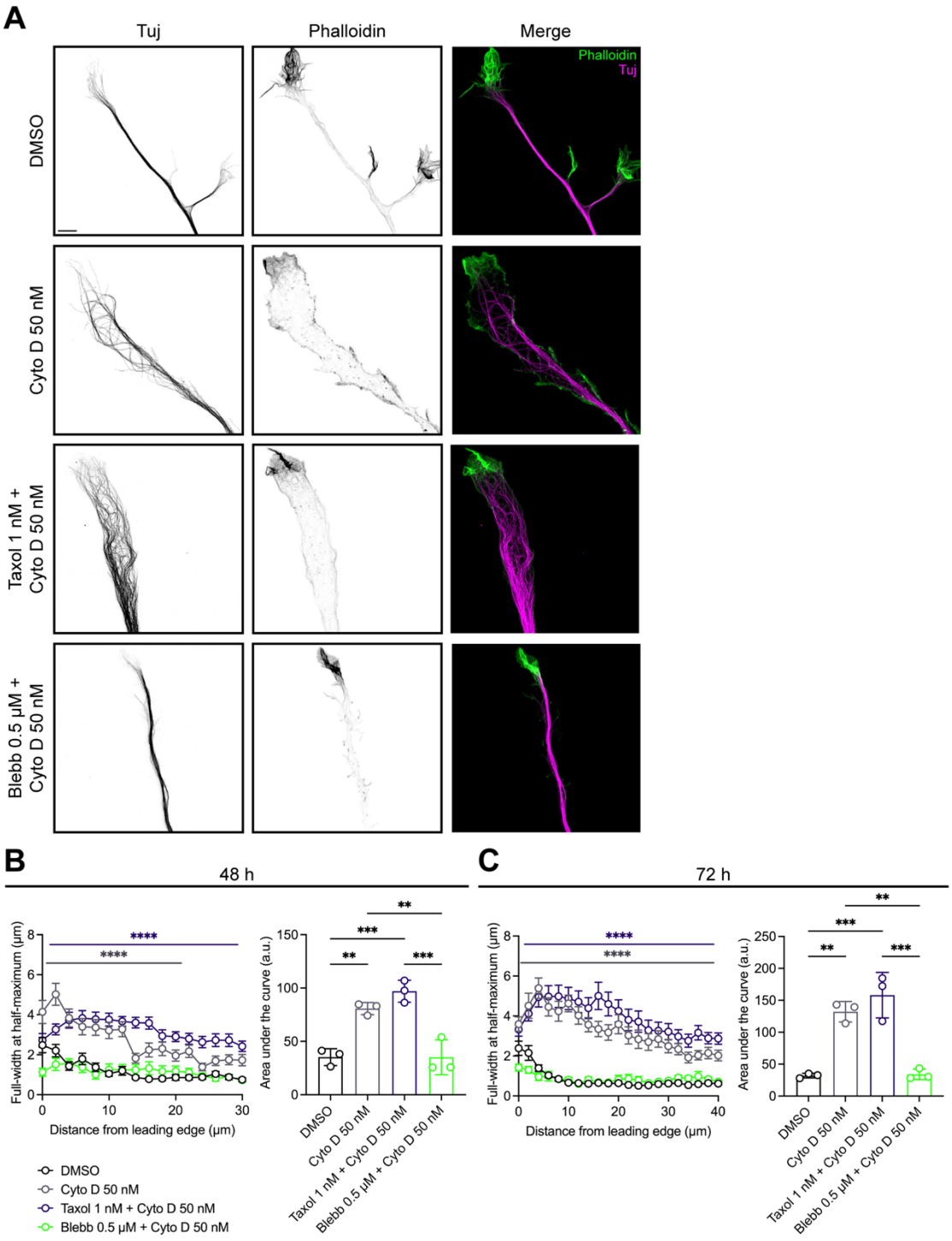

Figure 21: Blebbistatin prevents debundling of microtubules

(A) Representative high-resolution images of growth cones 48 h after plating. Neurons were treated with the indicated drugs 6 h after plating. Samples were stained for Tuj and F-actin with Phalloidin. Scale bar 5 µm. (B) Left, quantification for microtubule bundling of growth cones 48 h after plating. Microtubule bundling is quantified in 2 µm steps as the full-width at half-maximum intensity of Tuj along the longitudinal axis of the growth cone from the leading edge to the neurite shaft. Values are plotted as mean ± SEM from n = 3 experiments, with N = 24 (for each condition) individual growth cones analysed in total. ****p<0.0001, not significant not indicated by two-way ANOVA with Dunnett's multiple comparison post-test. Simple effects within rows were compared to the control group (DMSO) only. Simplified depiction of significant differences. Right, quantification of the area under the curve for the left plot. The area under the curve was quantified for every independent experiment representing the overall extent of microtubule debundling. Values are plotted as mean

± SD for n = 3 experiments and the same N as in the left plot. ***p<0.001, **p<0.01, not significant not indicated by one-way ANOVA with Tukey's multiple comparison post-test. Each mean was compared with every other mean. (C) Left, quantification for microtubule bundling of growth cones 72 h after plating. Microtubule bundling is quantified in 2 µm steps as the full-width at half-maximum intensity of Tuj along the longitudinal axis of the growth cone from the leading edge to the neurite shaft. Values are plotted as mean ± SEM from n = 3 experiments, with N = 24 (for each condition) individual growth cones analysed in total. ****p<0.0001, not significant not indicated by two-way ANOVA with Dunnett's multiple comparison post-test. Simple effects within rows were compared to the control group (DMSO) only. Simplified depiction of significant differences. Right, quantification of the area under the curve for the left plot. The area under the curve was quantified for every independent experiment representing the overall extent of microtubule debundling. Values are plotted as mean ± SD for n = 3 experiments and the same N as in the left plot. ***p<0.001, **p<0.01, not significant not indicated by one-way ANOVA with Tukey's multiple comparison post-test. Each mean was compared with every other mean.

In addition, I also analysed the tubulin intensity along the longitudinal axis of the neurite (Figure 22A). Indeed, quantification of the tubulin intensity after 72 h, revealed increased tubulin intensity along the neurite shaft when neurons were treated with 1 nM Taxol (Figure 22A and C). Since Taxol is a well-known microtubule stabilising compound (Schiff and Horwitz, 1980), it is not surprising that tubulin intensity is increased (Figure 22C). However, this increase in microtubules was not sufficient to restore normal growth rates when microtubules do not exert their pushing forces in a joint bundle. In line, the growth-enhancing effect of Taxol was blocked when actin polymerisation was inhibited at the same time (Figure 23B and D). The same was the case for Blebb. Inhibition of actin polymerisation by Cyto D reduced the growth-promoting effect of Blebb to control levels (Figure 23A and C). This shows that both treatments, which are known to enhance neurite length, depend on an undisturbed actin cytoskeleton at least in early stages of neuronal development (Dupraz et al., 2019; Witte et al., 2008).

To test whether stabilisation of microtubules can rescue growth defects in neurons that have already formed an axon (Figure 14C and D, Figure 15C and D), I treated DIV 3 neurons with Lat A and Taxol (Figure 24A and B). Similar to before, neurons were treated at DIV 3 (Figure 13A). After two or four days in culture, the length of the longest neurite was analysed. Like in young neurons, the stabilisation of microtubules with Taxol failed to restore neurite growth upon actin depolymerisation, also at this stage of development (Figure 24A and B). This indicates that also when neurons have polarised and extend the young axon, fast axonal elongation depends on actin filament polymerisation.

While the respective treatments in young neurons enhance neurite growth, the combination of both treatments did not change neurite length any further (Figure 24C and D). Either microtubule stabilisation or actin depolymerisation with a low dose is sufficient to overcome growth inhibition in young neurons. A combination of both did not lead to an additive or synergistic effect. On the other hand, both cytoskeleton components are required to function properly to maintain neurite growth in hippocampal neurons.

In addition, stabilisation of microtubules enhances neurite growth in young neurons (Figure 24D) (Witte et al., 2008). The same treatment did not enhance neurite length any further in DIV 3 neurons (Figure 23D and Figure 24B).

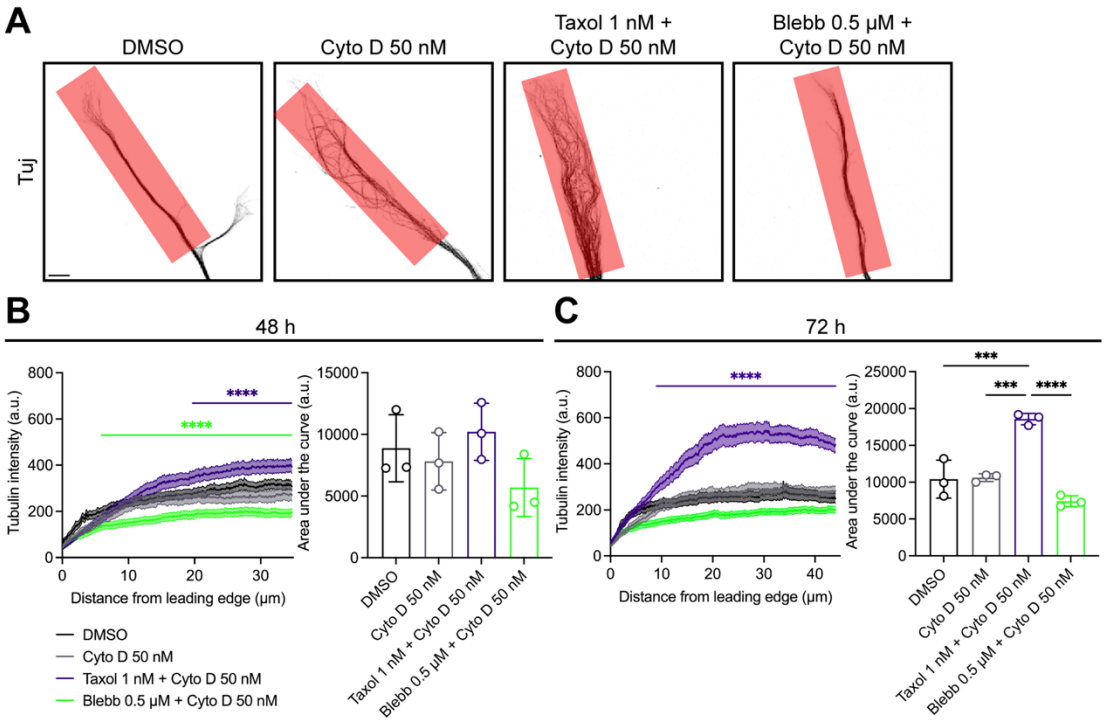

Figure 22: Increased Tubulin intensity in Taxol treated neurons

(A) Representative high-resolution images of growth cones 48 h after plating stained for Tuj. Neurons were treated with the indicated drugs 6 h after plating. Same images as in Figure 21. Red bars indicate the line scan performed to analyse tubulin intensity along the longitudinal axis of the growth cones (line width 250 pixels). Scale bar 5 µm. (B) Left, quantification of tubulin intensity along the longitudinal axis of the growth cone from the leading edge to the neurite shaft for growth cones fixed 48 h after plating. Values are plotted as mean ± SEM from n = 3 experiments, with N = 24 (for each condition) individual growth cones analysed in total. ****p<0.0001, not significant not indicated by two-way ANOVA with Dunnett's multiple comparison post-test. Simple effects within rows were compared to the control group (DMSO) only. Simplified depiction of significant differences. Right, quantification for the area under the curve for the left plot of tubulin intensity. The area under the curve was quantified for every independent experiment. Values are plotted as mean ± SD from n = 3 independent experiments with the same N as in the left plot. Not significant not indicated by one-way ANOVA with Tukey's multiple comparison post-test. Each mean was compared with every other mean. (C) Left, quantification of tubulin intensity along the longitudinal axis of the growth cone from the leading edge to the neurite shaft for growth cones fixed 72 h after plating. Values are plotted as mean ± SEM from n = 3 experiments, with N = 24 (for each condition) individual growth cones analysed in total. ****p<0.0001, not significant not indicated by two-way ANOVA with Dunnett's multiple comparison post-test. Simple effects within rows were compared to the control group (DMSO) only. Simplified depiction of significant differences. Right, quantification for the area under the curve for the left plot of tubulin intensity. The area under the curve was quantified for every independent experiment. Values are plotted as mean ± SD from n = 3 independent experiments with the same N as in the left plot. Not significant not indicated by one-way ANOVA with Tukey's multiple comparison post-test. Each mean was compared with every other mean. ****p<0.0001, ***p<0.001, not significant not indicated by one-way ANOVA with Tukey's multiple comparison post-test. Each mean was compared with every other mean.

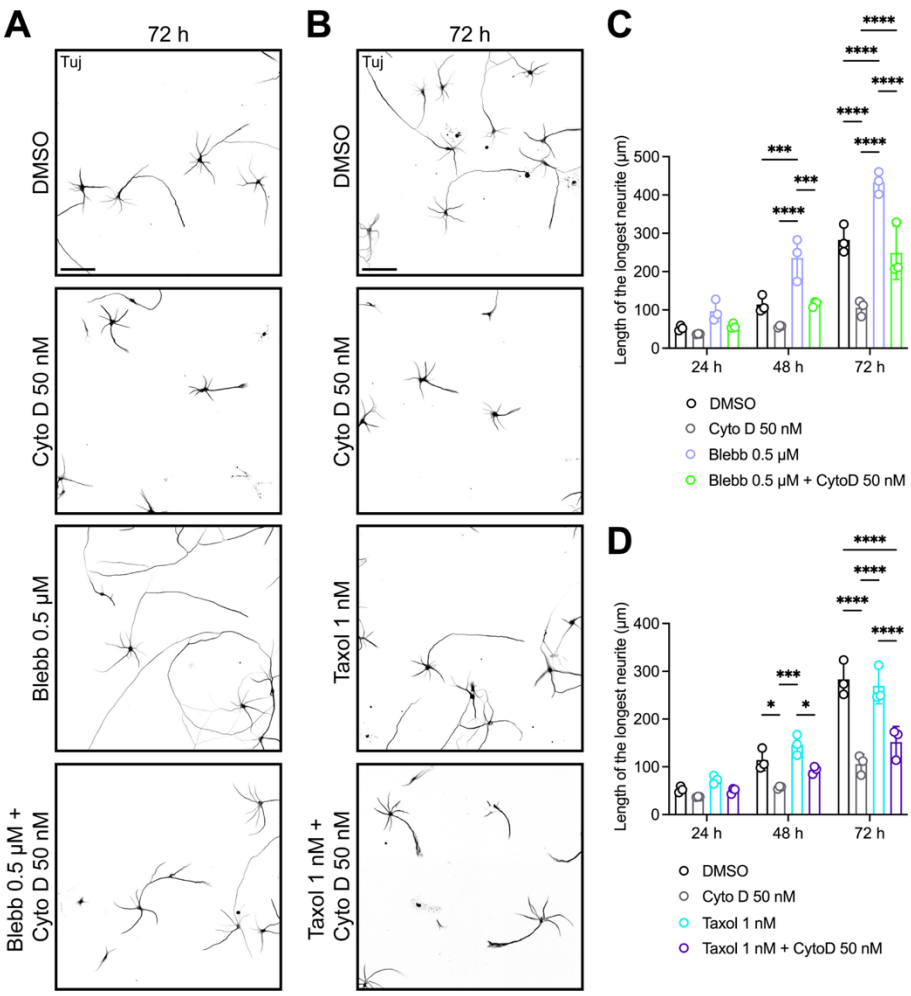

Figure 23: Actin depolymerisation reduces growth-promoting effect of Blebbistatin and Taxol

(A) and (B) Representative images of hippocampal neurons 72 h after plating. Neurons were treated with the indicated drugs 6 h after plating. Neurons were stained for Tuj. Images were generated from stitched tiles. Scale bar 100 µm. (C) Quantification for the length of the longest neurite of (A). Values are plotted as mean ± SD from n = 3 independent experiments, with N = 695 (DMSO), 661 (Cyto D 50 nM), 822 (Blebb 0.5 µM), 695 (Blebb 0.5 µM + Cyto D 50 nM) for 24 h, 719 (DMSO), 551 (Cyto D 50 nM), 662 (Blebb 0.5 µM), 600 (Blebb 0.5 µM + Cyto D 50 nM) for 48 h, and 590 (DMSO), 617 (Cyto D 50 nM), 583 (Blebb 0.5 µM), 557 (Blebb 0.5 µM + Cyto D 50 nM) for 72 h individual neurons analysed in total. Values for DMSO, Cyto D 50 nM and Blebb 0.5 µM + Cyto D 50 nM are the same data as in Figure 20. ****p<0.0001, ***p<0.001, not significant not indicated by two-way ANOVA with Tukey's multiple comparison post-test. Simple effects within rows were analysed, and each mean was compared to every other mean in the same group (DMSO vs. Cyto D 50 nM vs. Blebb 0.5 µM vs. Blebb 0.5 µM + Cyto D 50 nM). (D) Quantification for the length of the longest neurite of (B). Values are plotted as mean ± SD from n = 3 independent experiments, with N = 695 (DMSO), 661 (Cyto D 50 nM), 654 (Taxol 1 nM), 589 (Taxol 1 nM + Cyto D 50 nM) for 24 h, 719 (DMSO), 551 (Cyto D 50 nM), 701 (Taxol 1 nM), 735 (Taxol 1 nM + Cyto D 50 nM) for 48 h, and 590 (DMSO), 617 (Cyto D 50 nM), 730 (Taxol 1 nM), 666 (Taxol 1 nM + Cyto D 50 nM) for 72 h individual neurons analysed in total. Values for DMSO, Cyto D 50 nM and Taxol 1 nM + Cyto D 50 nM are the same data as in Figure 20. ****p<0.0001, ***p<0.001, *p<0.05, not significant not indicated by two-way ANOVA with Tukey's multiple comparison post-test. Simple effects within rows were analysed, and each mean was compared to every other mean in the same group (DMSO vs. Cyto D 50 nM vs. Blebb 0.5 µM vs. Blebb 0.5 µM + Cyto D 50 nM).

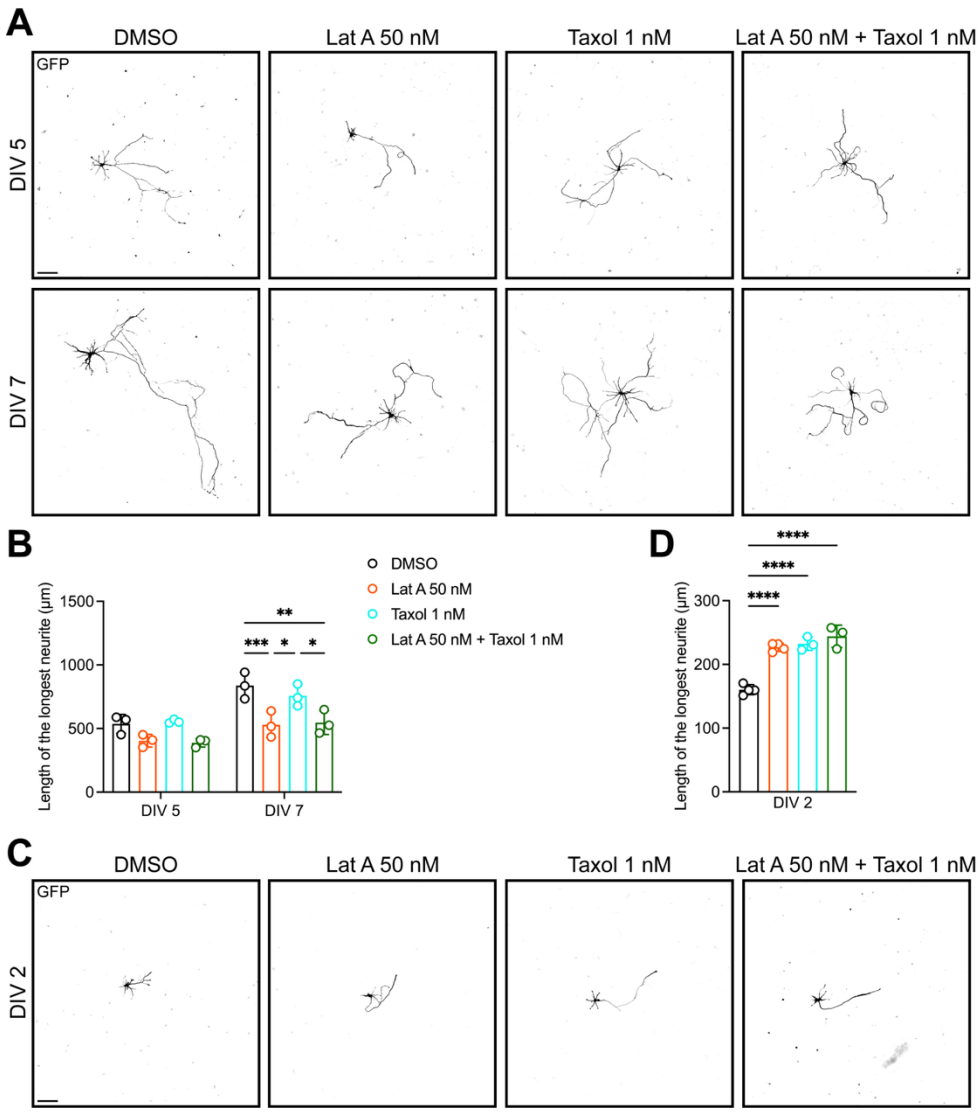

Figure 24: Actin depolymerisation mediated growth defect is not rescued with Taxol

(A) Representative images of hippocampal neurons at the indicated time points treated with either DMSO, 50 nM Lat A, 1 nM Taxol or the combination of 50 nM Lat A + 1 nM Taxol as indicated. Neurons were cultured for three days before the treatment was applied. Samples were stained for GFP. Images were generated from stitched tiles. Scale bar 100 µm. (B) Quantification for the length of the longest neurite of (A). Values are plotted as mean ± SD from n = 3 independent experiments, with N = 351 (DMSO), 437 (Lat A 50 nM), 359 (Taxol 1 nM) and 447 (Lat A 50 nM + Taxol 1 nM) for DIV 5, 398 (DMSO), 342 (Lat A 50 nM), 315 (Taxol 1 nM) and 321 (Lat A 50 nM + Taxol 1 nM) for DIV 7 individual neurons analysed. ***p<0.001, **p<0.01, *p<0.05, not significant not indicated by two-way ANOVA with Tukey's multiple comparison post-test. Simple effects within rows were analysed, and each mean was compared to every other mean in the same group (DMSO vs. Lat A 50 nM vs. Taxol 1 nM vs. Lat A 50 nM + Taxol 1 nM). (C) Representative images of hippocampal neurons at DIV 2 treated with either DMSO, 50 nM Lat A, 1 nM Taxol or the combination of 50 nM Lat A + 1 nM Taxol 6 h after plating. Samples were stained for GFP. Images were created from stitched tiles. Scale bar 50 µm. (D) Quantification for the length of the longest neurite of (C). Values are plotted as mean ± SD from n ≧ 3 independent experiments, with N = 683 (DMSO), 614 (Lat A 50 nM), 530 (Taxol 1 nM) and 567 (Lat A 50 nM + Taxol 1 nM) individual neurons traced in total. ****p<0.0001, not significant not indicated by one-way ANOVA with Tukey's multiple comparisons post-test. Each mean was compared to every other mean.

Overexpression of microtubule bundling proteins partially rescues the growth defect

Before, I showed that bundled microtubules are associated with normal and increased growth and that treatments that prevent unbundling restore growth (Figure 14, Figure 16,

and Figure 20). Unbundling and disorganisation of microtubules, in addition to increased growth cone size, was also described previously for paused growth cones (Biswas and Kalil, 2018; Dent and Kalil, 2001; Tanaka and Kirschner, 1991). Also, retraction bulbs of injured axons are enlarged compared to normal growth cones and exhibit disorganised microtubules (Ertürk et al., 2007).

Here, I observed that neurons exhibit an enlarged neurite tip with disorganised microtubules following actin polymerisation inhibition. At the same time, these neurons exhibited reduced neurite length. Is the disorganisation of microtubules the cause of reduced growth? To address this question, I overexpressed microtubule bundling proteins to prevent unbundling of microtubules and analysed the effect on neurite length. The MAP MAP2c has been shown to bundle microtubules (Dehmelt et al., 2003; Umeyama et al., 1993). I used a mNeonGreen-tagged version of MAP2c and nucleofected hippocampal neurons with the corresponding construct or GFP as control before plating. After 24 h in culture, neurons of the control and MAP2c group were either treated with DMSO as a control or 50 nM Cyto D (Figure 25A). Neurons were then fixed and analysed another 24 h or 48 h later (48 h respectively 72 h after plating). At 48 h as well as 72 h after plating, the overexpression of MAP2c prevented unbundling of microtubules as observed in Cyto D-treated cells with just GFP expression (Figure 25B, C and D). Further, the growth cone of MAP2c-expressing cells treated with 50 nM Cyto D seemed to be similar to the control. However, quantification of the length of the longest neurite showed that prevention of microtubule unbundling was not able to restore neurite length completely, but partially enhanced neurite growth (Figure 26A and B). The overexpression of MAP2c alone caused a slight reduction in neurite length.

To validate these results, I repeated the experiments with mTau, another MAP. Tau was recently shown to be involved in bundling of microtubules in the growth cone (Biswas and Kalil, 2018). Loss of mTau increased the spreading of microtubules in growth cones and reduced neurite length. Similar to the previous experiment, I nucleofected hippocampal neurons with an mScarlet-tagged mTau construct or just mScarlet as a control. After plating, neurons were cultured for 24 h before the treatment was applied (Figure 25A). Like MAP2c, overexpression of mTau prevented an unbundling of microtubules 24 h as well as 48 h after treatment, corresponding to 48 h and 72 h after plating (Figure 27A, B and C). Restoration of microtubule bundling partially rescued neurite length compared to control (Figure 28). In contrast to MAP2c, overexpression of mTau did not affect neurite length in itself. Both MAPs rescued neurite length to a similar extent of 161.9 µm ± 25.29 µm for MAP2c and 153.5 µm ± 39.22 µm in the case of Tau (mean ± SD).

Hence, the unbundling of microtubules partially contributes to the observed phenotype. However, other mechanisms that are also essential for proper neurite growth are still

disturbed in Cyto D-treated neurons with re-bundled microtubules and still cause a growth reduction.

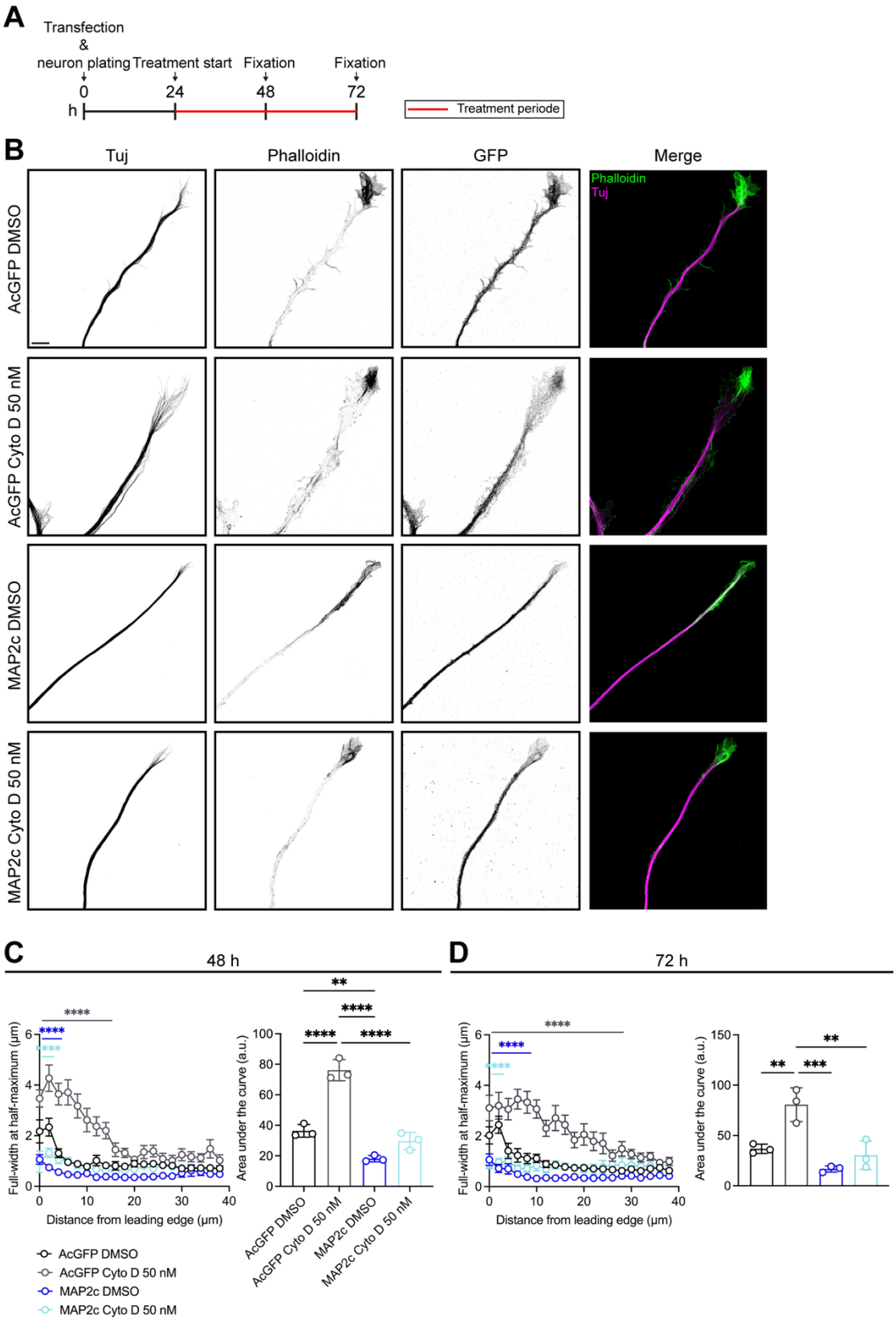

Figure 25: Overexpression of MAP2c prevents microtubule debundling upon Cyto D treatment

(A) Scheme for experimental design. Before plating, neurons were transfected with the indicated constructs in (B). Neurons were allowed to grow and express the construct for 24 h. After 24 h, neurons were treated. All groups were either treated with DMSO or 50 nM Cyto D and cultured for another 24 h or 48 h and then fixed

(48 h, respectively, 72 h after plating). (B) Representative high-resolution images of growth cones transfected with the stated constructs after 48 h in culture. Samples were stained for Tuj, F-actin and GFP. Scale bar 5 µm. In the merged image, the GFP signal is not shown. (C) Quantification of extent of microtubule debundling after 48 h in culture (24 h with treatment). Left, quantification for microtubule bundling of growth cones. Microtubule bundling is quantified in 2 µm steps as the full-width at half-maximum intensity of Tuj along the longitudinal axis of the growth cone from the leading edge to the neurite shaft. Values are plotted as mean ± SEM from n = 3 experiments, with N = 22 (*Aequorea coerulescens* (Ac)GFP, DMSO), 23 (AcGFP, Cyto D 50 nM) and 24 (MAP2c, DMSO and Cyto D 50 nM) individual growth cones analysed in total. ****p<0.0001, not significant not indicated by two-way ANOVA with Dunnett's multiple comparison post-test. Simple effects within rows were compared to the control group (AcGFP, DMSO) only. Simplified depiction of significant differences. Right, quantification of the area under the curve for the left plot. The area under the curve was quantified for every independent experiment representing the overall extent of microtubule debundling. Values are plotted as mean ± SD for n = 3 experiments and the same N as in the left plot. ****p<0.0001, **p<0.01, not significant not indicated by one-way ANOVA with Tukey's multiple comparison post-test. Each mean was compared with every other mean. (D) Quantification of the extent of microtubule debundling after 72 h in culture (48 h with treatment). Left, quantification for microtubule bundling of growth cones. Microtubule bundling is quantified in 2 µm steps as the full-width at half-maximum intensity of Tuj along the longitudinal axis of the growth cone from the leading edge to the neurite shaft. Values are plotted as mean ± SEM from n = 3 experiments, with N = 22 (AcGFP, DMSO), 24 (AcGFP, Cyto D 50 nM), 22 (MAP2c, DMSO) and 24 (MAP2c, Cyto D 50 nM) individual growth cone analysed in total. ****p<0.0001, not significant not indicated by two-way ANOVA with Dunnett's multiple comparison post-test. Simple effects within rows were compared to the control group (AcGFP, DMSO) only. Simplified depiction of significant differences. Right, quantification of the area under the curve for the left plot. The area under the curve was quantified for every independent experiment representing the overall extent of microtubule debundling. Values are plotted as mean ± SD for n = 3 experiments and the same N as in the left plot. ***p<0.001, **p<0.01, not significant not indicated by one-way ANOVA with Tukey's multiple comparison post-test. Each mean was compared with every other mean.

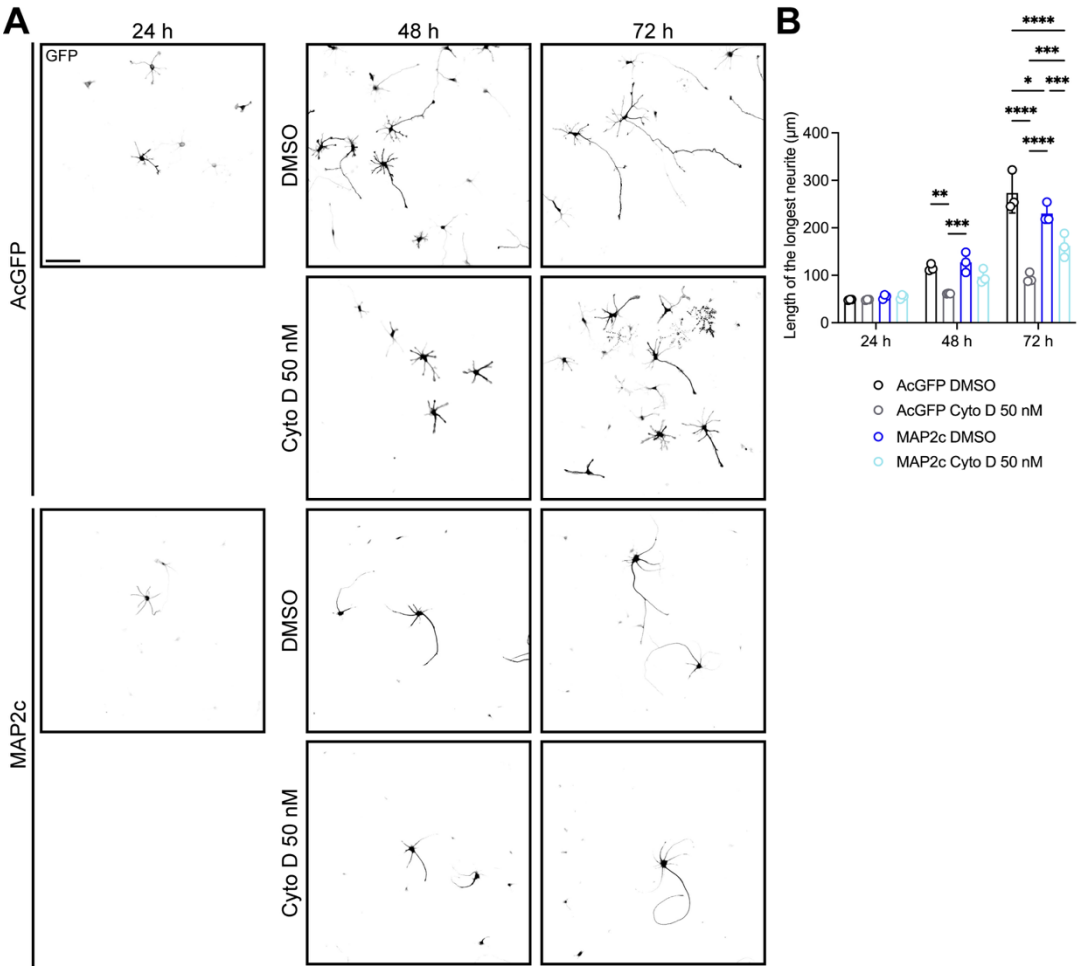

Figure 26: MAP2c overexpression partially rescues growth defect

(A) Representative images of hippocampal neurons expressing the indicated constructs with the stated treatment at the indicated time points in culture. Neurons were stained for GFP. Images were generated from stitched tiles. Scale bar 100 µm. (B) Quantification of the length of the longest neurite of (A). Values are plotted as mean ± SD from n = 3 independent experiments, with N = 493 (AcGFP, DMSO), 493 (AcGFP, Cyto D 50

nM), 309 (MAP2c, DMSO), 309 (MAP2c, Cyto D 50 nM) for 24 h, 512 (AcGFP, DMSO), 509 (AcGFP, Cyto D 50 nM), 361 (MAP2c, DMSO), 250 (MAP2c, Cyto D 50 nM) for 48 h, and 382 (AcGFP, DMSO), 354 (AcGFP, Cyto D 50 nM), 305 (MAP2c, DMSO), 245 (MAP2c, Cyto D 50 nM) for 72 h individual neurons analysed in total. Values for 24 h for DMSO and Cyto D groups are the same cells respectively for AcGFP as well as MAP2c. ****p<0.0001, ***p<0.001, **p<0.01, *p<0.05, not significant not indicated by two-way ANOVA with Tukey's multiple comparison post-test. Simple effects within rows were analysed and each mean was compared to every other mean in the same group (AcGFP DMSO vs. AcGFP Cyto D 50 nM vs. MAP2c DMSO vs. MAP2c Cyto D 50 nM).

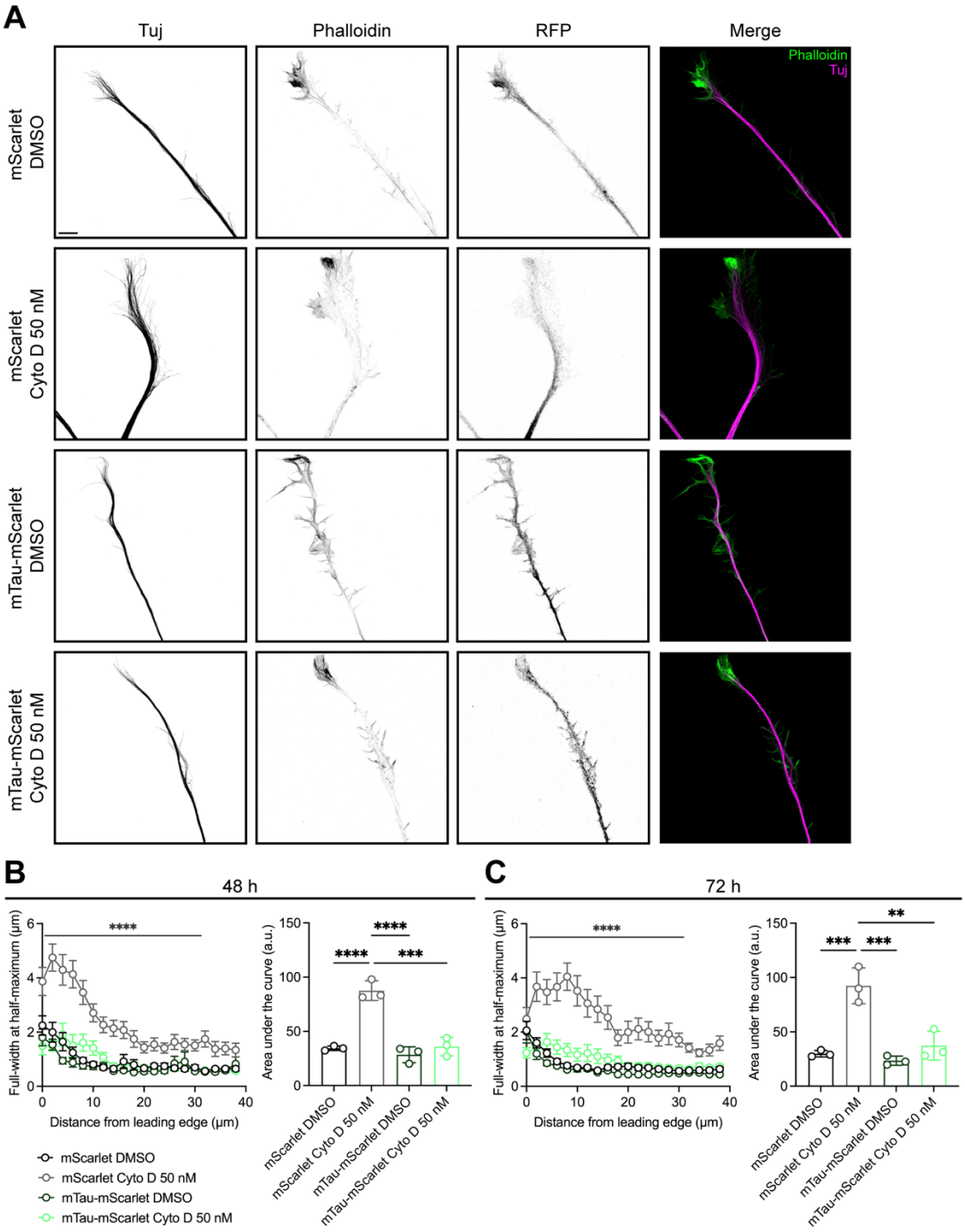

Figure 27: Overexpression of mTau prevents microtubule debundling

(A) Representative high-resolution images of growth cones transfected with the stated constructs after 48 h in culture. Samples were stained for Tuj, F-actin and red fluorescent protein (RFP). Scale bar 5 µm. In the merge image, the RFP signal is not shown. (B) Quantification of the extent of microtubule debundling after 48 h in culture (24 h with treatment). Left, quantification for microtubule bundling of growth cones. Microtubule bundling is quantified in 2 µm steps as the full-width at half-maximum intensity of Tuj along the longitudinal

axis of the growth cone from the leading edge to the neurite shaft. Values are plotted as mean ± SEM from n = 3 experiments, with N = 24 (mScarlet, DMSO and Cyto D 50 nM), 25 (mTau-mScarlet, DMSO) and 24 (mTau-mScarlet, Cyto D 50 nM) individual growth cone analysed in total. ****p<0.0001, not significant not indicated by two-way ANOVA with Dunnett's multiple comparison post-test. Simple effects within rows were compared to the control group (mScarlet, DMSO) only. Simplified depiction of significant differences. Right, quantification of the area under the curve for the left plot. The area under the curve was quantified for every independent experiment representing the overall extent of microtubule debundling. Values are plotted as mean ± SD for n = 3 experiments and the same N as in the left plot. ****p<0.0001, ***p<0.001, not significant not indicated by one-way ANOVA with Tukey's multiple comparison post-test. Each mean was compared with every other mean. (C) Quantification of the extent of microtubule debundling after 72 h in culture (48 h with treatment). Left, quantification for microtubule bundling of growth cones. Microtubule bundling is quantified in 2 µm steps as the full-width at half-maximum intensity of Tuj along the longitudinal axis of the growth cone from the leading edge to the neurite shaft. Values are plotted as mean ± SEM from n = 3 experiments, with N = 24 (mScarlet, DMSO and Cyto D 50 nM, mTau-mScarlet, DMSO and Cyto D 50 nM) individual growth cones analysed in total. ****p<0.0001, not significant not indicated by two-way ANOVA with Dunnett's multiple comparison post-test. Simple effects within rows were compared to the control group (mScarlet, DMSO) only. Simplified depiction of significant differences. Right, quantification of the area under the curve for the left plot. The area under the curve was quantified for every independent experiment representing the overall extent of microtubule debundling. Values are plotted as mean ± SD for n = 3 experiments and the same N as in the left plot. ***p<0.001, **p<0.01, not significant not indicated by one-way ANOVA with Tukey's multiple comparison post-test. Each mean was compared with every other mean.

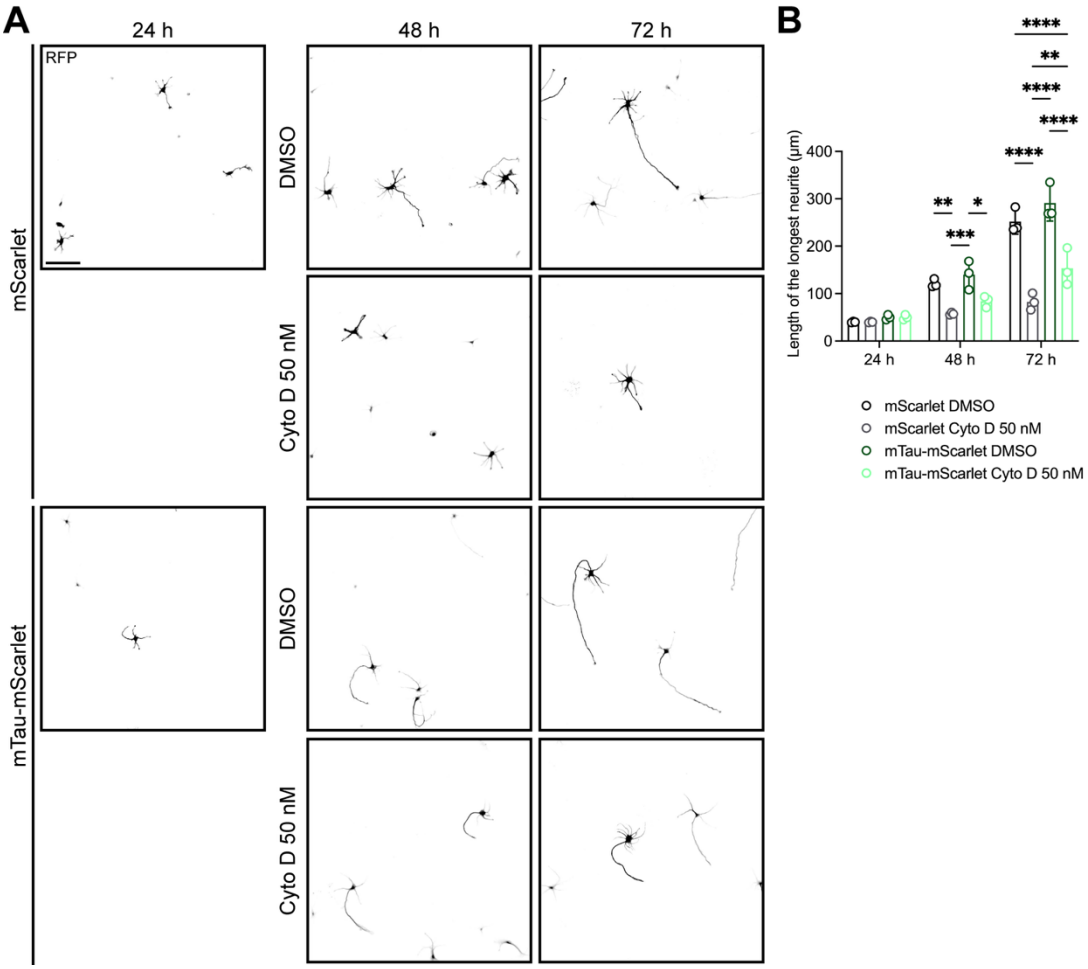

Figure 28: mTau overexpression partially rescues the actin depolymerisation based growth defect

(A) Representative images of hippocampal neurons expressing the indicated constructs with the stated treatment at the indicated time points in culture. Neurons were stained for RFP. Images were generated from stitched tiles. Scale bar 100 µm. (B) Quantification of the length of the longest neurite of (A). Values are plotted as mean ± SD from n = 3 independent experiments, with N = 459 (mScarlet, DMSO), 459 (mScarlet, Cyto D 50 nM), 383 (mTau-mScarlet, DMSO), 383 (mTau-mScarlet, Cyto D 50 nM) for 24 h, 353 (mScarlet, DMSO), 411 (mScarlet, Cyto D 50 nM), 361 (mTau-mScarlet, DMSO), 401 (mTau-mScarlet, Cyto D 50 nM) for 48 h, and 429 (mScarlet, DMSO), 434 (mScarlet, Cyto D 50 nM), 483 (mTau-mScarlet, DMSO), 454 (mTau-mScarlet, Cyto D 50 nM) for 72 h individual neurons analysed in total. Values for 24 h for DMSO and Cyto D groups are the same cells, respectively, for mScarlet as well as mTau-mScarlet. ****p<0.0001, ***p<0.001,

**p<0.01, *p<0.05, not significant not indicated by two-way ANOVA with Tukey's multiple comparison post-test. Simple effects within rows were analysed, and each mean was compared to every other mean in the same group (mScarlet DMSO vs. mScarlet Cyto D 50 nM vs. mTau-mScarlet DMSO vs. mTau-mScarlet Cyto D 50 nM).

Neurons overexpressing the actin-regulator Cofilin behave similarly to the Cyto D/Lat A-treated neurons

I observed that over time in culture, neurons reduce the actin turnover rate in axonal growth cones. This can be achieved by either a reduction of the depolymerisation rate of actin filaments at the pointed end or an increased stabilisation of existing actin filaments, preventing depolymerisation. How is this change in actin turnover regulated, and what is its function?

Several ABPs have been identified that are involved in the regulation of the actin cytoskeleton. One of the key regulators of actin dynamics is the ADF/cofilin family (Flynn et al., 2012; Ohashi, 2015; Shekhar and Carlier, 2017; Wioland et al., 2017). The actin depolymerisation activity of members of the ADF/cofilin family mediates the actin turnover and dynamics required for neurite formation (Flynn et al., 2012). Activity of cofilin is regulated via phosphorylation of serine-3, causing the inactivation of cofilin (Mizuno, 2013). Further, adult growth incompetent DRG neurons have higher levels of p-cofilin compared to regenerating sensory neurons, which activate cofilin to increase actin dynamics for enhanced growth (Tedeschi et al., 2019). Thus, the reduction in actin turnover I observed (Figure 12), could be the result of an increase in inactivation of cofilin, reducing actin dynamics and turnover.

To test this hypothesis, I analysed the cell lysates of cultured cortical neurons from different time points by western blotting (Figure 29A). Quantification of the ratio of phosphorylated (p-) cofilin-1 to total cofilin-1 revealed a rather constant ratio up to DIV 7 (Figure 29B). After DIV 7, the ratio of p-cofilin/cofilin increased, indicating an increased proportion of phosphorylated and thus inactive cofilin at later stages of development. Due to a high variation among the independent experiments, this observed change in p-cofilin/cofilin ratio was not significant. Further, with this approach of preparation of whole cell lysates only quantification of overall protein levels and phosphorylation states is possible. Information about potential subcellular differences in cofilin activity state is lost.

To overcome this loss in spatial information, in a second approach to investigate the activity level of cofilin, I stained fixed neurons from different developmental time points for p-cofilin-1 and total cofilin-1 (Figure 29C). Quantification of the ratio of p-cofilin-1 to total cofilin-1 specifically in growth cones revealed a potential increase in the ratio for DIV 7 and DIV 14 compared to 6 h after plating (Figure 29C and D). This experiment was done only once and needs to be repeated to be able to draw any conclusion about increased amounts of inactive cofilin-1 in growth cones of maturing neurons.

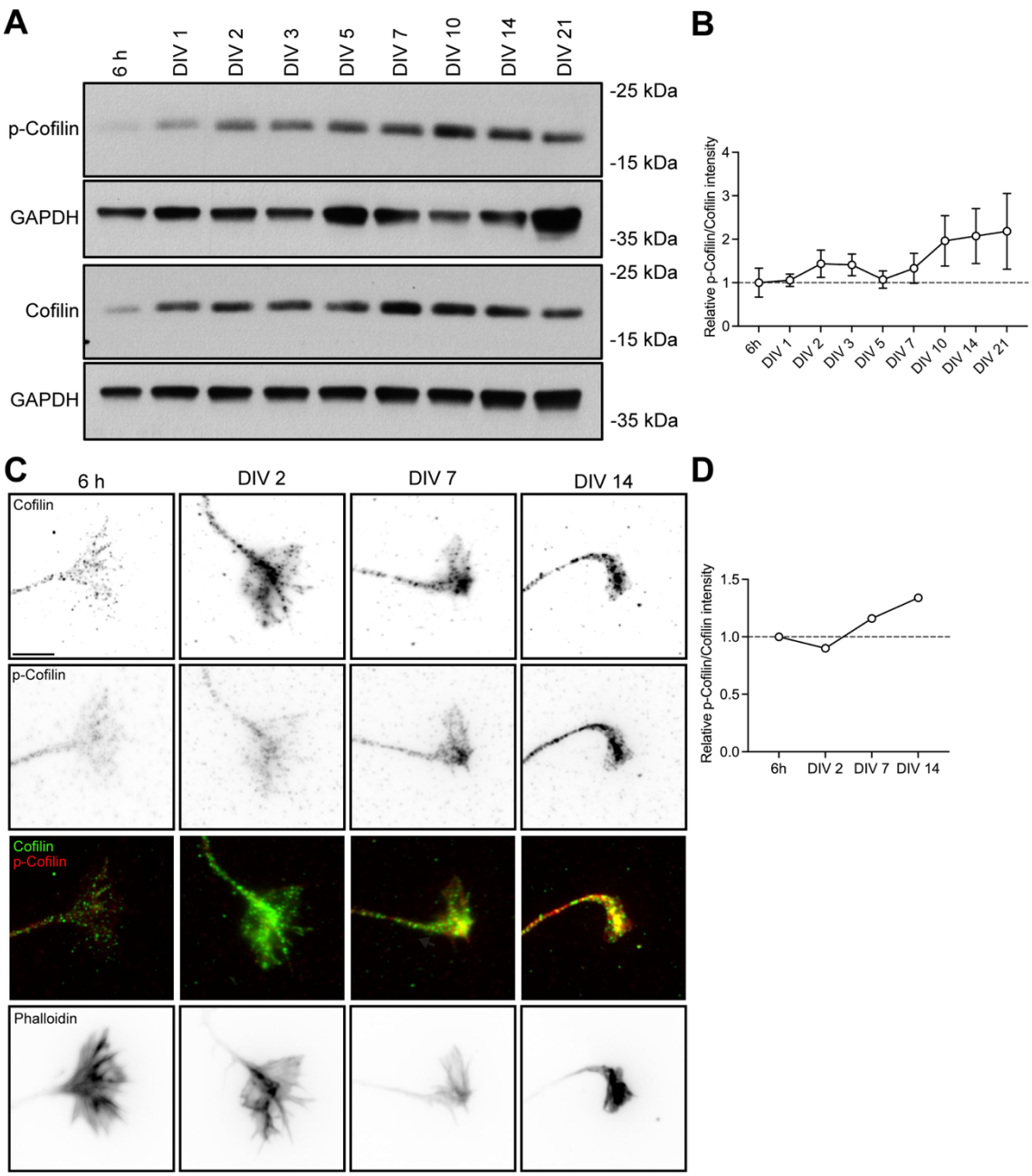

Figure 29: Cofilin phosphorylation state in cultured neurons over time

(A) Western blot for lysate of cortical neurons from the indicated time points in culture. Samples were analysed for phosphorylated (p)-cofilin-1, total cofilin-1, and glyceraldehyde-3-phosphate dehydrogenase (GAPDH) as a loading control. Protein size is indicated in kilodalton (kDa). (B) Quantification for the relative ratio of p-cofilin-1 to total cofilin-1. Values are plotted as mean ± SEM from n = 5 independent experiments. Not significant not indicated by one-way ANOVA with Dunnett's multiple comparison post-test. Every mean was compared to the mean of a control time point only (6 h). (C) Representative images of hippocampal neuron growth cones stained for total cofilin-1, p-cofilin-1, and F-actin at the indicated time points. Scale bar 5 µm. (D) Quantification of the relative p-cofilin-1 to total cofilin-1 intensity of growth cones as in (C). Value is plotted as the mean of n = 1 experiment, with N = 30 (6 h, DIV 2, DIV 7 and DIV 14) individual growth cones analysed.

ADF/cofilin regulates actin dynamics during neuronal development. Its activity is required for neurite formation, and the overexpression mediates increased neurite length in rat cortical and mouse hippocampal neurons (Flynn et al., 2012; Garvalov et al., 2007; Meberg and Bamburg, 2000). Overexpression of cofilin also enhanced growth in mouse

sensory neurons (Tedeschi et al., 2019). Manipulation of cofilin expression levels could be a tool to manipulate actin dynamics during the development of neurons. Re-enhancing actin turnover by using cofilin overexpression may help to decipher the developmental function of reduced actin turnover.

Transfection of hippocampal neurons with a construct encoding a human version of cofilin-1 (hCofilin-1) leads to robust expression after two days in culture (DIV 2) (Figure 30A and B). The introduced hCofilin-1 had a red fluorescent protein (RFP)-tag, to easily distinguish between transgenic cofilin and endogenous cofilin in western blots (Figure 30B). This enabled separate quantification of the activity levels of transgenic as well as endogenous cofilin. There was no change in the activity state of endogenous cofilin after overexpression of hCofilin-1 at DIV 2 (Figure 30B and C). Neurons that overexpressed hCofilin-1 showed a trend towards longer neurites compared to control (144.0 µm ± 18.82 µm vs. 106.8 µm ± 27.04 µm, mean ± SD) after 48 h in culture (Figure 31A and B). This increased neurite length was only a trend, but in line with previous reports (Garvalov et al., 2007; Meberg and Bamburg, 2000; Tedeschi et al., 2019).

Next, I investigated the effect of cofilin overexpression at later stages when neurons have polarised. As not to interfere with early developmental functions of cofilin, I decided to use an adeno-associated virus (AAV) to overexpress cofilin at later stages of development. The AAV was generated from the same plasmid that was used to transfect hippocampal neurons in the previous experiment (Figure 30A and B). The cofilin overexpression virus (AAV-hCofilin-1-RFP), or a control virus (AAV-RFP) with just RFP, was added to the culture of hippocampal neurons on DIV 2 to have robust expression after DIV 3 (Figure 30A). Evaluation of the expression level of cofilin and analysis of the length of the longest neurite were done one, three and five days after the virus was added to the culture. One day after infection, expression of transgenic cofilin was not observed, and the length of the longest neurite of both groups was similar (Figure 30D and E, Figure 31C and D). Three days after infection, a robust expression of transgenic hCofilin-1 was detected, which was already partially phosphorylated (Figure 30D). Two days later, the proportion of phosphorylated cofilin to total cofilin was further increased. In addition, both transgenic cofilin and endogenous cofilin were gradually more inactivated (Figure 30D, E and F). This indicates that neurons turn on signalling pathways to quickly inactivate excessive cofilin. Overexpression of cofilin at this stage reduced the length of the longest neurite (Figure 31C and D). The longest neurites of neurons infected with AAV-hCofilin-1-RFP were, on average, 18.56 % ± 7.70 % shorter than the longest neurites of AAV-RFP infected neurons. Neurons overexpressing the actin regulator cofilin behaved similarly to neurons treated with the actin polymerisation inhibitors Cyto D and Lat A at the different developmental stages (Figure 14, Figure 15 and Figure 31).

Of note, while expression of human cofilin-1 led to an equal distribution of the protein in neurons at DIV 2, DIV 7 neurons exhibited an uneven distribution (Figure 31A and C). Neurons infected with AAV-hCofilin-1-RFP showed protein accumulations mainly towards the tips of neurites (black arrows) (Figure 31C). These accumulations are reminiscent of cofilin rods (Jang et al., 2005). It was reported that cofilin rods inhibit intracellular trafficking, impair neuronal structure and function and are also linked to neurodegenerative diseases (Bamburg et al., 2010; Chen and Wang, 2015; Cichon et al., 2012; Wurz et al., 2022). Whether the observed reduction in neurite length is due to enhanced cofilin activity and thus actin turnover or because of the formation of cofilin-rods inhibiting growth cannot be deciphered here.

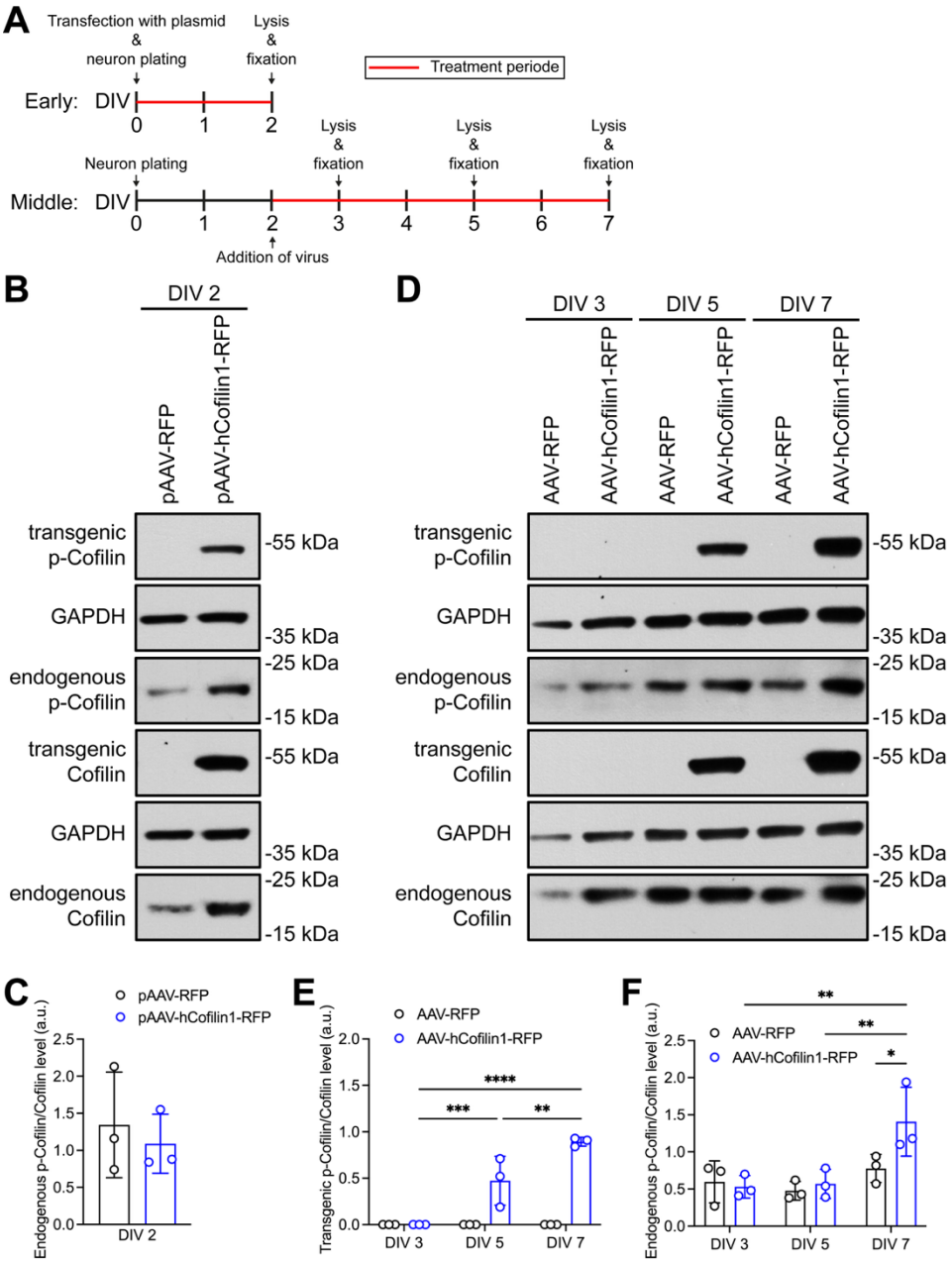

Figure 30: Overexpression of hCofilin-1 via plasmid and virus in hippocampal neurons

(A) Experimental design for approaches to overexpress cofilin in cultured neurons. For overexpression of cofilin in early stages, neurons were transfected with plasmids before plating. At DIV 2 neurons were fixed and lysed to analyse the effect. For the overexpression of cofilin in the middle stages, two days after plating, viruses were added to the cell culture media. Neurons were either fixed or lysed on DIV 3, 5 or 7 for further analysis. (B) Western blot for the overexpression of human (h)-cofilin-1 via plasmid (pAAV-hCofilin-1-RFP or control pAAV-RFP) and transfection of hippocampal neurons. Cell lysate was prepared on DIV 2. Western blots were probed for p-cofilin-1, total cofilin-1 and GAPDH as loading control. Protein size is indicated in kilodalton (kDa). (C) Quantification for the ratio of endogenous p-cofilin-1 to total cofilin-1 from western blots like (B). Protein level was normalised to the GAPDH loading control. Values are plotted as mean ± SD from n = 3 experiments. Not significant, not indicated by the unpaired two-tailed Student's t-test. (D) Western blot for the overexpression of hCofilin-1 via virus infection of cultured hippocampal neurons. Neurons were infected with either AAV-RFP as a control or AAV-hCofilin-1 and lysed at DIV 3, 5 or 7. Western blots were probed for p-cofilin-1, total-cofilin-1 or GAPDH as loading control. Protein size is indicated in kilodalton (kDa). (E) Quantification of the ratio of transgenic (-RFP tagged) p-cofilin-1 to total cofilin-1 at DIV 3, 5 and 7, respectively, for western blots like in (D). Protein levels were normalised to GAPDH loading control. Values are plotted as mean ± SD from n = 3 experiments. ****p<0.0001, ***p<0.001, **p<0.01, not significant not indicated by two-way ANOVA with Tukey's multiple comparison post-test. Simple effects within columns. Ratio of p-cofilin-1 to total cofilin-1 of AAV-RFP or AAV-hCofilin-1-RFP were compared in the respective group only. (F) Quantification of the ratio of endogenous p-cofilin-1 to total cofilin-1 at DIV 3, 5 and 7 for western blots, as in (D). Protein levels were normalised to GAPDH loading control. Values are plotted as mean ± SD from n = 3 experiments. **p<0.01, *p<0.05, not significant not indicated by two-way ANOVA with Tukey's multiple comparison post-test. Means were compared with other means in the same row and the same column.

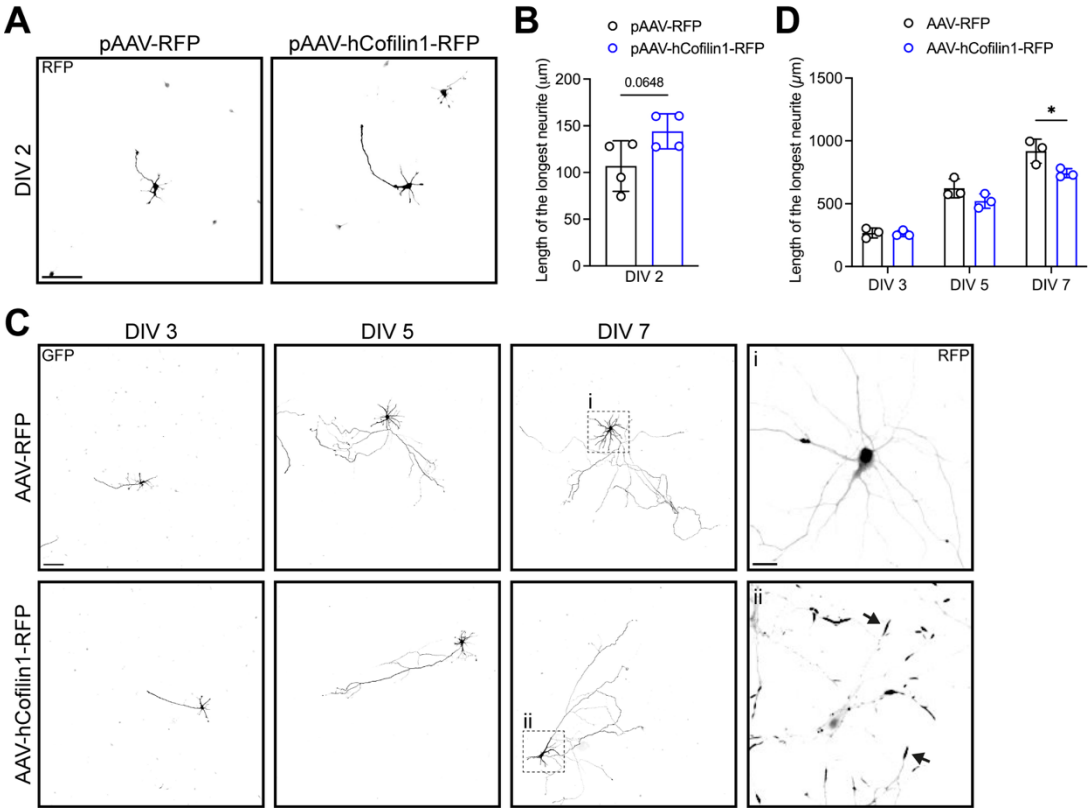

Figure 31: Cofilin overexpression differentially affects neurite growth at different stages of development

(A) Representative images of DIV 2 hippocampal neurons expressing the indicated constructs. Images were created from stitched tiles. Neurons were transfected with the indicated construct before plating and fixed on DIV 2. Samples were stained for RFP. Scale bar 100 µm. (B) Quantification for the length of the longest neurite from (A). Values are plotted as mean ± SD from n = 4 independent experiments, with N = 1229 (pAAV-RFP) and 1242 (pAAV-hCofilin-1-RFP) individual neurons traced. Not significant not indicated by unpaired two-tailed Student's t-test. (C) Representative images of neurons infected on DIV 2 with either AAV-RFP or AAV-hCofilin-1-RFP and fixed at DIV 3, 5 or 7. Neurons were stained for GFP. Scale bar 100 µm. Images were generated from stitched tiles. Insets show a magnification of the cell body area and expression of RFP constructs at DIV 7. Black arrows point to accumulated protein in AAV-hCofilin-1-RFP neurons. Scale bar 20 µm. (D) Quantification of the length of the longest neurite for the samples in (C). Values are plotted as mean ± SD from n = 3 experiments, with N = 588 (AAV-RFP) and 615 (AAV-hCofilin-1-RFP) for DIV 3, 525 (AAV-RFP) and 518 (AAV-hCofilin-1-RFP) for DIV 5, 488 (AAV-RFP) and 428 (AAV-hCofilin-1-RFP) for DIV 7, individual neurons

analysed. *p<0.05, not significant not indicated by two-way ANOVA with Sidak's multiple comparison post-test. Each mean was compared to the other mean in the same group (AAV-RFP vs. AAV-hCofilin-1-RFP).

Myosin-II activity regulates growth in young neurons but not in polarised neurons

While cofilin activity is required and beneficial for neurite formation and growth (Flynn et al., 2012; Tedeschi et al., 2019), the activity of the ABP non-muscle myosin-II negatively regulates growth of minor neurite processes (Dupraz et al., 2019; Kollins et al., 2009). Increased myosin-II activity prevents the developmental progress of neurons, increasing the number of neurons stuck in stage 1 (Kollins et al., 2009). Since myosin-II acts as a brake to control neurite growth via formation of actin arcs (Dupraz et al., 2019), the developmental decline in axon growth might also be regulated via myosin-II activity. In line, neuron-specific knockout of the myosin-II regulator Rho A enhances regeneration of injured neurons and also direct inhibition of myosin-II activity promotes regeneration when applied locally (Heo et al., 2025; Stern et al., 2021). After sufficient elongation of the axon to reach the intended target regions, neurons may upregulate myosin-II or increase its activity to reduce further growth. Such an upregulation could be induced by target interaction or is based on an intrinsic program instructing the neuron to stop to grow. Keeping myosin-II active in adulthood to prevent excessive growth then also inhibits regeneration.

To study the potential role of myosin-II in the downregulation of axon growth rates, I treated cultured neurons at different developmental time points with the myosin-II inhibitor Blebb. For the experiments, I used two different Blebb concentrations, 0.5 µM and 10 µM. When high concentrations of Blebb are used, several minor neurites will start to grow out (Kollins et al., 2009), which would lead to the generation of neurons with multiple axons. Low concentrations of the drug (0.5 µM) do not induce the formation of multiple axons, but are sufficient to enhance growth of a single neurite that will become the axon (Dupraz et al., 2019).

When I treated hippocampal neurons 6 h after plating with either 0.5 µM or 10 µM Blebb and analysed the length of the longest neurite at DIV 2 (Figure 13A), I found an increase in neurite length, similar to previous reports (Figure 32A, B, C and D) (Dupraz et al., 2019; Kollins et al., 2009). The treatment with a concentration of 10 µM Blebb increased the length of the longest neurite slightly more than the twenty times lower concentration (0.5 µM (271.9 µm ± 3.12 µm vs. 246.6 µm ± 14.19 µm; mean ± SD). However, treatment with low concentrations of Blebb did not seem to affect the growth of minor neurites, while 10 µM Blebb also affected and increased minor neurite length (not quantified), as one would expect from previous reports (Figure 32A and C) (Dupraz et al., 2019; Kollins et al., 2009).

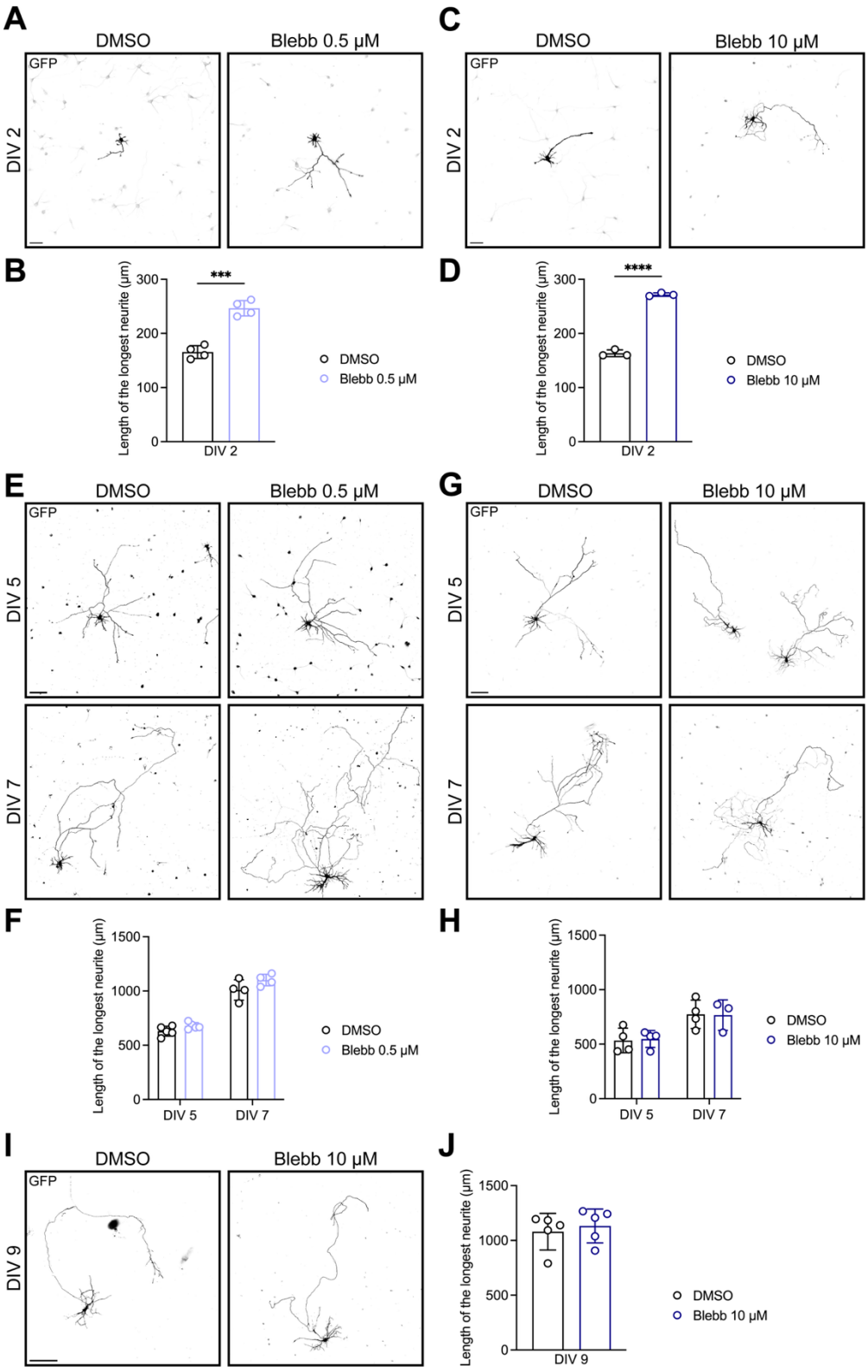

Figure 32: Blebbistatin enhances neurite growth in young neurons until DIV 2

(A) Representative images of hippocampal neurons treated with DMSO or 0.5 µM Blebb 6 h after plating and fixed at DIV 2. Neurons were stained for GFP. Images were created from stitched tiles. Scale bar 50 µm. (B) Quantification of the length of the longest neurite in (A). Values are plotted as mean ± SD from n = 4 independent experiments, with N = 649 (DMSO), and 713 (Blebb 0.5 µM) neurons analysed in total. ***p<0.001 by unpaired two-tailed Student's t-test. (C) Representative images of hippocampal neurons treated with DMSO or 10 µM Blebb 6 h after plating and fixed at DIV 2. Neurons were stained for GFP. Images were generated from stitched tiles. Scale bar 50 µm. (D) Quantification of the length of the longest neurite in (C). Values are plotted as mean ± SD from n = 3 independent experiments, with N = 519 (DMSO), and 524 (Blebb 10 µM)

individual neurons analysed in total. ****p<0.0001 by unpaired two-tailed Student's t-test. (E) Representative images of hippocampal neurons at the indicated time points treated with either DMSO or 0.5 µM Blebb as indicated. Neurons were cultured for three days before the treatment was applied, and the cells were fixed two or four days later. Neurons were stained for GFP. Images arose from stitched tiles. Scale bar 100 µm. (F) Quantification for the length of the longest neurite at the indicated time points for neurons with the indicated treatment. Values are plotted as mean ± SD from n = 5 experiments, with N = 926 (DMSO) and 838 (Blebb 0.5 µM) for DIV 5, 735 (DMSO) and 614 (Blebb 0.5 µM) for DIV 7, individual neurons quantified in total. Not significant not indicated by two-way ANOVA with Sidak's multiple comparison post-test. Every mean was compared to the other means within the same group (DMSO vs. Blebb 0.5 µM). (G) Representative images of hippocampal neurons at the indicated time points treated with either DMSO or 10 µM Blebb as indicated. Neurons were cultured for three days before the treatment was applied, and the cells were fixed two or four days later. Neurons were stained for GFP. Images arose from stitched tiles. Scale bar 100 µm. (H) Quantification for the length of the longest neurite at the indicated time points for neurons with the indicated treatment. Values are plotted as mean ± SD from n = 4 experiments, with N = 432 (DMSO) and 478 (Blebb 10 µM) for DIV 5, 465 (DMSO) and 305 (Blebb 10 µM) for DIV 7, individual neurons quantified in total. Not significant not indicated by two-way ANOVA with Sidak's multiple comparison post-test. Every mean was compared to the other means within the same group (DMSO vs. Blebb 10 µM). (I) Representative images of hippocampal neurons at DIV 9 treated for two days with DMSO or Blebb 10 µM as indicated. Samples were stained for GFP. Images arose from stitched tiles. Scale bar 200 µm. (J) Quantification for the length of the longest neurite of neurons treated with DMSO or Blebb 10 µM as indicated. Values are plotted as mean ± SD from n = 5 experiments with N = 493 (DMSO) and 454 (Blebb 10 µM) individual neurons traced in total. Not significant not indicated by unpaired two-tailed Student's t-test.

Conducting the same experiment with neurons that have been in culture for 3 DIV (Figure 13A) revealed no difference in the length of the longest neurite for either of the concentrations after two or four days of treatment (Figure 32E, F, G and H). A potential effect on the growth of minor neurites/dendrites was only quantified for the treatment with 10 µM Blebb. In contrast to the length of the longest neurite, the length of the second longest neurite was enhanced when myosin-II was inhibited in DIV 3 hippocampal neurons (Figure 37C). After two days with 10 µM Blebb, DIV 9 neurons exhibited no difference in the length of the longest neurite (Figure 32I and J). Myosin-II activity seems to be important in an early developmental phase when neurite growth needs to be restricted to coordinate polarisation of hippocampal neurons. Once the cell has polarised, the myosin-II brake is released, and axons elongate without any myosin-II-mediated restrictions, while minor neurites remain growth restricted by myosin-II activity.

An antagonism of the Arp2/3 complex and myosin-II allows the formation of a polarised morphology

Before neurons polarise and elongate one of their neurites to form the axon, the processes undergo a constant cycle of elongation and retraction (Bradke and Dotti, 1997). Myosin II activity is involved in the generation of neurite retraction (Amano et al., 1998; Wylie and Chantler, 2003). The actin nucleating complex Arp2/3 restricts myosin-II-dependent contractility (Yang et al., 2012). Lin and colleagues show that the oscillatory growth behaviour of neurites is driven by an antagonism of the Arp2/3 complex and myosin-II (Lin et al., manuscript in preparation). Arp2/3 complex-mediated branched actin network formation relaxes the actomyosin-dominated tension, enabling neurites to extend. When myosin-II dominates, neurites retract (Lin et al., manuscript in preparation). In unpolarised

neurites, this antagonism of the Arp2/3 complex and myosin-II keeps the neuron in an unpolarised and oscillatory state. When Arp2/3 is inhibited, formation of a branched actin network is inhibited and myosin-II-dominated actin structures lead to a retraction in neurite length.

Treatment of neurons 6 h after plating with the Arp2/3 inhibitor CK-666 inhibited the growth of the longest neurite (Figure 33A and B). Blocking myosin-II activity at the same time prevented reduced growth and restored neurite length (Figure 33A and B) (Lin et al., manuscript in preparation). When myosin-II activity is inhibited, activity of the Arp2/3 complex relaxes the dense actin network by forming branched filaments and neurite growth is initiated (Figure 33A and B). Axon formation occurs when one of the neurites escapes this antagonism (Lin et al., manuscript in preparation).

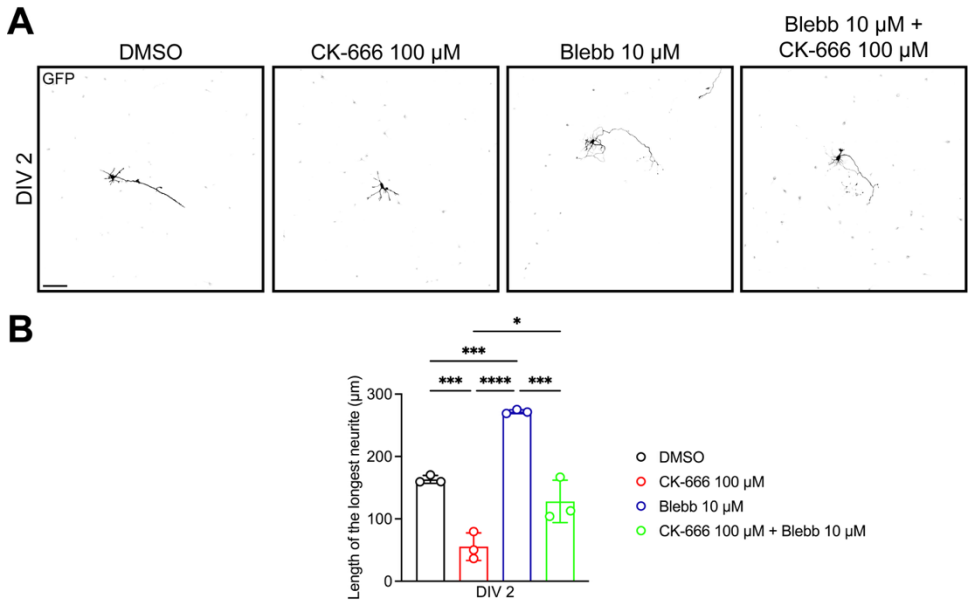

Figure 33: Antagonism of Arp2/3 complex and Myosin II in young neurons

(A) Representative images of hippocampal neurons treated with the indicated drugs 6 h after plating and fixed at DIV 2. Neurons were stained for GFP. Images were created from stitched tiles. Scale bar 50 µm. (B) Quantification of the length of the longest neurite in (A). Values are plotted as mean ± SD from n = 3 independent experiments, with N = 519 (DMSO), 423 (CK-666 100 µM), 524 (Blebb 10 µM) and 341 (CK-666 100 µM + Blebb 10 µM) neurons analysed in total. Values for DMSO and 10 µM Blebb are the same as in **Figure 32**D. ****p<0.0001, ***p<0.001, *p<0.05, not significant not indicated by one-way ANOVA with Tukey's multiple comparison post-test. Each mean was compared to every other mean.

I found that the length of the longest neurite did not change when DIV 3 neurons were treated with Blebb (Figure 32E, F, G and H). Hence, myosin-II activity does not restrict neurite growth in axons by generating contractile forces or acting as a growth brake. When myosin-II activity no longer restrains axon growth, neurons should not retract neurites anymore when the Arp2/3 complex is inhibited. To test this hypothesis, I performed retraction assays at different time points in culture. Late DIV 1 neurons (36 h after plating) were treated with a high dose of CK-666 (200 µM) (Figure 34A). After 12 h, neurons were fixed and the length of the longest neurite was analysed. Neurons treated with 200 µM

CK-666 had shorter neurites than the DMSO control (Figure 34B and C). When the same experiment was performed with late DIV 3 neurons, there was no difference in the length of the longest neurite anymore after 12 h (Figure 34B and C). Minor neurites of CK-666-treated neurons still retracted (Figure 34B and D). Since minor neurite and dendrite growth rates during the whole process of development are low, I wondered whether the Arp2/3 complex-myosin-II antagonism is the driver of keeping dendrites short. To answer this question, I used DIV 14 neurons for the retraction assay. When neurons were fixed after 12 h of CK-666 treatment, no difference in axonal or dendritic length was observed (Figure 34E, F and G). This result indicates that at least at DIV 14, dendrites are not actively kept short by an antagonism of the Arp2/3 complex and myosin-II activity. Thus, between DIV 3 and DIV 14 this antagonism of the both actin regulating proteins vanishes in dendrites. When exactly and how this happens, needs to be investigated in the future.

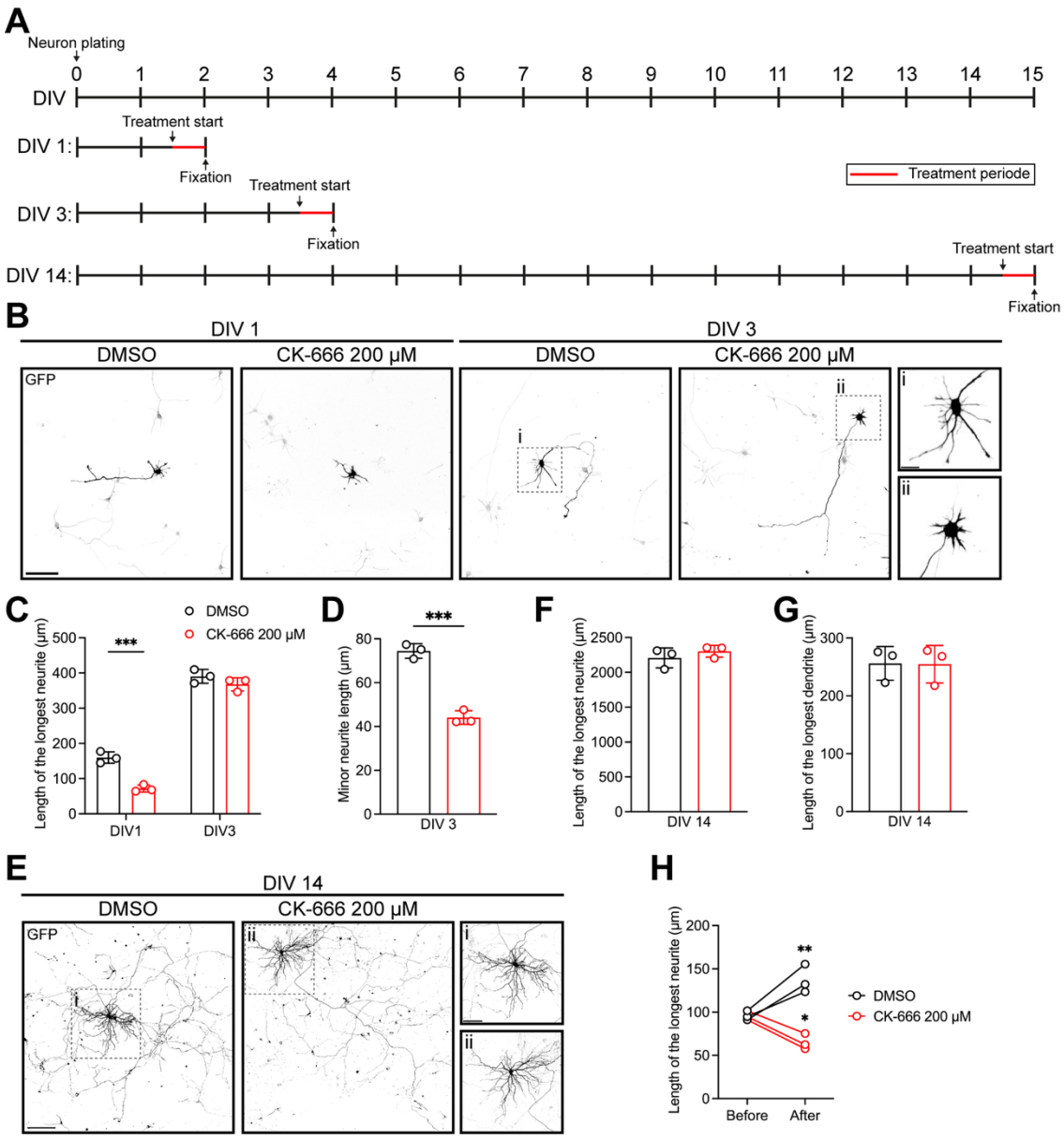

Figure 34: Arp3 inhibition causes retraction in young but not in mature neurons

(A) Scheme for retraction assay. Neurons were treated either on late DIV 1, DIV 3, or DIV 14 with 200 µM CK-666 and then fixed 12 h after treatment start. (B) Representative images of hippocampal neurons treated at the indicated time points with DMSO or 200 µM CK-666 for 12 h. Samples were stained for GFP. Images were generated from stitched tiles. Scale bar 100 µm. Insets show a magnification of the cell body compartment with minor neurites of neurons treated at DIV 3. Scale bar 25µm. (C) Quantification for the length of the longest neurite in (B). Values are plotted as mean ± SD from n = 3 experiments, with N = 373 (DMSO) and 322 (CK-666 200 µM) for DIV 1, and 374 (DMSO) and 322 (CK-666 200 µM) for DIV 3, individual neurons analysed. ***p<0.001, not significant not indicated by two-way ANOVA with Sidak's multiple comparison post-test. Each mean was compared to the other mean in that group (DMSO vs. CK-666 200 µM). (D) Quantification for minor neurite length in (B). Minor neurites were quantified for DIV 3 only, as the second longest neurite of the cell. Values are plotted as mean ± SD from n = 3 experiments, with N = 352 (DMSO) and 310 (CK-666 200 µM) individual cells analysed. ***p<0.001 by two-tailed Mann-Whitney test. (E) Representative images of hippocampal neurons treated at DIV 14 with DMSO or 200 µM CK-666 for 12 h. Cells were stained for GFP Images were created from stitched tiles. Scale bar 200 µM. Insets show a magnification of the dendrite compartment. Scale bar 100 µM. (F) Quantification of the length of the longest neurite for (E). Values are plotted as mean ± SD from n = 3 experiments, with N = 114 (DMSO) and 103 (CK-666 200 µM) individual neurons traced in total. Not significant not indicated by two-tailed Mann-Whitney test. (G) Quantification for dendrite length in (E). Dendrite length was quantified as the length of the second longest neurite of the cell. Values are plotted as mean ± SD from n = 3 experiments with N = 377 (DMSO) and 320 (CK-666 200 µ) individual neurons analysed in total. Not significant not indicated by unpaired two-tailed student's t-test. (H) Quantification for the length of the longest neurite in the retraction assay for DIV 1 neurons. A similar experiment as in (B) and (C) was performed but before the treatment start a batch of cells was fixed to analyse whether the reduction in neurite length is due to growth inhibition or retraction. Values are plotted as mean for every single experiment before and after treatment with either DMSO or CK-666 200 µM for n = 3 independent experiments, with N = 395 (before), 442 (after, DMSO) and 419 (after, CK-666 200 µM) neurons in total analysed. **p<0.01, *p<0.05 by one-way ANOVA with Dunnett's multiple comparison post-test. Mean of before was compared to the mean of DMSO or CK-666 200 µM.

To address the question of whether neurites of DIV 1 neurons really retract or the shorter length is due to reduced neurite growth, I repeated the retraction assay and fixed neurons before and after the treatment. Quantification of the length of the longest neurite showed that neurites of CK-666 treated neurons were shorter than before the treatment (Figure 34H). In DIV 1 neurons, inhibition of Arp2/3 activity leads to a retraction due to myosin-II-dominated actomyosin contractility.

Since the longest neurites did not retract once neurons had polarised (Figure 34C and F), I wondered whether the Arp2/3 complex still has a function in axon elongation. To address this question, I first looked at the expression level of the Arp2/3 complex subunits Arp3 and Arp2. Lysate of cultured cortical neurons from different developmental time points was analysed by western blot (Figure 35A). Arp3 and Arp2 are expressed throughout the development of cortical neurons in culture (Figure 35A, B and C). The expression level of Arp3 was rather constant over time in culture, in contrast, Arp2 levels seemed to increase over time. Since components of the Arp2/3 complex are expressed not only in early stages when the complex is involved in regulating neurite growth but also later, I hypothesised that the Arp2/3 complex also has a role in axon elongation.

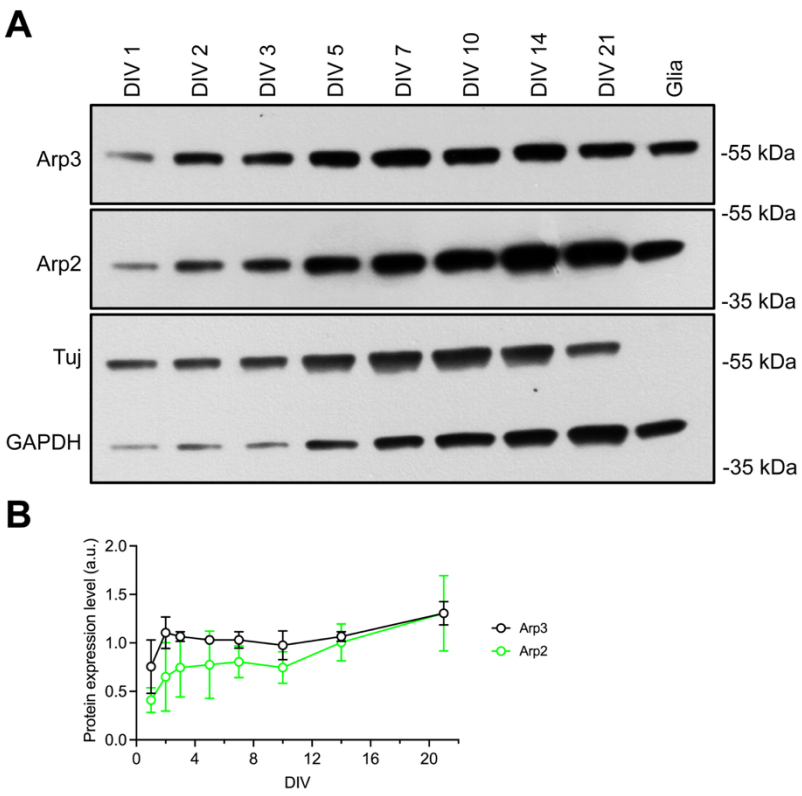

Figure 35: Arp3 and Arp2 are expressed throughout development in cultured cortical neurons

(A) Western blot for cortical lysate of the indicated time points in culture, analysed for protein level of Arp3, Arp2, and Tuj as well as GAPDH as loading control. In addition, expression of Arp3 and Arp2 in glia cell lysate is shown, where Tuj is not expressed. Protein size is indicated in kilodalton (kDa). (B) Quantification for the expression levels of Arp3 and Arp2 over time in cultured cortical neurons. Arp3 and Arp2 intensities were normalised to Tuj and GAPDH loading controls. Values are plotted as mean ± SD from n = 2 experiments.

To address this question, I treated DIV 3 neurons with 100 µM CK-666 and analysed the length of the longest neurite after two and four days, respectively (Figure 13A and Figure 36A). Quantification for the length of the longest neurite showed that inhibition of the Arp2/3 complex reduced axon elongation. Formation of a branched actin network and actin polymerisation via the Arp2/3 complex is required for axon elongation (Figure 36A and B). In contrast to the retraction assay, where I did not detect changes in the length of the longest neurite (Figure 34B and C), an increased treatment period revealed an effect on axon elongation at this stage of development (Figure 36A and B). When I performed the same experiment with neurons at 7 DIV, no effect on the length of the longest neurite was observed after two days (Figure 36D and E). Similar to the behaviour of minor neurites in the retraction assay (Figure 34B and D), the remaining neurites also retracted when treated with a lower concentration of CK-666 for several days (Figure 36A and C). In young neurons, the effect of inhibition of the Arp2/3 complex on neurite growth and morphology is due to its antagonism with myosin-II (Figure 33) (Lin et al., manuscript in preparation). Inhibition of myosin-II at middle or late stages did not affect the length of the longest neurite (Figure 32E, F, G, H, I and J), which suggests that the antagonism of Arp2/3 and myosin-

II in young neurons does not persist in more mature neurons. To verify this hypothesis, I tried to rescue the Arp2/3 inhibition-mediated growth defect with Blebb treatment. In young neurons, the combination of CK-666 and Blebb restored and rescued neurite growth (Figure 33). DIV 3 neurons were treated with either CK-666 or Blebb alone or with the combination of both (Figure 37). After four days of treatment, Blebb failed to rescue the length of the longest neurite (Figure 37A and B). At the same time, the combination of CK-666 and Blebb restored the growth of minor processes completely (Figure 37A and C). These results show two things. First, the Arp2/3 complex is required for axon elongation independent of the antagonisms of Arp2/3 and myosin-II found in young neurons. Second, however, this antagonism persists in minor neurites of developing neurons, preventing their enhanced outgrowth until an unknown point between DIV 3 and DIV 14.

In young neurons, the antagonism of Arp2/3 and myosin-II keeps the neurites in an oscillatory growth state, preventing polarisation. One of the neurites escapes this global growth inhibition and elongates while the other neurites remain under the control of a global growth inhibition based on myosin-II (Lin et al., manuscript in preparation). In this way, a polarised morphology of a single long axon and several short dendrites is achieved.

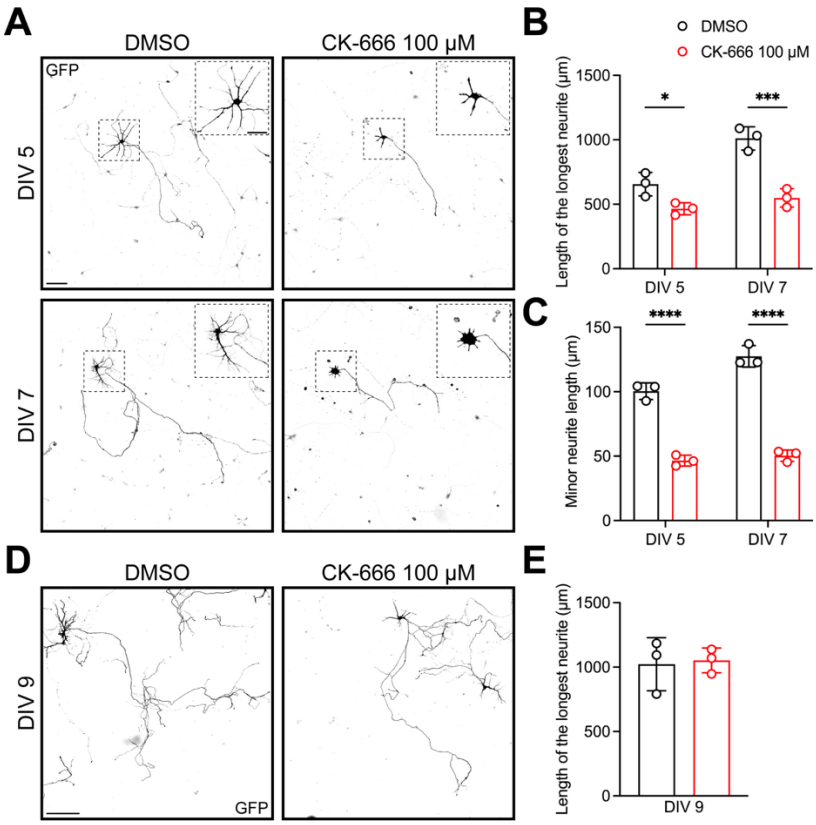

Figure 36: Arp3 is necessary for axon elongation

(A) Representative images of hippocampal neurons treated with either DMSO or CK-666 100 µM at DIV 3 and fixed after another two respectively four days in culture, as indicated. Neurons were stained for GFP. Images were created from stitched tiles. Scale bar 100 µm. Insets show a magnification of the cell body and minor neurite area. Scale bar 50 µm. (B) Quantification for the length of the longest neurite in (A). Values are plotted as mean ± SD from n = 3 independent experiments, with N = 321 (DMSO) and 229 (CK-666 100 µM) for DIV 5, 270 (DMSO) and 189 (CK-666 100 µM) for DIV 7, individual neurons traced in total. ***p<0.001, *p<0.05 by two-way ANOVA with Sidak's multiple comparison post-test. Each mean was compared to the other mean in

the same group (DMSO vs. CK-666 100 µM). (C) Quantification for minor neurite length of (A). Values are plotted as mean ± SD from n = 3 independent experiments, with N = 350 (DMSO) and 229 (CK-666 100 µM) for DIV 5, 342 (DMSO) and 205 (CK-666 100 µM) for DIV 7, individual neurons analysed in total. ****p<0.0001 by two-way ANOVA with Sidak's multiple comparison post-test. Each mean was compared to the other mean in the same group (DMSO vs. CK-666 100 µM). (D) Representative images of DIV 9 hippocampal neurons after two days of treatment with DMSO or CK-666 100 µM. Neurons were stained for GFP. Images were generated from stitched tiles. Scale bar 200 µm. (E) quantification for the length of the longest neurite in (D). Values are plotted as mean ± SD from n = 3 independent experiments, with N = 301 (DMSO) and 249 (CK-666 100 µM) individual cells analysed in total. Not significant not indicated by unpaired two-tailed Student's t-test.

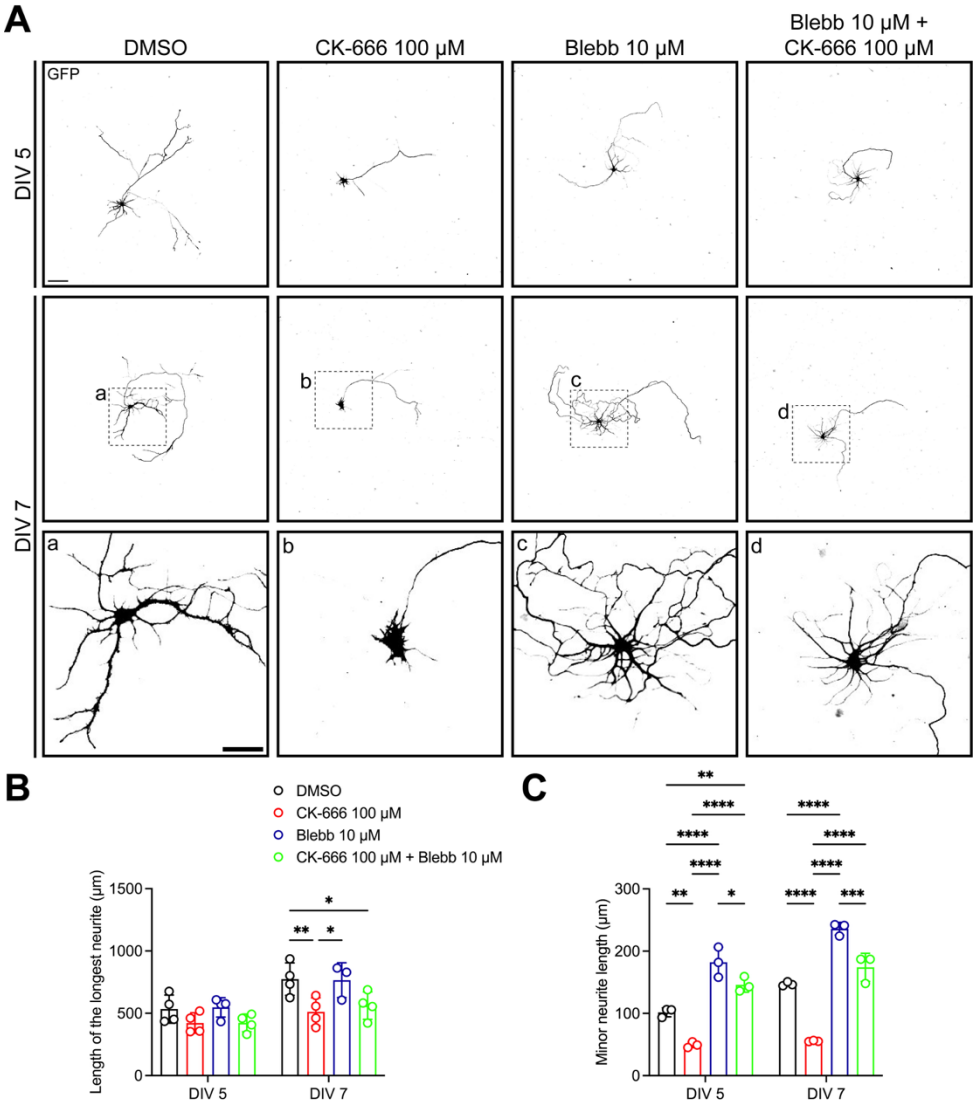

Figure 37: Blebbistatin rescues length of minor neurites but not length of the longest neurite after CK-666 treatment

(A) Representative images of hippocampal neurons treated at DIV 3 with the indicated drugs and fixed after two respectively four days of treatment, as indicated. Samples were stained for GFP. Images were generated from stitched tiles. Scale bar 100 µm. Insets show magnification of the cell body and dendrite compartment of DIV 7 neurons. Scale bar 50 µm. (B) Quantification for the length of the longest neurite in (A). Values are plotted as mean ± SD from n = 4 independent experiments, with N = 432 (DMSO), 394 (CK-666 100 µM), 478 (Blebb 10 µM) and 349 (CK-666 100 µM + Blebb 10 µM) for DIV 5, 465 (DMSO), 294 (CK-666 100 µM), 305 (Blebb 10 µM) and 268 (CK-666 100 µM + Blebb 10 µM) for DIV 7, individual neurons analysed in total. Data for DMSO and Blebb 10 µM are the same as in Figure 32H. **p<0.01, *p<0.05, not significant not indicated by two-way ANOVA with Tukey's multiple comparison post-test. Every mean was compared with every other mean in the group (DMSO vs. Ck-666 100 µM vs. Blebb 10 µM vs. Ck-666 100 µM + Blebb 10 µM). (C) Quantification for the length of minor neurites in (A). Minor neurite length was quantified as the length of the second longest neurite of the cell. Values are plotted as mean ± SD from n = 3 independent experiments, with N = 323 (DMSO), 313 (CK-666 100 µM), 348 (Blebb 10 µM) and 196 (CK-666 100 µM + Blebb 10 µM) for DIV 5, 349 (DMSO), 227 (CK-666 100 µM), 328 (Blebb 10 µM) and 185 (CK-666 100 µM + Blebb 10 µM) for DIV

7, individual cell analysed in total. ****p<0.0001, ***p<0.001, **p<0.01, *p<0.05, not significant not indicated by two-way ANOVA with Tukey's multiple comparison post-test. Each mean was compared with every other mean in the group (DMSO vs. CK-666 100 µM vs. Blebb 10 µM vs. CK-666 100 µM + Blebb 10 µM).

Arp3 is maybe required for axon elongation

The application of chemical compounds to interfere with specific proteins can lead to off-target effects. To verify that the observed reduction in neurite length is due to the inactivation of the Arp2/3 complex (Figure 36), I validated these experiments using an Arp3 knockout mouse line (Papalazarou et al., 2020).

To analyse the effect of a loss of Arp3 on neurite elongation at later stages of development, I crossed the $Arp3^{fl/fl}$ line with a GFP-reporter line described previously (Okabe et al., 1997) (Figure 38A). As I pointed out in a previous section, tracing of neuron morphology at later stages requires a sparse labelling of neurons (Figure 9). Crossing the $Arp3^{fl/fl}$ with the GFP-reporter line enables analysis of fluorescently labelled neurons where *Actr3* can be deleted. The preparation of the mixed culture with neurons that possess floxed *Actr3* loci is similar to the previous description (Figure 9A and Figure 38A). Further, a loss of Arp3 in early stages of neuronal development prevents the formation of axons and neurons get stuck in stage 2 (Lin et al., manuscript in preparation). To investigate Arp3 function in axon elongation, a KO of Arp3 must occur after axon formation to prevent neurons from being trapped in stage 2. Therefore, I decided to use a Cre recombinase protein (Cre)-expressing virus for infection of neurons initiating deletion of *Actr3*. 2 h after plating of neurons, either a control virus (AAV-RFP) or a Cre-expressing virus (AAV-RFP-Cre) was added to the culture (Figure 38B). Neurons were analysed three, five and seven days after plating. First, I confirmed that this approach reduced the Arp3 protein level in cultured neurons. Western blot analysis revealed a 50% reduction of Arp3 protein level three days after infection, which further decreased over time (Figure 38C and D). Infection of neurons with a Cre-expressing virus did not lead to a complete loss of Arp3 after seven days in culture, since 36.33% ± 23.71% (mean ± SD) of Arp3 control levels were still detectable in AAV-RFP-Cre samples (Figure 38D). This residual amount of Arp3 could be due to a less than 100% viral infection rate.

The early infection of $Arp3^{fl/fl}$ neurons, 2 h after plating, did not lead to impaired axon formation. At DIV 3, Arp3 KO as well as control neurons had a similar length of the longest neurite (Figure 39A and B). However, at DIV 7, axons of Arp3 KO neurons were shorter compared to axons of control neurons (Figure 39A and B). Though, the effect size of this *in vitro* KO of Arp3 was not a strong as observed for a treatment with the Arp2/3 inhibitor CK-666 (Figure 36A and B). It seems that Arp3 has a function in axon elongation. Though, the exact function of Arp2/3 in axon elongation remains open and it needs to be investigated whether the combination of the Arp3 KO with Blebb treatment rescues the growth reduction or not. An effect of the Arp3 KO on minor neurites was not quantified.

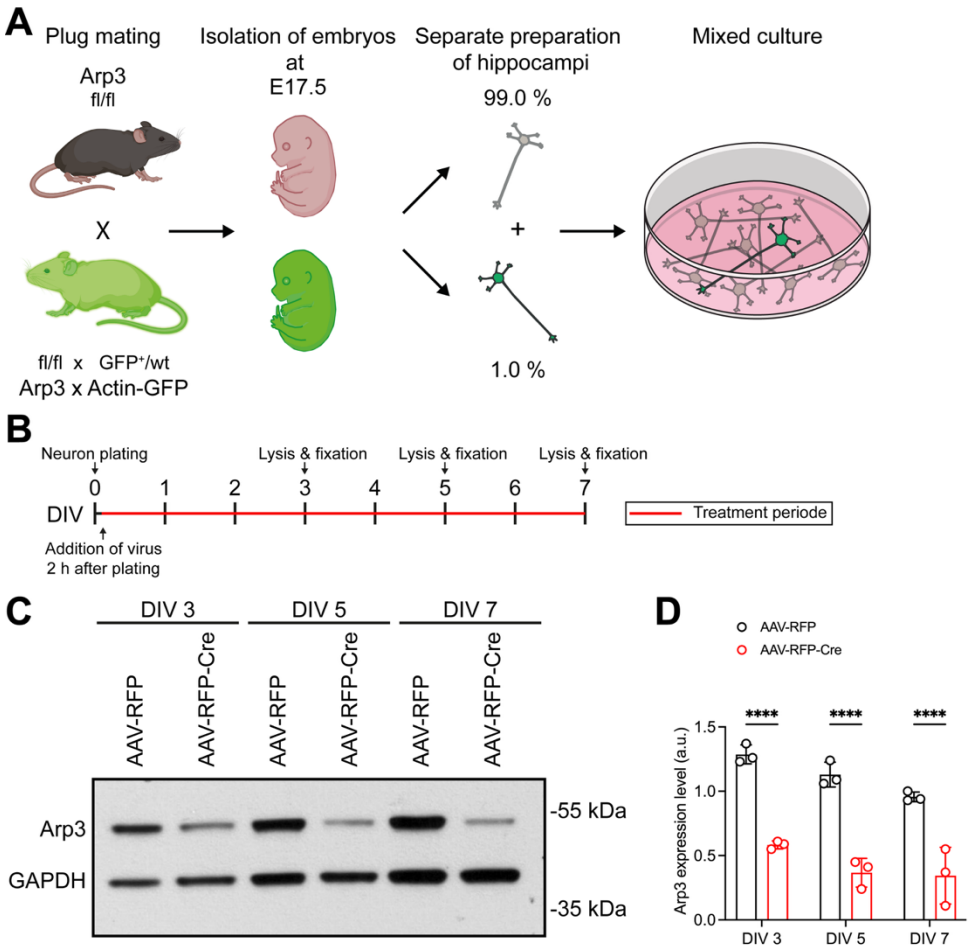

Figure 38: Arp3 protein level is reduced in cultured neurons after Cre expression

(A) Scheme for the mating strategy and preparation of 'mixed cultures' with neurons of the Arp3$^{fl/fl}$ mouse line to generate fluorescently labelled neurons where Arp3 can be knocked out. Identification of the genotype is as in Figure 9A. (B) Timeline for the experimental design for the study of genetically knockout of Arp3 in cultured neurons. 2 h after plating of the 'mixed culture', either AAV-RFP or AAV-RFP-Cre viruses are added to the culture dish. Neurons are lysed and fixed at DIV 3, 5 and 7, respectively. (C) Western blot for lysate of hippocampal neurons infected with one of the indicated viruses at the stated time in culture. Blots were probed for Arp3 and GAPDH as loading control. Protein size is indicated in kilodalton (kDa). (D) Quantification for Arp3 protein level in (C). Values are plotted as mean ± SD from n = 3 independent experiments. ****p<0.0001 by two-way ANOVA with Sidak's multiple comparison post-test. Each mean was compared to the other mean within the same group (AAV-RFP vs. AAV-RFP-Cre).

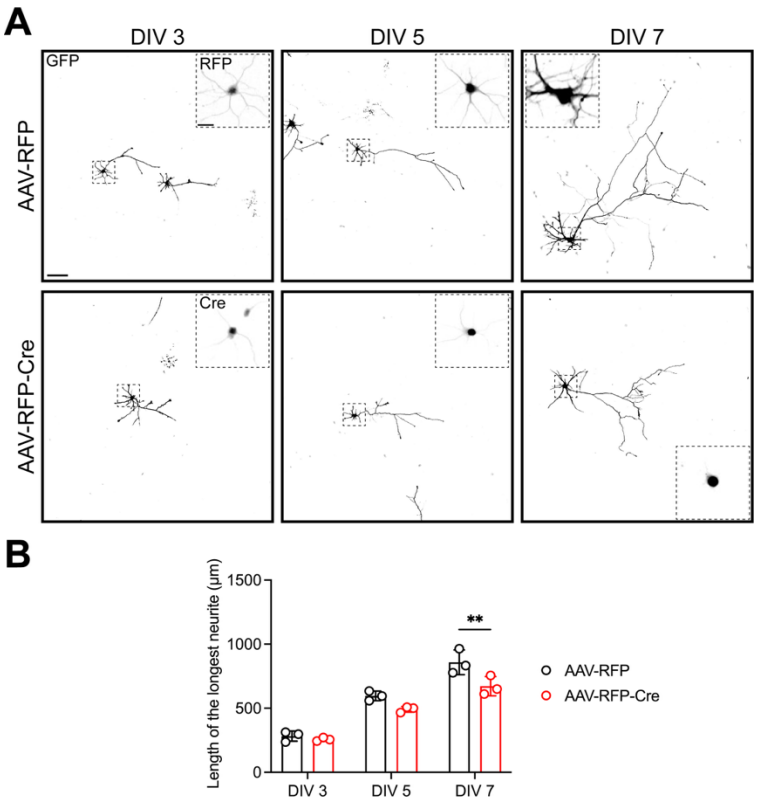

Figure 39: Arp3 loss reduces the length of the longest neurite

(A) Representative images of hippocampal neurons at the indicated time points in vitro. Cells were infected with either AAV-RFP or AAV-RFP-Cre 2 h after plating. Neurons were stained for GFP, and RFP or Cre. Images were created from stitched tiles. Scale bar 100 µm. Insets show magnification of the cell body and RFP or Cre expression in the cell. Scale bar of insets is 20 µm. (B) Quantification of the length of the longest neurite for (A). Values are plotted as mean ± SD from n = 3 independent experiments, with N = 475 (AAV-RFP) and 526 (AAV-RFP-Cre) for DIV 3, 419 (AAV-RFP) and 424 (AAV-RFP-Cre) for DIV 5, and 343 (AAV-RFP and 318 (AAV-RFP-Cre) for DIV 7, individual neurons traced. **p<0.01, not significant not indicated by two-way ANOVA with Sidak's multiple comparison post-test. Each mean was compared to the other mean in the same group (AAV-RFP vs. AAV-RFP-Cre).

Neurons become electrically active when growth rates are reduced

The downregulation of regenerative capacity during the development and maturation of neurons is not only based on the cytoskeleton. Further intracellular processes like gene expression, intracellular trafficking and synapse formation are involved in limiting regeneration when neurons mature (Hilton et al., 2024). The purpose of a neuron is the transmission of information. Previously, several reports indicate that the machinery for signal transmission, as well as signal transmission itself, contribute to growth and regeneration failure in DRG neurons (Enes et al., 2010; Hilton et al., 2022; Tedeschi et al., 2016). Cultured cortical neurons from rats lose their regenerative capacity in culture between DIV 4 and DIV 16 (Koseki et al., 2017). At this time, neurons develop electrophysiological properties associated with mature neurons. Treatment of adult DRG neurons with the depolarising agent potassium chloride inhibits growth in culture,

indicating that strong depolarisation in itself suppresses growth (Enes et al., 2010). In line, stimulation of firing activity of layer 2/3 neurons in the developmental cortex using optogenetic tools causes axon pausing (Malyshevskaya et al., 2013). Not only electrical activity itself negatively affects axon growth, but also components of the synaptic transmission machinery suppress growth. The voltage-gated calcium channel subunit a2d2, which triggers Ca^{2+} influx in response to AP firing, suppresses growth (Tedeschi et al., 2016). Further, the vesicle priming components RIM1, RIM2 and Munc13-1 of the presynaptic active zone inhibit axon growth (Hilton et al., 2022). Taken together, this indicates that components required for the fulfilment of the most important task, transmission of information, seem to prevent the neuron's growth and regeneration.

As previously reported for a reduction in regenerative capacity between DIV 4 and DIV 16, I showed that neurons start to downregulate growth rates between DIV 10 and DIV 14 (Figure 10) (Koseki et al., 2017). As this is the time when neurons in culture form functional synaptic connections (Ichikawa et al., 1993), I hypothesised that the onset of growth reduction correlates with the time hippocampal neurons become electrically active in culture.

To address this question, we measured and analysed the electrophysiological properties of growing and maturing hippocampal neurons in culture. For this purpose, the electrophysiological properties of neurons of different developmental ages were investigated with patch-clamp whole-cell recordings (Hamill et al., 1981). These experiments were performed by Dr. Andreas Husch. First, we looked at spontaneous excitatory postsynaptic currents (sEPSCs) as a measure for the formation of functional synaptic connections. When we quantified these spontaneous events at the indicated DIVs, we found that hippocampal neurons showed the first sEPSCs at DIV 7 (Figure 40A), 50% of the analysed neurons exhibited sEPSCs at this time point. The proportion of neurons with sEPSCs increased to 100% at DIV 14 (Figure 40A). Initially, the frequency of these postsynaptic currents was low up to DIV 10, but increased in DIV 14 and DIV 21 neurons (Figure 40B). Thus, at DIV 7 cultured neurons have functional synaptic connections, and the proportion of cells with functional synapses further increases on the subsequent days. However, at DIV 7 and DIV 10, when neurons have formed synaptic connections and are able to transmit information, the growth rate of these neurons is still high (Figure 10A, B and C).

Therefore, we next analysed the number of electrically active neurons, identified by the occurrence of spontaneous APs. Although the neurons were equipped with functional synapses to transmit information at DIV 7, the first spontaneous APs were only observed at DIV 10, respectively DIV 14 (Figure 40C). However, at DIV 10, only one neuron exhibited spontaneous APs. In contrast, 50% of the patched cells fired spontaneous APs at DIV 14, and 75% at DIV 21. Likewise, the spontaneous activity firing frequency

increased over time in culture (Figure 40D). The increase in the proportion of electrically active neurons at DIV 14 (Figure 40C), correlates with the onset of growth reduction observed between DIV 10 and DIV 14 (Figure 10C). Thus, as it was reported previously for cortical neurons (Koseki et al., 2017), hippocampal neurons became electrophysiological active and mature in culture when they decreased their growth propulsion. To what extent do the electrophysiological maturation and activity contribute to the downregulation of neurite growth in cultured neurons?

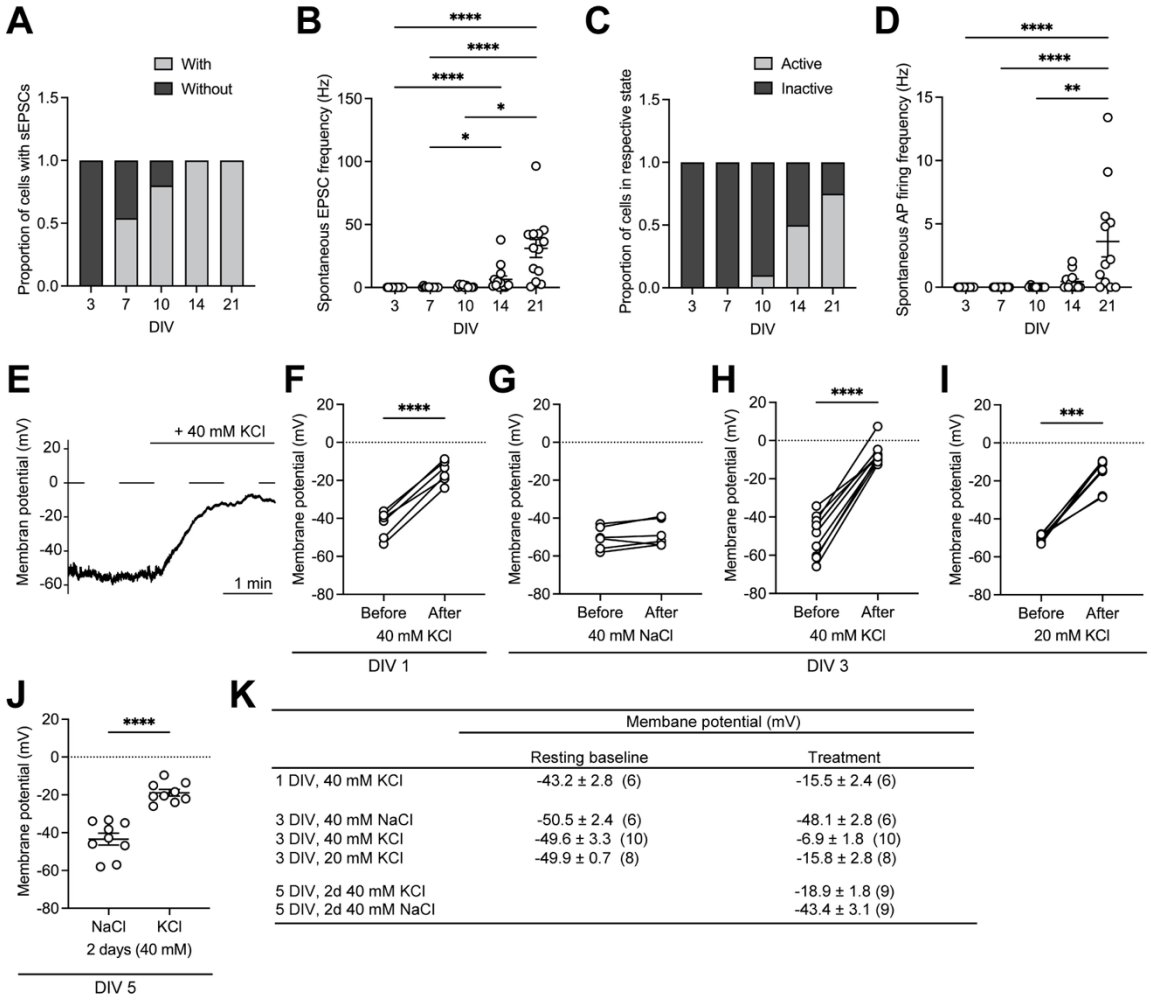

K

	Membane potential (mV)	
	Resting baseline	Treatment
1 DIV, 40 mM KCl	-43.2 ± 2.8 (6)	-15.5 ± 2.4 (6)
3 DIV, 40 mM NaCl	-50.5 ± 2.4 (6)	-48.1 ± 2.8 (6)
3 DIV, 40 mM KCl	-49.6 ± 3.3 (10)	-6.9 ± 1.8 (10)
3 DIV, 20 mM KCl	-49.9 ± 0.7 (8)	-15.8 ± 2.8 (8)
5 DIV, 2d 40 mM KCl		-18.9 ± 1.8 (9)
5 DIV, 2d 40 mM NaCl		-43.4 ± 3.1 (9)

Figure 40: Neurons become electrically active during maturation and are depolarised upon KCl treatment

(A) Proportion of patched hippocampal neurons with or without spontaneous excitatory postsynaptic currents (sEPCs) at the indicated time point *in vitro*. Values are plotted as the proportion of cells in the indicated state with n ≧ 2 independent cultures, with N = 15 (DIV 3), 13 (DIV 7), 10 (DIV 10), 14 (DIV 14), and 13 (DIV 21) individual neurons patched and analysed in total. (B) Quantification of the frequency of sEPCs at the indicated DIV. Values are plotted for every individual neuron analysed with mean ± SEM with the same number as in A. ****p<0.0001, *p<0.05, not significant not indicated by Kruskal-Wallis test with Dunn's multiple comparison post-test. Each mean was compared to every other mean. (C) Proportion of patched cells exhibiting spontaneous action potential (AP) firing (active) or no AP firing (inactive) at the indicated DIV. Values are plotted as the proportion of cells in the indicated group with n ≧ 2 independent cultures, with N = 14 (DIV 3), 12 (DIV 7), 10 (DIV 10), 12 (DIV 14), and 12 (DIV 21) individual neurons patched and analysed in total. (D) Quantification of the spontaneous AP firing frequency of the neurons in C. For inactive neurons, the firing frequency was set to 0. Values are plotted for individual cells with mean ± SEM with the same number as in C. ****p<0.0001, **p>0.01, not significant not indicated by Kruskal-Wallis test with Dunn's multiple comparison post-test. Each mean was compared to every other mean. (E) Representative trace recording of a patched neuron at DIV 3 with baseline recording in Ringer solution and the effect of influx of Ringer solution with elevated KCl (40 mM) as indicated. (F) Quantification of the membrane potential of patched hippocampal

neurons before and after application of 40 mM KCl at DIV 1. Values are plotted for every individual cell measured with n = 2, with N = 6 individual neurons measured in total. ****p<0.0001 by unpaired two-tailed Student's t-test. (G, H and I) Quantification of the membrane potential of patched hippocampal neurons before and after application of 40 mM NaCl, 40 mM KCl or 20 mM KCl at DIV 3 as indicated. Values are plotted for every individual cell measured with n ≧ 2 independent experiments, with N = 6 (40 mM NaCl), 10 (40 mM KCl), and 8 (20 mM KCl) individual neurons analysed in total. ****p<0.0001, ***p<0.001, not significant not indicated by unpaired two-tailed Mann-Whitney test. (J) Quantification of the membrane potential of patched hippocampal neurons at DIV 5 after two days in 40 mM NaCl or KCl as indicated. Values are plotted for individual neurons analysed with n = 3 independent experiments, with N = 9 individual neurons analysed (NaCl and KCl). ****p<0.0001, by unpaired two-tailed Student's t-test. (K) Summary table of the quantifications in F, G, H, I and J. Values for the membrane potential are stated as mean ± SEM for the resting baseline and treatment conditions.

Chronic depolarisation inhibits growth in polarised neurons

To study and mimic the effect of electrical activity and membrane depolarisation on various neuronal mechanisms, a wide variety of studies have used elevated extracellular potassium chloride (KCl) to depolarise the membrane of cultured neurons (Enes et al., 2010; Rienecker et al., 2020). For DRG neurons, it is known that elevated extracellular KCl blocks axon growth (Enes et al., 2010).

First, we confirmed that bath application of KCl leads to a depolarisation of the neuronal membrane (Figure 40E, F, G, H and I). Bath application of 40 mM KCl increased the membrane potential of DIV 1 hippocampal neurons from -43.6 ± 2.8 mV to -15.5 ± 2.4 mV (mean ± SEM), and DIV 3 from -49.6 ± 3.3 mV to -6.9 ± 1.8 mV (mean ± SEM), while 40 mM NaCl did not change the membrane potential, as expected. Also, an increase in extracellular KCl by only 20 mM leads to a depolarisation of the neuron's membrane (from -49.9 ± 0.7 mV to -15.8 ± 2.8 mV). After two days in elevated potassium, membrane potential was still increased compared to sodium chloride (NaCl) controls (-18.9 ± 1.8 vs. -43.4 ± 3.1 mV; mean ± SEM). These values are in line with reports for changes in membrane potential in response to elevated external K^+ (Rienecker et al., 2020). To evaluate the effect of increased extracellular K^+ on neuronal growth, young neurons were treated with 40 mM KCl 6 h after plating and analysed at DIV 2, similar to the previous described treatment scheme (Figure 13A). Quantification of the length of the longest neurite revealed no difference between NaCl or KCl treated neurons (Figure 41A and B). Further, elevated potassium levels did not affect polarisation of the young neurons (Figure 41C). When the same treatment was applied to DIV 3 neurons and the length of the longest neurite was measured at DIV 5 or DIV 7, depolarisation caused a reduction in neurite length (Figure 41D and E). After two days, only an increase to 40 mM external K^+ concentration caused a reduction in growth, while elevation to 20 mM had initially no effect on growth (Figure 41D and E). However, after four days in 20 mM KCl, neurons exhibited a reduction in the length of the longest neurite, which was not as strong as compared to 40 mM KCl. Hippocampal neurons were affected by elevated K^+ when they had polarised. Are hippocampal neurons only sensitive to high external K^+ around the time of polarisation? To test this, I treated DIV 5 neurons with high KCl and analysed the length

of the longest neurite two days after application. Treatment of DIV 5 neurons with 40 mM external KCl resulted in a 43% reduction in the length of the longest neurite (Figure 42A and B). Thus, hippocampal neurons become sensitive to elevated potassium levels and depolarisation of the membrane after polarisation when they elongate their axon.

To further investigate whether the reduction in neurite length was due to the depolarisation of the membrane and is reversible if neurons regain normal membrane potential, a rescue experiment was performed (Figure 42C). Hippocampal neurons at 3 DIV were exposed to either elevated KCl or NaCl as a control. After two days in elevated external salt concentrations, one batch of samples was kept for two further days in these conditions. Another batch of samples was flipped to new culture dishes with 40 mM NaCl (Figure 42C). Quantification of the length of the longest neurite showed that KCl-treated neurons had shorter neurites than the control after two days, as before (Figure 42C, D and E). When kept for another two days in these conditions, the difference in neurite length increased, indicating inhibited neurite growth in conditions of elevated K^+. When neurons after two days in 40 mM KCl were flipped to 40 mM NaCl on DIV 5 and allowed to grow for another two days, the restoration of normal membrane potential increased neurite length compared to continuous KCl treatment (Figure 42D and E). Hippocampal neurons become sensitive to membrane depolarisation when they have formed an axon, and depolarisation-mediated growth influence was reversible. However, chronic depolarisation of the membrane is not a physiological pattern and further experiments are required to elucidate how electrical activity affects and mechanistically prevents growth in CNS neurons.

Overall, my experiments have shown that initially the actin cytoskeleton is a regulator of neurite and axon growth. In young neurons it is growth restricting in form of actomyosin, but also involved in elongation, as actin polymerisation seems to enable fast growth rates. However, this role of actin changes and axon growth becomes less dependent on actin dynamics. Thus, the attenuated actin dynamics I observed are probably not the reason for growth reduction in maturing neurons. In contrast, the onset of electrical activity and its transmission in form of AP firing seem to be a cell-intrinsic cause of growth decline and suppression.

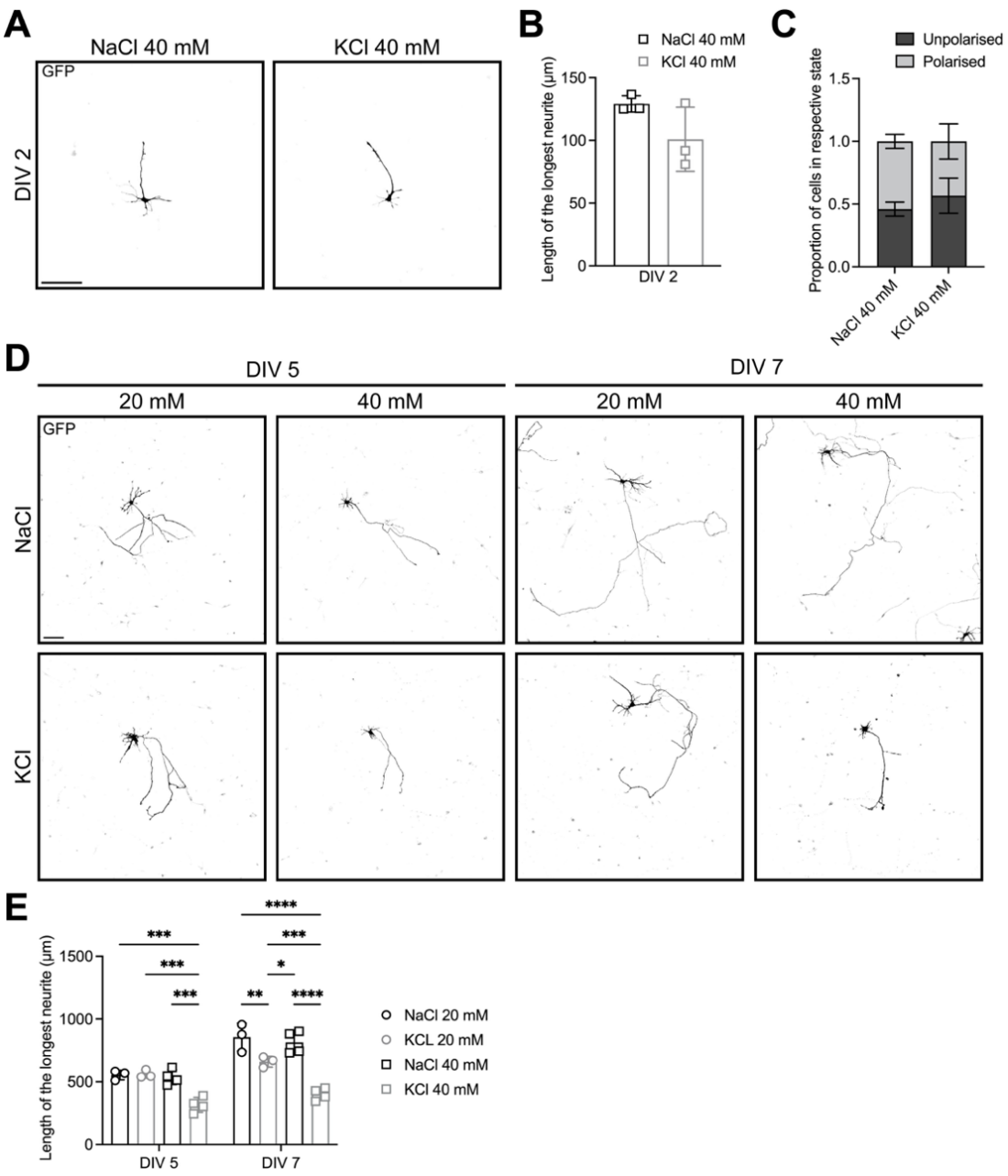

Figure 41: KCl treatment does not affect young neurons but middle stage neurons

(A) Representative images of hippocampal neurons at DIV 2 treated with 40 mM NaCl or 40 mM KCl 6 h after plating. Samples were stained for GFP. Images were created from stitched tiles. Scale bar 100 µm. (B) Quantification for the length of the longest neurite in (A). Values are plotted as mean ± SD from n = 3 independent experiments, with N = 374 (NaCl 40 mM) and 443 (KCl 40 mM) individual neurons quantified in total. Not significant not indicated by unpaired two-tailed Student's t-test. This experiment was performed and analysed by Annika Vohn. (C) Quantification for polarisation of neurons as percentage of neurons in the respective state, as indicated from (A). Neurons were considered polarised when the longest neurite was > 100 µm. Values are plotted as mean ± SD from n = 3 independent experiments with the same N as in (B). Not significant not indicated by two-way ANOVA with Sidak's multiple comparison post-test. (D) Representative images of hippocampal neurons with the indicated treatments on DIV 3 and fixed two or four days after. Neurons were stained for GFP. Images were generated from stitched tiles. Scale bar 100 µm. (E) Quantification for the length of the longest neurite from (D). Values are plotted mean ± SD from n = 3 independent experiments, with N = 327 (NaCl 20 mM), 424 (KCl 20 mM), 370 (NaCl 40 mM) and 305 (KCl 40 mM) for DIV 5, 335 (NaCl 20 mM), 336 (KCl 20 mM), 405 (NaCl 40 mM) and 184 (KCl 40 mM) for DIV 7, individual neurons quantified in total. ****p<0.0001, ***p<0.001, **p>0.01, *p<0.05, not significant not indicated by two-way ANOVA with Tukey's multiple comparison post-test. Each mean was compared with every other mean in the respective group.

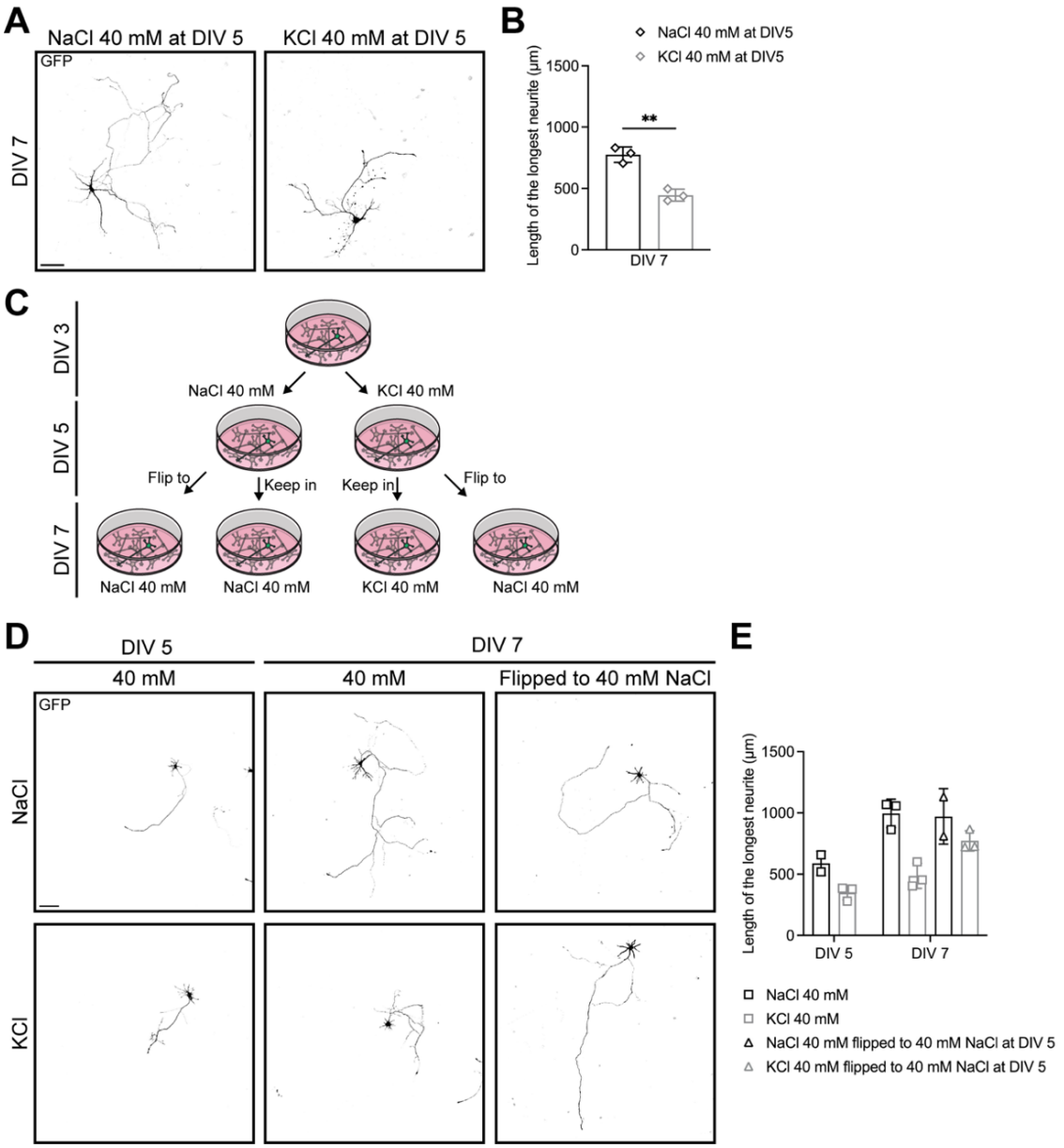

Figure 42: KCl induced growth reduction is reversible

(A) Representative images of DIV 7 hippocampal neurons treated at DIV 5 with either 40 mM NaCl or 40 mM KCl as indicated. Neurons were stained for GFP. Images were created from stitched tiles. Scale bar 100 µm. (B) Quantification for the length of the longest neurite in (A). Values are plotted as mean ± SD from n = 3 independent experiments, with N = 386 (NaCl 40 mM) and 164 (KCl 40 mM) individual neurons traced in total. **p<0.01 by unpaired two-tailed Student's t-test. (C) Experimental design for rescue of the KCl effect. On DIV 3, cultured hippocampal neurons are either treated with 40 mM NaCl or KCl. After two days, neurons are either kept for another two days in the previous treatment or are flipped to a new dish with 40 mM NaCl for two days. (D) Representative images of hippocampal neurons with the indicated treatment fixed at the stated time in culture. Treatment was applied at DIV 3. Neurons were stained for GFP. Images were generated from stitched tiles. Scale bar 100 µm. (E) Quantification for the length of the longest neurite for neurons in (D). Values are plotted as mean ± SD from n ≧ 2 independent experiments, with N = 260 (NaCl 40 mM) and 428 (KCl 40 mM) for DIV 5, 292 (NaCl 40 mM), 283 (KCl 40 mM), 174 (NaCl 40 mM flipped to 40 mM NaCl at DIV 5) and 190 (KCl 40 mM flipped to 40 mM NaCl at DIV 5) for DIV 7, individual neurons quantified in total. This experiment was performed by Annika Vohn.

Discussion

Neurons are the building blocks of our nervous system and the foundation for our complex abilities, especially in cognition, but also in controlling our body. During development, neurons possess an enormous growth capacity, able to connect to the various parts of an organism. In adult CNS neurons, this growth capacity is blocked by an inhibitory environment and a low intrinsic growth propulsion (Bradbury and Burnside, 2019; He and Jin, 2016; Quraishe et al., 2018).

One factor that is involved in orchestrating growth during development, and is required for regeneration in adulthood, is a dynamic actin cytoskeleton (Bradke and Dotti, 1999; Tedeschi et al., 2019). For maturing neurons, an increased stability of F-actin was reported (Zhang and Benson, 2001). Therefore, to study mechanisms that are involved in neuron growth during development and in the downregulation of growth propulsion in maturing neurons, I focused on the actin cytoskeleton. Using a cell culture approach, combined with pharmacological and genetic treatments, I found that F-actin intensity and turnover rates are reduced in developing neurons while they are still able to extend their axons. Further, pharmacological stabilisation of actin filaments and inhibition of actin polymerisation affected neurite length in early, but not at later stages of neuronal development. In contrast, depolarisation of neurons, induced by elevated KCl reduced neurite length only in polarised neurons. Thus, developing neurons reduce their dependency on actin filaments for growth propulsion in the course of development and become vulnerable to depolarisation.

Growth reduction of maturing hippocampal neurons is not caused by reduced actin turnover rates

I observed that cultured neurons start to decrease their growth rate during late development, after 10-14 days in culture (Figure 10), when neurons have formed functional synaptic connections and became electrically active and mature (Figure 40) (Basarsky et al., 1994; Koseki et al., 2017). In the developing organism, neurons grow until they reach their designated target area, branch out and form synaptic connections. Though in the brain, most of the synaptic connections are formed along the axon shaft as *en passant* synapses and not at axon terminals (Sudhof, 2021), axons have to remain within the correct tissue region. Therefore, to specifically form contacts with partners in such designated areas, neurons have to downregulate their growth at the right place and at the right time to not cross their target area without stopping, otherwise neurons might misconnect (Bradke, 2022). The mechanisms that induce the reduction in elongation speed or instruct the neuron to stop growing are unclear. Among these mechanisms could

be guidance cues, adhesion molecules, target-derived stop signals, or an intrinsic program that instructs the neuron when to stop.

In superior cervical ganglion (SCG) neurons of the sympathetic nervous system of the PNS, morphology and growth are regulated by target-contact with cardiac myocytes and downregulation of bone morphogenetic protein-dependent growth pathways (Moon and Birren, 2008). These neuron-target interactions contribute to target-dependent growth arrest. Comparatively, in CNS neurons, ephrins regulate the formation of terminal axonal arbors (Gao et al., 1999; Mann et al., 2002). Precursor and pre-migratory cerebellar granule neurons possess a stop-growing signal only for their appropriate afferent mossy fibres, dependent on heparin-binding factors (Baird et al., 1992; Manzini et al., 2006). Heparin-binding factors both inhibit and promote axon growth, depending on the context and specific interactions with other molecules (Kinnunen et al., 1996). In *Drosophila*, two subfamilies of the immunoglobulin superfamily, defective proboscis extension response (Dpr) proteins and Dpr interaction proteins, were identified as candidates for synapse targeting that allow the formation of specific neuronal connectivity (Ashley et al., 2019; Cheng et al., 2019). Based on a “lock and key” structure of these proteins, neurons identify the correct target and form synaptic connections. It is possible, that the binding of such synaptic targeting proteins may instruct the neuron to stop growing as it reaches its specific target. Whether such a targeting mechanism is involved in the suppression of regeneration in injured neurons is of great interest.

Such target-dependent growth suppression does not only have to originate from the axonal terminus, but might also suppress growth, sprouting and branching and maybe even regeneration along the axon shaft, since neurons in the brain mainly form *en passant* synapses (Sudhof, 2021). Many different adhesion molecules are involved in synapse formation, including neural cell adhesion molecule, neuroligin/neurexin, and protocadherins (Washbourne et al., 2004). In line with such a hypothesis, neurexin-1α regulates neurite growth in rat hippocampal neurons (Wang et al., 2019). Addition of the neurexin-1α ligand neuroligin to the media, decreased neurite growth in a Ca^{2+}-dependent manner. However, whether target-derived stop signals and the binding and formation of pre- and postsynaptic molecules and sites instruct a growth reduction *in vitro* is debateable. A pure primary hippocampal culture does not provide neuronal targets as *in vivo*. Hippocampal pyramidal neurons also form projections to other areas in the brain (Arszovszki et al., 2014; Lee et al., 2024) and might receive their stop-growing signals from such extrahippocampal regions. Though, pyramidal neurons also form intra-hippocampal connections.

I found that cultured hippocampal neurons already have functional synapses at DIV 7 (Figure 40A and B), which is in line with observations of previous studies in cultured rat hippocampal neurons (Grabrucker et al., 2009), similar to the time point observed here

(Figure 40). The proportion of neurons with sEPSCs further increased over time in culture. Growth rates of neurons are still high at DIV 7 and DIV 10, thus, formation of synaptic connections by itself does not seem to be a cause of growth reduction *in vitro*. Whether an active transmission of signals via synaptic connections affects growth will be discussed later.

The downregulation in growth speed and capacity might not only be instructed by extracellular mechanisms but could also be based on an intrinsic program that causes neurons to stop. Actin filaments and microtubules are the main cytoskeleton components required for various developmental processes. The current concept is that dynamic actin filaments and stable microtubules are required for neurite formation, axon elongation, and regeneration of injured axons (Hilton et al., 2024; Neukirchen and Bradke, 2011). In young neurons, a more rigid actin cytoskeleton restricts the outgrowth of the axon (Bradke and Dotti, 1999). My results are partially in line with this. Only low concentrations of actin polymerisation inhibitors Cyto D and Lat A enhanced neurite growth (Figure 14 and Figure 15). The growth promoting effect of 10 nM Cyto D correlates with more bundled microtubules that protrude further into the leading edge of neurite tips (Figure 16 and Figure 17). A similar effect was observed for low concentrations of Lat A (Dupraz et al., 2019), thus, the growth promoting effect of 50 nM Lat A I report here, might also be a result of more bundled microtubules. Low amounts of Lat A (5 nM) caused a reduction in actin arcs, similar to inhibition of myosin-II with Blebb. Probably, the low concentrations of actin polymerisation-inhibiting drugs affect mainly actin arcs and actomyosin, which act as gate keeper for microtubules to enter the P-domain in young neurons (Dupraz et al., 2019). Higher concentrations of Cyto D and Lat A caused a growth reduction in young neurons, partially caused by de-bundled microtubules. Similar to low concentrations of Cyto D and Lat A, the higher turnover rate of the actin cytoskeleton in the growth cone of the neurite designated to become the axon (Bradke and Dotti, 1999), might be a mechanism to remove actin arcs and actomyosin, enabling axon formation in WT neurons.

Reducing actin turnover, making actin filaments more rigid may also restrict and reduce the growth of mature neurons. In line with previous reports (Bradke and Dotti, 1999), I found that young polarised neurons exhibit a high turnover rate in axonal growth cones, as the majority of F-actin was depolymerised within 10 minutes of Cyto D treatment (Figure 12). In contrast, more mature neurons exhibited reduced actin turnover rates in axonal growth cones as more F-actin remained after 10 minutes in presence of 1 µM Cyto D. At the same time, the highest growth rates of neurons were observed after seven to ten days in culture (Figure 10). Thus, reduced actin turnover, *per se*, does not cause a reduction in growth speed in old hippocampal neurons. This suggests that the dependency on high actin turnover for neurite growth changes in the course of development. In young neurons, actin turnover is required for the formation of neurites and outgrowth of the specified axon

(Bradke and Dotti, 1999; Flynn et al., 2012). The proposed developmental switch in the dependency on actin turnover is supported by the fact that the neurite extension rate of young neurons within the first two days in culture is negatively affected by treatment with the actin stabilising drug Jasp (Figure 13). In contrast, after polarisation, neurons seem to tolerate mild stabilisation of actin filaments and extend their axons undisturbed between DIV 3 and DIV 9. Previously, it was described that 5 nM Jasp, the same concentration used here, prevents the transition from stage 1 to stage 2 and the formation of neurites (Flynn et al., 2012). Further, Jasp affected axon length of embryonic chick DRGs and retinal ganglion cells in a concentration-dependent manner (Gallo et al., 2002). 5 nM Jasp decreased the axon length of these neurons by two-thirds. Also, inhibition of actin turnover resulted in axon retraction by myosin-II activity. Such a Jasp-mediated axon retraction phenotype was not observed here. It cannot be excluded that higher Jasp concentrations may have an effect at late developmental stages, but it seems that actin turnover rates are especially important in early phases of development in the context of neurite and axon formation. Though neurons reduced turnover rates after polarisation, they were able to enhance their elongation rates (Figure 10). Thus, actin turnover rates are not necessarily correlated with growth rates, but they are essential for initiating neurite formation, axon specification and regeneration (Bradke and Dotti, 1999; Flynn et al., 2012; Tedeschi et al., 2019). Whether the reduction in actin turnover rates is a developmental requirement is not clear. To address this question, one needs to enhance the actin turnover at later developmental time points and analyse the effect. One way to experimentally enhance actin turnover could be the overexpression or manipulation of cofilin and its activity state. Cofilin is involved and able to enhance actin turnover (Flynn et al., 2012; Tedeschi et al., 2019). Further, it is feasible that the reduction in actin turnover is only a side effect with little biological relevance later in development.

At the same time, when actin turnover rates were decreased, axonal growth cone size also decreased (Figure 11). In *Aplysia* bag cell neurons and rat hippocampal neurons, increased growth cone size correlates with decreased neurite growth rates (Bradke and Dotti, 1997; Ren and Suter, 2016). Here, a decrease in growth cone size over time in culture was observed (Figure 11). In the first week of culture, this decreased growth cone size is paralleled by an acceleration of neurite growth rates (Figure 10 and Figure 11). Although the growth cone size continued to decrease during the second week of culture, up to DIV 14, the growth rates also declined during this period (Figure 10 and Figure 11). Therefore, growth cone size alone is not predictive of growth rates. However, when hippocampal neurons are cultured in a 3D environment, growth cones have a reduced volume compared to 2D conditions and extend neurites faster (Santos et al., 2020). This enhanced neurite length is not attributed to reduced growth cone size but rather to the absence of actin arcs, which restrict microtubule advance into the P-domain (Dupraz et

al., 2019; Santos et al., 2020). The well-known organisation of growth cones with a separation of the C- and P-domain by actin arcs in the transition zone (Figure 8), is probably attributed to the unphysiological culture condition on stiff glass coverslips in a 2D environment, augmenting actin arc formation (Santos et al., 2020). Since 3D environments more closely resemble *in vivo* conditions, it is likely that growth cones in the developing organism are rather similar to those observed in a 3D gel instead of a 2D culture. However, studies investigating the organisation of growth cones *in situ* are still lacking, but are necessary to unravel how growth cones move through the complex environment of a developing organism (Alfadil and Bradke, 2023).

Smaller growth cones are also associated with better regeneration and growth *in vivo (Ertürk et al., 2007)*. When CNS axons are injured, they mainly form an enlarged bulb-like structure at the axon tip with restricted axonal growth. The formation of these retraction bulbs is based on destabilised and disorganised microtubules. Microtubule stabilisation prevents and supports the transformation of retraction bulbs into regrowing growth cones (Ertürk et al., 2007; Ruschel et al., 2015). Also, paused growth cones are associated with disorganised microtubules (Dent and Kalil, 2001). Growth paused neurites have larger growth cones than actively growing neurites. In such paused growth cones, microtubules form loops and are bent (Dent and Kalil, 2001). My work shows that, when actin filaments are depolymerised, the growth cone becomes enlarged and neurons extend slower than vehicle treated neurons (Figure 14 and Figure 16). These growth cones lose the clear separation of axon shaft and growth cone area at the growth cone neck and look bulb-like. Such bulb-like structures were observed after treatment of E8 DRG chick embryo neurons with Cyto B (Yamada et al., 1971). These “rounded-up” growth cones stop elongating.

On the other hand, chick embryonic DRGs extend neurites for several hundred micrometres in the presence of Cyto B without forming filopodia, lamellipodia or a typical growth cone (Marsh and Letourneau, 1984). Also, it was reported that for axon formation in hippocampal neurons, a growth cone is not necessary (Ruthel and Hollenbeck, 2000). Though, the growth state of a neurite branch was reflected by the growth cone size. The growing neurite had a more elaborate and dynamic growth cone, while, the non-growing neurite had a small and inactive growth cone (Ruthel and Hollenbeck, 2000). In contrast, it seems to be the opposite *in vivo*, where rapidly elongation axons had growth cones with a rather simple morphology (Bovolenta and Mason, 1987; Tosney and Landmesser, 1985). Paused axons, however, showed a more complex and elaborate morphology of growth cones. Successful regeneration is linked to neurons being able to re-form a growth cone (Bradke et al., 2012). It is undisputed that the growth cone guides the axon to its target region and is therefore essential for correct pathfinding and guidance for proper wiring of the whole system (Kalil and Dent, 2005). Even the leading edge of migrating neurons forms a growth cone involved in driving neuronal migration (Nakajima et al.,

2024). Whether guidance of growing and migrating neurons is its only function or whether and how it contributes to growth itself is still unclear. It might be that in certain conditions a growth cone is needed, while in others neurons grow without a typical growth cone. In line with this, DRG neurons from different developmental stages of chick embryos were able to extend at similar rates, though exhibiting different sizes and morphologies of growth cones (Jones et al., 2006).

Actin polymerisation is required for fast axon elongation in early developmental phases

The actin cytoskeleton and its role in growth have been controversially debated. Actin dynamics are indispensable for axon guidance and pathfinding, as it is the main component responsible for growth cone formation and morphology, as well as steering (Kalil and Dent, 2005). Some reports consider actin polymerisation necessary for growth and elongation while others show opposing results. Is actin filament polymerisation required for neurite growth?

I observed a decrease of 50% of F-actin intensity in growth cones of DIV 14 neurons compared to younger neurons (Figure 11). Less actin filaments implies also reduced polymerisation activity based on the number of filaments. If actin polymerisation at the leading edge would drive growth cone advance, as it drives cell motility of keratocytes (Pollard and Borisy, 2003) or myelin sheath formation of oligodendrocytes (Nawaz et al., 2015), then a decrease in F-actin intensity could explain decreasing growth rates because of reduced pushing forces at the leading edge (Figure 10). A similar developmental decrease in actin filament intensity in neurons is observed in explants of embryonic chicken DRG neurons (Jones et al., 2006). In E14 DRG explants, growth cones have reduced F-actin content compared to E7 DRG neurons. However, despite less actin filaments, extension rates are similar. Further, while E14 neurons are able to elongate neurites when actin polymerisation is blocked by Cyto D or Lat A, neurons of embryonic stage 7 require actin filaments and their polymerisation, suggesting a developmental switch in the dependency on actin filaments for neurite elongation, as I propose above.

I discovered a similar effect for inhibition of actin polymerisation at different developmental stages in hippocampal neurons. When I treated young neurons either 6 h after plating or at DIV 3 with Cyto D or Lat A, neurite length was reduced. There was no effect on neurite length when DIV 7 neurons were treated, thus, neurons reduced their dependency on actin filament polymerisation during development. However, in young neurons, the polymerisation of actin filaments contributes to the forces required for fast elongation of neurites (Figure 23). Actin polymerisation is a main driver of cell motility, and almost every form of cell migration relies on assembly and disassembly of actin filaments (Mogilner and

Oster, 1996; Schaks et al., 2019). Different models of cell migration have been used to explain axon growth mechanisms. These include the coupling of cell-internal forces generated by actin polymerisation and its retrograde flow to the extracellular matrix via integrin-dependent adhesions, enabling the growth cone to pull itself forward (Alfadil and Bradke, 2023; Lowery and Van Vactor, 2009). Others report that actin polymerisation is the main driver of neurite growth even in a low-adhesive environment (Chia et al., 2016). Thus, similar to cell motility of keratocytes, it is suggested that actin polymerisation is the driver of plasma membrane protrusion leading to the advancement of the growth cone (Fritz-Laylin and Titus, 2023; Pollard and Borisy, 2003; Schaks et al., 2019). My results support the model in which actin polymerisation, at least partially, contributes to drive growth cone advance.

Contrary, others reported that neurons of the embryonic mouse or rat hippocampus were able to form and extend an axon with depolymerised actin filaments and outgrowth rates were shown to even increase with such conditions (Ruthel and Hollenbeck, 2000; Santos et al., 2020). In a further study, no effect on axon length after Cyto B or Lat A treatment in cortical neurons of Syrian hamsters was observed (Dent and Kalil, 2001). All showing that neurite and axon elongation is not dependent or even hindered by the actin cytoskeleton. Such an independence on actin filaments for axon elongation, I only observed at late developmental stages. DIV 7 neurons grew undisturbed in the presence of Cyto D and Lat A (Figure 14 and Figure 15). Further, while DIV 14 neurons have 50% less F-actin intensity compared to DIV 2 neurons, they showed similar elongation rates (Figure 10 and Figure 11). These observations support the hypothesis that maturing neurons undergo a switch in the dependency on F-actin for their mode of growth. This also means that the reduced intensity of actin filaments and thus less actin polymerisation at the leading edge in growth cones of DIV 14 neurons is not the reason why neurons exhibit reduced growth rates at this stage. At a certain stage of development, neurons become less dependent on these structures, as shown by my observations that actin turnover rates decrease in DIV 7 and older neurons and that these neurons tolerate actin filament stabilisation by Jasp. Together these findings suggest a developmental shift in the role of actin dynamics.

Microtubule bundling and their contribution for neurite elongation

In unpolarised neurons, 6h after plating, the effect of actin depolymerisation on neurite growth was concentration dependent. Very low amounts of Cyto D or Lat A (10 nM and 50 nM, respectively) resulted in enhanced neurite length after 42 h of treatment. Higher concentration restricted neurite growth. Such a concentration-dependent effect on neurite length was reported before for embryonic chick DRG neurons, though not statistically

significant (Letourneau et al., 1987). When I used the same concentrations at a time point when neurons were polarised (DIV 3), all treatments reduced the length of the longest neurite (Figure 14 and Figure 15). This growth-reducing effect was not observed anymore in older neurons at DIV 7. Are these differential effects solely explained by different requirements for actin polymerisation, or does the actin cytoskeleton have a further function?

When I looked at growth cones of Cyto D-treated neurons at the different stages, I observed that the effect on neurite length at the different stages can be explained by differences in microtubule bundling (Figure 14 and Figure 16). A low concentration of Cyto D (10 nM) resulted in more bundled microtubules in DIV 1 neurons, which extended further into the leading edge compared to the control, causing longer neurites (Figure 14, Figure 16 and Figure 17). A similar effect was previously reported for the treatment of hippocampal neurons with 5 nM Lat A (Dupraz et al., 2019). In this study, the treatment with the actin polymerisation inhibitor reduced the formation of actin arcs, allowing microtubules to protrude further into the leading edge, as observed here. Additionally, growth cones with bundled microtubules were observed more frequently (Dupraz et al., 2019). So probably, also here, the low concentration of Cyto D removes actomyosin that blocks microtubules and causes a splay of these polymers in the growth cone T-zone. In contrast, when a fivefold higher concentration of Cyto D was used, the splay of microtubules was enhanced and began already further down the axon shaft (Figure 16).

Why are neurons treated with high concentrations (0.5/1 µM) of Cytochalasins able to extend a neurite?

With low concentrations of Cyto B and also Cyto D, neurite ends form enlarged growth cones and give microtubules the space to disorganise. This could be due to the maintenance of cortical actin underneath the membrane and microtubules directing their pushing force unorganised against the site of the growth cone and axon shaft (Alves-Silva et al., 2012; Miller and Suter, 2018). With higher concentrations of Cytochalasins, also the cortical actin is dismantled and collapses, and neurite tips and shafts become thin. These thin neurite tips keep microtubules together, thereby enabling growth to a certain degree, similar to the microtubule bundling experiments performed here (Figure 25, Figure 26, Figure 27, and Figure 28) (Bradke and Dotti, 1999; Bradke and Dotti, 2000; Marsh and Letourneau, 1984; Santos et al., 2020).

Thus, actin filaments have an important function in organising microtubules and guiding them in the right direction, keeping them bundled. When microtubules are disorganised, they will direct their force against the sides of the axon and growth cone (Miller and Suter, 2018). This is exactly what can be observed in retraction bulbs that form after an axonal injury (Ertürk et al., 2007), in growth cones when actin-microtubule-crosslinkers like Tau are knocked down (Biswas and Kalil, 2018), and in neurite tips when actin filaments are

depolymerised as observed here (Figure 16). In neurons that have already polarised, a splay and debundling of microtubules was observed for all Cyto D treatments, reducing axon elongation (Figure 14 and Figure 16). In more mature neurons, the depolymerisation of actin filaments did not cause microtubule de-bundling, because, presumably, other structures or proteins maintain microtubule organisation at this stage.

One structure that could be responsible for keeping microtubules bundled at this stage is the MPS composed of actin-spectrin rings (Costa and Sousa, 2021). These actin-spectrin rings start to form in the proximal axon but are not present in distal axon regions in young neurons at DIV 2 (Zhong et al., 2014). Over time, the MPS is also established in more distal parts of the axon and becomes more stable based on the recruitment of the actin filament capping protein adducin (Zhong et al., 2014). In older neurons, at DIV 10, high Lat A concentrations take longer to affect the periodic pattern of these rings. These concentrations of Lat A (20 µM) are at least 40 times higher than the concentrations used in my experiments. It is possible that at later stages, at DIV 7, the MPS is not affected by the low amounts of Cyto D and Lat A that were used here, keeping the microtubules bundled, maintaining normal axon elongation rates. Super-resolution imaging techniques are required to investigate whether the MPS is affected at DIV 7 by the applied treatment. Another possibility is that the expression of microtubule bundling proteins, such as Tau, MAP2c or doublecortin, is increased and keeps microtubules bundled (Bodakuntla et al., 2019). However, these proteins are already expressed in young neurons and fail to maintain microtubule bundling at this stage (Figure 16) (Dehmelt et al., 2003; Dotti et al., 1987; Fung et al., 2011). Another protein similar to TRIM46 may become expressed in the course of maturation to maintain microtubule bundles in the distal axon. TRIM46 forms stable compartments with bundles of parallel microtubules in the proximal axon (van Beuningen et al., 2015).

When microtubules are de-bundled, neurons showed enhanced EB3 comet growth speed (Figure 19), though this increase cannot compensate for the disorganisation of microtubule bundles. Also increased microtubule stability did not restore neurite elongation rates (Figure 20). Thus, even an increased microtubule number in the neurite shaft (Figure 22) fails to push the neurite forward when they are not properly organised. In line with this, when the de-bundling of microtubules was prevented by overexpression of the MAPs MAP2c and Tau, the neurite length was partially restored (Figure 25, Figure 26, Figure 27 and Figure 28). Here, splaying of microtubules was prevented by increasing the amount of microtubule bundling proteins before the treatment was applied, which causes microtubule splay. It should be investigated whether overexpression of MAPs can re-bundle microtubules that are already de-bundled. Tau was previously shown to be involved in bundling of microtubules in the growth cone (Biswas and Kalil, 2018). Both MAPs also bind and interact with actin filaments (Biswas and Kalil, 2018; Roger et al.,

2004), to which extent the interaction of these MAPs with F-actin contributes to the partial rescue in neurite length, should be addressed in the future.

Restoring microtubule bundling might also be a strategy to overcome the formation of retraction bulbs that form after an injury to the axon (Ertürk et al., 2007). For this purpose, a MAP like Tau could be overexpressed in injured neurons. Here, Tau can fulfil two functions: it can stabilise microtubules and stimulate their growth, but also keep these microtubules together in a bundle. Site-specific pseudo-phosphorylation of Tau promote distinct microtubule organisations into single stable microtubules, stable bundles or dynamic bundles (Prezel et al., 2018). Transforming retraction bulbs into a growth cone promotes regeneration, as reported for the stabilisation of microtubules with Epothilone B (Ruschel et al., 2015). Therefore, overexpression of Tau in injured neurons could potentially fulfil a similar function. Using Tau to stabilise and bundle microtubules in injured axons would require targeted delivery and potentially a neuron-specific expression of a Tau construct.

Nevertheless, a global treatment with a microtubule stabilising compound like Taxol or Epothilone B, has the advantage of also decreasing fibrotic scarring in the injured spinal cord, making the environment more permissive for regeneration (Hellal et al., 2011; Ruschel et al., 2015). It remains to be tested whether the regeneration promoting effect of microtubule stabilisation is based on the stabilisation in the neurons, fibroblasts or the combination of both. However, with a virus-based delivery system one could overcome systemic administration-based side effects which could appear when a compound is injected intraperitoneal or subcutaneously, and one could specifically target a certain cell-population. Thus, an expression-based system has the advantage of enabling to target specific cell-populations and can prevent side-effects based on a global systemic application of a drug. Expression of a microtubule bundling and stabilising protein in a specific cell-type may also help to disentangle whether the observed regeneration promoting effect of microtubule stabilising drugs is based on the effect on neurons, fibroblast or the combination of both (Hellal et al., 2011; Ruschel et al., 2015). Though, in case of microtubule stabilisation, it is beneficial to not only target neurons but also affect fibroblasts to reduce scarring, but in other scenarios like a Rho A knockout, affecting also glia cells has a negative effect on regeneration (Hellal et al., 2011; Ruschel et al., 2015; Stern et al., 2021). This shows that it is important to investigate the effect of a treatment not only in one cell type but also in all those cells that are affect by the treatment to evaluate their influence on the outcome.

Microtubule bundling defects are also relevant in other disease contexts. In a mouse model of Huntington's disease, axon growth is attenuated and neurons exhibit disorganised and de-bundled microtubules in their growth cones (Capizzi et al., 2022). The bundling defect is attributed to the microtubule-binding nuclear/mitotic apparatus

protein 1, which directly binds and bundles microtubules. These microtubule-bundling defects result in axons that fail to reach their final destination missing their envisaged connection partners (Capizzi et al., 2022). This highlights the requirement of properly bundled microtubules for axon elongation during development.

However, restoring microtubule bundling is not enough to fully compensate for blocked actin polymerisation and restore neurite length. Miller and Suter stated that the pushing force of microtubules is too small to drive axon elongation (Miller and Suter, 2018). In line with this, the joint force of bundled microtubules is not enough to have a similar neurite length as control neurons after treatment with actin polymerisation inhibitors Cyto D or Lat A, or when microtubules are stabilised by Taxol (Figure 20 and Figure 24). Thus, actin polymerisation contributes to the mechanism that drives axon elongation but probably independent of adhesions (Santos et al., 2020).

Over time in culture, microtubules in neurite tips become more bundled (Figure 18), which could explain increasing growth rates (Figure 10 and Figure 18). In a 3D environment, growth cones are smaller and microtubule volume is decreased compared to 2D growth cones (Santos et al., 2020). Thus, also here, increased bundling of microtubules could be an explanation for increased neurite length. It is clear that when microtubules are bundled together, they can join their forces upon assembly and push together. In contrast, when microtubules are splayed and more loosely arranged, the pushing force generated by every single microtubule spread over a larger area and results in lower growth rates.

In the concept of Miller and Suter, microtubules would need to stall against a barrier to generate the required pushing force, stating that microtubules are not stalled. What if actin filaments and the retrograde flow of actin in the growth cone periphery are such a stalling barrier? Currently, the actin cytoskeleton is considered only as a hindrance and barrier for microtubules, preventing them from pushing the growth cone forward. This theory was demonstrated by Forscher and Smith, who have shown that microtubules quickly fill the actin-rich area of a growth cone when actin is depolymerised (Forscher and Smith, 1988). In line with this, I observed, similar to others, that depolymerisation of actin filaments promotes microtubule protrusion into the periphery (Figure 17) (Dupraz et al., 2019; Santos et al., 2020). However, here, I observed this enhanced protrusion of microtubules only in one condition, low Cyto D in young neurons (DIV 1), which also exhibited longer neurites. With higher Cyto D concentrations and in older neurons, the depolymerisation of actin did not cause enhanced microtubule advance towards the leading edge based on quantification of tubulin intensity (Figure 17). Filopodia can guide microtubules into the P-domain (Schaefer et al., 2002). When actin organisation is affected (Figure 16), it could be that filopodia no longer guide microtubules to the periphery and these then fail to protrude further to the leading edge because of missing guidance.

The interaction of actin filaments and microtubules is organised by crosslinking proteins. These crosslinkers coordinate different dynamics of actin and microtubules (Coles and Bradke, 2015). The crosslinker MACF1 is required for axon and dendrite outgrowth (Ka and Kim, 2016). Similarly, when Tau was knocked down, dynamic microtubules remained in the central domain of the growth cone and were unable to align, reducing axon elongation (Biswas and Kalil, 2018). Coupling growing microtubule ends to actin via crosslinkers at the overlap between these filaments can generate and transmit forces (Alkemade et al., 2022). I propose that coupling growing microtubule ends to actin filaments stalls the polymerising microtubules and generates a pushing force to drive neurite elongation. In line with this hypothesis, EB3 comet speed is reduced in the P-domain compared to the C-domain of hippocampal neurons (Dupraz et al., 2019). When actin arcs are removed, microtubules advance further to the leading edge, increasing the overlap of microtubules and actin filaments, enabling more interaction and cross-linking, potentially providing more force, enhancing neurite elongation. If all actin filaments are depolymerised, the interaction of microtubules with retrogradely flowing actin is disturbed, and neurite elongation is stalled.

Other microtubule dynamics, including microtubule sliding and bulk forward movement of microtubules, were considered as drivers of growth (Athamneh et al., 2017). Though, also for bulk forward movement, assembly of microtubules is necessary. Recently, microtubule retrograde flow was reported as an additional form of microtubule dynamics (Burute et al., 2022; Schelski and Bradke, 2022). Slowdown of microtubule retrograde flow is sufficient to induce the formation of an axon. How these various forms of microtubule dynamics, besides polymerisation, contribute to driving axon elongation needs to be addressed and disentangled in the future.

Other eukaryotic cells migrate by coupling the intracellular force of the actin cytoskeleton to the environment (Reversat et al., 2020). In contrast, as elaborated before, neurons depend on microtubules, but it seems that actin filaments also play a role in the growth mechanism, at least in early phases of neurite and axonal growth, as I have shown by my experiments.

Usually, force coupling to the environment is mediated by transmembrane adhesion receptors, as hypothesised for axon growth mode in the “clutch” hypothesis (Lowery and Van Vactor, 2009). However, hippocampal neurons grow independent of coupling the actin cytoskeleton to the environment based on transmembrane adhesion receptors like integrin (Santos et al., 2020). Cell migration mediated by retrograde flow of actin filaments does not necessarily need the coupling to the extracellular environment (Reversat et al., 2020). Adhesion-dependent and -independent migration are variants of the same principle, of coupling retrograde flow to the environment (Reversat et al., 2020). In a confined environment, the retrograde flow generates shear forces based on the

topographical features of the substrates sufficient to propel the cell body forward. Thus, axon growth within the dense environment of the developing brain could also be mediated by retrograde actin flow and still be independent of adhesions. In line with this, oligodendrocytes were observed to use such a mechanism for the formation of myelin sheaths (Nawaz et al., 2015). The leading edge of the oligodendrocyte is confined between the axonal membrane and the outer membrane of the oligodendrocyte, generating friction. When oligodendrocytes start to form membrane sheets, a large motile membrane is found at the tip that is driven by F-actin polymerisation (Nawaz et al., 2015). Depolymerisation of actin filaments with Lat A led to cessation of membrane motility, and adhesive contacts were triggered. However, since the axon is a long cellular process growing far away from the cell body, its supply depends on microtubules as transport tracks. Further, a pushing force generated by polymerisation of microtubules and/or their bulk transport are necessary. Thus, the mechanism of how neurons extend their axons includes microtubules as well as actin filaments. The actual mode of growth can only be determined in the developing organism. Considering the dense and confining environment, actin retrograde flow can also create a pushing force, using the topographical features of the extracellular matrix (Reversat et al., 2020).

Myosin-II activity restricts growth and maintains polarity

The actin cytoskeleton is often seen as a growth barrier. Indeed, such a growth barrier is mainly generated by myosin-II, contracting actin filaments, and forming actin arcs (Amano et al., 1998; Dupraz et al., 2019; Santos et al., 2020; Wylie and Chantler, 2003). These myosin-II-containing actin arcs were shown to contribute to compressing and bundling of microtubules in the growth cone neck to form a new part of the axon shaft during growth cone advance (Burnette et al., 2008). When I inhibited myosin-II activity with Blebb, I did not observe increased splay of microtubules (Figure 21). Inhibition of myosin-II caused a re-bundling of microtubules and restored neurite length completely (Figure 20). Also, the morphology of the growth cone resembled more control conditions with a clear separation of the growth cone and neurite shaft. Myosin-II is involved in the formation of cortical actin underneath the plasma membrane (Chugh and Paluch, 2018; Jawahar et al., 2024). Inhibition of myosin-II with Blebb can lead to the collapse of this cortical actin network and the subsequent collapse of the cell morphology, with the advantage that microtubules are bundled again. This re-bundling of microtubules promoted neurite elongation (Figure 20). This effect was only investigated in early stages of neural development until 72 h after plating. Whether the treatment with Blebb after actin depolymerisation can enhance growth at stages after DIV 3 needs to be investigated. Nonetheless, compared to the treatment with only Blebb, the combination with Cyto D and Blebb limits the potential outgrowth rate. Neurons treated with only Blebb exhibited longer neurites (Figure 23). A

similar effect was observed for the combination of Cyto D and Taxol. Actin polymerisation inhibition reduced neurite length compared to control even in presence of Taxol. Both results highlight again, that microtubules are not the only driver of neurite and axon elongation but also actin polymerisation generates growth propulsion. Different actin structures have different roles in promoting or restricting growth. The complexity of different actin structures contributing to different cellular mechanism at the same time, makes it complicated to decipher which processes are growth inhibiting or growth supportive. A global treatment with an actin manipulating drug potentially affects all different actin populations, including filopodia, lamellipodia, actomyosin, cortical actin and actin rings.

Myosin-II activity is a negative regulator of neurite outgrowth, as stated above. Lin and colleagues show that myosin-II counteracts the Arp2/3 complex mediated relaxation of the actin network and *vice versa* (Lin et al. manuscript in preparation). Here, I confirmed this finding by showing that inhibition of Arp2/3 by CK-666 blocked neurite extension in young neurons (Figure 33). Simultaneous inhibition of Arp2/3 and myosin-II with CK-666 and Blebb restores neurite length. Arp2/3 complex-based nucleation of branched actin networks leads to a relaxation of the tension in the growth cone and promotes its advance, enabling axon formation. When myosin-II dominates, the actin network is contracted, and the tension leads to retraction of the neurite. This antagonism of Arp2/3 and myosin-II keeps the neuron in an unpolarised state resulting in extension and retraction cycles of minor neurites. Such a “tug-of-war” between Arp2/3-mediated generation of a pushing force and myosin-II-generated contraction is observed at adherens junctions in epithelial cells (Efimova and Svitkina, 2018; Gautreau et al., 2022; Li et al., 2020).
Myosin-II inhibition enhanced the length of the longest neurite only in young neurons, until DIV 2, as shown before (Dupraz et al., 2019). When DIV 3 or DIV 7 neurons were treated with the same concentrations of Blebb, no growth-promoting effect was observed anymore (Figure 32). Further, in polarised neurons, only minor neurites retracted upon Arp2/3 inhibition (Figure 34), and their retraction was rescued with myosin-II inhibition (Figure 37). This finding underlies the role of myosin-II in regulating polarity. While the axon escapes the growth restraint imposed by myosin-II, minor neurites remain under the growth control of myosin-II. In this way, it is ensured that only a single neurite develops into an axon, establishing and maintaining polarity. How this process is regulated is unclear. In culture, it could be a random process that by chance one neurite escapes myosin-II activity. Since also in culture neurons only form one axon, it is more likely that the escape of myosin-II activity is due to a coordinated mechanism. The inactivation of upstream regulators of myosin-II specifically in one neurite could be a plausible explanation.

One upstream regulator of myosin-II is Rho A (Amano et al., 1998; Dupraz et al., 2019), which activates the myosin-regulatory light chain via ROCK. Recently, a dual spatio-temporal role for Rho A was reported (Wojnacki et al., 2024). During axon formation, Rho A is less active in the growth cone of the future axon. Later on, Rho A becomes active again but does not act via ROCK anymore (Wojnacki et al., 2024). This change in Rho A activity and its signalling pathway could explain how a neurite escapes the growth restraint of myosin-II. *In vivo*, extracellular signalling cues are probably involved in instructing the site and neurite for axon formation (Lewis et al., 2013).

In the early stages of development, myosin-II activity restricts the outgrowth of minor neurites. I found that myosin-II is not active in elongating axons and does not influence growth at this stage anymore (Figure 32). However, the possibility that myosin-II is reactivated at later stages of development to restrict growth again should be addressed in the future. Upregulation of myosin-II activity in axonal tips could be a way in which the neuron controls and prevents excessive growth. In line with this idea, a neuron-specific deletion of Rho A, one of the upstream regulators of myosin-II, promoted regeneration (Stern et al., 2021). Also, direct inhibition of myosin-II with a novel inhibitor, NMIIi2, enabled regeneration (Heo et al., 2025). Though these observations do not necessarily show that myosin-II activity is developmentally reactivated in adult neurons. Possibly, the activation of myosin-II can also be triggered by the injury itself, but also by the extracellular environment. After an injury, reactive astrocytes produce CSPGs in large quantities (Yang et al., 2024). CSPGs trigger and activate myosin-II via Rho A and thereby prevent regeneration (Stern et al., 2021). Still, myosin-II may become developmentally activated again when the axon is supposed to stop growing.

The Arp2/3 complex is involved in axon elongation

The axon escaped the growth control imposed by myosin-II activity and did not retract upon Arp2/3 inhibition. Does this mean that the Arp2/3 complex is also not required for axon elongation anymore once the myosin-II-mediated growth restraint is resolved? Pharmacological inhibition and genetic knockout of Arp2/3 reduced the length of the longest neurite (Figure 36). In contrast to minor neurites, the reduction in length of the longest neurite was not rescued by blocking myosin-II (Figure 37). Thus, Arp2/3 activity is required for axon elongation independent of its antagonistic function with myosin-II observed in unpolarised neurons and minor neurites of polarised neurons (Figure 33 and Figure 37) (Lin et al., manuscript in preparation). The remaining Arp3 protein, 25% of control levels, could explain why the effect of an *in vitro* knockout of Arp3 was not as effective as the treatment with CK-666. However, the Arp2/3 complex seems to be involved in axon elongation. Since Arp2/3 is the main actin nucleator that forms branched

actin networks, it supports the view that actin polymerisation is indeed required in the growth and elongation mechanism of axons.

Long, flexible actin filaments cannot sustain a pushing force without buckling, cells overcome this by formation of short-branched filaments, creating a dense array to sustain these forces (Pollard and Borisy, 2003). Such a branched actin network formed by the Arp2/3 complex generates pushing forces that then drive cell motility, or here, axon elongation. Components of the Arp2/3-complex are expressed continuously in culture, until at least DIV 21 (Figure 35) and also play a role later in development, when the complex is involved in dendritic spine formation and maturation (Spence et al., 2016).

It must be noted that when DIV 7 neurons are treated with CK-666, no effect on axon elongation was observed anymore (Figure 36). On one side, this could indicate that at this time point Arp2/3-mediated actin nucleation is not required for axon elongation anymore, which is in line with my previous suggestion of a developmental switch in dependence on actin polymerisation for axon elongation at this stage. However, recently, Cao and colleagues reported that the inhibition efficacy of CK-666 on the Arp2/3 complex depends on the isoform composition of this complex (Cao et al., 2024). They showed that both, CK-666 and CK-869, inhibit Arp2/3 complexes containing ArpC1A, but only CK-869 inhibits complexes that contain ArpC1B. Others pointed out that this finding is not fully in line with published results for cell lines that contain both ArpC1 variants but are fully sensitive to CK-666 treatment (Stradal et al., 2025). Further, while CK-666 inhibits activity of Arp2/3 complexes containing Arp3 and Arp3B, CK-869 only inhibits Arp3 and not Arp3B (Cao et al., 2024). It is possible that the composition of the Arp2/3 complex changes in the course of development, making the complex less sensitive to CK-666 at later stages. Since I only investigated the Arp3 knockout neurons until DIV 7, such a change in the composition of the Arp2/3 complex might occur. It can be tested by adding CK-869 to DIV 7 neurons or by repeating the knockout experiments and extending the time of culture. These experiments will then reveal whether Arp2/3 activity is not required after DIV 7 for axon elongation or a differently compiled Arp2/3 complex contributes to the elongation of the axon. However, CK-869 affects microtubule assembly in cultured mammalian cells while CK-666 has no direct effect on microtubules (Yamagishi et al., 2018) and therefore, the effect should be taken into account when interpreting the obtained results with CK-869.

Cofilin activity during development

As I describe above, I found that actin turnover is reduced in growth cones over time in culture (Figure 12). It is not clear whether this is a developmental requirement or just a side effect as actin polymerisation becomes less important for axon elongation, as I suggest.

Candidates potentially involved in the decrease of actin turnover are members of the ADF/cofilin family. In cell-free assays, only an actin nucleator, a capping protein, and ADF/cofilin are required to induce actin treadmilling, though other ABPs can modulate the turnover rate (Flynn, 2013; Loisel et al., 1999; Michelot et al., 2007). Besides this, ADF/cofilin also drives actin retrograde flow (Flynn et al., 2012; Tedeschi et al., 2019). Since I observed that more actin filaments remaining within the peripheral domain of the growth cone in DIV 7 and DIV 14 neurons after 10 minutes of Cyto D treatment, I reasoned that this might be due to reduced actin depolymerisation. The mechanism that controls actin dynamics is dominated by ADF/cofilin-mediated filament severing (Michelot et al., 2007). Reduced severing and depolymerisation of actin filaments at the pointed end limit the amount of available G-actin that can be added at the barbed end and slows down turnover. Therefore, I analysed whether cofilin is inactivated over time in cultured neurons. In whole cell lysates, I observed a trend towards increased levels of inactive, phosphorylated cofilin starting after one week in culture (Figure 29). However, no significant change was observed. It might be that cofilin becomes inactivated specifically in the growth cone, slowing down actin turnover rates. In line with this, the local regulation of ADF/cofilin is of importance to synapse formation, maintenance and physiology, as well as dendritic spine enlargement or stabilisation (Rust, 2015).

In my experiments, I only analysed coflin-1 activity. However, one has to also consider the expression and activity of the other family members, ADF and cofilin-2. It is possible that, despite a potential inactivation of cofilin-1, these other members take over the function of cofilin-1. In adult mice, only a triple knockout of ADF, cofilin-1 and cofilin-2 completely abolishes neurite growth (Tedeschi et al., 2019). Though in early neuron development, only ADF and cofilin-1 seem to be important, as the double knockout is sufficient to completely prevent actin retrograde flow before neurite formation (Flynn et al., 2012). However, cofilin-2 was found to be expressed already at postnatal stages in the brain and in adult DRG neurons (Bläsius, 2016; Tedeschi et al., 2019). Brain-specific deletion of cofilin-2 revealed reduced dendritic arborisation and effects on spine morphology.

In early stages of development, active cofilin is necessary for neurite formation, and overexpression of cofilin enhances neurite length (Flynn et al., 2012; Garvalov et al., 2007; Meberg and Bamburg, 2000). I found a similar trend when I overexpressed cofilin-1 in young neurons up to DIV 2 (Figure 30). However, virus-mediated overexpression of cofilin-1 from DIV 2 onward, led to the formation of cofilin rods and caused increasing inactivation of transgenic as well as endogenous cofilin. At this stage, the overexpression caused a reduction in the length of the longest neurite (Figure 31). Thus, neurons overexpressing cofilin-1 at different developmental stages behaved similarly to treatment with Cyto D. However, the appearance of cofilin-rods after virus infection calls into questions whether the reduced axon length is caused by enhanced actin dynamics or by cofilin rods. Though

mainly found in distal dendrites, these structures also form in the axon and the aggregations can block intracellular trafficking and thereby affect growth (Cichon et al., 2012). Here, cofilin rods appeared to mainly localise to dendrites. The length of dendrites was not quantified, but could be an indication of the extent to which cofilin rods may affect growth.

In the past years, cofilin-actin rods were linked to neurodegenerative diseases, but their exact role remains unclear (Wurz et al., 2022). These rods are mainly composed of dephosphorylated cofilin and ADP-actin in a 1:1 ratio, which could indicate why neurons increase cofilin-phosphorylation pathways after virus-mediated cofilin-1 overexpression (Figure 30). The triterpene Cucurbitacin E inhibits cofilin phosphorylation (Nakashima et al., 2010). Cells treated with Cucurbitacin B show actin aggregations and formation of cofilin-actin rods (Wurz et al., 2022). In young neurons, the formation of cofilin-rods was not observed, and the overexpressed protein showed an even distribution within the cells. The formation of rods makes it difficult to investigate how increased activation of cofilin at later stages affects axon elongation.

As an alternative strategy, instead of overexpressing cofilin, one could target the regulatory pathways that control cofilin. The activity state of cofilin is regulated via the phosphatases SSH1, -2 and -3 and kinases LIMK1 and -2. Inhibition of LIMK with 9-benzoyloxy-5,11-dimethyl-2*H*,6*H*-pyrido(4,3-*b*)carbazole-1-one (Pyr1) leads to reduced amounts of phosphorylated cofilin (Prudent et al., 2012). In a mouse model, the drug alters spine density and morphology in cultured neurons as well as *in vivo*, demonstrating that it passes the blood-brain barrier (Gory-Faure et al., 2021). At the same time, Pyr1 stabilises microtubules by increasing the level of detyrosinated tubulin (Prudent et al., 2012). Further, Pyr1 also decreases the proliferation of breast cancer cells *in vitro* (Prunier et al., 2016).

This dual effect on the actin regulator cofilin and the microtubule stabilising effect make Pyr1 an interesting candidate to induce axon regeneration in a therapeutic setting. After a conditioning lesion, cofilin becomes dephosphorylated and thereby active, though not by decreased LIMK activity but increased SSH activity (Tedeschi et al., 2019). Both, increasing actin dynamics as well as stabilising microtubules separately promote axon regeneration (Hellal et al., 2011; Ruschel et al., 2015; Tedeschi et al., 2019). Similar to Pyr1, Taxol increases the amount of detyrosinated tubulin at the injury site (Hellal et al., 2011). In contrast to Pyr1, Taxol does not affect the proliferation of fibroblasts and reduces fibrotic scarring by a proliferation-independent mechanism. A drug that potentially targets both processes, actin dynamics as well as microtubule stabilisation could be of interest for therapeutic intervention in regeneration. However, when I treated young neurons with Lat A and at the same time stabilised microtubules with Taxol, treatments that alone increased length, together they had no additional or synergistic effect on neurite length compared to

the individual treatments (Figure 24). This shows that in this stage the growth rate is not limited by the cytoskeleton but other processes, for example membrane transport and availability at the growing neurite tip (Futerman and Banker, 1996; Roy and Tedeschi, 2021). Nevertheless, it would be interesting to investigate whether the combination of actin dynamisation and microtubule stabilisation enhances regeneration of injured axons beyond the individual regeneration-promoting effects (Hellal et al., 2011; Ruschel et al., 2015; Tedeschi et al., 2019).

There are several other LIMK inhibitors available that can be tested for their effect on cofilin activity in cultured neurons (Collins et al., 2022). Alternatively, the effect of cofilin inactivation on neurite length at later stages of development could be analysed by targeting SSH. Different SSH inhibitors have been identified to block cofilin dephosphorylation (Lee et al., 2017; Li et al., 2015). Further, a conditional cofilin knockout mouse line could be used to address this question. Similar to the experiment with Arp3 (Figure 38), a virus could be added to induce a cofilin knockout at later stages, to not interfere with earlier requirements for cofilin activity.

Cofilin activity itself does not necessarily need to be inactivated to block the severing and depolymerisation activity to influence actin turnover. ABPs like tropomyosins can limit the accessibility and binding of cofilin to actin filaments. Different tropomyosins regulate cofilin differently. Tropomyosin 1.12 promotes the association of ADF/cofilin with actin filaments, enhancing filament turnover, while tropomyosin 3.1 prevents binding of ADF to F-actin (Gunning et al., 2015). More than 40 isoforms of tropomyosin are known, making it difficult to analyse their function (Gray et al., 2017). However, several isoforms of tropomyosin influence neuronal morphology and therefore play a role during development. It is possible that a tropomyosin isoform, limiting F-actin accessibility for ADF/cofilin, is expressed during later stages of axon elongation and thereby stabilises the filaments and reduces actin turnover.

The role of electrical activity in axon growth

The transition from a developmental state, in which the neuron and its components are dynamic and enable rapid elongation, to a static state, where the cell is designated to transmit information, is considered a cause why neurons lose their intrinsic growth potential (Hilton et al., 2024). During maturation the cell is equipped with the transmission machinery for its function as transmitter of electrical signals, as observed here (Figure 40A, B, C and D). The electrical maturation of a neuron is accompanied by the reduction of its regenerative capacity (Koseki et al., 2017).

Here, I also observed a correlation between onset of electrical activity and downregulation of growth rates (Figure 10 and Figure 40), but the downregulation of growth did not correlate with the formation of functional synapses itself. Since we measured sEPSCs in

the patched cells, we assume that these cells also have formed presynaptic sites. Instead, it is the active transmission of electrical impulses that potentially reduces growth and not the formation of the machinery to transmit these signals. However, since the frequency of sEPSCs increased at DIV 14, it could also be the number of formed synaptic connections and the frequency of sEPSCs that is the reason for growth reduction.

In horizontally projecting layer 2/3 neurons in the cortex, the triggering of high frequence activity results in growth pausing of these cells, which is blocked in presence of tetrodotoxin (TTX), showing that growth pausing is activity dependent (Malyshevskaya et al., 2013). In DRG neurons, electrical activity is a reason for reduced growth competence (Enes et al., 2010). After a conditioning lesion, the electrical activity is downregulated and neurons become growth competent. When DRG neurons are in a growth-competent state after a peripheral nerve lesion, chronic depolarisation with KCl does not inhibit growth of these neurons (Enes et al., 2010). A similar effect was observed here (Figure 41). Young neurons that were not polarised yet exhibited no effect on growth after treatment with KCl. Only after polarisation, when neurons extended their axon, they became sensitive to chronic depolarisation and reduced growth rates. The observation that an increase by 20 mM extracellular KCl had initially no effect on neurite length, could be due to the effect that extracellular KCl and membrane voltage are directly proportional, while signalling strength may be non-linearly correlated with Ca^{2+} influx levels (Rienecker et al., 2020; Wheeler et al., 2008).

The growth reduction was reversed when neurons were switched to high Na^{+} after two days in elevated KCl (Figure 42), showing that the effect is transient and reversible. Brief as well as prolonged stimulations with extracellular KCl increases intracellular calcium for the duration of the treatment (Rienecker et al., 2020). Indeed, in DRG neurons, the effect of elevated KCl is mediated by calcium influx and changes in gene transcription (Enes et al., 2010). When gene transcription is inhibited, a growth-reducing effect of chronic depolarisation was not observed. Whether the observed effect of KCl treatment on hippocampal neurons is also mediated by changes in intracellular calcium and gene transcription has not been investigated here. Since the effect was analysed after two days of treatment, a gene transcription-mediated effect is possible and should be addressed in future experiments.

Changes in intracellular calcium can regulate the growth cone cytoskeleton by phosphorylation signalling cascades and thereby effect growth (Gasperini et al., 2017) but also many other signalling cascades are regulated via Ca^{2+} as well. In line with this, the calcium channel subunit a2d2 inhibits regeneration in sensory neurons (Tedeschi et al., 2016). Inhibition of the calcium channel with pregabalin promoted growth. Whether such a mechanism is also in place in hippocampal neurons is not yet known. Overexpression of the subunit a2d1 did not affect axon length, but the overexpression of a2d3 enhanced

axon length and branching in interneurons (Bikbaev et al., 2020). In DRG neurons, both subunits, a2d1 and a2d3, only slightly decrease the length of the longest neurite (Tedeschi et al., 2016). However, these results show that the effect is channel unit subtype specific and therefore does not rule out a growth-inhibiting effect of a2d2 in hippocampal neurons. Combining elevated KCl with a calcium channel inhibitor could reveal whether the observed effect is mediated by increased intracellular Ca^{2+} levels. If so, how does elevated calcium affect the axon elongation mechanism?

It is already known that calcium transients in the developing neuron regulate axon outgrowth (Tang et al., 2003). These calcium transients are more prevalent in enlarged, paused growth cones. Blocking L-type voltage-gated calcium channels, which also cause calcium influx after high KCL treatment, mediates this effect. Blocking these types of ion channels increases axon length (Tang et al., 2003). In airway smooth muscle cells, KCl treatment evokes contraction via activation of RhoA/ROCK pathway, secondary to voltage-dependent Ca^{2+} influx (Janssen et al., 2004). Thus, the observation that only polarised neurons become sensitive to KCl treatment might be due to the inactivation of the RhoA/ROCK pathway in the axon, as mentioned above, which is reactivated with elevated extracellular KCl.

Elevated KCl also increases the stability of actin filaments (Zhang and Benson, 2001). Since I observed more stable actin filaments already when neurons still elongate their axons (Figure 10 and Figure 12), it is questionable whether the effect of increased extracellular potassium on actin filaments stability is the reason why electrical activity prevents growth. Therefore, deciphering the signalling pathways and mechanisms by which elevated KCl blocks growth is necessary to pinpoint the growth-inhibiting mechanism.

However, increasing extracellular KCl and chronically depolarising the cell is not a physiological phenomenon and poorly represents the *in vivo* situation (Rienecker et al., 2020). Only a slight increase in the extracellular KCl concentration by 5 mM compared to the baseline concentration of 5 mM leads to enhanced AP triggering. A higher increase by 10 mM or more causes an attenuation of spontaneous activity. Within two days, the lower increase by 20 mM KCl has no growth effect initially compared to an increase by 40 mM (Figure 41). The influx of calcium with a low increase of external KCl might be too small to induce changes in intracellular calcium signalling.

In the early developmental stages, neurons do not elicit spontaneous APs (Figure 40C). To investigate how real neuronal activity influences growth, one has to use other methods to induce or mimic electrical activity than elevated extracellular KCl. Several other tools are available to manipulate electrical activity (Wiegert et al., 2017). Among others, these tools include TTX, which blocks voltage-gated sodium channels, requiring that the cell

itself is active and fires APs. The same is true for botulinum and tetanus toxin, which inhibit synaptic activity. In the past decades, chemogenetic tools have been developed to control neuronal activity. These designer receptors exclusively activated by designer drugs (DREADD)-based approaches are commonly used by neuroscientists and allow increasing as well as decreasing excitability of transfected neurons, depending on the DREADD type (Roth, 2016). However, once the specific drug is added to a culture system or injected into living animals, it cannot be easily removed and mimicking defined electrical activity patterns observed in mature neurons is not possible. Therefore, as a strategy to test physiologically relevant electrical activity patterns, I propose to use light-regulated ion channels. Channelrhodopsins (ChRs) are controlled by light and allow high temporal resolution of activation (Deisseroth and Hegemann, 2017). As ChRs are easily controlled by switching light on and off, one could stimulate young neurons with more mature activity patterns (Figure 40D). With a similar strategy, high-frequency photo-stimulation of horizontally growing axons in cortical layer 2/3 caused increased pause behaviour (Malyshevskaya et al., 2013). When neurons are cultured with TTX, high-frequency photo-stimulation does not affect axonal growth rates, indicating that the effect is due to the AP firing. Therefore, a similar approach can be used to induce AP firing in young neurons that would usually not exhibit electrical activity, to investigate the effect of activity on growth and the underlying mechanism.

Not only do electrical transmission and influx of calcium limit regeneration, but also components of the synaptic release machinery itself inhibit regeneration. The synaptic vesicle priming and docking components RIM1, RIM2 and Munc13 were identified as growth inhibitors in DRG neurons (Hilton et al., 2022). Their role in axon elongation in hippocampal neurons remains unknow. In young hippocampal neurons, Munc13 knockout reduces neurite outgrowth (Broeke et al., 2010), but the reduction in neurite length is compensated at later developmental stages. In this study, only a double knockout of Munc13-1 and Munc13-2 was used. Hilton and colleagues used a triple knockout, by including Munc13-3 for their experiments. Therefore, it could be that in developing hippocampal neurons, Munc13-3 compensates for the loss of the two other Munc13 forms. Overexpression of Munc13 in developing hippocampal neurons will reveal whether it inhibits growth, as it does in DRG neurons. The exact mechanism by how RIM and Munc13 prevent regeneration in DRG neurons is still unclear.

These described mechanisms show that the equipping of the cell with the transmission machinery and transmission itself suppresses growth. Is the low intrinsic growth potential based on a downregulation of growth-mediating components or on the upregulation of growth inhibitors when neurons mature? In DRG neurons, the re-acquiring of growth competence is associated with the downregulation of growth-supressing genes than with

an upregulation of growth-promoting factors (Hilton et al., 2022). As those neurons that downregulate the growth-suppressing factors grow well, it indicates that the general growth program is still in place and does not need to be upregulated. This might indicate that the reduction in growth competence of CNS neurons is also based on the suppression of the growth program rather than its downregulation. On the other hand, there is also evidence that growth-promoting factors like the growth-associated protein 43 are developmentally downregulated during neuronal maturation (Karimi-Abdolrezaee et al., 2002). This shows that the reduction of growth competence in maturing neurons is based on both factors, the downregulation of growth-promoting genes while during maturation growth-suppressing genes are upregulated. However, similar to DRG neurons that maintain a growth machinery acting after downregulation of suppressing genes (Hilton et al., 2022), also cultured hippocampal neurons seem to have the needed growth machinery in place. After axotomy, cultured hippocampal neurons are plastic and grow out a new axon from a dendrite or regenerate their axon, depending on the location of axotomy (Bradke and Dotti, 2000; Gomis-Ruth et al., 2014; Gomis-Ruth et al., 2008). However, neurons used in these studies were analysed at DIV 10, a time point where I observed the highest growth rates, and only subsequently, growth rates were reduced (Figure 10), so these neurons might still be in a growth competent state. Though axotomy also induce changes in gene expression, altering the growth program (Abankwa et al., 2002).

Outlook - How to elicit regeneration after spinal cord injury?

Focusing on the actin cytoskeleton, based on my observations, I propose that growing axons switch their mode of growth during development. In early stages, it is more dependent on actin filaments and polymerisation, which supports microtubules to drive neurite growth and axon elongation. At later stages, the dependency on actin dynamics is reduced, and axons elongate less dependent on F-actin. My data suggest that axons employ different growth modes. Also, different cell types may use various growth modes. Therefore, it will be important to investigate cell type and developmental stage-dependent growth mechanisms, across different extracellular environments (CNS vs. PNS).

Even the latest models to explain neurite growth are not capable of bringing together all the diverse findings postulated to contribute to growth. An unbiased approach is needed to identify, probably different, modes neurons use to grow. This includes adhesion-dependent as well as -independent growth mechanisms that are driven, to different extends, by a cooperation between actin filaments and microtubules. Even when microtubules alone can drive axon elongation in CNS neurons, they are not capable of reaching extension rates that are observed when actin dynamics are in play. How microtubules drive the elongation of neurites is also still an open question. Is it only the polymerisation of microtubules that drives growth, or is their bulk forward movement the

driver of neurite elongation? Cytoskeleton-based treatments identified so far to promote axon regeneration after spinal cord injury, also enhance axon formation during early neuronal development. This includes increasing actin dynamics via cofilin, inhibition of Rho A-regulated myosin-II, and the stabilisation of microtubules. However, I found that all these treatments that I tested here, are either growth-reducing after polarisation or not effective. On the other side, growth-inhibiting mechanisms that prevent polarisation are removed in elongating axons, including the myosin-II-mediated brake. Therefore, the axon contains the optimised machinery for growth, and in this stage, no treatment was able to enhance growth rates any further.

Thus, it seems like initiating regeneration is a recapitulation of axon formation during development, which would be in line with the hypothesis that inducing regeneration is a recapitulation of developmental processes (Hilton and Bradke, 2017). In contrast, while more stable actin filaments prevent axon outgrowth in early stages, the reduction in actin turnover does not lead to reduced growth. This is probably due to the different population of actin filaments that limit growth. In young neurons, growth-inhibiting actin is organised by myosin-II. The axon escapes this growth inhibition and polarisation is maintained by keeping minor neurites under the growth-restricting control of myosin-II. How the axon escapes myosin-II activity, should be addressed in the future. More stable actin filaments later on in development, are based on a different population not regulated by myosin-II, at least until DIV 9.

It remains to be investigated which mechanisms lead to a growth stop when axons reach their targets and how target connection might be involved in growth suppression. Identification of such growth stop-instructing mechanisms will may help to find a regeneration-eliciting treatment. So far, many potential targets have been identified to promote regeneration to a certain level. However, several factors limit the growth of injured axons. I advocate for combining different treatments. For example, the stabilisation of microtubules could be combined with the electrical silencing of neurons with Pregabalin. Similar to DRG neurons, electrical activity potentially influences the growth potential of hippocampal neurons. Identification of the exact mechanism by which electrical activity influences the growth process will help to understand the growth mode of axons, and provide new targets to promote regeneration.

Despite intense research, so far, no therapy or treatment for regeneration of CNS neurons has been found. During development, neurons possess an enormous growth potential, which is downregulated or suppressed in the course of maturation. To successfully develop a cure or treatment for patients requiring nerve regeneration, we need to understand the mechanisms how growth is suppressed and downregulated in maturing neurons, how neurons grow during development and whether regenerating neurons use the same growth mechanism as in the developing organism.

Materials and Methods

Materials

Chemicals

Name	Supplier	Product number
Ammonium chloride	Supleco	1.01145.1000
B-27 supplement (50x)	Gibco	17504-044
Boric acid	Sigma	B6768-500G
Bovine Serum Albumin (BSA)	Sigma	A3294-100G
Bradford Reagent	AppliChem	A6932.0250
Calcium chloride dihydrate	Sigma	C5080-500G
Chemiluminescence solution Pierce	Thermo Scientific	32209
Chemiluminescence solution Pico SuperSignal Plus	Thermo Scientific	34577
Chemiluminescence solution Dura SuperSignal Extended Duration	Thermo Scientific	34076
Deconex® 11 Universal	Borer Chemie AG	500100.00-F10W
Deoxyribonuclease I (DNase I)	Cell Systems	LS002007
Dimethyl sulfoxide (DMSO)	Carl Roth	4720.4
Dipotassium-adenosine-triphosphate	Sigma	A8937-5G
Ethylene glycol-bis(2-aminoethyleter)-N,N,N',N'-tetraacetic acid (EGTA)	AppliChem	A0878.0100
Fetal Bovine Serum (FBS)	Thermo Scientific	A5256801
Fish skin gelatine	Sigma	G7765
Fluoromount Mounting Medium	Sigma	F4680-25ML
D(+)-glucose monohydrate	Merck	1.04074.1000
Glucose solution (5%)	B. Braun Melsungen AG	3154910
Glutaraldehyde solution (25%)	Sigma	G6257-100ML
Glycerol	Carl Roth	7530.1
Glycine	Sigma	G8898-1KG
HBSS	Gibco	14025-100
HEPES buffer solution (1M)	Gibco	15630-056
HEPES free-acid	Millipore	391338-500GM
Horse serum (HS)	Biowest	S0910-500
Hydrochloric acid (≥37%)	Carl Roth	2607.1
L-Glutamine (200 mM; 100x)	Gibco	25030-081

Magnesium chloride	Sigma	M8266-100G
Minimal essential media (MEM) (10x)	Gibco	11430-030
MEM amino acids (50x)	Gibco	11130-036
MEM non-essential amino acids (100x)	Gibco	11140-035
2-Mercaptoethanol	Sigma	M3148-100ML
Milk powder, non-fat, dry	Cell Signalling	9999S
MOPS buffer (20x)	Invitrogen	NP0001
Mouse neuron Nucleofection Kit	Lonza	VPG-1001
Neuropan 2 supplement (100x)	PAN-Biotech	P07-11100
Nitric acid (68%)	VWR	20422.242
Paraffin	AppliChem	253211.0914
Paraformaldehyde (PFA)	Carl Roth	0335.3
Phosphate-buffered saline (10x), powder	AppliChem	A0965
PhosSTOP	Roche	4906845001
Pipes, 1,4-Piperazinediethanesulfonic acid	Sigma	P6757-25G
Poly-L-lysine hydrobromide	Sigma	P2636-1G
Potassium chloride	AppliChem	A3980.0500
Potassium gluconate	Sigma	P1847-100G
Protease inhibitor cocktail (PIC) cOmplete	Roche	4693116001
Ripa buffer (10x)	Millipore	20-188
Sodium chloride	AppliChem	A2942.1000
Sodium dodecyl sulfate (SDS)	Sigma	L4509-500G
Sodium-guanosine-triphosphate	Sigma	G887-250MG
Sodium hydrogen carbonate	Merck	1.06329.0500
Sodium hydroxide pellets (NaOH)	AppliChem	141687.121
Sodium pyruvate (100 mM)	Sigma	S8636-100ML
Sodium tetraborate anhydrous	Sigma	71996-250G
D(+)-Sucrose	Carl Roth	4621.2
Triton X-100	Sigma	X100-100ML
Trizma base (Tris)	Sigma	93350-1KG
Trypsin-EDTA (0.05%), phenol red	Gibco	25300-096
Trypsin-EDTA (0.25%), phenol red	Gibco	25200-056
Tween20	AppliChem	A4974.0500

Drugs

Name	Solvent	Supplier	Product number	Function
Blebbistatin	DMSO	Sigma	B0560-5MG	Inhibition of myosin-II
Buprenorphine hydrochloride (Bupresol)	5% glucose	WDT	04928	Analgesic
CK-666	DMSO	Sigma	SML0006-5MG	Inhibition of Arp2/3 complex
Cytochalasin D	DMSO	Enzo Life Sciences	BML-T109-0001	Actin polymerisation inhibition
Isoflurane (Vetfluran-Forene)	-	WDT	24279	Anaesthetic
Jasplakinolide	DMSO	Cayman Chemical	Cay11706-100	Actin filament stabilisation
Ketamine (10%)	0.9% NaCl	WDT	24324	Anaesthetic and analgesic
Latrunculin A	DMSO	Sigma	428021-100UG	Actin polymerisation inhibition
Taxol	DMSO	Cayman Chemical	10461-25	Microtubule stabilisation
Xylazine (20 mg/ml)	0.9% NaCl	WDT	25648	Analgesic

Equipment

Name	Supplier	Model
Amaxa Nucleofector II	Lonza	AAB-1001
Anaesthesia system	VetEquip Inc.	931401
Axon Digidata 1550B	Axon Instruments	
Bead bath	Lab Armor	74200-720
Cawomat X-ray film developer	Cawo	2000IR
Centrifuge	Eppendorf	5427R
Cold light source	Schott	KL 1500 LCD
Dumont #5 forceps	Fine Science Tools	11251-23
Dumont #5 forceps	Fine Science Tools	11251-30
Dumont #7 fine forceps	Fine Science Tools	11274-20
Fine Scale	Kern	APJ-NM
Incubator	HERAcell	240i
Magnetic stirrer	IKA	RH Basic 2
Microscope	Zeiss	Axioobserver.Z1
Microscope	Zeiss	PrimoVert
MultiClamp 700B	Axon Instruments	

pH-meter	Mettler Toledo	Seven Easy
Photometer	Eppendorf	6132
Pipetting controller	Integra	Pipetboy
Scale	Scout	Scout Pro 400 g
Spring scissors - angled to side	Fine Science Tools	15006-09
Sterile hood	Thermo Scientific	SAFE 2020
Tabletop centrifuge	Corning LSE	Mini Microcentrifuge
Temperature controller VII	Luigs-Neumann	
Thermo oven	Thermo Scientific	HERA THERM
Ultra-centrifuge	Optima	L80-XP
Vacuum pump	Vacuubrand	BVC21
Vortex	Corning LSE	VortexMixer

Consumables

Name	**Supplier**	**Product number**
Centrifuge tube PP, 15 ml	Nerbe Plus	02-502-3001
Centrifuge tube PP, 50 ml	Nerbe Plus	02-572-3001
CL-Xposure film	Thermo Scientific	34090
Corning centrifuge tube, 15 ml	Merck	CLS430053-500EA
Cover slip, 15 mm	Marienfeld	0111550
Cover slip, 30 mm	Marienfeld	111700
Eppendorf tubes 1.5 ml	Eppendorf	VB-0306
Frosted Microscope Slides, 90°	Fisher Scientific	16245172
G-actin/F-actin In Vivo Assay Biochem Kit	Cytoskeleton Inc.	BK037
Nunc cell culture/petri dish, 6 cm	Thermo Scientific	150288
Nunc EasYFlask™ 75 for cell culture	Thermo Scientific	156499
NuPAGE™ 4-12% Bis-Tris gradient gel	Thermo Scientific	NP0335BOX
Pasteur pipette (with filter)	VWR	612-1799
Pipette filter tips	Gilson	F171103
Pipette filter tips	Nerbe Plus	06-602-5300
		06-622-5300
		06-662-5300
		06-695-5300
Pipette tips	Nerbe Plus	07-360-2015
		06-365-2018
		06-379-2018
PVDF Immobilon-PSQ Transfer Membrane	Millipore	ISEQ00010
Stericup Quick Release-GP Sterile Vacuum Filtration System 250 ml	Millipore	S2GPU02RE

Stericup Quick Release-GP Sterile Vacuum Filtration System 500 ml	Millipore	S2GPU05RE
Steriflip-GP, 0.22 µm	Millipore	SCGP00525
Stripette, serological	Fisher Scientific	10420201
		10084450
		10606151
µ-Slide 4 well glass bottom dish	ibidi	80427-90

Media, buffers, and solution

Name	**Recipe**	**Preparation and storage**
Ammonium chloride (NH_4Cl) 50 mM for quenching	1.34 g NH4Cl in 500 ml 1x PBS	Store at RT
Blocking solution for Immunocytochemistry	2% Fetal Calf Serum 2% Bovien Serum Albumin 0.2% Fish skin gelatine in H_2O	Aliquot and store at -20°C
Borate buffer	1.24 g boric acid 1.9 g Borax (Sodium borate) in 400 ml H_2O	Adjust to pH 8.5, store at RT
Deoxyribonuclease I (DNase I)	1 mg/ml in 0.001 M HCl	Aliquots of 500 µl, store at -20°C
Extracellular solution (Ringer)	7.305 g NaCl 0.224 g KCl 0.203 g $MgCl_2$ 2.383 g HEPES 1.802 g D-glucose 0.221 g $CaCl_2$ in 1 l H_2O	Prepare always fresh, adjust to pH 7.3, check osmolarity
Glycine 0.1M for quenching	3.75 g glycine in 500 ml 1x PBS	Store at RT
Intracellular solution	31.624 g K-gluconate 0.746 g KCl 2.383 g HEPES 0.038 g EGTA 0.407 g $MgCl_2$ 1.858 g K-ATP 0.157 g Na-GTP in 1 l H_2O	Adjust to pH 7.2, check osmolarity, store aliquots at -20°C
MEM-HS1%	1x MEM 1x essential and nonessential amino acids 2 mM L-glutamine 0.22% $NaHCO_3$ 0.6% glucose 1% horse serum (HS)	Store at 4°C

MEM-HS10%	1x MEM 1x essential and nonessential amino acids 2 mM L-glutamine 0.22% $NaHCO_3$ 0.6% glucose 10% horse serum (HS)	Store at 4°C
MOPS buffer (20x)	52.31 g MOPS 30.29 g Tris-Base 5 g SDS 10 ml 0.5 M EDTA fill up to 250 ml H_2O	Store at RT, dilute to 1x before use
N2 media	1x MEM 1 mM sodium pyruvate 1% Neuropan 2 supplement 2 mM L-glutamine 0.22% $NaHCO_3$ 0.6% glucose 1x B27 supplement	Store at 4°C
Paraformaldehyde/sucrose (16%)	16 g Paraformaldehyde 16 g Sucrose in 100 ml 1xPBS	Adjust pH to 7.4, filter and store aliquots at -20°C
PHEM buffer (1x)	18.14 g Pipes 5.95 g HEPES 3.8 g EGTA 0.19g $MgCl_2$ in 1 l H_2O	Adjust pH to 7.4, filter and store at RT
PHEM/PFA (1x) (4%PFA/ 4% sucrose)	PHEM buffer (1x) 20 g PFA 20g Sucrose in 500 ml PHEM buffer	Heat up to 56°C for 1 h increase pH when PFA is dissolved adjust pH to 7.4 filter and store aliquots at -20°C
Poly-L-lysine solution (PLL)	1 mg/ml poly-L-lysine hydrobromide in borate buffer	Solution is sterile filtered and stored at 4°C for up to two weeks
Phosphate-buffered saline (PBS) 1x	114.9 g Na_2HPO_4 26.41g NaH_2PO_4 90 g NaCl add 1 l H_2O	Preheat to 50°C until solution is clear, adjust pH to 7.4, store at RT
SDS/Laemmli buffer (5x)	4 ml 1.5 M Tris-HCl pH 6.8 10 ml glycerol 5 ml 2-mercaptoethanol 2 g sodium dodecyl sulfate 1 ml 1% bromophenol blue	Store aliquots at -20°C
Transfer buffer (10x)	144 g glycine 30 g Tris	Dilute to 1x before use, including 20% methanol

	fill up to 1 l with H_2O	
Tris-buffered saline (TBS) (10x)	48.4 g Trizma (Tris) 160 g NaCl fill up to 2 l with H_2O	Adjust pH to 7.6, dilute to 1x before use, store at RT
Triton 10%	5 ml Triton X-100 45 ml 1x PBS	Dilute 1:100 for use, store at RT
Trypsin-EDTA 0.05%	100 ml 0.05% trypsin-EDTA 0.7 ml 1M HEPES	Aliquot in 5 ml and store at -20°C
Trypsin-EDTA 0.25%	100 ml 0.25% trypsin-EDTA 0.7 ml 1M HEPES	Aliquot in 5 ml and store at -20°C
For all solutions or washing steps either ddH_2O or Milli-Q® water was used		

Antibodies

Target	**Host species**	**Dilution**	**Supplier**	**Product number**
pan-actin	Mouse	1:1000	Cytoskeleton	AAN02
Arp2	Rabbit	1:1500	Cell Signalling	5614S
Arp3	Mouse	1:8000	Sigma	A5979
α-Tubulin	Mouse	1:4000	Sigma	T5168
β-III-Tubulin	Rabbit	1:2000	Sigma	T2200
β-III-Tubulin	Mouse	1:10000	Biolegend	801201
Cofilin1	Mouse	1:100	Abcam	ab54532
Cofilin1	Rabbit	1:1000	Cell Signalling	5175S
Cofilin1 phospho (Ser3)	Rabbit	1:50	Cell Signalling	3313S
Cre	Rabbit	1:1000	Covance	PRB-106P
GAPDH	Mouse	1:5000	OriGene	5G4-6C5
GFP	Chicken	1:1000	Abcam	ab13970
HRP conjugated IgG Anti-Mouse	Goat	1:10000	Thermo Scientific	31432
HRP conjugated IgG Anti-Rabbit	Donkey	1:10000	Thermo Scientific	31458
RFP	Rat	1:1000	Chromotek	5F8
Alexa Fluor 488 Anti-Chicken	Goat	1:1000	Invitrogen	A11039
Alexa Fluor 488 Anti-Mouse	Goat	1:1000	Invitrogen	A11029
Alexa Fluor 488 Anti-Rabbit	Goat	1:1000	Invitrogen	A11034
Alexa Fluor 555 Anti-Rabbit	Goat	1:1000	Invitrogen	A21429
Alexa Fluor 555 Anti-Rat	Goat	1:1000	Invitrogen	A21434
Alexa Fluor 647 Anti-Mouse	Goat	1:1000	Invitrogen	A21236
Phalloidin Alexa Fluor 488	-	1:250	Invitrogen	A12379
Phalloidin Alexa Fluor Plus 647	-	1:400	Invitrogen	A30107

Methods

Animals

All animal experiments were conducted in accordance with the Animal Welfare Act as well as the guidelines of the Landesamt für Verbraucherschutz und Ernährung (LAVE); reference number for approval (Aktenzeichen: 84-02.04.2015.A334 and Aktenzeichen 81-02.04.2021.A208). Adult female WT mice (C57BL/6J) were purchased from Janvier Labs or Charles River or bred in house. Mice ubiquitously expressing enhanced GFP under a "CAG" promoter (Okabe et al., 1997), here called 'Actin-GFP', were purchased from Jackson laboratory (JAX stock #003291) and were bred in house. For experiments, only animals heterozygous for GFP-expressing allele were used ($GFP^{tg/wt}$). Mice homozygous for the loxP-site flanked *Actr3* allele (*Actr3*$^{fl/fl}$) were a kind gift from the Arnold lab and were described before (Papalazarou et al., 2020). Mice of this line were bred in house. For generation of GFP-expressing $Arp3^{fl/fl}$ neurons, mice homozygous for the loxP-site flanked *Actr3* allele (*Actr3*$^{fl/fl}$) were crossed with heterozygous Actin-GFP mice (Actin-$GFP^{tg/wt}$). The resulting Actin-$GFP^{tg/wt}$, $Arp3^{fl/wt}$ mice were then backcrossed with the *Actr3*$^{fl/fl}$ line to receive $Arp3^{fl/fl}$ x $GFP^{tg/wt}$ mice. All mice were kept on a C57BL/6J background. Animals were housed in groups (up to five mice per cage) with controlled room temperature at 21° to 22°C in addition to an artificial 12-hour light:12-hour dark cycle. Pregnant mice were single housed. Mice were given food and water *ad libitum* throughout the experiment.

Primary hippocampal and cortical neuron culture

Primary hippocampal and cortical neurons were dissected from embryonic day 16.5 (E16.5) to E17.5 mouse brains. For embryo collection from timed-pregnant mice, animals were injected with buprenorphine (0.1 mg/kg) (Bupresol Vet, WDT, 04928) at least 30 min before incision and anesthetised by isoflurane (WDT, 24279) inhalation anaesthesia (5% isoflurane for induction, and 2.5% during the surgery). Alternatively, a mixture of ketamine (100 mg/kg)-xylazine (10 mg/kg) (WDT, 24324 and 25648) was injected intraperitoneally. Embryo heads were collected in Hanks' balanced salt solution (HBSS) with magnesium and calcium (Gibco™, 14025100) supplemented with 7 mM HEPES (Gibco™, 15630-056). Hippocampi or cortices were dissected from the embryonic brain and collected in HBSS supplemented with 7 mM HEPES. Next, hippocampi and cortices were digested in 0.25% trypsin-EDTA (Gibco™, 25200-056) supplemented with 7 mM HEPES and incubated at 37°C for 15 min. After enzymatic digestion, samples were washed three times with minimum essential medium (MEM)-1% horse serum (HS) (MEM-HS 1%) medium, containing 1x MEM (Gibco™, 11430-030), 1x essential and nonessential amino acids (both Gibco™, 11130-036 and 11140-035), 2mM L-glutamine (Gibco™, 25030-081), 0.22% $NaHCO_3$ (Merck, 1.06329.0500), 0.6% glucose (Merck, 1.04074.1000) and 1% HS

(Biowest, S0910-500). Instead of washing with MEM-HS1%, samples of cortices were washed three times with HBSS. In the first washing step, 5 µg/ml DNase I (Cell Systems, LS002007) was included in the HBSS solution. After washing, tissue was mechanically dissociated with fire-polished glass-Pasteur pipettes (VWR, 612-1799). Cover slips were coated with poly-L-lysine (1mg/ml) (Sigma, P2636-1G) in borate buffer at room temperature (RT) overnight, washed with H_2O four times and placed in the incubator at 36.5°C and 5% CO_2 with MEM-HS 10% media to equilibrate for at least one day before plating of cells. Before, cover slips were washed with Deconex® 11 Universal (Borer Chemie AG, 500100.00-F10W) on a vertical shaker for at least 30 min and subsequently washed three times with H_2O. Then, cover slips were incubated in nitric acid (68%) overnight at RT. On the next day, cover slips were washed four times with H_2O for 30 min each. Afterwards, cover slips were sterilised in a thermo oven, for at least 8 h at 220°C.

For fixation and staining of neurons in mixed cultures and transfected neurons (Figure 10A and E, Figure 13B, D and F, Figure 14A, C and E, Figure 15A, C and E, Figure 24A and C, Figure 25A, Figure 26A, Figure 27A, Figure 28A, Figure 31A and C, Figure 32A, C, E, G, and I, Figure 33A, Figure 34B, E and H, Figure 36A and D, Figure 37A, Figure 39A, Figure 41A and D, and Figure 42A and D), 35 neurons/mm^2 were plated on 15 mm glass-coverslips (Marienfeld, 0111550) with self-made paraffin dots (AppliChem, 253211.0914). Two to four hours after plating, glass coverslips with neurons were flipped on a glia feeding layer with neuronal medium (N2) (1x MEM, 1 mM sodium pyruvate (Sigma, S8636), 1% Neuropan 2 supplement (Pan-Biotech, P07-11100), 0.22% $NaHCO_3$, 0.6% glucose, 2 mM L-glutamine and 1x B-27™ supplements (Gibco™, 17504-044), which was preconditioned for two to three days on the glia feeding layer. For the glia feeding layer, 9 mouse glia cells/mm^2 were plated in a 6 cm culture dish (Thermo Scientific, 150288) and kept in MEM-HS 10%. Three to two days before culture of neurons, media was exchanged to N2 for preconditioning. Glia cells were cultured from embryonic E16.5 to E17.5 mouse brains. Whole hemispheres were collected in HBSS and tissue was digested in 0.05% trypsin-EDTA (Gibco™, 25300-096) supplemented with 7 mM HEPES. After 15 min at 37°C, hemispheres were washed three times with either MEM-HS 1% or HBSS. Subsequently, the tissue was dissociated with fire-polished Pasteur pipettes. Mouse cells were platted in cell culture flasks (Thermo Scientific, 156499) in MEM-HS 10% and incubated at 36.5°C and 5% CO_2. Glia cells were maintained for up to three months and used to prepare glia feeding layers for co-cultures.

For lower density cultures (Figure 11A, B and E, Figure 12B and E, Figure 16A, Figure 17A, Figure 18A, Figure 20A, Figure 21A, Figure 22A, Figure 23A and B), 15 neurons/mm^2 were plated on 15 mm glass-coverslips as described before. For live-cell imaging of neurons (Figure 19A), 61 neurons/mm^2 were plated after transfection in four-well glass-bottom dishes (ibidi, 80427-90). For lysate preparation for the G-/F-actin assays as well

as for protein expression analysis by Western blot, 354-707 neurons/mm^2 of hippocampal or cortical neurons, were plated on 30 mm glass-coverslips (Marienfeld, 0111700) with self-made paraffin dots. Similar to before, two to four hours after plating, glass coverslips with self-made paraffin dots were flipped on glia feeding layer with preconditioned N2 media or plating-media was replaced with conditioned N2 media.

At the indicated time in culture, the drugs or chemicals Cytochalasin D (concentration as indicated, Enzo Life Sciences, BML-T109-0001), Jasplakinolide (5 nM, Cayman Chemical, Cay11706-100), Latrunculin A (concentration as indicated, Sigma, 428021-100UG), Blebbistatin (concentration as indicated, Sigma, B0560-5MG), Taxol (1 nM, Cayman Chemicals, 10461-25), CK-666 (concentration as indicated, Sigma, SML0006-5MG), NaCl (concentration as indicated, AppliChem, A2942.1000) and KCl (concentration as indicated, AppliChem, A3980.0500) were added to the media as indicated. To add the drugs or chemicals to the media of cultured neurons, one ml of the media was removed from the dish and the respective drug was added, and the solution was returned to the culture dish. Neurons were then incubated for the indicated time at 36.5°C and 5% CO_2.

Neuron transfection and infection

Cell transfections were done using the Amaxa Nucleofector II (Lonza, AAB-1001), with the program 0-005 for murine hippocampal neurons. The mouse neuron Nucleofector Kit (Lonza, VPG-1001) was used according to the manufacturer's instructions. Briefly, for each reaction, 4*10^5 neurons were pelleted at 77 rcf for 5 min at RT. The supernatant was carefully removed and cells were resuspended in 100 µl nucleofection solution per reaction with supplements added, provided by the kit. For each transfection, cell suspension was mixed with varying amounts for different plasmids: 5 µg of pAAV-CBA-EB3-mNeon-Green, 4 µg of pCAG-AcGFP (kind gift from Frank Bradke (Addgene plasmid #196849) (Vinopal et al., 2023)) or pCAG-MAP2c-mNeonGreen (kind gift from Charlotte Coles), pCAG-mScarlet (kind gift from Sebastian Dupraz) or pCAG-mTau-mScarlet (kind gift from Max Schelski), and 2 µg of pAAV-CAG-RFP-WPRE or pAAV-CAG-hCofilin1-RFP-WPRE (both Vector Biolabs). After nucleofection in the Amaxa Nucleofector II with the stated program, transfected neurons were plated in culture dishes with MEM-HS10% and cultured for two to four hours until media was replaced with conditioned N2 or glass coverslips were flipped to pre-conditioned glia-feeding layer with N2 media.

To genetically manipulate neurons at any time point after plating, adeno-associated viruses of serotype 1 (AAV1) were used to infect the cells. The following AAV's were purchased from Vector Biolabs: AAV1-CAG-RFP-WPRE (VB5073), AAV1-CAG-h-Coflin1-RFP-WPRE (AAV-230115), AAV1-CAG-RFP (VB1335) and AAV1-CAG-RFP-T2A-iCre (customised). Titres of used viruses ranged from 7.96*10^{12} genome copies (GC)/ml to 1.12*10^{13} GC/ml. To achieve a broad and simultaneous infection of neurons

with the virus, a low dilution of 1:625 of the stock concentrations was used and viruses were added to the culture media at the indicated time points. To add the virus to the culture, one ml media was removed and the virus was added. The mixture was then added back to the culture dish. Successful infection of neurons was validated by immunocytochemistry and Western blotting.

DNA constructs and generation of expression vectors

The expression vector pAAV-CBA-EB3-mNeon was generated by digestion of the backbone of pAAV-CBA-iCre-2A-Fplo (kind gift from Sebastian Dupraz) with BamHI and HindIII releasing iCre-2A-Fplo. EB3-mNeonGreen was amplified from pCMV-EB3-mNeonGreen (kind gift from Charlotte Coles) with primers: forward primer AAV-CBA-(BamHI)-EB3-5'TGGCAAAGAATTGGATCCgccaccatggccgtcaatg-3' and reverse primer AAV-CBA-mNeonGreen-(HindIII)-5'-GAGGTTGATTATCGATAAGCTTTTACTTGTACAGCTCGTC-3'. The polymerase chain reaction product was cloned into the linearised vector ligation independently. All sequences were confirmed with Sanger sequencing by Eurofins Genomics.

Immunocytochemistry

Neurons were incubated for the indicated time points at 36.5°C and 5% CO_2 and then fixed under following conditions: cells were either fixed with 4% paraformaldehyde (PFA)/ 4% sucrose (both Carl Roth, 0335.3 and 4621.2) in 1x phosphate-buffered saline (PBS) for 20 min at RT (Figure 11B and E, and Figure 12B and E), with 4% PFA/ 4% sucrose in PHEM buffer containing 60 mM Pipes (Sigma, P6757-25G), 25 mM HEPES (Millipore, 391338-500GM), 10 mM EGTA (AppliChem, A0878.0100), and 2 mM $MgCl_2$ (Sigma, M8266-100G) for 20 min at RT (Figure 9B, Figure 10A and E, Figure 13B, D and F, Figure 14A, C and E, Figure 15A, C and E, Figure 24A and C, Figure 26A, Figure 28A, Figure 29C, Figure 31A and C, Figure 32A, C, E, G and I, Figure 33A, Figure 34B, E and H, Figure 36A and D, Figure 37A, Figure 39A, Figure 41A and D, and Figure 42A and D), or with 4% PFA/ 4% sucrose in PHEM fixation buffer containing additionally 0.1% Triton X-100 (Sigma, X100-100ML), and 0.25% glutaraldehyde (Sigma, G6257-100ML) for 15 min at RT (Figure 11A, Figure 16A, Figure 17A, Figure 18A, Figure 20A, Figure 21A, Figure 22A, Figure 23A and B, Figure 25B, and Figure 27A). After fixation, samples were washed three times with 1x PBS for fixation with 4% PFA/ 4% sucrose in 1x PBS, or two times with 1x PHEM buffer (without fixatives) and once with 1x PBS when fixatives diluted in PHEM buffer were used. Fixed cells were quenched with either 50 mM ammonium chloride (NH_4Cl) (Supleco, 1.01145.1000) or 0.1 M glycine (Sigma, G8898-1KG) in 1x PBS for 10 min at RT. Quenching with 0.1 M glycine was performed for samples fixed with

glutaraldehyde containing solutions. After quenching, samples were washed three times with 1x PBS and stored in 1x PBS at 4°C or directly used for immunostaining. For immunostaining, samples were blocked at RT for 1 h with 2% Fetal Bovine Serum (FBS) (Thermo Scientific, A5256801), 2% Bovine Serum Albumin (BSA) (Sigma, A3294-100G), and 0.2% fish skin gelatine (Sigma, G7765) in H_2O. After blocking, cells were incubated with the primary antibodies (α-tubulin 1:4.000, Sigma T5168; β-III-tubulin 1:2.000, Sigma T2200; Cofilin 1:100, Abcam ab54532; Cofilin phospho (Ser3) 1:50, Cell Signalling 3313S; Cre 1:1.000, Covance PRB-106P; GFP 1:1.000, Abcam ab13970; RFP 1:1.000, Chromotek 5F8) diluted in 10% blocking solution in 1x PBS for 1 h at RT. Subsequently, samples were washed four times with 1x PBS and then incubated with the secondary antibodies and dyes (Alexa Fluor 488 anti-Chicken 1:1.000, Invitrogen A11039; Alexa Fluor 488 anti-Mouse 1:1.000, Invitrogen A11029; Alexa Fluor 488 anti-Rabbit, Invitrogen A11034; Alexa Fluor 555 anti-Rabbit 1:1.000, Invitrogen A21429; Alexa Fluor 555 anti-Rat 1:1.000, Invitrogen A21434; Alexa Fluor 647 anti-Mouse 1:1.000, Invitrogen A21236; Phalloidin-Alexa Fluor 488 1:250, Invitrogen A12379 (Figure 11B and E, Figure 12B and E); Phalloidin-Alexa-Fluor Plus 647 1:400, Invitrogen A30107 (Figure 16A, Figure 17A, Figure 18A, Figure 21A, Figure 25B, Figure 27A, Figure 29C)) in 10% blocking solution in 1x PBS for 30 min at RT. After incubation, cells were washed three times with 1x PBS and once with H_2O. Then, coverslips with cells were mounted onto microscope slides (Fisher Scientific, 16245172) with Fluoromount™ (Sigma, F4680-25ML). After mounting, samples were protected from light, dried overnight (O/N) at RT and stored at 4°C afterwards.

Since the GFP version that was used to generate the mouse line (Actin-GFP) was one of the earliest GFP constructs available, it is not as bright and photostable as other fluorescent proteins that were engineered in recent years. To increase brightness and photostability of GFP-expressing neurons, samples were always additionally stained with an GFP-antibody (Abcam, ab13970) combined with an Alexa Fluor 488 antibody (Invitrogen, A11039) for better visualisation (e.g. Figure 9B).

G/F-actin assay

For the determination of the ratio of G-actin to F-actin the G-actin/F-actin *In Vivo* Assay Biochem Kit from Cytoskeleton Inc. was used (Cytoskeleton Inc., BK037) following manufactures' instructions. Briefly, at the indicated time points (Figure 11H and I), hippocampal neurons were harvested in provided lysis and F-actin stabilisation buffer containing 1 mM ATP and 1x protease inhibitor cocktail (PIC) at 37°C. Samples were homogenised with a 200 µl pipet tip and subsequently, lysates were incubated for 10 min at 37°C. After lysis, samples were centrifuged for 5 min at 350 rcf and 37°C to pellet unbroken cells. The supernatant was transferred to ultracentrifuge tubes and samples were centrifuged for 1 h at 100.000 rcf and 37°C to pellet F-actin. After ultracentrifugation,

the supernatant containing G-actin was removed and added to fresh tubes, leaving the pellet of F-actin in the ultracentrifuge tube. F-actin depolymerisation buffer was added to each pellet and incubated on ice for 1 h. Every 15 min, samples were pipetted up and down to increase resuspension of F-actin. 5x SDS/Laemmli buffer was added to both pellet and supernatant samples. The ratio of G-/F-actin was analysed by western blot.

Western blot

For determination of protein amounts in neurons, cells were lysed at the indicated time points. For lysis of neurons, samples were washed once with ice-cold 1x PBS and neurons were harvested in 1x RIPA buffer (Millipore, 20-188) supplemented with phosphatase and protease inhibitors 1x Phos-STOP™ (Roche, 4906845001) and 1x PIC cOmplete™ (Roche, 4693116001) on ice. Samples were incubated for 5 min on ice and then centrifuged for 5 min at 13.000 rcf at 4°C. The supernatant was transferred to a fresh tube and mixed with 5x SDS/Laemmli buffer to a 1x concentration. Afterwards, samples were boiled for 5 min at 95 °C on a heating-shaker. For every sample a small amount of cell lysate for determination of protein concentrations was kept. Protein concentration in the lysate was determined using the Bradford Reagent (AppliChem, A6932.0250). Briefly, a 0.5 µg/ml protein solution of BSA was prepared in H_2O for generation of a standard curve. Known and unknown amounts of protein were mixed with 2.5 µl of lysis buffer, 200 µl of Bradford Reagent and 800 µl H_2O. After incubation for 5 min at RT, the absorption at 595 nm was measured in a photometer (Eppendorf). Protein concentrations in samples were determined based on standard curves calculated from known protein concentrations.
Same amounts of protein (5 µg to 10 µg) were loaded on 4-12% NuPAGE™ Bis-Tris gradient gels (Thermo Scientific, NP0335BOX) and fractioned by 3-(N-morpholino)-propane sulfonic acid (MOPS)/SDS-polyacrylamide gel electrophoresis (PAGE) (20x MOPS buffer, Invitrogen, NP0001). After running the gel to completion at 110 V in 1x MOPS buffer, proteins were transferred to a PVDF membrane (Millipore, ISEQ00010) at 150 mA per gel in ice-cold 1x transfer buffer with 20% methanol on ice. Membranes were directly blocked with 5% milk (Cell Signalling, 9999S) (Figure 11H, Figure 35A, Figure 38C) or 5% BSA (Figure 29A, and Figure 30B and D) in 1x Tris-buffered saline (TBS) with 0.1% Tween20 (AppliChem, A4974.0500) (TBS-T) on a vertical shaker for 1 h at RT. Primary antibodies (pan-actin 1:1.000, Cytoskeleton AAN02; Arp2 1:1500, Cell Signalling 5614S; Arp3 1:8.000, Sigma A5979; Cofilin 1:1.000, Cell Signalling 5175S; Cofilin phosphor (Ser3) 1:1.000, Cell Signalling 3313S; GAPDH 1:5.000, OriGene 5G4-6C5; β-III-tubulin 1:10.000, Biolegend 801201) were diluted in 10% blocking solution in 1x TBS-T and incubated O/N at 4°C on a shaker. After incubation, blots were washed three times with 1x TBS-T for 10-15 min each. Subsequently, secondary antibodies (Horse radish peroxidase (HRP) conjugated anti-Rabbit 1:10.000, Thermo Scientific 31458; HRP

conjugated anti-Mouse 1:10.000, Thermo Scientific 31432) were applied for 1 h on a vertical shaker at RT. After three times washing with 1x TBS-T for 10-15 min each, the membranes were incubated with chemiluminescence solutions Pierce, Pico or Dura (all Thermo Scientific, 32209, 34577, and 34076) and the signal was fixed on CL-Xposure™ film (Thermo Scientific, 34090) and developed with an automatic Cawomat (Cawo, 2000IR) developer.

Microscopy

Live-cell imaging

For live-cell imaging of microtubule dynamics (Figure 19), WT neurons were transfected with a plasmid encoding the expression of EB3-mNeonGreen and neurons were plated in 4-well µ-dishes as described above. Drug treatments (as indicated) were performed 18 h before imaging start. GFP images were acquired every 2 s for 3 min with a PlanApochromat 60x/1.42 infinity/0.17/FN26.5 objective (Olympus) on a DeltaVision RT (Applied Precision) based on an Olympus IX71 inverted microscope, with a CO_2 regulated incubation chamber maintained at 37°C (Solent Scientific). Images were acquired with a Photometrics CoolSnap HQ camera (Roper Scientific) using SoftWoRX 3.5.0 imaging software (Applied Precision).

Imaging of fixed samples

Imaging of whole cover slips or individual regions of interest (ROIs') was conducted using a fully motorised AxioObserver.D1(Zeiss) inverted epifluorescence widefield microscope equipped with a Colibri 7 LED light source and ZenBlue software (version 3.11) (all from Zeiss) at RT. Images were taken with an Axiocam 512 mono camera using a Plan-Apochromat 10x air objective with a numerical aperture (NA) of 0.45, a Plan-Apochromat 40x air objective with a NA of 0.95 (Figure 11B and E, and Figure 12B and E), or a Plan-Apochromat 63x oil objective with a NA of 1.4 (Figure 29C). A dichroic Quad filter (QBS 405, 493, 575 and 653) and single band-pass emission filters for the green channel (525/50), and the red channel (605/40) and a quad band-pass filter (425/30 + 514/30 + 592/25 + 709/100) for the far-red channel were used. For the green, the red, and the far-red channel, a 475 nm LED-module, a 555 nm LED-module, and a 630 nm LED-module were used. For imaging of whole cover slips with a diameter of 15 mm, the tile scan regions for the individual cover slips were set in ZenBlue software (version 3.11). To this aim, a 15 mm circular tile region was created and its edge was aligned with the edge of the actual cover slip. To maintain the focus, a 12-point focus map was generated to capture the focus plane of the neurites. After acquisition, the tile regions were stitched from a 10% overlap. For high resolution imaging, a AxioObserver.Z1 with an Airyscan 2 detector of a laser-scanning-microscope (LSM) 900 equipped with a laser module controlled with ZenBlue

software (version 3.11) was used (all Zeiss). Images were taken with a Plan-Apochromat 40x oil objective with a NA of 1.4 (Figure 11A) or a Plan-Apochromat 63x oil objective with a NA of 1.4 (Figure 16A, Figure 17A, Figure 18A, Figure 21A, Figure 22A, Figure 25B, Figure 27A). For the green, the red, and the far-red channel, a laser with the wavelength of 488 nm, 561 nm, and 640 nm and a detection wavelength of 495-550 nm, 545-620 nm and 639-700 nm was used. For imaging of neurite tips and growth cones, a z-stack was captured with 6 slices and an interval of 0.15 µm. The acquired images were post-processed for super resolution imaging based on 2D channels with the ZenBlue software set to auto filter. Cells for imaging of neurite tips were selected randomly or based on visible expression of a transfected construct.

Patch clamp electrophysiological recordings

For the analysis of intrinsic and synaptic electrophysiological properties, primary hippocampal neurons of WT and Actin-GFP mice were cultured as described above and plated in a density of 35 neurons/mm^2 on 15 mm glass coverslips with 1% GFP$^+$ cells. At the indicated time points, cells were transferred from the culture media to a Ringer solution (extracellular solution) containing 125 mM NaCl, 3 mM KCl, 1 mM MgCl2, 1.5 mM CaCl2 (Sigma, C5080-500G), 10 mM HEPES, and 10 mM D(+)-glucose (adjusted to pH 7.3 with NaOH). Freshly pulled borosilicate glass pipettes (3-6 MΩ) were filled with an intracellular solution containing 135 mM K-gluconate (Sigma, P1847-100G), 10 mM KCl, 10 mM HEPESS, 0.1 mM EGTA, 2 mM $MgCl_2$, 3 mM K-ATP (Sigma, A8937-5G), and 0.3 mM Na-GTP (Sigma, G8877-250MG) (adjusted to pH 7.2 with KOH). Recordings were carried out at 31-32 °C, controlled by Temperature Controller VII (Luigs-Neumann) in flowing Ringer solution. For measurements of electrophysiological properties of neurons in presence of elevated extracellular potassium, the concentration of KCl was increased by 40 mM, or 40 mM NaCl as a control, in the Ringer solution. For measurements of the acute effect, neurons on glass coverslips were placed in normal Ringer solution first, and a baseline measurement was taken. Subsequently, the patched cells were exposed to elevated KCL or NaCl as a control by flowing in Ringer solution with elevated salt concentrations. MultiClamp 700B (Axon Instruments) was used to amplify and AxonDigidata 1550B (Axon Instruments) was used to digitise (10 kHz sampling rate) the signals. Membrane potential was measured in current clamp mode. Membrane input resistance was calculated based on voltage deflection in response to negative current injections. Spontaneous excitatory postsynaptic currents (sEPSCs) were measured in voltage clamp mode with holding potential of -60 mV. EPSC detection was carried out using the clampfit event detection template search tool. AP detection to calculate spontaneous activity was carried out using the event detection threshold search (Clampfit, Version 11, Axon Instruments).

Use of generative artificial intelligence

Generative artificial intelligence (AI), was used to aid in the generation of ImageJ macros, for the analysis of experimental data. No text or images generated by AI were copied into this manuscript.

Analysis and quantification

Quantification of the length of the longest neurite and second longest neurite

Stitched images of whole cover slips were split into their different channels and converted to 8bit files. The longest or second longest neurite was then manually traced by visual identification of the respective neurite path and quantified using the NeuronJ plugin (Meijering et al., 2004) of Fiji/ImageJ (Schindelin et al., 2012). The longest neurite, if longer than 100 µm, was considered to be the axon. For minor neurite/dendrite length, the second longest neurite was identified based on visual identification and measured. For quantification of mixed cultures, all GFP^+-neurons on the whole coverslip were quantified. When the neurite length could not be determined from the cell body to the tip, the neuron was not considered for analysis. When neurons expressed a construct of interest, only expressing cells were used for quantification of neurite length. In case WT neurons were used without any genetic labelling, a defined area of similar size for all quantified cover slips was used and all Tuj^+ cells in this area were included in the measurement of the longest neurite. For quantification of neurite length after infection with a virus in mixed cultures, all GFP^+-neurons on the whole cover slip were quantified without distinguishing infected (RFP^+/Cre^+) and non-infected neurons (Figure 31C and D, and Figure 39A and B).

Image analysis

Quantification of actin intensities in ROIs was done with ImageJ. Raw files were opened in Fiji and the different channels were split. In the actin channel, the background was subtracted with the subtract background command in ImageJ and the rolling ball radius set to a size of 50 pixels. For whole cell analysis of actin intensity, the mean actin intensity of the whole ROI was used (Figure 11B and C, and Figure 12B and C). Cell area within the ROIs was quantified based on thresholding the α-tubulin signal (Figure 11D, and Figure 12D). To specifically look at actin intensities in growth cones, the growth cone area was defined based on Phalloidin staining and manually drawn using the freehand selection tool of Fiji (Figure 11E, F and G, and Figure 12E, F and G). Within this defined area, the mean actin intensity was quantified and the area was used as a measure of growth cone size. The localisation of remaining actin filaments within the growth cone was quantified by manually drawing a straight line from the leading edge of the growth cone to the neurite shaft with a width of 1 pixel in Fiji as indicated in Figure 12E. The actin intensity along this line was plotted. For every individual experiment, the area under the curve of actin intensity along the line scan, from the leading edge to the neurite shaft, was quantified in PRISM 10.

For quantification of cofilin and p-cofilin intensity and the respective ratio, the background was subtracted in the respective channel using the subtract background tool in Fiji with a rolling ball size set to 50 pixels. Mean cofilin and p-cofilin intensities in the growth cone were measured by manually defining the area based on phalloidin staining (Figure 29C and D).

To quantify microtubule bundling and width of Tuj signal along the neurite, from the leading edge towards the soma, the VasoMetrics plugin in ImageJ was used (McDowell et al., 2021). Maximum intensity projections of z-stacks (6 slices) were generated, files were split in the different channels and saved as .tiff files. The Tuj channel was opened in the VasoMetrics plugin and a throughline was manually drawn exactly through the centre of the neurite along the longitudinal axis, from the leading edge towards the soma. The crossline length was manually set to 400 pixels and the distance between crosslines was set to 2 µm. The full-width at half-maximum intensity was defined at every crossline and plotted (Figure 16B, D and F, Figure 18B, Figure 21B and C, Figure 25C and D, and Figure 27B and C). For every individual experiment, the area under the curve for the full-width at half-maximum intensity was quantified in PRISM 10.

Similarly, the bundling of microtubules was quantified after live cell imaging. Therefore, maximum intensity projections were generated from 3 min EB3-mNeonGreen live imaging videos (Figure 19A, C and D). The spreading of microtubules was quantified with the same settings as described above.

For quantification of actin and tubulin intensity in neurite tips, the maximum intensity projections of the super resolution images were used and a segmented line with a width of 100 pixels was drawn manually from the leading edge towards the neurite shaft in Fiji, as indicated in Figure 17A. The fluorescence intensity of actin and tubulin along the line was quantified and plotted (Figure 17B and D). The line width was set to 250 pixels for quantification of tubulin intensity in Figure 22 to capture tubulin intensity for the whole neurite width.

Quantification of neuronal polarisation

Neuronal polarisation was defined based on length (Figure 10D, and Figure 41C). A neurite longer then 100 µm was considered as an axon and the neuron was counted as polarised. No quantification for neurons with multiple axons was done, if a neuron had more than one neurite longer than 100 µm it was also considered as polarised. Neurons with neurites short then 100 µm were defined as unpolarised. Minor neurites were defined as cell process with a length > 10 µm but < 100 µm. This definition of polarisation was used until dendrites reached a length > 100 µm at around DIV 7. Afterwards, axons and dendrites were distinguished based on morphological characteristics of neurite shaft diameter and overall length. No axonal or dendritic marker was used.

Quantification of immunoblots

Protein amount in immunoblots was assessed by quantification of the average mean intensity of the protein bands measured in Fiji and divided by the protein amount of the corresponding loading control (Figure 38C and D). Glyceraldehyde-3-phosphate dehydrogenase (GAPDH) was used as protein loading control or additionally Tuj (Figure 35A and B). For the F- to G-actin ratio assay, the protein amount of F-actin was divided by the protein amount of G-actin for each of the according conditions (Figure 11H and I). To record differences in phosphorylation level, first the amount of phospho- and total protein was quantified and divided by the respective loading control, and then the ratio was done (Figure 29A and B, and Figure 30B, C, D, E and F). The number of independent experiments for each condition is indicated in the corresponding figure legend.

Tracking and quantification of EB3 comets

The quantification of EB3 comets as a measure of microtubule dynamics was done with the plusTipTracker in the u-track software (version 2.3) of the Danuser lab in Matlab (Applegate et al., 2011). Live-imaging videos were uploaded to the software in Matlab and the following parameters were set to detect comets: 'Low-Pass Gaussian Standard Deviation' was set to 2 pixels, 'High-Pass Gaussian Standard Deviation' was set to 5 pixels, 'Minimum Threshold' was set to 6 SD, and 'Threshold Step' was set to 1 SD. For tracking and track analysis the default set parameters were used. Individual values of all cells/growth cones quantified were used for statistical analysis.

Statistical analysis and preparation of graphs

Statistical analysis for all quantifications and preparation of graphs was performed with GraphPad Prism 10. Statistical analysis was done from mean values of at least three independent experiments, if not stated differently in the figure legends. Details for statistical tests, number of independent experiments (n) and number of individual cells (N) used for the quantifications are indicated in the corresponding figure legend. Briefly, where only two conditions were compared, a Student's t-test was performed. When more than two conditions were compared, statistical analysis was done via one-way ANOVA with multiple comparisons post-hoc test applicable to the respective experimental design, as indicated in the figure legends. For comparisons of multiple conditions over several groups, two-way ANOVA with a post-hoc test applicable to the respective experimental design was used, as indicated in the figure legends. For all analyses performed, significance was defined as *$p<0.05$, **$p<0.01$, ***$p<0.001$, ****$p<0.0001$ and not significant when no * in the graph is shown.

References

Abankwa, D., P. Kury, and H.W. Muller. 2002. Dynamic changes in gene expression profiles following axotomy of projection fibres in the Mammalian CNS. *Mol Cell Neurosci* 21:421-435.

Abouelezz, A., H. Stefen, M. Segerstrale, D. Micinski, R. Minkeviciene, L. Lahti, E.C. Hardeman, P.W. Gunning, C.C. Hoogenraad, T. Taira, T. Fath, and P. Hotulainen. 2020. Tropomyosin Tpm3.1 Is Required to Maintain the Structure and Function of the Axon Initial Segment. *iScience* 23:101053.

Alfadil, E., and F. Bradke. 2023. Moving through the crowd. Where are we at understanding physiological axon growth? *Semin Cell Dev Biol* 140:63-71.

Alkemade, C., H. Wierenga, V.A. Volkov, M. Preciado Lopez, A. Akhmanova, P.R. Ten Wolde, M. Dogterom, and G.H. Koenderink. 2022. Cross-linkers at growing microtubule ends generate forces that drive actin transport. *Proc Natl Acad Sci U S A* 119:e2112799119.

Allen, N.J., and D.A. Lyons. 2018. Glia as architects of central nervous system formation and function. *Science* 362:181-185.

Allison, D.W., V.I. Gelfand, I. Spector, and A.M. Craig. 1998. Role of Actin in Anchoring Postsynaptic Receptors in Cultured Hippocampal Neurons - Differential Attachment of NMDA versus AMPA Receptors. *The Journal of Neuroscience* 18:2423-2436.

Alves-Silva, J., N. Sanchez-Soriano, R. Beaven, M. Klein, J. Parkin, T.H. Millard, H.J. Bellen, K.J. Venken, C. Ballestrem, R.A. Kammerer, and A. Prokop. 2012. Spectraplakins promote microtubule-mediated axonal growth by functioning as structural microtubule-associated proteins and EB1-dependent +TIPs (tip interacting proteins). *J Neurosci* 32:9143-9158.

Amano, M., K. Chihara, N. Nakamura, Y. Fukata, T. Yano, M. Shibata, M. Ikebe, and K. Kaibuchi. 1998. Myosin II activation promotes neurite retraction during the action of Rho and Rho-kinase. *Genes Cells* 3:177-188.

Applegate, K.T., S. Besson, A. Matov, M.H. Bagonis, K. Jaqaman, and G. Danuser. 2011. plusTipTracker: Quantitative image analysis software for the measurement of microtubule dynamics. *J Struct Biol* 176:168-184.

Arimura, N., and K. Kaibuchi. 2007. Neuronal polarity: from extracellular signals to intracellular mechanisms. *Nat Rev Neurosci* 8:194-205.

Arnold, D.B., and G. Gallo. 2014. Structure meets function: actin filaments and myosin motors in the axon. *J Neurochem* 129:213-220.

Arszovszki, A., Z. Borhegyi, and T. Klausberger. 2014. Three axonal projection routes of individual pyramidal cells in the ventral CA1 hippocampus. *Front Neuroanat* 8:53.

Ashley, J., V. Sorrentino, M. Lobb-Rabe, S. Nagarkar-Jaiswal, L. Tan, S. Xu, Q. Xiao, K. Zinn, and R.A. Carrillo. 2019. Transsynaptic interactions between IgSF proteins DIP-alpha and Dpr10 are required for motor neuron targeting specificity. *Elife* 8:

Ashraf, S.S., V. Hosseinpour Sarmadi, G. Larijani, S. Naderi Garahgheshlagh, S. Ramezani, S. Moghadamifar, S.L. Mohebi, P. Brouki Milan, S.M.A. Haramshahi, N. Ahmadirad, and N. Amini. 2023. Regenerative medicine improve neurodegenerative diseases. *Cell Tissue Bank* 24:639-650.

Athamneh, A.I.M., Y. He, P. Lamoureux, L. Fix, D.M. Suter, and K.E. Miller. 2017. Neurite elongation is highly correlated with bulk forward translocation of microtubules. *Sci Rep* 7:7292.

Azevedo, F.A., L.R. Carvalho, L.T. Grinberg, J.M. Farfel, R.E. Ferretti, R.E. Leite, W. Jacob Filho, R. Lent, and S. Herculano-Houzel. 2009. Equal numbers of neuronal and nonneuronal cells make the human brain an isometrically scaled-up primate brain. *J Comp Neurol* 513:532-541.

Baird, D.H., C.A. Baptista, L.C. Wang, and C.A. Mason. 1992. Specificity of a target cell-derived stop signal for afferent axonal growth. *J Neurobiol* 23:579-591.

Balcer, H.I., K. Daugherty-Clarke, and B.L. Goode. 2010. The p40/ARPC1 subunit of Arp2/3 complex performs multiple essential roles in WASp-regulated actin nucleation. *J Biol Chem* 285:8481-8491.

Bamburg, J.R., B.W. Bernstein, R.C. Davis, K.C. Flynn, C. Goldsbury, J.R. Jensen, M.T. Maloney, I.T. Marsden, L.S. Minamide, C.W. Pak, A.E. Shaw, I. Whiteman, and O. Wiggan. 2010. ADF/cofilin-actin rods in neurodegenerative diseases. *Current Alzheimer Research* 7:241-250.

Banker, G.A., and W.M. Cowman. 1977. Rat Hippocampal Neurons in Dispersed Cell Culture. *Brain Research* 126:397-425.

Basarsky, T.A., V. Parpura, and P.G. Haydon. 1994. Hippocampal Synaptogenesis in Cell Culture: Developmental Time Course of Synapse Formation, Calcium Influx, and Synaptic Protein Distribution. *The Journal of Neuroscience* 14:6402-6411.

Behrooz, A.B., and S. Shojaei. 2024. Mechanistic insights into mesenchymal-amoeboid transition as an intelligent cellular adaptation in cancer metastasis and resistance. *Biochim Biophys Acta Mol Basis Dis* 1870:167332.

Benson, D.L., F.H. Watkins, O. Steward, and G.A. Banker. 1994. Characterization of GABAergic neurons in hippocampal cell cultures. *Journal of Neurocytology* 23:279-295.

Biffi, E., G. Regalia, A. Menegon, G. Ferrigno, and A. Pedrocchi. 2013. The influence of neuronal density and maturation on network activity of hippocampal cell cultures: a methodological study. *PLoS One* 8:e83899.

Bikbaev, A., A. Ciuraszkiewicz-Wojciech, J. Heck, O. Klatt, R. Freund, J. Mitlohner, S. Enrile Lacalle, M. Sun, D. Repetto, R. Frischknecht, C. Ablinger, A. Rohlmann, M. Missler, G.J. Obermair, V. Di Biase, and M. Heine. 2020. Auxiliary alpha2delta1 and alpha2delta3 Subunits of Calcium Channels Drive Excitatory and Inhibitory Neuronal Network Development. *J Neurosci* 40:4824-4841.

Binder, L.I., A. Frankfurter, and L.I. Rebhun. 1986. Differential localization of MAP-2 and tau in mammalian neurons in situ. *Ann N Y Acad Sci* 466:145-166.

Biswas, S., and K. Kalil. 2018. The Microtubule-Associated Protein Tau Mediates the Organization of Microtubules and Their Dynamic Exploration of Actin-

Rich Lamellipodia and Filopodia of Cortical Growth Cones. *J Neurosci* 38:291-307.

Bläsius, K. 2016. Study on the role of Cofilin 2 in the brain. In Institut für Genetik. Rheinische Friedrich-Wilhelms-Universität Bonn, 222.

Bodakuntla, S., A.S. Jijumon, C. Villablanca, C. Gonzalez-Billault, and C. Janke. 2019. Microtubule-Associated Proteins: Structuring the Cytoskeleton. *Trends Cell Biol* 29:804-819.

Bovolenta, P., and C. Mason. 1987. Growth Cone Morphology Varies with Position in the Developing Mouse Visual Pathway from Retina to First Targets. *The Journal of Neuroscience* 7:1447-1460.

Bradbury, E.J., and E.R. Burnside. 2019. Moving beyond the glial scar for spinal cord repair. *Nat Commun* 10:3879.

Bradke, F. 2022. Mechanisms of Axon Growth and Regeneration: Moving between Development and Disease. *J Neurosci* 42:8393-8405.

Bradke, F., and C.G. Dotti. 1997. Neuronal Polarity: Vectorial Cytoplasmic Flow Precedes Axon Formation. *Neuron* 19:1175-1186.

Bradke, F., and C.G. Dotti. 1999. The Role of Local Actin Instability in Axon Formation. *Science* 283:1931-1934.

Bradke, F., and C.G. Dotti. 2000. Differentiated neurons retain the capacity to generate axons from dendrites. *Current Biology* 10:1467-1470.

Bradke, F., J.W. Fawcett, and M.E. Spira. 2012. Assembly of a new growth cone after axotomy: the precursor to axon regeneration. *Nat Rev Neurosci* 13:183-193.

Broeke, J.H., M. Roelandse, M.J. Luteijn, T. Boiko, A. Matus, R.F. Toonen, and M. Verhage. 2010. Munc18 and Munc13 regulate early neurite outgrowth. *Biol Cell* 102:479-488.

Buchsbaum, I.Y., and S. Cappello. 2019. Neuronal migration in the CNS during development and disease: insights from in vivo and in vitro models. *Development* 146:

Burdett, T.C., and M.R. Freeman. 2014. Neuroscience. Astrocytes eyeball axonal mitochondria. *Science* 345:385-386.

Burnette, D.T., L. Ji, A.W. Schaefer, N.A. Medeiros, G. Danuser, and P. Forscher. 2008. Myosin II activity facilitates microtubule bundling in the neuronal growth cone neck. *Dev Cell* 15:163-169.

Burnette, D.T., S. Manley, P. Sengupta, R. Sougrat, M.W. Davidson, B. Kachar, and J. Lippincott-Schwartz. 2011. A role for actin arcs in the leading-edge advance of migrating cells. *Nat Cell Biol* 13:371-381.

Burute, M., K.I. Jansen, M. Mihajlovic, T. Vermonden, and L.C. Kapitein. 2022. Local changes in microtubule network mobility instruct neuronal polarization and axon specification. *Science Advances* 8:

Caceres, A., J. Mautino, and K.S. Kosik. 1992. Suppression of MAP2 in Cultured Cerebeller Macroneurons Inhibits Minor Neurite Formation. *Neuron* 9:607-618.

Caceres, A., S. Potrebic, and K.S. Koski. 1991. The Effect of Tau Antisense Oligonucleotides on Neurite Formation of Cultured Cerebellar Macroneurons. *The Journal of Neuroscience* 11:1515-1523.

Cammarata, G.M., E.A. Bearce, and L.A. Lowery. 2016. Cytoskeletal social networking in the growth cone: How +TIPs mediate microtubule-actin cross-linking to drive axon outgrowth and guidance. *Cytoskeleton (Hoboken)* 73:461-476.

Cao, L., S. Huang, A. Basant, M. Mladenov, and M. Way. 2024. CK-666 and CK-869 differentially inhibit Arp2/3 iso-complexes. *EMBO Rep* 25:3221-3239.

Capizzi, M., R. Carpentier, E. Denarier, A. Adrait, R. Kassem, M. Mapelli, Y. Coute, and S. Humbert. 2022. Developmental defects in Huntington's disease show that axonal growth and microtubule reorganization require NUMA1. *Neuron* 110:36-50 e35.

Carlier, M.-F., C. Jean, K.J. Rieger, M. Lenfant, and D. Pantaloni. 1993. Modulation of the interaction between G-actin and thymosin beta4 by the ATP/ADP

ratio: Possible implication in the regulation of actin dynamics. *Proc Natl Acad Sci U S A* 90:5034-5038.

Carlier, M.F., V. Laurent, J. Santolini, R. Melki, D. Didry, G.-X. Xia, Y. Hong, N.-H. Chua, and D. Pantaloni. 1997. Actin Depolymerizing Factor (ADF/Cofilin) Enhances the Rate of FIlament Turnover: Implication in Actin-based Motility. *The Journal of Cell Biology* 136:1307-1323.

Challacombe, J.F., D.M. Snow, and P.C. Letourneau. 1997. Dynamic Microtubule Ends Are Required for Growth Cone Turning to Avoid an Inhibitory Guidance Cue. *The Journal of Neuroscience* 17:3085-3095.

Chauhan, P., K. Jethwa, A. Rathawa, G. Chchaunauhan, and S. Mehra. 2021. The Anatomy of the Hippocampus. In Cerebral Ischemia. Exon Publications, Brisbane (AU).

Chen, B., and Y. Wang. 2015. Cofilin Rod Formation in Neurons Impairs Neuronal Structure and Function. *CNS & Neurological Disorders - Drug Targets* 14:554-560.

Chen, J., E. Kholina, A. Szyk, V.A. Fedorov, I. Kovalenko, N. Gudimchuk, and A. Roll-Mecak. 2021. alpha-tubulin tail modifications regulate microtubule stability through selective effector recruitment, not changes in intrinsic polymer dynamics. *Dev Cell* 56:2016-2028 e2014.

Chen, J., D. Yan, and Y. Chen. 2023. Understanding the driving force for cell migration plasticity. *Biophys J* 122:3570-3576.

Cheng, S., J. Ashley, J.D. Kurleto, M. Lobb-Rabe, Y.J. Park, R.A. Carrillo, and E. Ozkan. 2019. Molecular basis of synaptic specificity by immunoglobulin superfamily receptors in Drosophila. *Elife* 8:

Chesarone, M.A., A.G. DuPage, and B.L. Goode. 2010. Unleashing formins to remodel the actin and microtubule cytoskeletons. *Nature Reviews Molecular Cell Biology* 11:62-74.

Chia, J.X., N. Efimova, and T.M. Svitkina. 2016. Neurite outgrowth is driven by actin polymerization even in the presence of actin polymerization inhibitors. *Mol Biol Cell* 27:3695-3704.

Chia, P.H., P. Li, and K. Shen. 2013. Cell biology in neuroscience: cellular and molecular mechanisms underlying presynapse formation. *J Cell Biol* 203:11-22.

Chugh, P., and E.K. Paluch. 2018. The actin cortex at a glance. *J Cell Sci* 131:

Cichon, J., C. Sun, B. Chen, M. Jiang, X.A. Chen, Y. Sun, Y. Wang, and G. Chen. 2012. Cofilin aggregation blocks intracellular trafficking and induces synaptic loss in hippocampal neurons. *J Biol Chem* 287:3919-3929.

Cingolani, L.A., and Y. Goda. 2008. Actin in action: the interplay between the actin cytoskeleton and synaptic efficacy. *Nat Rev Neurosci* 9:344-356.

Coles, C.H., and F. Bradke. 2015. Coordinating neuronal actin-microtubule dynamics. *Curr Biol* 25:R677-691.

Collins, R., H. Lee, D.H. Jones, J.M. Elkins, J.A. Gillespie, C. Thomas, A.G. Baldwin, K. Jones, L. Waters, M. Paine, J.R. Atack, S.E. Ward, O. Grubisha, and D.W. Foley. 2022. Comparative Analysis of Small-Molecule LIMK1/2 Inhibitors: Chemical Synthesis, Biochemistry, and Cellular Activity. *J Med Chem* 65:13705-13713.

Cooke, P., H. Janowitz, and S.E. Dougherty. 2022. Neuronal Redevelopment and the Regeneration of Neuromodulatory Axons in the Adult Mammalian Central Nervous System. *Front Cell Neurosci* 16:872501.

Cooper, J.A. 1987. Effects of Cytochalasin and Phalloidin on Actin. *The Journal of Cell Biology* 105:1473-1478.

Costa, A.R., and M.M. Sousa. 2020. Non-Muscle Myosin II in Axonal Cell Biology: From the Growth Cone to the Axon Initial Segment. *Cells* 9:

Costa, A.R., and M.M. Sousa. 2021. The role of the membrane-associated periodic skeleton in axons. *Cell Mol Life Sci* 78:5371-5379.

Coué, M., S.L. Brenner, I. Spector, and E.D. Korn. 1987. Inhibition of actin polymerization by latrunculin A. *FEBS Letters* 213:316-318.

Craig, A.M., R.J. Wyborski, and G.A. Banker. 1995. Preferential addition of newly synthesized membrane protein at axonal growth cones. *Nature* 375:592-594.

Cramer, L.P. 1999. Role of actin-filament disassembly in lamellipodium protrusion in motile cells revealed using the drug jasplakinolide. *Current Biology* 9:1095-1105.

de Anda, F.C., G. Pollarolo, J.S. Da Silva, P.G. Camoletto, F. Feiguin, and C.G. Dotti. 2005. Centrosome localization determines neuronal polarity. *Nature* 436:704-708.

Dehmelt, L., and S. Halpain. 2004. The MAP2/Tau family of micortubule-associated proteins. *Genome Biol* 6:

Dehmelt, L., F.M. Smart, R.S. Ozer, and S. Halpain. 2003. The Role of Microtubule-Associated Protein 2c in the Reorganization of Microtubules and Lamellipodia during Neurite Initiation. *The Journal of Neuroscience* 23:9479-9490.

Deisseroth, K., and P. Hegemann. 2017. The form and function of channelrhodopsin. *Science* 357:

Dent, E.W. 2020. Dynamic microtubules at the synapse. *Curr Opin Neurobiol* 63:9-14.

Dent, E.W., S.L. Gupton, and F.B. Gertler. 2011. The growth cone cytoskeleton in axon outgrowth and guidance. *Cold Spring Harb Perspect Biol* 3:

Dent, E.W., and K. Kalil. 2001. Axon Branching Requires Interactions between Dynamic Microtubules and Actin Filaments. *The Journal of Neuroscience* 21:9757-9769.

Dietz, V., and K. Fouad. 2014. Restoration of sensorimotor functions after spinal cord injury. *Brain* 137:654-667.

Dotti, C.G., and G.A. Banker. 1987. Experimentally induced alteration in the polarity of developing neurons. *Nature* 330:254-256.

Dotti, C.G., G.A. Banker, and L.I. Binder. 1987. The Expression and Distribution of the Microtubule-Associated Proteins Tau and Microtubule-Associated Protein 2 in Hippocampal Neurons in the Rat in situ and in Cell Culture. *Neuroscience* 23:121-130.

Dotti, C.G., C.A. Sullivan, and G.A. Banker. 1988. The Establishment of Polarity by Hippocampal Neurons in Culture. *Journal of Neuroscience* 8:1454-1468.

Doussau, F., and G.J. Augustine. 2000. he actin cytoskeleton and neurotransmitter release: An overview. *Biochimie* 82:353-363.

Dupraz, S., D. Grassi, M.E. Bernis, L. Sosa, M. Bisbal, L. Gastaldi, I. Jausoro, A. Caceres, K.H. Pfenninger, and S. Quiroga. 2009. The TC10-Exo70 complex is essential for membrane expansion and axonal specification in developing neurons. *J Neurosci* 29:13292-13301.

Dupraz, S., B.J. Hilton, A. Husch, T.E. Santos, C.H. Coles, S. Stern, C. Brakebusch, and F. Bradke. 2019. RhoA Controls Axon Extension Independent of Specification in the Developing Brain. *Curr Biol* 29:3874-3886 e3879.

Efimova, N., and T.M. Svitkina. 2018. Branched actin networks push against each other at adherens junctions to maintain cell-cell adhesion. *J Cell Biol* 217:1827-1845.

Elie, A., E. Prezel, C. Guerin, E. Denarier, S. Ramirez-Rios, L. Serre, A. Andrieux, A. Fourest-Lieuvin, L. Blanchoin, and I. Arnal. 2015. Tau co-organizes dynamic microtubule and actin networks. *Sci Rep* 5:9964.

Enes, J., N. Langwieser, J. Ruschel, M.M. Carballosa-Gonzalez, A. Klug, M.H. Traut, B. Ylera, S. Tahirovic, F. Hofmann, V. Stein, S. Moosmang, I.D. Hentall, and F. Bradke. 2010. Electrical activity suppresses axon growth through Ca(v)1.2 channels in adult primary sensory neurons. *Curr Biol* 20:1154-1164.

Erck, C., L. Peris, A. Andrieux, C. Meissirel, A.D. Gruber, M. Vernet, A. Schweitzer, Y. Saoudi, H. Pointu, C. Bosc, P.A. Salin, D. Job, and J. Wehland. 2005. A

vital role of tubulin-tyrosine-ligase for neuronal organization. *PNAS* 102:7853-7858.

Ertürk, A., F. Hellal, J. Enes, and F. Bradke. 2007. Disorganized microtubules underlie the formation of retraction bulbs and the failure of axonal regeneration. *J Neurosci* 27:9169-9180.

Eshun-Wilson, L., R. Zhang, D. Portran, M.V. Nachury, D.B. Toso, T. Lohr, M. Vendruscolo, M. Bonomi, J.S. Fraser, and E. Nogales. 2019. Effects of alpha-tubulin acetylation on microtubule structure and stability. *Proc Natl Acad Sci U S A* 116:10366-10371.

Fährmann, K. 2025. Proteomic screen of dorsal root ganglion neuron growth states reveals Glypican 1 as an autocrine and paracrine activator of axon growth. In Deutsches Zentrum für Neurodegenerative Erkrankungen e.V. Rheinische Friedrich-Wilhelms-Universität Bonn.

Ferron, F., G. Rebowski, S.H. Lee, and R. Dominguez. 2007. Structural basis for the recruitment of profilin-actin complexes during filament elongation by Ena/VASP. *EMBO J* 26:4597-4606.

Fine, R.E., and D. Bray. 1971. Actin in Growing Nerve Cells. *Nature New Biology* 234:115-118.

Flynn, K.C. 2013. The cytoskeleton and neurite initiation. *Bioarchitecture* 3:86-109.

Flynn, K.C., F. Hellal, D. Neukirchen, S. Jacob, S. Tahirovic, S. Dupraz, S. Stern, B.K. Garvalov, C. Gurniak, A.E. Shaw, L. Meyn, R. Wedlich-Soldner, J.R. Bamburg, J.V. Small, W. Witke, and F. Bradke. 2012. ADF/cofilin-mediated actin retrograde flow directs neurite formation in the developing brain. *Neuron* 76:1091-1107.

Forscher, P., and S.J. Smith. 1988. Actions of cytochalasins on the organization of actin filaments and microtubules in a neuronal growth cone. *J Cell Biol* 107:1505-1516.

Franze, K. 2020. Integrating Chemistry and Mechanics: The Forces Driving Axon Growth. *Annu Rev Cell Dev Biol* 36:61-83.

Fritz-Laylin, L.K., and M.A. Titus. 2023. The evolution and diversity of actin-dependent cell migration. *Mol Biol Cell* 34:pe6.

Fung, S.J., D. Joshi, K.M. Allen, S. Sivagnanasundaram, D.A. Rothmond, R. Saunders, P.L. Noble, M.J. Webster, and C.S. Weickert. 2011. Developmental patterns of doublecortin expression and white matter neuron density in the postnatal primate prefrontal cortex and schizophrenia. *PLoS One* 6:e25194.

Futerman, A.H., and G.A. Banker. 1996. The economics of neurite outgrowth - the addition of new membrane to growing axons. *Trends Neuroscience* 19:144-149.

Gallo, G., H.F. Yee, Jr., and P.C. Letourneau. 2002. Actin turnover is required to prevent axon retraction driven by endogenous actomyosin contractility. *J Cell Biol* 158:1219-1228.

Gan, W.-B., and J.W. Lichtman. 1998. Synaptic Segregation at the Developing Neuromuscular Junction. *Science* 282:1508-1511.

Gao, P.-P., Y. Yue, D.P. Cerretti, C. Dreyfus, and R. Zhou. 1999. Ephrin-dependent growth and pruning of hippocampal axons. *PNAS* 96:4073-4077.

Garcia-Arcos, J.M., A. Jha, C.M. Waterman, and M. Piel. 2024. Blebology: principles of bleb-based migration. *Trends Cell Biol* 34:838-853.

Garvalov, B.K., K.C. Flynn, D. Neukirchen, L. Meyn, N. Teusch, X. Wu, C. Brakebusch, J.R. Bamburg, and F. Bradke. 2007. Cdc42 regulates cofilin during the establishment of neuronal polarity. *J Neurosci* 27:13117-13129.

Gasperini, R.J., M. Pavez, A.C. Thompson, C.B. Mitchell, H. Hardy, K.M. Young, J.K. Chilton, and L. Foa. 2017. How does calcium interact with the cytoskeleton to regulate growth cone motility during axon pathfinding? *Mol Cell Neurosci* 84:29-35.

Gautreau, A.M., F.E. Fregoso, G. Simanov, and R. Dominguez. 2022. Nucleation, stabilization, and disassembly of branched actin networks. *Trends Cell Biol* 32:421-432.

Gertler, F.B., K. Niebuhr, M. Reinhard, J. Wehland, and P. Soriano. 1996. Mena, a Relative of VASP and Drosophila Enabled, Is Implicated in the Control of Microfilament Dynamics. *Cell* 87:227-239.

Ginhoux, F., and M. Prinz. 2015. Origin of microglia: current concepts and past controversies. *Cold Spring Harb Perspect Biol* 7:a020537.

Gomis-Ruth, S., M. Stiess, C.J. Wierenga, L. Meyn, and F. Bradke. 2014. Single-cell axotomy of cultured hippocampal neurons integrated in neuronal circuits. *Nat Protoc* 9:1028-1037.

Gomis-Ruth, S., C.J. Wierenga, and F. Bradke. 2008. Plasticity of polarization: changing dendrites into axons in neurons integrated in neuronal circuits. *Curr Biol* 18:992-1000.

Gory-Faure, S., R. Powell, J. Jonckheere, F. Lante, E. Denarier, L. Peris, C.H. Nguyen, A. Buisson, L. Lafanechere, and A. Andrieux. 2021. Pyr1-Mediated Pharmacological Inhibition of LIM Kinase Restores Synaptic Plasticity and Normal Behavior in a Mouse Model of Schizophrenia. *Front Pharmacol* 12:627995.

Goslin, K., and G.A. Banker. 1989. Experimental Observations on the Development of Polarity by Hippocampal Neurons in Culture. *The Journal of Cell Biology* 108:1507-1516.

Grabrucker, A., B. Vaida, J. Bockmann, and T.M. Boeckers. 2009. Synaptogenesis of hippocampal neurons in primary cell culture. *Cell Tissue Res* 338:333-341.

Gray, K.T., A.S. Kostyukova, and T. Fath. 2017. Actin regulation by tropomodulin and tropomyosin in neuronal morphogenesis and function. *Mol Cell Neurosci* 84:48-57.

Griffin, J.M., S. Hingorani Jai Prakash, T. Bockemuhl, J.M. Benner, B. Schaffran, V. Moreno-Manzano, A. Buschges, and F. Bradke. 2023. Rehabilitation enhances epothilone-induced locomotor recovery after spinal cord injury. *Brain Commun* 5:fcad005.

Grintsevich, E.E., V.E. Galkin, A. Orlova, A.J. Ytterberg, M.M. Mikati, D.S. Kudryashov, J.A. Loo, E.H. Egelman, and E. Reisler. 2010. Mapping of drebrin binding site on F-actin. *J Mol Biol* 398:542-554.

Guha, S., A. Patil, H. Muralidharan, and P.W. Baas. 2021. Mini-review: Microtubule sliding in neurons. *Neurosci Lett* 753:135867.

Gunning, P.W., E.C. Hardeman, P. Lappalainen, and D.P. Mulvihill. 2015. Tropomyosin - master regulator of actin filament function in the cytoskeleton. *J Cell Sci* 128:2965-2974.

Gurniak, C.B., E. Perlas, and W. Witke. 2005. The actin depolymerizing factor n-cofilin is essential for neural tube morphogenesis and neural crest cell migration. *Dev Biol* 278:231-241.

Halpain, S., and L. Dehmelt. 2006. The MAP1 family of microtubule-associated proteins. *Genome Biol* 7:224.

Hamill, O.P., A. Marty, E. Neher, B. Sakmann, and F.J. Sigworth. 1981. Improved Patch-Clamp Techniques for High-Resolution Current Recording from Cells and Cell-Free Membrane Patches. *Plügers Archiv: European Journal of Physiology* 391:85-100.

Hansen, A.H., C. Duellberg, C. Mieck, M. Loose, and S. Hippenmeyer. 2017. Cell Polarity in Cerebral Cortex Development-Cellular Architecture Shaped by Biochemical Networks. *Front Cell Neurosci* 11:176.

Harrison, R.G. 1907. Observations of the living developing nerve fiber. *The Anatomical Record* 116-128.

Haviv, L., D. Gillo, F. Backouche, and A. Bernheim-Groswasser. 2008. A cytoskeletal demolition worker: myosin II acts as an actin depolymerization agent. *J Mol Biol* 375:325-330.

He, Y., W. Yu, and P.W. Baas. 2002. Microtubule Reconfiguration during Axonal Retraction Induced by Nitric Oxide. *The Journal of Neuroscience* 22:5982-5991.

He, Z., and Y. Jin. 2016. Intrinsic Control of Axon Regeneration. *Neuron* 90:437-451.

Hedstrom, K.L., Y. Ogawa, and M.N. Rasband. 2008. AnkyrinG is required for maintenance of the axon initial segment and neuronal polarity. *J Cell Biol* 183:635-640.

Hellal, F., A. Hurtado, J. Ruschel, K.C. Flynn, C.J. Laskowski, M. Umlauf, L.C. Kapitein, D. Strikis, V. Lemmon, J. Bixby, C.C. Hoogenraad, and F. Bradke. 2011. Microtubule Stabilization Reduces Scarring and Causes Axon Regeneration After Spinal Cord Injury. *Science* 331:928-931.

Heo, K., T.S. Ho, X. Zeng, B.L. Turnes, M. Arab, S. Jayakar, K. Chen, G. Kimourtzis, M.C. Condro, E. Fazzari, X. Song, J. Tabitha Hees, Z. Xu, X. Chen, L.B. Barrett, L. Perrault, R. Pandey, K. Zhang, A. Bhaduri, Z. He, H.I. Kornblum, J. Hubbs, and C.J. Woolf. 2025. Non-muscle myosin II inhibition at the site of axon injury increases axon regeneration. *Nat Commun* 16:2975.

Hilton, B.J., and F. Bradke. 2017. Can injured adult CNS axons regenerate by recapitulating development? *Development* 144:3417-3429.

Hilton, B.J., J.M. Griffin, J.W. Fawcett, and F. Bradke. 2024. Neuronal maturation and axon regeneration: unfixing circuitry to enable repair. *Nat Rev Neurosci* 25:649-667.

Hilton, B.J., A. Husch, B. Schaffran, T.C. Lin, E.R. Burnside, S. Dupraz, M. Schelski, J. Kim, J.A. Muller, S. Schoch, C. Imig, N. Brose, and F. Bradke. 2022. An active vesicle priming machinery suppresses axon regeneration upon adult CNS injury. *Neuron* 110:51-69 e57.

Hilton, D.M., R.M. Aguilar, A.B. Johnston, and B.L. Goode. 2018. Species-Specific Functions of Twinfilin in Actin Filament Depolymerization. *J Mol Biol* 430:3323-3336.

Hohmann, T., and F. Dehghani. 2019. The Cytoskeleton-A Complex Interacting Meshwork. *Cells* 8:

Hotulainen, P., and C.C. Hoogenraad. 2010. Actin in dendritic spines: connecting dynamics to function. *J Cell Biol* 189:619-629.

Hutchins, B.I., and K. Kalil. 2008. Differential outgrowth of axons and their branches is regulated by localized calcium transients. *J Neurosci* 28:143-153.

Ichetovkin, I., W. Grant, and J. Condeelis. 2002. Cofilin Produces Newly Polymerized Actin Filaments that Are Preferred for Dendritic Nucleation by the Arp2/3 Complex. *Current Biology* 12:79-84.

Ichikawa, M., K. Muramoto, K. Kobayashi, M. Kawahara, and Y. Kuroda. 1993. Formation and maturation of synapses in primary cultures of rat cerebral cortical cells: an electron microscopic study. *Neuroscience Research* 16:95-103.

Innocenti, M. 2018. New insights into the formation and the function of lamellipodia and ruffles in mesenchymal cell migration. *Cell Adh Migr* 12:401-416.

Iwanski, M.K., A.K. Serweta, H.N. Verwei, B.C. Donders, and L.C. Kapitein. 2025. Polarity reversal of stable microtubules during neuronal development. *bioRxiv* 2025.2002.2007.636940.

James, S.L., A. Theadom, R.G. Ellenbogen, M.S. Bannick, W. Montjoy-Venning, L.R. Lucchesi, N. Abbasi, R. Abdulkader, H.N. Abraha, J.C. Adsuar, M. Afarideh, S. Agrawal, A. Ahmadi, M.B. Ahmed, A.N. Aichour, I. Aichour, M.T.E. Aichour, R.O. Akinyemi, N. Akseer, F. Alahdab, A. Alebel, S.A. Alghnam, B.A. Ali, U. Alsharif, K. Altirkawi, C.L. Andrei, M. Anjomshoa, H. Ansari, M.G. Ansha, C.A.T. Antonio, S.C.Y. Appiah, F. Ariani, N.G. Asefa, S.W. Asgedom, S. Atique, A. Awasthi, B.P. Ayala Quintanilla, T.B. Ayuk, P.S. Azzopardi, H. Badali, A. Badawi, S. Balalla, A. Banstola, S.L. Barker-Collo, T.W. Bärnighausen, N. Bedi, M. Behzadifar, M. Behzadifar, B.B. Bekele, A.B. Belachew, Y.A. Belay, D.A. Bennett, I.M. Bensenor, A. Berhane, M. Beuran, A. Bhalla, S. Bhaumik, Z.A. Bhutta, B. Biadgo, M. Biffino, A. Bijani, N. Bililign, C. Birungi, S. Boufous, A. Brazinova, A.W. Brown, M. Car, R. Cárdenas, J.J. Carrero, F. Carvalho, C.A. Castañeda-Orjuela, F. Catalá-López, Y. Chaiah, A.P. Champs, J.-C. Chang, J.-Y.J. Choi, D.J. Christopher, C. Cooper, C.S. Crowe, L. Dandona, R. Dandona,

A. Daryani, D.V. Davitoiu, M.G. Degefa, G.T. Demoz, K. Deribe, S. Djalalinia, H.P. Do, D.T. Doku, T.M. Drake, M. Dubey, E. Dubljanin, Z. El-Khatib, R. Ofori-Asenso, S. Eskandarieh, A. Esteghamati, S. Esteghamati, A. Faro, F. Farzadfar, M.H. Farzaei, S.-M. Fereshtehnejad, E. Fernandes, G.T. Feyissa, I. Filip, F. Fischer, T. Fukumoto, M. Ganji, F.G. Gankpe, A.K. Gebre, T.T. Gebrehiwot, K.E. Gezae, G. Gopalkrishna, A.C. Goulart, J.A. Haagsma, A. Haj-Mirzaian, A. Haj-Mirzaian, R.R. Hamadeh, S. Hamidi, J.M. Haro, H. Hassankhani, H.Y. Hassen, R. Havmoeller, C. Hawley, S.I. Hay, M.I. Hegazy, D. Hendrie, A. Henok, D.T. Hibstu, H.J. Hoffman, M.K. Hole, E. Homaie Rad, S.M. Hosseini, S. Hostiuc, G. Hu, M.A. Hussen, O.S. Ilesanmi, S.S.N. Irvani, M. Jakovljevic, S. Jayaraman, R.P. Jha, J.B. Jonas, K.M. Jones, Z. Jorjoran Shushtari, J.J. Jozwiak, M. Jürisson, A. Kabir, A. Kahsay, M. Kahssay, R. Kalani, A. Karch, A. Kasaeian, G.M. Kassa, T.D. Kassa, Z.Y. Kassa, A.P. Kengne, Y.S. Khader, M.A. Khafaie, N. Khalid, I. Khalil, E.A. Khan, M.S. Khan, Y.-H. Khang, H. Khazaie, A.T. Khoja, J. Khubchandani, A.A. Kiadaliri, D. Kim, Y.-E. Kim, A. Kisa, A. Koyanagi, K.J. Krohn, B. Kuate Defo, B. Kucuk Bicer, G.A. Kumar, M. Kumar, R. Lalloo, F.H. Lami, V.C. Lansingh, D.O. Laryea, A. Latifi, C.T. Leshargie, M. Levi, S. Li, M.L. Liben, P.A. Lotufo, R. Lunevicius, N.B. Mahotra, M. Majdan, A. Majeed, R. Malekzadeh, A.-L. Manda, M.A. Mansournia, B.B. Massenburg, K.K.V. Mate, M.M. Mehndiratta, V. Mehta, H. Meles, A. Melese, P.T.N. Memiah, W. Mendoza, G. Mengistu, A. Meretoja, T.J. Meretoja, T. Mestrovic, T. Miazgowski, T.R. Miller, G.K. Mini, A. Mirica, E.M. Mirrakhimov, B. Moazen, M. Mohammadi, S. Mohammed, A.H. Mokdad, M. Molokhia, L. Monasta, S. Mondello, M. Moosazadeh, G. Moradi, M. Moradi, M. Moradi-Lakeh, M. Moradinazar, S.D. Morrison, M.M. Moschos, S.M. Mousavi, S. Murthy, K.I. Musa, G. Mustafa, M. Naghavi, G. Naik, F. Najafi, V. Nangia, B.R. Nascimento, I. Negoi, T.H. Nguyen, E. Nichols, D.N.A. Ningrum, Y.L. Nirayo, P.S. Nyasulu, F.A. Ogbo, I.-H. Oh, A. Okoro, A.T. Olagunju, T.O. Olagunju, P.R. Olivares, S.S. Otstavnov, M.O. Owolabi, M. P A, S. Pakhale, A.R. Pandey, K. Pesudovs, G.D. Pinilla-Monsalve, S. Polinder, H. Poustchi, S. Prakash, M. Qorbani, A. Radfar, A. Rafay, A. Rafiei, A. Rahimi-Movaghar, V. Rahimi-Movaghar, M. Rahman, M.A. Rahman, R.K. Rai, F. Rajati, U. Ram, D.L. Rawaf, S. Rawaf, R.C. Reiner, C. Reis, A.M.N. Renzaho, S. Resnikoff, S. Rezaei, S. Rezaeian, L. Roever,

L. Ronfani, G. Roshandel, N. Roy, G.M. Ruhago, B. Saddik, H. Safari, S. Safiri, M.A. Sahraian, P. Salamati, R.d.F. Saldanha, A.M. Samy, J. Sanabria, J.V. Santos, M.M.M. Santric Milicevic, B. Sartorius, M. Satpathy, K. Savuon, I.J.C. Schneider, D.C. Schwebel, S.G. Sepanlou, H. Shabaninejad, M.A.A. Shaikh, M. Shams-Beyranvand, M. Sharif, M. Sharif-Alhoseini, S.M. Shariful Islam, J. She, A. Sheikh, J. Shen, K.N. Sheth, K. Shibuya, M.S. Shiferaw, M. Shigematsu, R. Shiri, I. Shiue, H. Shoman, S. Siabani, T.J. Siddiqi, J.P. Silva, D.G.A. Silveira, D.N. Sinha, M. Smith, A.M. Soares Filho, S. Sobhani, M. Soofi, J.B. Soriano, I.N. Soyiri, D.J. Stein, M.A. Stokes, M.a.B. Sufiyan, B.F. Sunguya, J.E. Sunshine, B.L. Sykes, C.E.I. Szoeke, R. Tabarés-Seisdedos, B.J. Te Ao, A. Tehrani-Banihashemi, M.G. Tekle, M.-H. Temsah, O. Temsah, R. Topor-Madry, M. Tortajada-Girbés, B.X. Tran, K.B. Tran, L. Tudor Car, K.N. Ukwaja, I. Ullah, M.S. Usman, O.A. Uthman, P.R. Valdez, T.J. Vasankari, N. Venketasubramanian, F.S. Violante, F.W.S. Wagnew, Y. Waheed, Y.-P. Wang, K.G. Weldegwergs, A. Werdecker, T. Wijeratne, A.S. Winkler, G.M.A. Wyper, Y. Yano, M. Yaseri, Y.J. Yasin, P. Ye, E.M. Yimer, P. Yip, E. Yisma, N. Yonemoto, S.-J. Yoon, M.G. Yost, M.Z. Younis, M. Yousefifard, C. Yu, Z. Zaidi, S.B. Zaman, M. Zamani, Z.M. Zenebe, S. Zodpey, V.L. Feigin, T. Vos, and C.J.L. Murray. 2019. Global, regional, and national burden of traumatic brain injury and spinal cord injury, 1990–2016: a systematic analysis for the Global Burden of Disease Study 2016. *The Lancet Neurology* 18:56-87.

Jang, D.-H., J.-H. Han, S.-H. Lee, Y.-S. Lee, H. Park, S.-H. Lee, H. Kim, and B.-K. Kaang. 2005. Cofilin expression induces cofilin-actin rod formation and disrupts synaptic structure and function in Aplysia synapses. *PNAS* 102:16072-16077.

Janssen, L.J., T. Tazzeo, J. Zuo, E. Pertens, and S. Keshavjee. 2004. KCl evokes contraction of airway smooth muscle via activation of RhoA and Rho-kinase. *American Journal of Physiology-Lung Cellular and Molecular Physiology* 287:L852-L858.

Jaqaman, K., D. Loerke, M. Mettlen, H. Kuwata, S. Grinstein, S.L. Schmid, and G. Danuser. 2008. Robust single-particle tracking in live-cell time-lapse sequences. *Nat Methods* 5:695-702.

Jawahar, A., J. Vermeil, J. Heuvingh, O. du Roure, and M. Piel. 2024. The third dimension of the actin cortex. *Curr Opin Cell Biol* 89:102381.

Jedrzejewska-Szmek, J., and K.T. Blackwell. 2019. From membrane receptors to protein synthesis and actin cytoskeleton: Mechanisms underlying long lasting forms of synaptic plasticity. *Semin Cell Dev Biol* 95:120-129.

Jensen, M.H., E.J. Morris, R. Huang, G. Rebowski, R. Dominguez, D.A. Weitz, J.R. Moore, and C.L. Wang. 2012. The conformational state of actin filaments regulates branching by actin-related protein 2/3 (Arp2/3) complex. *J Biol Chem* 287:31447-31453.

Jiang, K., and A. Akhmanova. 2011. Microtubule tip-interacting proteins: a view from both ends. *Curr Opin Cell Biol* 23:94-101.

Jones, E.V., D. Cook, and K.K. Murai. 2012. A neuron-astrocyte co-culture system to investigate astrocyte-secreted factors in mouse neuronal development. *Methods Mol Biol* 814:341-352.

Jones, S.L., M.E. Selzer, and G. Gallo. 2006. Developmental regulation of sensory axon regeneration in the absence of growth cones. *J Neurobiol* 66:1630-1645.

Jouhilahti, E.M., S. Peltonen, and J. Peltonen. 2008. Class III beta-tubulin is a component of the mitotic spindle in multiple cell types. *J Histochem Cytochem* 56:1113-1119.

Ka, M., and W.Y. Kim. 2016. Microtubule-Actin Crosslinking Factor 1 Is Required for Dendritic Arborization and Axon Outgrowth in the Developing Brain. *Mol Neurobiol* 53:6018-6032.

Kalil, K., and E.W. Dent. 2005. Touch and go: guidance cues signal to the growth cone cytoskeleton. *Curr Opin Neurobiol* 15:521-526.

Kalil, K., and E.W. Dent. 2014. Branch management: mechanisms of axon branching in the developing vertebrate CNS. *Nat Rev Neurosci* 15:7-18.

Karimi-Abdolrezaee, S., V.M. Verge, and D.J. Schreyer. 2002. Developmental down-regulation of GAP-43 expression and timing of target contact in rat corticospinal neurons. *Exp Neurol* 176:390-401.

Katsetos, C.D., M.M. Herman, and S.J. Mork. 2003. Class III beta-tubulin in human development and cancer. *Cell Motil Cytoskeleton* 55:77-96.

Kemal, S., H.S. Richardson, E.D. Dyne, and M.M. Fu. 2022. ER and Golgi trafficking in axons, dendrites, and glial processes. *Curr Opin Cell Biol* 78:102119.

Ketschek, A.R., S.L. Jones, and G. Gallo. 2007. Axon extension in the fast and slow lanes: Substratum-dependent engagement of myosin II functions. *Developmental Neurobiology* 67:1305-1320.

Kevenaar, J.T., and C.C. Hoogenraad. 2015. The axonal cytoskeleton: from organization to function. *Front Mol Neurosci* 8:44.

Khalaf-Nazzal, R., and F. Francis. 2013. Hippocampal development - old and new findings. *Neuroscience* 248:225-242.

Kinnunen, T., E. Raulo, R. Nolo, M. Maccarana, U. Lindahl, and H. Rauvala. 1996. Neurite outgrowth in brain neurons induced by heparin-binding growth-associated molecule (HB-GAM) depends on the specific interaction of HB-GAM with heparan sulfate at the cell surface. *J Biol Chem* 271:2243-2248.

Kollins, K.M., J. Hu, P.C. Bridgman, Y.Q. Huang, and G. Gallo. 2009. Myosin-II negatively regulates minor process extension and the temporal development of neuronal polarity. *Dev Neurobiol* 69:279-298.

Koseki, H., M. Donega, B.Y. Lam, V. Petrova, S. van Erp, G.S. Yeo, J.C. Kwok, C. Ffrench-Constant, R. Eva, and J.W. Fawcett. 2017. Selective rab11 transport and the intrinsic regenerative ability of CNS axons. *Elife* 6:

Koskinen, M., E. Bertling, R. Hotulainen, K. Tanhuanpaa, and P. Hotulainen. 2014. Myosin IIb controls actin dynamics underlying the dendritic spine maturation. *Mol Cell Neurosci* 61:56-64.

Kovacs, M., J. Toth, C. Hetenyi, A. Malnasi-Csizmadia, and J.R. Sellers. 2004. Mechanism of blebbistatin inhibition of myosin II. *J Biol Chem* 279:35557-35563.

Laan, L., J. Husson, E.L. Munteanu, J.W.J. Kerssemakers, and M. Dogterom. 2008. Force-generation and dynamic instability of microtubule bundles. *PNAS* 105:8920-8925.

Lane, M.A., J.S. Truettner, J.P. Brunschwig, A. Gomez, M.B. Bunge, W.D. Dietrich, K.M. Dziegielewska, C.J. Ek, J.L. Vandeberg, and N.R. Saunders. 2007. Age-related differences in the local cellular and molecular responses to injury in developing spinal cord of the opossum, Monodelphis domestica. *Eur J Neurosci* 25:1725-1742.

Lanier, L.M., M.A. Gates, W. Witke, A.S. Menzies, A.M. Wehmann, J.D. Macklis, D. Kwiatkowski, P. Soriano, and F.B. Gertler. 1999. Mena Is Required for Neurulation and Commissure Formation. *Neuron* 22:313-325.

Lappalainen, P., T. Kotila, A. Jegou, and G. Romet-Lemonne. 2022. Biochemical and mechanical regulation of actin dynamics. *Nat Rev Mol Cell Biol* 23:836-852.

Lawrence, E.J., and M. Zanic. 2019. Rescuing microtubules from the brink of catastrophe: CLASPs lead the way. *Curr Opin Cell Biol* 56:94-101.

Lebrand, C., E.W. Dent, G.A. Strasser, L.M. Lanier, M. Krause, T.M. Svitkina, G.G. Borisy, and F.B. Gertler. 2004. Critical Role of Ena/VASP Proteins for Filopodia Formation in Neurons and in Function Downstream of Netrin-1. *Neuron* 42:37-49.

Lee, C.W., E.A. Vitriol, S. Shim, A.L. Wise, R.P. Velayutham, and J.Q. Zheng. 2013. Dynamic localization of G-actin during membrane protrusion in neuronal motility. *Curr Biol* 23:1046-1056.

Lee, J., J. Park, M. Jeong, S.J. Oh, J.H. Yoon, and Y.S. Oh. 2024. Anatomical topology of extrahippocampal projections from dorsoventral CA pyramidal neurons in mice. *Front Neuroanat* 18:1421034.

Lee, S.Y., W. Kim, Y.G. Lee, H.J. Kang, S.H. Lee, S.Y. Park, J.K. Min, S.R. Lee, and S.J. Chung. 2017. Identification of sennoside A as a novel inhibitor of the slingshot (SSH) family proteins related to cancer metastasis. *Pharmacol Res* 119:422-430.

Leite, S.C., R. Pinto-Costa, and M.M. Sousa. 2021. Actin dynamics in the growth cone: a key player in axon regeneration. *Curr Opin Neurobiol* 69:11-18.

Leterrier, C. 2018. The Axon Initial Segment: An Updated Viewpoint. *J Neurosci* 38:2135-2145.

Letourneau, P.C. 1975. Possible Roles for Cell-to-Substratum Adhesion in Neuronal Morphogenesis. *Developmental Biology* 44:77-91.

Letourneau, P.C., T.A. Shattuck, and A.H. Ressler. 1987. "Pull" and "push" in neurite elongation: observations on the effects of different concentrations of cytochalasin B and taxol. *Cell Motil Cytoskeleton* 8:193-209.

Lewis, A.K., and P.C. Bridgman. 1992. Nerve Growth Cone Lamellipodia Contain Two Populations of Actin Filaments That Differ in Organization and Polarity. *The Journal of Cell Biology* 119:1219-1243.

Lewis, T.L., Jr., J. Courchet, and F. Polleux. 2013. Cell biology in neuroscience: Cellular and molecular mechanisms underlying axon formation, growth, and branching. *J Cell Biol* 202:837-848.

Li, J.X.H., V.W. Tang, and W.M. Brieher. 2020. Actin protrusions push at apical junctions to maintain E-cadherin adhesion. *Proc Natl Acad Sci U S A* 117:432-438.

Li, K.S., P. Xiao, D.L. Zhang, X.B. Hou, L. Ge, D.X. Yang, H.D. Liu, D.F. He, X. Chen, K.R. Han, X.Y. Song, X. Yu, H. Fang, and J.P. Sun. 2015. Identification of para-Substituted Benzoic Acid Derivatives as Potent Inhibitors of the Protein Phosphatase Slingshot. *ChemMedChem* 10:1980-1987.

Lintz, M., A. Munoz, and C.A. Reinhart-King. 2017. The Mechanics of Single Cell and Collective Migration of Tumor Cells. *J Biomech Eng* 139:0210051-0210059.

Loisel, T.P., R. Boujemaa, D. Pantaloni, and C. Marie-France. 1999. Reconstitution of actin-based motility of Listeria and Shigella using pure proteins. *Nature* 401:613-616.

Lowery, L.A., and D. Van Vactor. 2009. The trip of the tip: understanding the growth cone machinery. *Nat Rev Mol Cell Biol* 10:332-343.

Maciver, S.K., and P.J. Hussey. 2002. The ADF/cofilin family: actin-remodeling proteins. *Genome BIology* 3:

Malyshevskaya, O., Y. Shiraishi, F. Kimura, and N. Yamamoto. 2013. Role of electrical activity in horizontal axon growth in the developing cortex: a time-lapse study using optogenetic stimulation. *PLoS One* 8:e82954.

Mann, F., C. Peuckert, F. Dehner, R. Zhou, and J. Bolz. 2002. Ephrins regulate the formation of terminal axonal arbors during the development of thalamocortical projections. *Development* 129:3945-3955.

Manzini, M.C., M.S. Ward, Q. Zhang, M.D. Lieberman, and C.A. Mason. 2006. The stop signal revised: immature cerebellar granule neurons in the external germinal layer arrest pontine mossy fiber growth. *J Neurosci* 26:6040-6051.

Marsh, L., and P.C. Letourneau. 1984. Growth of Neurites without Filopodial or Lamellipodial Activity in the Presence of Cytochalasin B. *The Journal of Cell Biology* 99:2041-2047.

McDowell, K.P., A.A. Berthiaume, T. Tieu, D.A. Hartmann, and A.Y. Shih. 2021. VasoMetrics: unbiased spatiotemporal analysis of microvascular diameter in multi-photon imaging applications. *Quant Imaging Med Surg* 11:969-982.

Meberg, P.J., and J.R. Bamburg. 2000. Increase in Neurite Outgrowth Mediated by Overexpression of Actin Depolymerizing Factor. *The Journal of Neuroscience* 20:2459-2469.

Medeiros, N.A., D.T. Burnette, and P. Forscher. 2006. Myosin II functions in actin-bundle turnover in neuronal growth cones. *Nat Cell Biol* 8:215-226.

Meichsner, M., T. Doll, D. Reddy, B. Weisshaar, and A. Matus. 1993. The Low Molecular Weight Form Of Microtubule-Associated Protein 2 Is Transported Into Both Axons and Dendrites. *Neuroscience* 54:873-880.

Meijering, E., M. Jacob, J.C. Sarria, P. Steiner, H. Hirling, and M. Unser. 2004. Design and validation of a tool for neurite tracing and analysis in fluorescence microscopy images. *Cytometry A* 58:167-176.

Melkova, K., V. Zapletal, S. Narasimhan, S. Jansen, J. Hritz, R. Skrabana, M. Zweckstetter, M. Ringkjobing Jensen, M. Blackledge, and L. Zidek. 2019. Structure and Functions of Microtubule Associated Proteins Tau and MAP2c: Similarities and Differences. *Biomolecules* 9:

Mellor, H. 2010. The role of formins in filopodia formation. *Biochim Biophys Acta* 1803:191-200.

Melton, A.J., V.L. Palfini, Y. Ogawa, J.A. Oses Prieto, A. Vainshtein, A.L. Burlingame, E. Peles, and M.N. Rasband. 2024. TRIM46 Is Required for Microtubule Fasciculation In Vivo But Not Axon Specification or Axon Initial Segment Formation. *J Neurosci* 44:

Menon, S., and S.L. Gupton. 2016. Building Blocks of Functioning Brain: Cytoskeletal Dynamics in Neuronal Development. *Int Rev Cell Mol Biol* 322:183-245.

Michelot, A., J. Berro, C. Guerin, R. Boujemaa-Paterski, C.J. Staiger, J.L. Martiel, and L. Blanchoin. 2007. Actin-filament stochastic dynamics mediated by ADF/cofilin. *Curr Biol* 17:825-833.

Miller, K.E., and D.M. Suter. 2018. An Integrated Cytoskeletal Model of Neurite Outgrowth. *Front Cell Neurosci* 12:447.

Mitchison, T., and M. Kirschner. 1988. Cytoskeletal Dynamics and Nerve Growth. *Neuron* 1:761-772.

Mizuno, K. 2013. Signaling mechanisms and functional roles of cofilin phosphorylation and dephosphorylation. *Cell Signal* 25:457-469.

Moffat, J.J., M. Ka, E.M. Jung, A.L. Smith, and W.Y. Kim. 2017. The role of MACF1 in nervous system development and maintenance. *Semin Cell Dev Biol* 69:9-17.

Mogilner, A., and G. Oster. 1996. Cell Motility Driven by Actin Polymerization. *Biophysical Journal* 71:3030-3045.

Moon, J.-I., and S.J. Birren. 2008. Target-dependent inhibition of sympathetic neuron growth via modulation of BMP signaling pathway. *Dev Biol* 315:404-417.

Moutin, M.J., C. Bosc, L. Peris, and A. Andrieux. 2021. Tubulin post-translational modifications control neuronal development and functions. *Dev Neurobiol* 81:253-272.

Nakajima, C., M. Sawada, E. Umeda, Y. Takagi, N. Nakashima, K. Kuboyama, N. Kaneko, S. Yamamoto, H. Nakamura, N. Shimada, K. Nakamura, K. Matsuno, S. Uesugi, N.A. Veprek, F. Kullmer, V. Nasufovic, H. Uchiyama, M. Nakada, Y. Otsuka, Y. Ito, V. Herranz-Perez, J.M. Garcia-Verdugo, N. Ohno, H.D. Arndt, D. Trauner, Y. Tabata, M. Igarashi, and K. Sawamoto. 2024. Identification of the growth cone as a probe and driver of neuronal migration in the injured brain. *Nat Commun* 15:1877.

Nakashima, S., H. Matsuda, A. Kurume, Y. Oda, S. Nakamura, M. Yamashita, and M. Yoshikawa. 2010. Cucurbitacin E as a new inhibitor of cofilin phosphorylation in human leukemia U937 cells. *Bioorg Med Chem Lett* 20:2994-2997.

Nawaz, S., P. Sanchez, S. Schmitt, N. Snaidero, M. Mitkovski, C. Velte, B.R. Bruckner, I. Alexopoulos, T. Czopka, S.Y. Jung, J.S. Rhee, A. Janshoff, W. Witke, I.A.T. Schaap, D.A. Lyons, and M. Simons. 2015. Actin filament turnover drives leading edge growth during myelin sheath formation in the central nervous system. *Dev Cell* 34:139-151.

Nelson, J.C., A.K. Stavoe, and D.A. Colon-Ramos. 2013. The actin cytoskeleton in presynaptic assembly. *Cell Adh Migr* 7:379-387.

Neukirchen, D., and F. Bradke. 2011. Neuronal polarization and the cytoskeleton. *Semin Cell Dev Biol* 22:825-833.

Noiges, R., R. Eichinger, W. Kutschera, I. Fischer, Z. Németh, G. Wiche, and F. Propst. 2002. Microtubule-Associated Protein 1A (MAP1A) and MAP1B: Light Chains Determine Distinct Functional Properties. *The Journal of Neuroscience* 22:2106-2114.

Ohashi, K. 2015. Roles of cofilin in development and its mechanisms of regulation. *Dev Growth Differ* 57:275-290.

Ohashi, K., K. Nagata, M. Maekawa, T. Ishizaki, S. Narumiya, and K. Mizuno. 2000. Rho-associated Kinase ROCK Activates LIM-kinase 1 by Phosphorylation at Threonine 508 within the Activation Loop. *Journal of Biological Chemistry* 275:3577-3582.

Okabe, M., M. Ikawa, K. Kominami, T. Nakanishi, and Y. Nishimune. 1997. 'Green mice' as a source of ubiquitous green cells. *FEBS Lett* 407:313-319.

Pak, C.W., K.C. Flynn, and J.R. Bamburg. 2008. Actin-binding proteins take the reins in growth cones. *Nat Rev Neurosci* 9:136-147.

Pankova, K., D. Rosel, M. Novotny, and J. Brabek. 2010. The molecular mechanisms of transition between mesenchymal and amoeboid invasiveness in tumor cells. *Cell Mol Life Sci* 67:63-71.

Papalazarou, V., K. Swaminathan, F. Jaber-Hijazi, H. Spence, I. Lahmann, C. Nixon, M. Salmeron-Sanchez, H.H. Arnold, K. Rottner, and L.M. Machesky. 2020. The Arp2/3 complex is crucial for colonisation of the mouse skin by melanoblasts. *Development* 147:

Parato, J., and F. Bartolini. 2021. The microtubule cytoskeleton at the synapse. *Neurosci Lett* 753:135850.

Paridaen, J.T., and W.B. Huttner. 2014. Neurogenesis during development of the vertebrate central nervous system. *EMBO Rep* 15:351-364.

Pelkey, K.A., R. Chittajallu, M.T. Craig, L. Tricoire, J.C. Wester, and C.J. McBain. 2017. Hippocampal GABAergic Inhibitory Interneurons. *Physiol Rev* 97:1619-1747.

Peris, L., M. Wagenbach, L. Lafanechere, J. Brocard, A.T. Moore, F. Kozielski, D. Job, L. Wordeman, and A. Andrieux. 2009. Motor-dependent microtubule disassembly driven by tubulin tyrosination. *J Cell Biol* 185:1159-1166.

Pfenninger, K.H. 1986. Of nerve growth cones, leukocytes and memory: second messenger systems and growth-regulated proteins. *Trends in Neuroscience* 9:562-565.

Pollard, T.D. 2016. Actin and Actin-Binding Proteins. *Cold Spring Harb Perspect Biol* 8:

Pollard, T.D., and G.G. Borisy. 2003. Cellular Motility Driven by Assembly and Disassembly of Actin Filaments. *Cell* 112:453-465.

Poukkula, M., E. Kremneva, M. Serlachius, and P. Lappalainen. 2011. Actin-depolymerizing factor homology domain: a conserved fold performing diverse roles in cytoskeletal dynamics. *Cytoskeleton (Hoboken)* 68:471-490.

Prezel, E., A. Elie, J. Delaroche, V. Stoppin-Mellet, C. Bosc, L. Serre, A. Fourest-Lieuvin, A. Andrieux, M. Vantard, and I. Arnal. 2018. Tau can switch microtubule network organizations: from random networks to dynamic and stable bundles. *Mol Biol Cell* 29:154-165.

Prudent, R., E. Vassal-Stermann, C.H. Nguyen, C. Pillet, A. Martinez, C. Prunier, C. Barette, E. Soleilhac, O. Filhol, A. Beghin, G. Valdameri, S. Honore, S. Aci-Seche, D. Grierson, J. Antonipillai, R. Li, A. Di Pietro, C. Dumontet, D. Braguer, J.C. Florent, S. Knapp, O. Bernard, and L. Lafanechere. 2012. Pharmacological inhibition of LIM kinase stabilizes microtubules and inhibits neoplastic growth. *Cancer Res* 72:4429-4439.

Prunier, C., V. Josserand, J. Vollaire, E. Beerling, C. Petropoulos, O. Destaing, C. Montemagno, A. Hurbin, R. Prudent, L. de Koning, R. Kapur, P.A. Cohen, C. Albiges-Rizo, J.L. Coll, J. van Rheenen, M. Billaud, and L. Lafanechere.

2016. LIM Kinase Inhibitor Pyr1 Reduces the Growth and Metastatic Load of Breast Cancers. *Cancer Res* 76:3541-3552.

Qu, X., A. Kumar, H. Blockus, C. Waites, and F. Bartolini. 2019. Activity-Dependent Nucleation of Dynamic Microtubules at Presynaptic Boutons Controls Neurotransmission. *Curr Biol* 29:4231-4240 e4235.

Quintá, H.R. 2021. Development of corticospinal tract axons. In Factors Affecting Neurodevelopment. 227-235.

Quraishe, S., L.H. Forbes, and M.R. Andrews. 2018. The Extracellular Environment of the CNS: Influence on Plasticity, Sprouting, and Axonal Regeneration after Spinal Cord Injury. *Neural Plast* 2018:2952386.

Ralph, P.C., S.W. Choi, M.J. Baek, and S.J. Lee. 2024. Regenerative medicine approaches for the treatment of spinal cord injuries: Progress and challenges. *Acta Biomater* 189:57-72.

Ramon y Cajal, S. 1928. Degeneration and regeneration of the nervous system.

Redeker, V. 2010. Mass Spectrometry Analysis of C-terminal Posttranslational Modifications of Tubulins. *Methods in Cell Biology* 95:77-103.

Ren, Y., and D.M. Suter. 2016. Increase in Growth Cone Size Correlates with Decrease in Neurite Growth Rate. *Neural Plast* 2016:3497901.

Reversat, A., F. Gaertner, J. Merrin, J. Stopp, S. Tasciyan, J. Aguilera, I. de Vries, R. Hauschild, M. Hons, M. Piel, A. Callan-Jones, R. Voituriez, and M. Sixt. 2020. Cellular locomotion using environmental topography. *Nature* 582:582-585.

Richardson, P.M., and V.M.K. Issa. 1984. Peripheral injury enhances central regeneration of primary sensory neurones. *Nature* 309:791-793.

Rienecker, K.D.A., R.G. Poston, and R.N. Saha. 2020. Merits and Limitations of Studying Neuronal Depolarization-Dependent Processes Using Elevated External Potassium. *ASN Neuro* 12:1759091420974807.

Rodriguez Cruz, P.M., J. Cossins, D. Beeson, and A. Vincent. 2020. The Neuromuscular Junction in Health and Disease: Molecular Mechanisms

Governing Synaptic Formation and Homeostasis. *Front Mol Neurosci* 13:610964.

Roger, B., J. Al-Bassam, L. Dehmelt, R.A. Milligan, and S. Halpain. 2004. MAP2c, but not tau, binds and bundles F-actin via its microtubule binding domain. *Curr Biol* 14:363-371.

Roostalu, J., C. Thomas, N.I. Cade, S. Kunzelmann, I.A. Taylor, and T. Surrey. 2020. The speed of GTP hydrolysis determines GTP cap size and controls microtubule stability. *Elife* 9:

Roth, B.L. 2016. DREADDs for Neuroscientists. *Neuron* 89:683-694.

Roy, D., and A. Tedeschi. 2021. The Role of Lipids, Lipid Metabolism and Ectopic Lipid Accumulation in Axon Growth, Regeneration and Repair after CNS Injury and Disease. *Cells* 10:

Ruschel, J., F. Hellal, K.C. Flynn, S. Dupraz, D.A. Elliott, A. Tedeschi, M. Bates, C. Sliwinski, G. Brook, K. Dobrindt, M. Peitz, O. Brüstle, M.D. Norenberg, A. Blesch, N. Weidner, M. Bartlett Bunge, J.L. Bixby, and F. Bradke. 2015. Systemic administration of epothilone B promotes axon regeneration after spinal cord injury. *Science* 348:347-352.

Rust, M.B. 2015. ADF/cofilin: a crucial regulator of synapse physiology and behavior. *Cell Mol Life Sci* 72:3521-3529.

Rust, M.B., and T. Maritzen. 2015. Relevance of presynaptic actin dynamics for synapse function and mouse behavior. *Exp Cell Res* 335:165-171.

Ruthel, G., and P.J. Hollenbeck. 2000. Growth Cones Are Not Required for Initial Establishment of Polarity or Differential Axon Branch Growth in Cultured Hippocampal Neurons. *The Journal of Neuroscience* 20:2266-2274.

Santos, T.E., B. Schaffran, N. Broguiere, L. Meyn, M. Zenobi-Wong, and F. Bradke. 2020. Axon Growth of CNS Neurons in Three Dimensions Is Amoeboid and Independent of Adhesions. *Cell Rep* 32:107907.

Sayas, C.L., and J. Avila. 2014. Regulation of EB1/3 proteins by classical MAPs in neurons. *Bioarchitecture* 4:1-5.

Schaefer, A.W., N. Kabir, and P. Forscher. 2002. Filopodia and actin arcs guide the assembly and transport of two populations of microtubules with unique dynamic parameters in neuronal growth cones. *J Cell Biol* 158:139-152.

Schaks, M., G. Giannone, and K. Rottner. 2019. Actin dynamics in cell migration. *Essays Biochem* 63:483-495.

Schelski, M., and F. Bradke. 2017. Neuronal polarization: From spatiotemporal signaling to cytoskeletal dynamics. *Mol Cell Neurosci* 84:11-28.

Schelski, M., and F. Bradke. 2022. Microtubule retrograde flow retains neuronal polarization in a fluctuating state. *Science Advances* 8:

Schevzov, G., N.S. Bryce, R. Almonte-Baldonado, J. Josephine, J.J.-C. Lin, E. Hardeman, R. Weinberger, and P. Gunning. 2005. Specific Features of Neuronal Size and Shape Are Regulated by Tropomyosin Isoforms. *Molecular Biology of the Cell* 16:3425-3437.

Schiff, P.B., and S.B. Horwitz. 1980. Taxol stabilizes microtubules in mouse fibroblast cells. *PNAS* 77:1561-1565.

Schindelin, J., I. Arganda-Carreras, E. Frise, V. Kaynig, M. Longair, T. Pietzsch, S. Preibisch, C. Rueden, S. Saalfeld, B. Schmid, J.Y. Tinevez, D.J. White, V. Hartenstein, K. Eliceiri, P. Tomancak, and A. Cardona. 2012. Fiji: an open-source platform for biological-image analysis. *Nat Methods* 9:676-682.

Schneider, F., I. Metz, and M.B. Rust. 2023. Regulation of actin filament assembly and disassembly in growth cone motility and axon guidance. *Brain Res Bull* 192:21-35.

Schutt, C.E., M. Karlen, and R. Karlsson. 2022. A structural model of the profilin-formin pacemaker system for actin filament elongation. *Sci Rep* 12:20515.

Schwamborn, J.C., and A.W. Puschel. 2004. The sequential activity of the GTPases Rap1B and Cdc42 determines neuronal polarity. *Nat Neurosci* 7:923-929.

Shekhar, S., and M.F. Carlier. 2017. Enhanced Depolymerization of Actin Filaments by ADF/Cofilin and Monomer Funneling by Capping Protein

Cooperate to Accelerate Barbed-End Growth. *Curr Biol* 27:1990-1998 e1995.

Shikimoto, R., Y. Arai, S. Yuasa, Y. Gondo, S. Yasumoto, Y. Abe, and N. Hirose. 2022. Clinical course of the longest-lived man in the world: A case report. *Exp Gerontol* 159:111679.

Short, C.A., E.A. Suarez-Zayas, and T.M. Gomez. 2016. Cell adhesion and invasion mechanisms that guide developing axons. *Curr Opin Neurobiol* 39:77-85.

Smith, D.S., and J.H.P. Skene. 1997. A Transcription-Dependent Switch Controls Competence of Adult Neurons for Distinct Modes of Axon Growth. *The Journal of Neuroscience* 17:646-658.

Spence, E.F., D.J. Kanak, B.R. Carlson, and S.H. Soderling. 2016. The Arp2/3 Complex Is Essential for Distinct Stages of Spine Synapse Maturation, Including Synapse Unsilencing. *J Neurosci* 36:9696-9709.

Stepanova, T., J. Slemmer, C.C. Hoogenraad, G. Lansbergen, B. Dortland, C.I. De Zeeuw, F. Grosveld, G. van Cappellen, A. Akhmanova, and N. Galjart. 2003. Visualization of Microtubule Growth in Cultured Neurons via the Use of EB3-GFP (End-Binding Protein 3-Green Fluorescent Protein). *The Journal of Neuroscience* 23:2655-2664.

Stern, S., B.J. Hilton, E.R. Burnside, S. Dupraz, E.E. Handley, J.M. Gonyer, C. Brakebusch, and F. Bradke. 2021. RhoA drives actin compaction to restrict axon regeneration and astrocyte reactivity after CNS injury. *Neuron* 109:3436-3455 e3439.

Stiess, M., N. Maghelli, L.C. Kapitein, S. Gomis-Ruth, M. Wilsch-Bräuninger, C.C. Hoogenraad, I.M. Tolic-Norrelykke, and F. Bradke. 2010. Axon Extension Occurs Independently of Centrosomal Microtubule Nucleation. *Science* 327:704-707.

Stradal, T.E.B., M. Boiero Sanders, and P. Bieling. 2025. Arp2/3-complex regulation - Novel insights and open questions. *Curr Opin Cell Biol* 95:102565.

Strasser, G.A., N.A. Rahim, K.E. VanderWaal, F.B. Gertler, and L.M. Lanier. 2004. Arp2/3 is a negative regulator of growth cone translocation. *Neuron* 43:81-94.

Suchowerska, A.K., S. Fok, H. Stefen, P.W. Gunning, E.C. Hardeman, J. Power, and T. Fath. 2017. Developmental Profiling of Tropomyosin Expression in Mouse Brain Reveals Tpm4.2 as the Major Post-synaptic Tropomyosin in the Mature Brain. *Front Cell Neurosci* 11:421.

Sudhof, T.C. 2021. The cell biology of synapse formation. *J Cell Biol* 220:

Suter, D.M., A.W. Schaefer, and P. Forscher. 2004. Microtubule dynamics are necessary for SRC family kinase-dependent growth cone steering. *Curr Biol* 14:1194-1199.

Tahirovic, S., F. Hellal, D. Neukirchen, R. Hindges, B.K. Garvalov, K.C. Flynn, T.E. Stradal, A. Chrostek-Grashoff, C. Brakebusch, and F. Bradke. 2010. Rac1 regulates neuronal polarization through the WAVE complex. *J Neurosci* 30:6930-6943.

Takei, Y., J. Teng, A. Harada, and N. Hirokawa. 2000. Defects in Axonal Elongation and Neuronal Migration in Mice with Disrupted *tau* and *map1b* Genes. *The Journal of Cell Biology* 150:989-1000.

Tanaka, E.M., and M.W. Kirschner. 1991. Microtubule Behavior in the Growth Cones of Living Neurons during Axon Elongation. *The Journal of Cell Biology* 115:345-363.

Tang, F., E.W. Dent, and K. Kalil. 2003. Spontaneous Calcium Transients in Developing Cortical Neurons Regulate Axon Outgrowth. *The Journal of Neuroscience* 23:927-936.

Tedeschi, A., S. Dupraz, M. Curcio, C.J. Laskowski, B. Schaffran, K.C. Flynn, T.E. Santos, S. Stern, B.J. Hilton, M.J.E. Larson, C.B. Gurniak, W. Witke, and F. Bradke. 2019. ADF/Cofilin-Mediated Actin Turnover Promotes Axon Regeneration in the Adult CNS. *Neuron*

Tedeschi, A., S. Dupraz, C.J. Laskowski, J. Xue, T. Ulas, M. Beyer, J.L. Schultze, and F. Bradke. 2016. The Calcium Channel Subunit Alpha2delta2 Suppresses Axon Regeneration in the Adult CNS. *Neuron* 92:419-434.

Teng, J., Y. Takei, A. Harada, T. Nakata, J. Chen, and N. Hirokawa. 2001. Synergistic effects of MAP2 and MAP1B knockout in neuronal migration, dendritic outgrowth, and microtubule organization. *J Cell Biol* 155:65-76.

Thau, L., V. Reddy, and P. Singh. 2025. Anatomy, Central Nervous System. In StatPearls. StatPearls Publishing

Tosney, K.W., and L.T. Landmesser. 1985. Growth Cone Morphology and Trajectory in the Lumbosacral Region of the Chick Embryo. *The Journal of Neuroscience* 5:2345-2358.

Umeyama, T., S. Okabe, Y. Kanai, and N. Hirokawa. 1993. Dynamics of Microtubules Bundled by Microtubule Associated Protein 2C (MAP2C). *The Journal of Cell Biology* 120:451-465.

van Asperen, J.V., F. Kotaich, D. Caillol, and P. Bomont. 2024. Neurofilaments: Novel findings and future challenges. *Curr Opin Cell Biol* 87:102326.

van Beuningen, S.F., and C.C. Hoogenraad. 2016. Neuronal polarity: remodeling microtubule organization. *Curr Opin Neurobiol* 39:1-7.

van Beuningen, S.F.B., L. Will, M. Harterink, A. Chazeau, E.Y. van Battum, C.P. Frias, M.A.M. Franker, E.A. Katrukha, R. Stucchi, K. Vocking, A.T. Antunes, L. Slenders, S. Doulkeridou, P. Sillevis Smitt, A.F.M. Altelaar, J.A. Post, A. Akhmanova, R.J. Pasterkamp, L.C. Kapitein, E. de Graaff, and C.C. Hoogenraad. 2015. TRIM46 Controls Neuronal Polarity and Axon Specification by Driving the Formation of Parallel Microtubule Arrays. *Neuron* 88:1208-1226.

Viar, G.A., and G. Pigino. 2024. Tubulin posttranslational modifications through the lens of new technologies. *Curr Opin Cell Biol* 88:102362.

Vinopal, S., and F. Bradke. 2025. Centrosomal and acentrosomal microtubule nucleation during neuronal development. *Curr Opin Neurobiol* 92:103016.

Vinopal, S., S. Dupraz, E. Alfadil, T. Pietralla, S. Bendre, M. Stiess, S. Falk, G. Camargo Ortega, N. Maghelli, I.M. Tolic, J. Smejkal, M. Gotz, and F. Bradke. 2023. Centrosomal microtubule nucleation regulates radial migration of projection neurons independently of polarization in the developing brain. *Neuron* 111:1241-1263 e1216.

Vinson, V.K., E.M. De La Cruz, H.N. Higgs, and T.D. Pollard. 1998. Interactions of *Acanthamoeba* Profilin with Actin and Nucleotides Bound to Actin. *Biochemistry* 37:10871-10880.

Vitriol, E.A., and J.Q. Zheng. 2012. Growth cone travel in space and time: the cellular ensemble of cytoskeleton, adhesion, and membrane. *Neuron* 73:1068-1081.

Wang, A., Y.-Y. Xiang, B.B. Yang, and W.-Y. Lu. 2019. Neurexin-1alpha regulates neurite growth of rat hippocampal neurons. *Int J Physiol Pathophysiol Pharmacol* 11:115-125.

Wang, T., Y. Liu, X.H. Xu, C.Y. Deng, K.Y. Wu, J. Zhu, X.Q. Fu, M. He, and Z.G. Luo. 2011. Lgl1 activation of rab10 promotes axonal membrane trafficking underlying neuronal polarization. *Dev Cell* 21:431-444.

Washbourne, P., A. Dityatev, P. Scheiffele, T. Biederer, J.A. Weiner, K.S. Christopherson, and A. El-Husseini. 2004. Cell adhesion molecules in synapse formation. *J Neurosci* 24:9244-9249.

Wei, D., N. Gao, L. Li, J.X. Zhu, L. Diao, J. Huang, Q.J. Han, S. Wang, H. Xue, Q. Wang, Q.F. Wu, X. Zhang, and L. Bao. 2018. alpha-Tubulin Acetylation Restricts Axon Overbranching by Dampening Microtubule Plus-End Dynamics in Neurons. *Cereb Cortex* 28:3332-3346.

Wheeler, D.G., C.F. Barrett, R.D. Groth, P. Safa, and R.W. Tsien. 2008. CaMKII locally encodes L-type channel activity to signal to nuclear CREB in excitation-transcription coupling. *J Cell Biol* 183:849-863.

Wiegert, J.S., M. Mahn, M. Prigge, Y. Printz, and O. Yizhar. 2017. Silencing Neurons: Tools, Applications, and Experimental Constraints. *Neuron* 95:504-529.

Wioland, H., B. Guichard, Y. Senju, S. Myram, P. Lappalainen, A. Jegou, and G. Romet-Lemonne. 2017. ADF/Cofilin Accelerates Actin Dynamics by Severing Filaments and Promoting Their Depolymerization at Both Ends. *Curr Biol* 27:1956-1967 e1957.

Wit, C.B., and P.R. Hiesinger. 2023. Neuronal filopodia: From stochastic dynamics to robustness of brain morphogenesis. *Semin Cell Dev Biol* 133:10-19.

Witke, W. 2004. The role of profilin complexes in cell motility and other cellular processes. *Trends Cell Biol* 14:461-469.

Witte, H., D. Neukirchen, and F. Bradke. 2008. Microtubule stabilization specifies initial neuronal polarization. *J Cell Biol* 180:619-632.

Wojnacki, J., G. Quassollo, M.D. Bordenave, N. Unsain, G.F. Martinez, A.M. Szalai, O. Pertz, G.G. Gundersen, F. Bartolini, F.D. Stefani, A. Caceres, and M. Bisbal. 2024. Dual spatio-temporal regulation of axon growth and microtubule dynamics by RhoA signaling pathways. *J Cell Sci* 137:

Worth, D.C., C.N. Daly, S. Geraldo, F. Oozeer, and P.R. Gordon-Weeks. 2013. Drebrin contains a cryptic F-actin-bundling activity regulated by Cdk5 phosphorylation. *J Cell Biol* 202:793-806.

Wurz, A.I., A.M. Schulz, C.T. O'Bryant, J.F. Sharp, and R.M. Hughes. 2022. Cytoskeletal dysregulation and neurodegenerative disease: Formation, monitoring, and inhibition of cofilin-actin rods. *Front Cell Neurosci* 16:982074.

Wylie, S.R., and P.D. Chantler. 2003. Myosin IIA Drives Neurite Retraction. *Molecular Biology of the Cell* 14:4654-4666.

Xu, K., G. Zhong, and X. Zuhuang. 2013. Actin, Spectrin, and Associated Proteins Form a Periodic Cytoskeletal Structure in Axons. *Science* 339:452-456.

Yagoubat, A., and P.T. Conduit. 2025. Asymmetric microtubule nucleation from Golgi stacks promotes opposite microtubule polarity in axons and dendrites. *Curr Biol* 35:1311-1325 e1314.

Yamada, K.M., B.S. Spooner, and N.K. Wessells. 1971. Ultrastructure and function of growth cones and axons of cultured nerve cells. *The Journal of Cell Biology* 49:614-635.

Yamagishi, Y., K. Oya, A. Matsuura, and H. Abe. 2018. Use of CK-548 and CK-869 as Arp2/3 complex inhibitors directly suppresses microtubule assembly both in vitro and in vivo. *Biochem Biophys Res Commun* 496:834-839.

Yang, Q., Y. Ke, J. Luo, and Y. Tang. 2017. Protocol for culturing low density pure rat hippocampal neurons supported by mature mixed neuron cultures. *J Neurosci Methods* 277:38-45.

Yang, Q., X.F. Zhang, T.D. Pollard, and P. Forscher. 2012. Arp2/3 complex-dependent actin networks constrain myosin II function in driving retrograde actin flow. *J Cell Biol* 197:939-956.

Yang, R., Y. Zhang, J. Kang, C. Zhang, and B. Ning. 2024. Chondroitin Sulfate Proteoglycans Revisited: Its Mechanism of Generation and Action for Spinal Cord Injury. *Aging Dis* 15:153-168.

Yano, H., M. Yamamoto-Hino, M. Abe, R. Kuwahara, S. Haraguchi, I. Kusaka, W. Awano, A. Kinoshita-Toyoda, H. Toyoda, and S. Goto. 2005. Distinct functional units of the Golgi complex in *Drosophila* cells. *PNAS* 102:13467-13472.

Yau, K.W., P. Schatzle, E. Tortosa, S. Pages, A. Holtmaat, L.C. Kapitein, and C.C. Hoogenraad. 2016. Dendrites In Vitro and In Vivo Contain Microtubules of Opposite Polarity and Axon Formation Correlates with Uniform Plus-End-Out Microtubule Orientation. *J Neurosci* 36:1071-1085.

Yon, W.J., T. Ha, Y. Zheng, and R.T.A. Pedersen. 2025. A tubulin-binding protein that preferentially binds to GDP-tubulin and promotes GTP exchange. *J Biol Chem* 301:110401.

Young, T.H., J.H. Huang, S.H. Hung, and J.P. Hsu. 2000. The role of cell density in the survival of cultured cerebellar granule neurons. *J Biomed Mater Res* 52:748-753.

Zanet, J., A. Jayo, S. Plaza, T. Millard, M. Parsons, and B. Stramer. 2012. Fascin promotes filopodia formation independent of its role in actin bundling. *J Cell Biol* 197:477-486.

Zanic, M., J.H. Stear, A.A. Hyman, and J. Howard. 2009. EB1 recognizes the nucleotide state of tubulin in the microtubule lattice. *PLoS One* 4:e7585.

Zhang, W., and D.L. Benson. 2001. Stages of Synapse Development Defined by Dependence on F-Actin. *The Journal of Neuroscience* 21:5169-5181.

Zhong, G., J. He, R. Zhou, D. Lorenzo, H.P. Babcock, V. Bennett, and X. Zhuang. 2014. Developmental mechanism of the periodic membrane skeleton in axons. *Elife* 3:

Zhou, F.Q., C.M. Waterman-Storer, and C.S. Cohan. 2002. Focal loss of actin bundles causes microtubule redistribution and growth cone turning. *J Cell Biol* 157:839-849.

Zhou, J., A. Wang, Y. Song, N. Liu, J. Wang, Y. Li, X. Liang, G. Li, H. Chu, and H.W. Wang. 2023. Structural insights into the mechanism of GTP initiation of microtubule assembly. *Nat Commun* 14:5980.

Zuchero, J.B., and B.A. Barres. 2015. Glia in mammalian development and disease. *Development* 142:3805-3809.

Zweifel, M.E., and N. Courtemanche. 2020. Profilin's Affinity for Formin Regulates the Availability of Filament Ends for Actin Monomer Binding. *J Mol Biol* 432:166688.

Acknowledgements

Somehow it feels unreal that I finally get to write these lines now. It was always my dream to be a researcher at a renowned institute, to be curious and to try to better understand the big world of these little neurons that are so fascinating to me since I saw them the first time under a microscope. For this possibility, I would like to thank some people:
First of all, thank you Frank, for having me as a doctoral student, for your patience with me, when I constantly wanted to go in a different direction and wanted to explore every little thing I became interested in on this long journey. I am happy that I found at least one person that really laughs about my bad jokes.
Further, I express my gratitude to the members of my thesis committee, Prof. Walter Witke, Prof. Jörg Höhfeld and Prof. Sarah Egert.
All this work would not have been possible without the best support by Blanca, Sina and Jessy, for organisation of the lab, preparation of countless neuron cultures, writing of Tierversuchsanträge to be allowed to do experiments, and organising all these things a PhD student, out of a sudden, needs, immediately and as soon as possible. A big thank you to our wonderful assistants, Nasti, Nancy and Debbie, for your great support with all administrative affairs, organising business trips, helping to move through travel expense accountings and so much more. I also express my deepest gratitude to all members of the Bradke lab with whom I had the pleasure to work with. Thanks to Barbara for being also a friend after leaving the lab, for the great pizza nights and all other wonderful moments. Thanks to Seba, you fountain of knowledge, you are one of the most brilliant scientists I know, thank you for teaching me so much. Thanks to Andreas for sharing your taste of music, your balanced and calm nature and your electrophysiology skills and advice. Thanks to Max for the board game nights and of course discussing science and letting me contribute to the paper of your computational model that is a mathematical mystery to me. Thanks to Jarred for your positivity and great company in the docu zone, it is cool to have a friend on the other site of the world. The same is true for Emily H., thank you for your help and fun that we had, one day I will come to visit you and the Tasmanian devils. Thanks to Tien-chen, for always being open to discuss my ideas, experiments and thoughts, all the time. Thanks to Shweta, for your feedback and sharing your culture. Thanks to Kai for trying to improve my pronunciation of English words, of mayonnaise and soy sauce, for being a wonderful host for the bike-tour-barbeques and your company on the RE5 from time to time. Thanks to Emily B. for accepting my Danish flag, explaining to everyone that it is not the flag of England, for your superb knowledge about spinal cord injury and sharing British humour. Thanks to Juliane for your ideas, suggestions and advice for experiments and having us for a Spanish wedding. Thanks to Eissa for your support and the discussions for the paper revisions we were involved in together. Thanks to Annika, ‘my

student', for executing all the experiments and ideas I came up with, with your calm, relaxed and focused manner. It was a pleasure to have you as a student and to supervise you. Thanks to Cedric, 'my neighbour', for our discussions and being helpful with many things but also motivating me again and again to go running.

The biggest thank you is reserved for my parents and my family, my sister, my grandparents, aunts and uncles. Thank you for trusting me and giving me the opportunity to follow my dreams, and your boundless love and support. I know that it is only thanks to you and your support that I have made it to where I am now.

Thanks to all my friends who enrich my life with so many moments of joy and unforgettable memories and that encourage me that I am exactly right the way I am. Thank you Eva & Laura, Paul, Christoph, Martha & Benni, Nils, Barbara & Gigi, and all friends at the DZNE.

A very special thanks goes to Jerry, who brightens my life so infinitely with humour, joy, respect and love. Thank you for being by my side and loving me with all my rough edges, for accompanying me almost the entire way through my doctoral studies, and for being always there, exactly when I need you and your support. I love you!

I say thank you!